INFORMATION TO USERS

This manuscript has been reproduced from the microfilm master. UMI films the text directly from the original or copy submitted. Thus, some thesis and dissertation copies are in typewriter face, while others may be from any type of computer printer.

The quality of this reproduction is dependent upon the quality of the copy submitted. Broken or indistinct print, colored or poor quality illustrations and photographs, print bleedthrough, substandard margins, and improper alignment can adversely affect reproduction.

In the unlikely event that the author did not send UMI a complete manuscript and there are missing pages, these will be noted. Also, if unauthorized copyright material had to be removed, a note will indicate the deletion.

Oversize materials (e.g., maps, drawings, charts) are reproduced by sectioning the original, beginning at the upper left-hand corner and continuing from left to right in equal sections with small overlaps.

Photographs included in the original manuscript have been reproduced xerographically in this copy. Higher quality 6" x 9" black and white photographic prints are available for any photographs or illustrations appearing in this copy for an additional charge. Contact UMI directly to order.

Bell & Howell Information and Learning
300 North Zeeb Road, Ann Arbor, MI 48106-1346 USA
800-521-0600

GPS Studies of Crustal Deformation in the Northern Cascadia Subduction Zone

by

Joseph Alan Henton
B.S., New Mexico Institute of Mining & Technology, 1990
M.S., New Mexico Institute of Mining & Technology, 1994

A Dissertation Submitted in Partial Fulfillment of the
Requirements for the Degree of

DOCTOR OF PHILOSOPHY

in the School of Earth and Ocean Sciences

We accept this dissertation as conforming
to the required standard

Dr. Herb Dragert, Additional Member & Co-Supervisor (Research) (Pacific Geoscience Centre, Geological Survey of Canada)

Dr. Roy D. Hyndman, Member & Co-Supervisor (Research) (Pacific Geoscience Centre, Geological Survey of Canada; School of Earth and Ocean Sciences, & Department of Physics and Astronomy, University of Victoria)

Dr. George D. Spence, Co-Supervisor (Academic) (School of Earth and Ocean Sciences, & Department of Physics and Astronomy, University of Victoria)

Dr. Garry C. Rogers, Member, (Pacific Geoscience Centre, Geological Survey of Canada; School of Earth and Ocean Sciences, University of Victoria)

Dr. Rolf G. Lueck, Member, (School of Earth and Ocean Sciences, University of Victoria)

Dr. Jeffrey T. Freymueller, External Examiner, (Geophysical Institute, University of Alaska, Fairbanks)

Co-Supervisors: Dr. Herb Dragert and Dr. Roy D. Hyndman

ABSTRACT

Vancouver Island, located in southwestern coastal British Columbia, overlies the northern portion of the Cascadia Subduction Zone. This region is characterized by extensive seismicity which includes M~7 crustal earthquakes and less frequent M~9 megathrust events. Crustal deformation measurements have been carried out in this region since 1978 using various geodetic field techniques: levelling, tide gauge studies, precise gravity, laser ranging, and most recently, GPS. Earlier survey data provided key constraints to elastic slip-dislocation models for estimating the size and location of the rupture area for the next subduction-thrust earthquake. Recent estimates of crustal motions within the North Cascadia Margin based on both campaign GPS network surveys and up to 6.5 years of data from continuous GPS sites are consistent with the strain accumulation expected from a locked subduction fault. The deformation vectors are in the direction of plate convergence within the uncertainty of plate motion models. The observed strain rate across Vancouver Island is, however, smaller (by approximately a factor of 1.5) than the dislocation model prediction, suggesting the presence of visco-elastic effects. Crustal deformation measurements for central Vancouver Island fail to resolve motions that could be associated with the occurrence of large crustal earthquakes, and also suggest that the extent of the seismogenic subduction thrust zone north of the Nootka Fault Zone is extremely limited.

Examiners:

Dr. Herb Dragert, Additional Member & Co-Supervisor (Research) (Pacific Geoscience Centre, Geological Survey of Canada)

Dr. Roy D. Hyndman, Member & Co-Supervisor (Research) (Pacific Geoscience Centre, Geological Survey of Canada; School of Earth and Ocean Sciences, & Department of Physics and Astronomy, University of Victoria)

Dr. George D. Spence, Co-Supervisor (Academic) (School of Earth and Ocean Sciences, & Department of Physics and Astronomy, University of Victoria)

Dr. Garry C. Rogers, Member, (Pacific Geoscience Centre, Geological Survey of Canada; School of Earth and Ocean Sciences, University of Victoria)

Dr. Rolf G. Lueck, Member, (School of Earth and Ocean Sciences, University of Victoria)

Dr. Jeffrey T. Freymueller, External Examiner, (Geophysical Institute, University of Alaska, Fairbanks)

TABLE OF CONTENTS

LIST OF TABLES

LIST OF FIGURES

ACKNOWLEDGMENTS

I wish to thank my entire graduate committee for their time, encouragement, guidance, and support over the past years. I appreciate all of their recent efforts and patience in reviewing my dissertation, especially under the tight deadlines and circumstances necessary to meet the graduation requirements for Spring convocation. I additionally would like to thank Drs. Garry Rogers and George Spence for their assistance with my initial application to, and subsequent enrollment in the School of Earth and Ocean Sciences at the University of Victoria. I am greatly honoured to have worked with Drs. Herb Dragert and Roy Hyndman, my supervisors, on this project. I cannot fully express how grateful I am to them.

I also wish to thank *everyone* I've worked with at the Pacific Geoscience Centre. I do not wish to diminish the help or friendship of any person with this blanket statement, but rather to acknowledge the terrific, universal support I have enjoyed at PGC. It has been a truly stimulating environment to pursue my studies. I thank the Geological Survey of Canada for providing work space and access to a wonderful facility. I would, in particular, like to thank all of my PGC Swamp colleagues (Dan, Ben, Taimi, Paul, Alison, and Alex) for their friendship and contributions to a great working environment. Kelin Wang has offered exceptional support as an "honourary" committee member. Yuan Lu and Richard Baldwin have provided generous assistance with computer systems and problems. Additionally, Mike Schmidt has provided immeasurable assistance with much of the GPS data.

I wish to thank my family for all of their support. I am especially grateful to my wife, Erin, for her love, patience, and support. I could not have won a PGC Gold Star award for "Best Excuse for Thesis Procrastination" (*i.e.* marriage) without her.

Finally, I would like to dedicate this dissertation to my mother, Rosemary.

CHAPTER 1 - INTRODUCTION

This dissertation is an investigation of plate interactions at an active tectonic margin and the resulting patterns of current crustal deformation. The strain and velocity fields have been mapped in the northern and landward portion of the Cascadia Subduction Zone (CSZ) region employing geodetic-quality Global Positioning System (GPS) based techniques. The measured pattern of deformation has been compared to the predictions from models of deformation cycles for large subduction-thrust earthquakes. The dissertation includes a technical contribution through a refinement of the GPS technique for monitoring interseismic crustal deformation. This refinement resulted from studying the nature of the noise and other non-tectonic signals present in the GPS-determined deformation time-series and removing them to achieve the cleanest possible tectonic signals. Through the constraints of this high accuracy deformation field and the associated fault modelling, the scientific contributions of this dissertation are a vastly improved definition of the northern portion of the CSZ fault surface that is locked and may produce large earthquakes, the first estimates of full strain rate tensors for crustal deformation on Vancouver Island, and the delineation of possible relationships between the megathrust great earthquake cycle and nearby large crustal earthquakes.

1.1 - Stepping Back to a Broader Context

The Cascadia Subduction Zone (CSZ) is one of a few margins located around the Pacific Rim where young (<20 Ma) oceanic lithosphere is being subducted (Figures 1.1 & 1.2). Most of these "young" subduction margins have produced great (M > 8) historical thrust earthquakes [*Rogers*, 1988]. The youth of the subducting oceanic lithosphere makes the CSZ analogous to the Nankai Trough (SW Japan), the Rivera Margin and the Northern

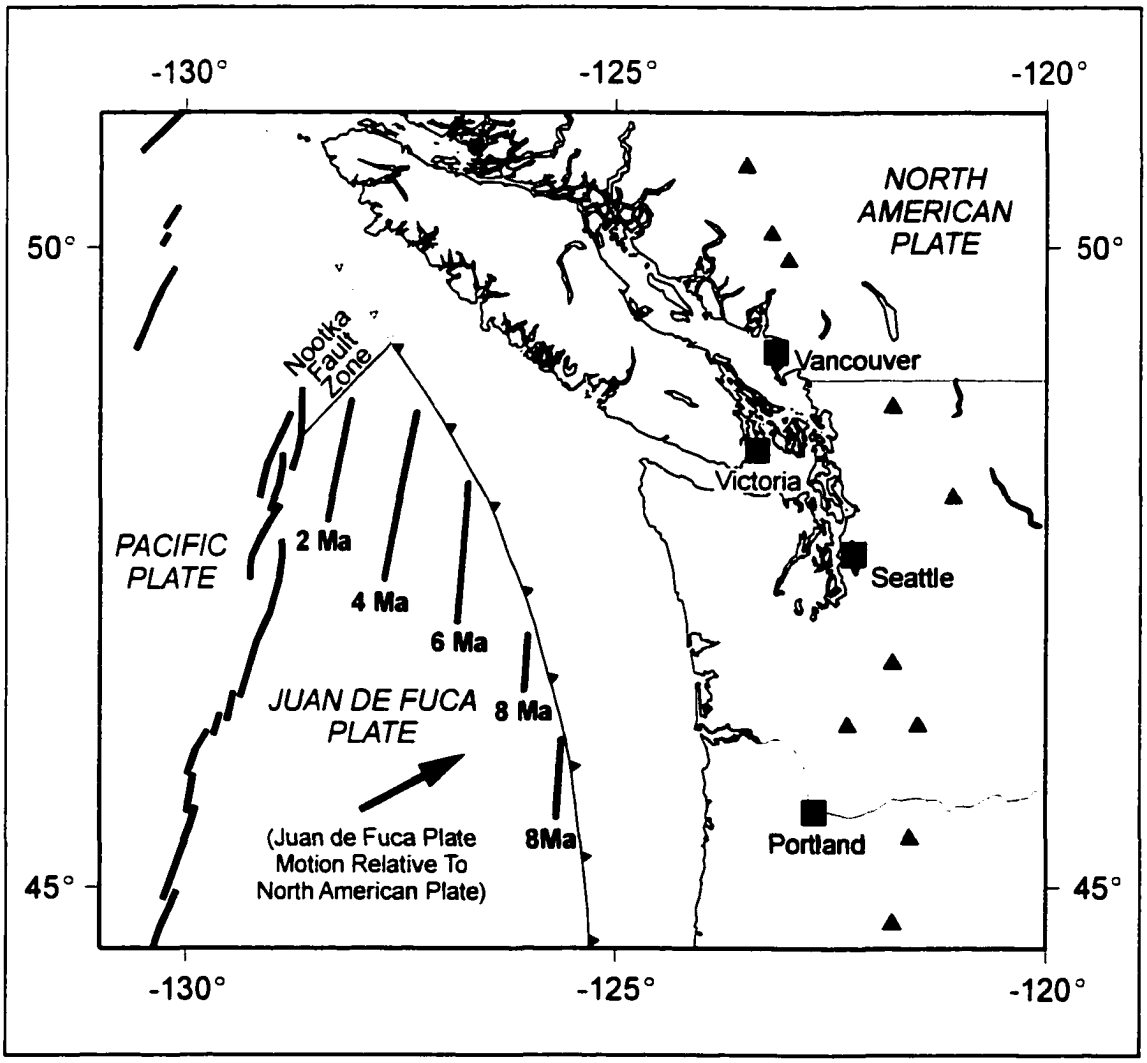

Figure 1.1. Distribution of age of the northern portion of the subducting Juan de Fuca plate along the Cascadia Subduction Zone margin. Ages are in millions of years before the present (after *Davis & Hyndman* [1989]).

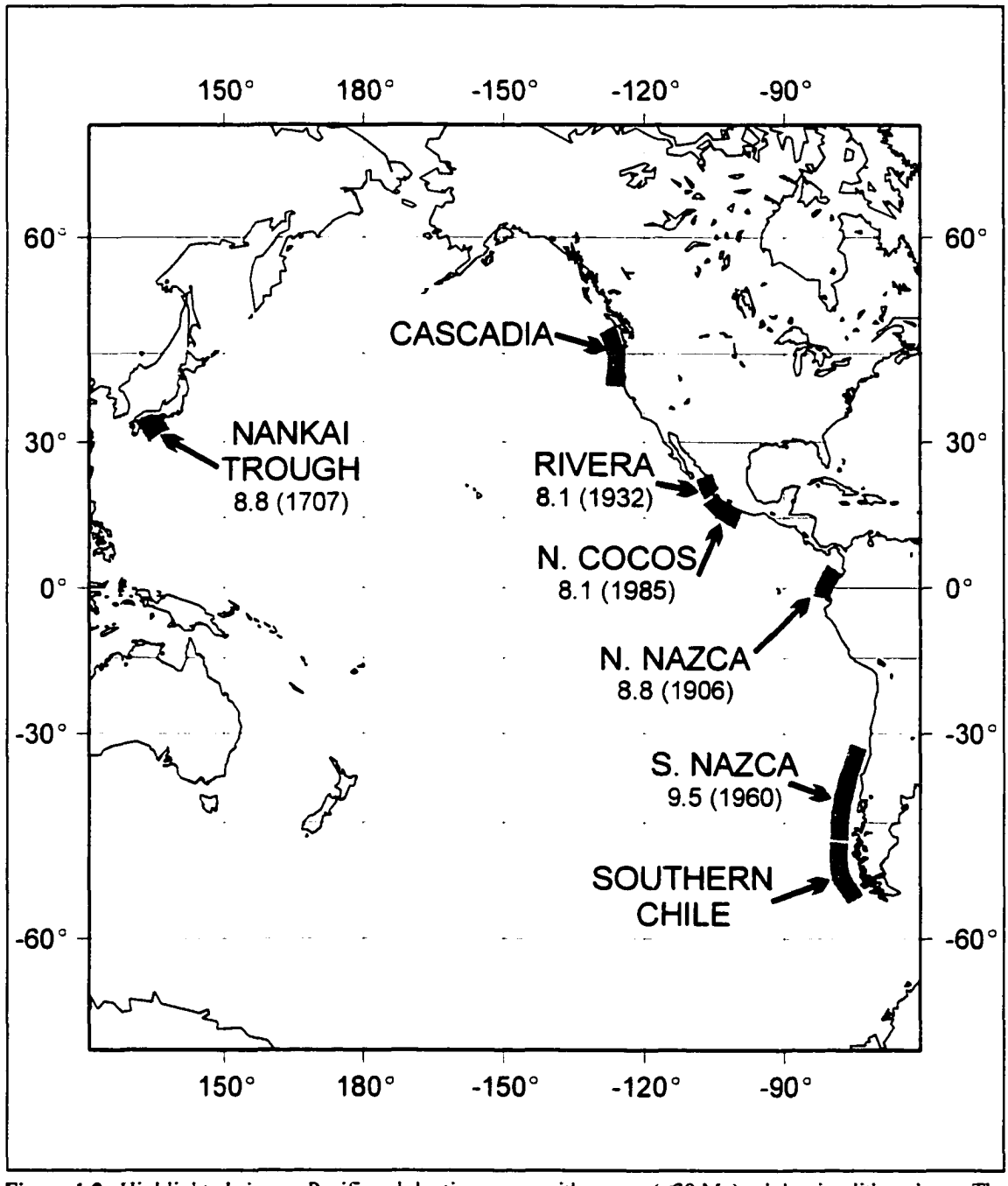

Figure 1.2. Highlighted circum-Pacific subduction zones with young (<20 Ma) subducting lithosphere. The magnitude (and year) of the largest historically known earthquake for each margin are given (Cascadia and Southern Chile have had no historically recorded great earthquakes) (after *Rogers* [1988]).

Cocos Trench (Mexico), the Northern Nazca Trench (Colombia), and the Southern Chile and the Southern Nazca Trenches (Chile) [*Rogers*, 1988]. In general terms, this study addresses the great earthquake hazard that appears to be characteristic of young subduction zones.

The main factors affecting earthquake hazard in subduction zones are the maximum magnitude of earthquakes, their frequency of occurrence, and the landward limit of the rupture zone. In the CSZ and other similar tectonic regimes, the young subducting oceanic lithosphere is initially gravitationally buoyant [*Molnar and Atwater*, 1978; *Rogers*, 1988]. Hence, the subduction angle is typically shallower for younger lithosphere. A correlation between lithospheric age (and plate convergence rate) with the maximum earthquake magnitude for subduction zones was advanced by *Ruff and Kanamori* [1980]:

$$M_w = -0.00889T + 0.134V + 7.96 \qquad (1.1)$$

where M_w is the maximum moment magnitude, T is age (Ma) of the subducting plate at the trench, and V is the relative convergence speed (cm/yr). Although other subduction zone parameters have been investigated, the best correlation with moment release appears to be the one with T and V found by *Ruff and Kanamori* [1980] [*e.g. Scholz*, 1990; *Rogers*, 1988; *Jarrard*, 1986]. Additionally, Kelin Wang (GSC-PGC) notes that margins with young subducting oceanic lithosphere are capable of rupture along nearly their entire lengths [*pers. com.*, 2000].

However, while the relationship of the age of subducted lithosphere to the seismic moment release of subduction zone thrust earthquakes may provide a rough measure of maximum magnitude, it yields little insight on the timing or frequency of great (M>8)

events. A reliable estimate of the return periods of great earthquakes and of the rupture area are fundamental to the accurate estimation of seismic hazard. Since the frequency of great earthquakes in the CSZ is low, the nature and the spatial and temporal distribution of these events are poorly known [*Rogers*, 1988]. Paleoseismic studies have been used to extend the great earthquake record back in time in the CSZ. Working predominantly in coastal zones and the deep-sea floor along the Cascadia margin, paleoseismic research has yielded information on the temporal history of regional megathrust subduction earthquakes [*e.g. Atwater*, 1987; *Adams*, 1990; *Atwater et al.*, 1995; *Clague*, 1997; *Clague and Bobrowski*; 1994].

The earthquake hazard associated with large (M>7) crustal earthquakes that occur on Canada's west coast is also difficult to determine accurately from the short historical record of such events. Furthermore, the spatial pattern of smaller magnitude earthquakes appears to be different from that of the large events, so the frequent small events cannot be used to predict the frequency and spatial distribution of large events. Geologic mapping of recent faults to investigate the problem of large intracrustal earthquakes has proven to be difficult in this area because few earthquakes have surface rupture and so far, such mapping has provided little constraint to earthquake hazard estimates.

1.2 - Technical Perspectives

Recent developments in the use of GPS and other high-precision geodetic methods for monitoring crustal motions now allow the identification of regions with elastic strain buildup where large earthquakes are likely to occur, and provide insights into the underlying

causes of these earthquakes. In this study, crustal strain accumulation has been measured and its variations mapped along the plate margin. Since permanent strain at rates of greater than ~1 mm/yr (*i.e.* 1 km/Ma) across the width of the margin would produce large deformation structures over geologically short times that are not observed, such deformation rates may be taken as mainly elastic, to be released in future earthquakes.

Previous crustal deformation studies in the region included repeated high-precision levelling, long-term tide gauges, repeated laser ranging, precise gravity, and trilateration [*Dragert et al.*, 1994]. The newest and most rapidly expanding technique to monitor crustal deformation employs the satellite-based Global Positioning System (GPS). The GPS technique as a tool for helping to address crustal geodynamics problems is not a *fait accompli*, but rather a developing technology. This dissertation makes a technical contribution by refining the GPS technique as a tool for measuring crustal deformation. As the deformation signal in the CSZ region is rather modest, generally <10mm/yr (relative to North America), it is particularly important to remove as much noise and non-tectonic signal as possible. This is especially true if the objectives of deformation monitoring include the resolution of even smaller spatial strain variations associated with M~7 events in the forearc crust.

The source of GPS data used in this study includes both a sparse network of continuously recording sites, and two dense networks of repeat-measurement campaign sites. Continuous GPS tracker sites that monitor crustal motion at a limited number of critical locations provide regional reference sites and yield insight into the temporal GPS noise budget. Higher density GPS campaign strain networks in combination with the continuous

GPS tracker network allow more detailed regional strain estimates. Important technical questions concern the nature of the GPS noise and other non-tectonic signals in the GPS data. There are probably non-tectonic periodic and transient signals present in the site position continuous time-series. It is unlikely that these non-tectonic signals are unique to the time-series of this study and their identification may have a broader significance as GPS networks elsewhere begin to address smaller deformation signals.

1.3 - Scientific Perspectives

This dissertation targets the northern portion of the Cascadia Subduction Zone, where the plate interactions are poorly constrained and the regional strain pattern was largely unknown. While a general model of deformation for the CSZ had been produced previously, there were only a few unconnected areas where deformation measurements had been reported for the northern region. GPS data from this study have enabled the mapping of the regional velocity field resulting from the locked subduction thrust fault, thereby establishing better constraints for the regional tectonic model.

A young subducted lithosphere typically is seismically well-coupled to the overriding plate. The degree and region of coupling on the megathrust surface is an important problem addressed in this study. Plate coupling in this study refers to the amount of interseismic plate motion accommodated across a fault surface (*i.e.* a fully locked fault is 100% coupled and will have a slip deficit equal to the amount of relative plate motion). Heterogeneous coupling along the plate contact will result in a heterogeneous strain distribution. Interplate regions that are less than 100% coupled will acquire smaller slip-deficits than the plate

convergence rate. The presence of a reduced slip-deficit can be resolved through deformation measurements.

A high spatial density of GPS sites that monitor crustal deformation allows both megathrust problems and large intracrustal earthquake problems to be addressed. In particular, the spatial distribution of strain accumulation can be mapped on two scales with precise GPS monitoring. First, the regional pattern defines the locked seismogenic portion of the megathrust surface. Second, by removing this signal, it is possible to identify smaller strain patterns that are not directly associated with the megathrust surface, and may be related to M~7 crustal events.

With respect to these issues, the scientific problems addressed by this dissertation can be summarized as follows:

1.) *The three-dimensional area of the locked portion of the northern Cascadia (Juan de Fuca Plate) megathrust fault.* What is the location, geometry and plate coupling of the seismogenic zone, including the northern boundary, that produces the regional deformation field and that will rupture to generate the next great subduction-thrust earthquake in this region? Are there areas where the fault is not completely locked?

2.) *The nature of the strain field that produces large, shallow crustal earthquakes (such as those that occurred in 1872, 1918, and 1946).* Are large crustal earthquakes a response to margin-parallel compression in the forearc? Are they associated with coupling on

the subduction thrust? Can strain measurements indicate whether such damaging earthquakes occur in well defined areas or are likely to occur throughout the region?

3.) *The nature of plate margin geometry and plate interactions for the Explorer Plate and Nootka transform fault to the north of the main portion of the CSZ.* How may the strain associated with these interactions influence the nature and frequency of significant earthquakes?

CHAPTER 2 - TECTONIC SETTING

2.1 - Introduction

The Cascadia Subduction Zone (CSZ) is the dominant tectonic feature along the coastal regions of southwestern Canada and the Pacific Northwest of the United States. At the CSZ, the oceanic Juan de Fuca plate subducts beneath the overriding continental North American plate (Figure 2.1). Occurring in an approximately east-northeasterly direction at a rate of 40-45 mm/yr [*De Mets et al.*, 1994, 1990; *Riddihough*, 1984], relative plate convergence is margin-normal for the northern portion of the CSZ and oblique to the central and southern portions of the Cascadia margin. To the north of the CSZ, north of Vancouver Island, the Queen Charlotte fault system is a transform margin between the Pacific oceanic and North American continental plates. The present tectonics (*e.g.* convergence rate and direction) of both the Winona Block and the Explorer sub-plate, which lie between the Juan de Fuca system to the south and the Queen Charlotte system to the north, are not well-constrained [*Rohr and Furlong*, 1995]. To the south, subduction ceases near the Medocino Triple Junction and right-lateral Pacific-North America transform motion occurs to the south along the San Andreas Fault system.

The CSZ itself displays many properties associated with subduction zones including: a deformed accretionary sedimentary prism, a dipping Benioff-Wadati earthquake zone, an active volcanic arc (*e.g.* historical eruptions of Mount St. Helens & Mt. Lassen), typical patterns of gravity anomalies and heat flow, earthquake seismicity in the overriding plate,

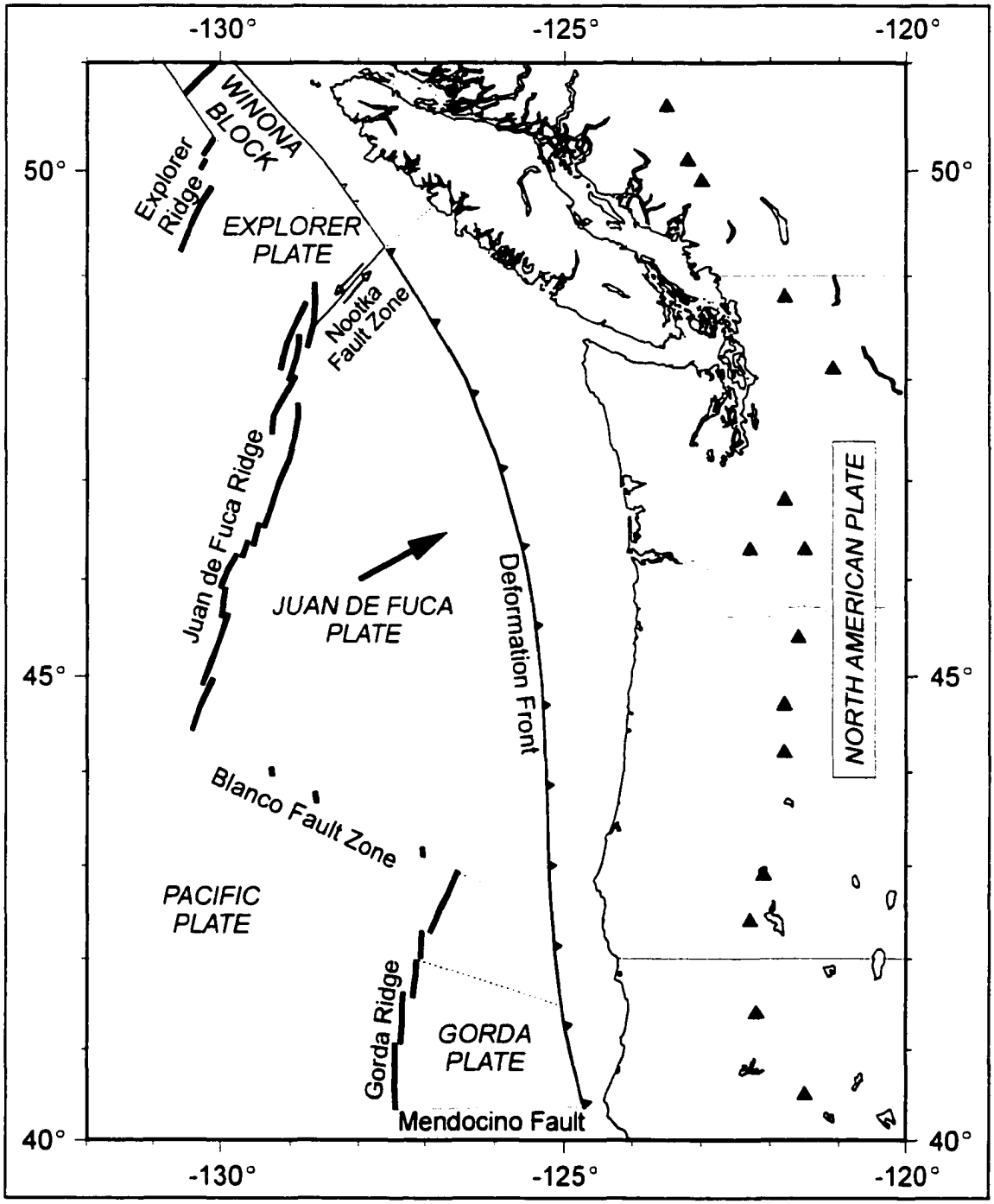

Figure 2.1. Map of the Cascadia Subduction Zone margin. Juan de Fuca plate convergence motion relative to North America occurs in a northeastly direction as shown by the large, solid arrow. Triangles represent the volcanic centres of the Cascadia Subduction Zone volcanic arc.

and current crustal deformation along the coastal zone. Cascadia is distinct from "typical" subduction zones in that the subducting lithosphere is young and there have been no large earthquakes on the subduction thrust surface in historical time [*Rogers*, 1988; *Milne et al.*, 1978]. Although there have been no historical earthquakes on the thrust surface, elastic strain is observed to be accumulating in the CSZ with resulting surface deformation rates on the order of millimetres per year [*Savage et al.*, 1991; *Dragert et al.*, 1994; *Mitchell et al.*, 1994; *Dragert and Hyndman*, 1995; *Henton et al.*, 1998, 1999]. Additionally, there is clear paleoseismic evidence of great pre-historic thrust earthquakes along this margin [e.g. *Atwater*, 1987; *Atwater et al.*, 1995; *Adams*, 1990; *Clague and Bobrowski*, 1994; *Clague*, 1997].

2.2 - Earthquake Hazard Sources and Their Deformation Patterns

Earthquake hazard in the region of the CSZ is not limited to megathrust interplate events; there are two additional seismic hazards that are important in subduction zones: deep earthquakes within the underthrusting oceanic slab, and shallow earthquakes within the continental crust (Figure 2.2). Historical large and destructive events have occurred in the northern CSZ region from both of these additional source regions. The largest recorded slab earthquakes were ~50 km deep below the southern Puget Sound region and occurred in 1949 (M=6.9) and 1965 (M=6.5). However, due to their depths, this type of event is unlikely to produce an interseismic surface deformation signal resolvable by current geodetic techniques.

Numerous small (M<5) crustal earthquakes occur in the vicinity of northern

Cascadia, primarily around the Puget Sound-Strait of Georgia region (Figure 2.3). These earthquakes are caused by north-south compression in the forearc generated by the oblique plate convergence in the CSZ system [*Wang et al.*, 1995; *Wang*, 2000] and/or by northward moving coastal blocks [*Wells et al.*, 1998]. Three historical large crustal earthquakes (M≥7) have occurred in the northern Cascadia region in areas with reduced present-day background seismicity: 1918 (M=7.0) and 1946 (M=7.3) near central Vancouver Island, and 1872 (M=7.4) near the United States-Canada border [*Rogers*, 1983]. The accumulation of strain

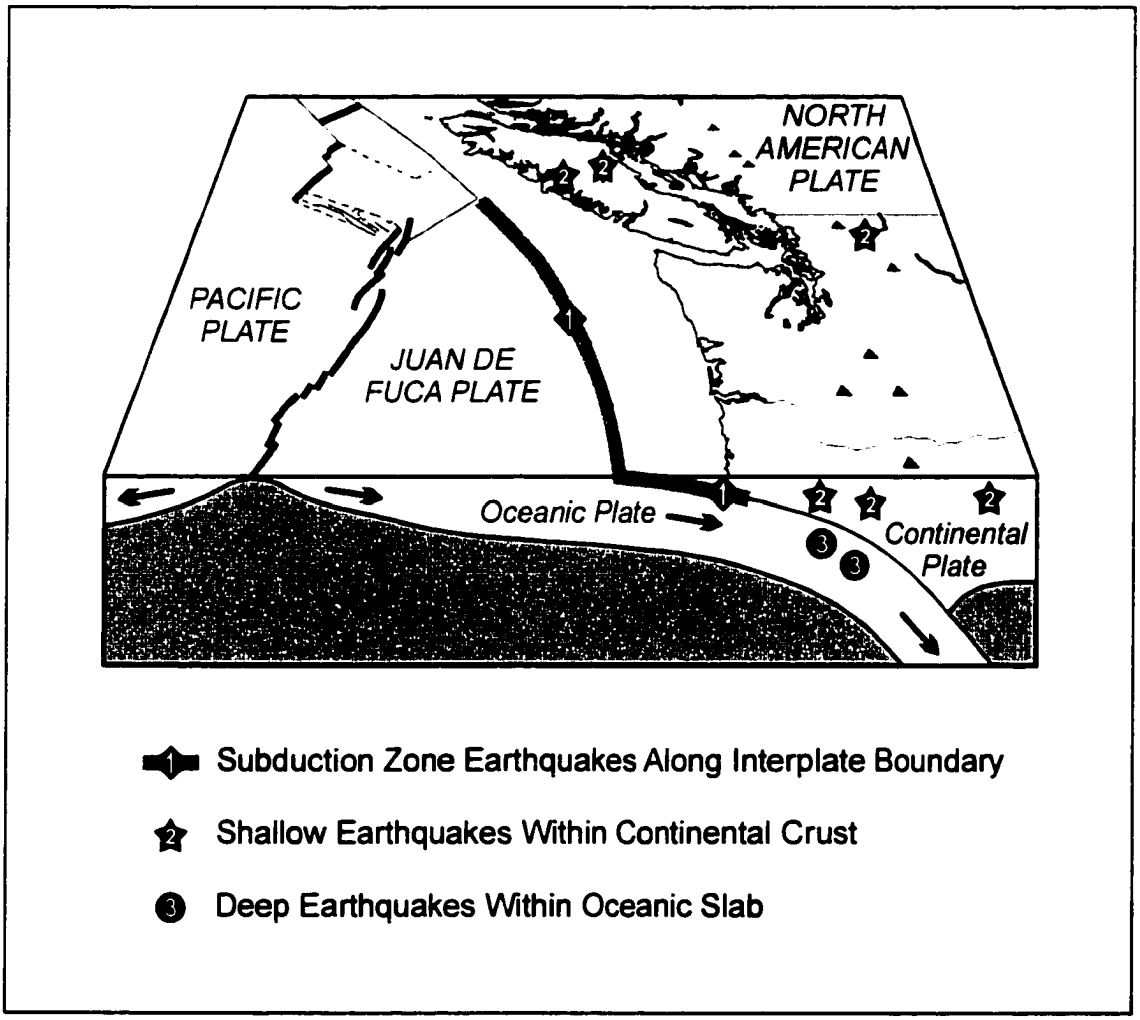

Figure 2.2. Earthquake hazard source regions in northern Cascadia. The three regions capable of producing large earthquakes are illustrated

associated with this type of crustal earthquake may produce an observable surface deformation signal. For inland locations, large crustal earthquakes (M ~6-7) comprise a greater seismic hazard due to the greater frequency of these events (relative to Cascadia megathrust events) and their shallower hypocentres. However, the tectonic origin and the nature of the deformation associated with these larger intracrustal events are not clear. The central Vancouver Island events could be associated with the shear generated by the underthrusting Nootka fault zone. Alternatively, they could be the result of margin parallel

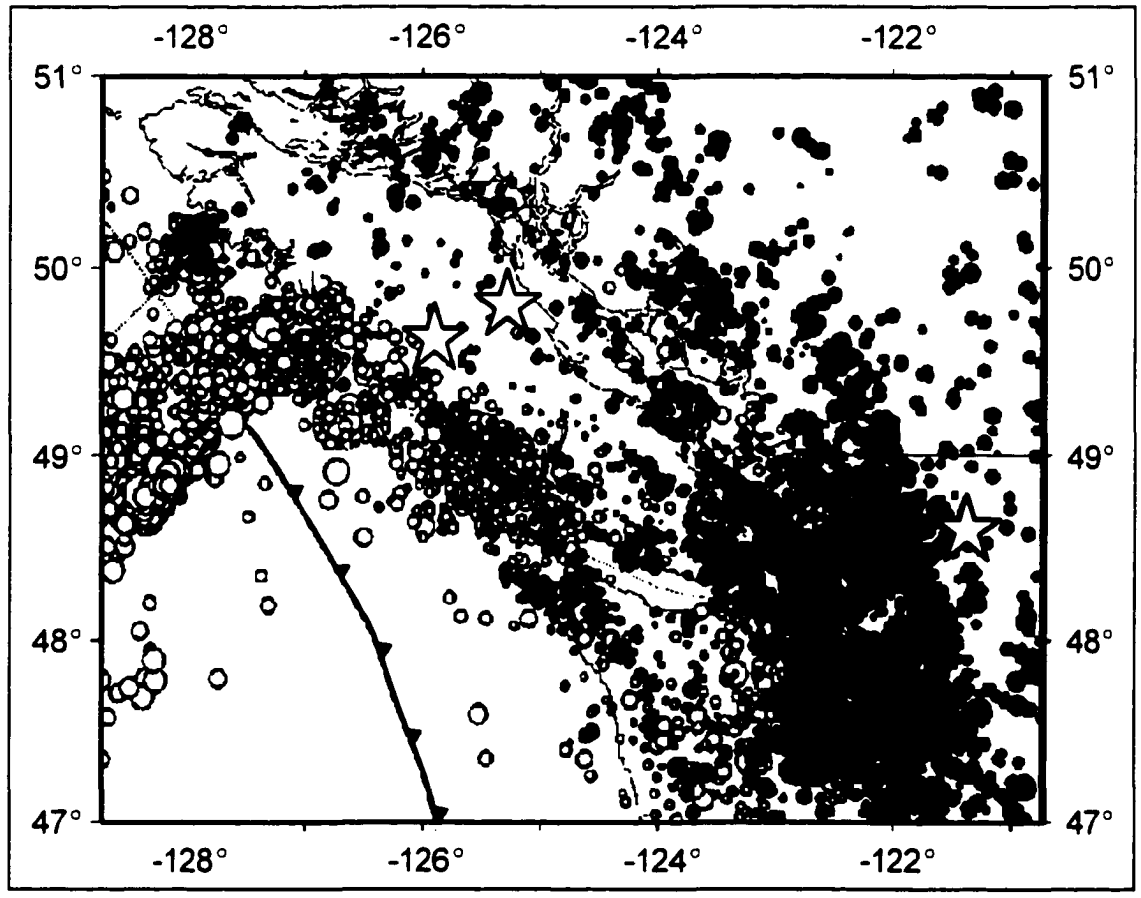

Figure 2.3. Earthquake seismicity of the northern Cascadia region. Open stars represent the three largest historical crustal earthquakes. Circles represent instrumentally recorded seismicity for the period 1980-1996 (*data from* GSC and UW catalogues, provided by PGC Seismology Group) and are scaled by magnitude (open circles indicate events within the oceanic plate; filled circles indicate events within the continental plate). Stars indicate the locations of large (M≥7), historical crustal earthquakes in the region.

compression from oblique subduction. Among the questions that remain are: Is the permanent (non-elastic) deformation fully accounted for by the present-day, numerous small events or are more frequent larger crustal earthquakes required? Is the crustal strain distributed uniformly over the entire seismic region or are there areas with concentrated strain accumulation indicative of an interseismic signal of an impending large earthquake?

The primary crustal deformation signal expected along the Cascadia margin is that associated with the great thrust-earthquake cycle of the Cascadia Subduction Zone. The earthquake cycle can be simplified into two stages (Figure 2.4). In the interseismic period, between events, the two plates are locked over some finite area of the contact zone between the two plates. Plate convergence continues and results in elastic strain accumulation in regions of the crust close to the locked fault zone. The upper plate compresses resulting in uplift and horizontal shortening across the coastal zone, and the width and location of the locked zone can be constrained from the pattern of surface deformation. Earthquake rupture of the locked zone results in coseismic subsidence and horizontal extension or rebound across the coastal zone as elastic strain built up during the interseismic period is released. A number of complications to this simple 2-D model, such as end effects, the three-dimensional nature of the fault surface geometry, and non-elastic deformation are discussed in the modelling section.

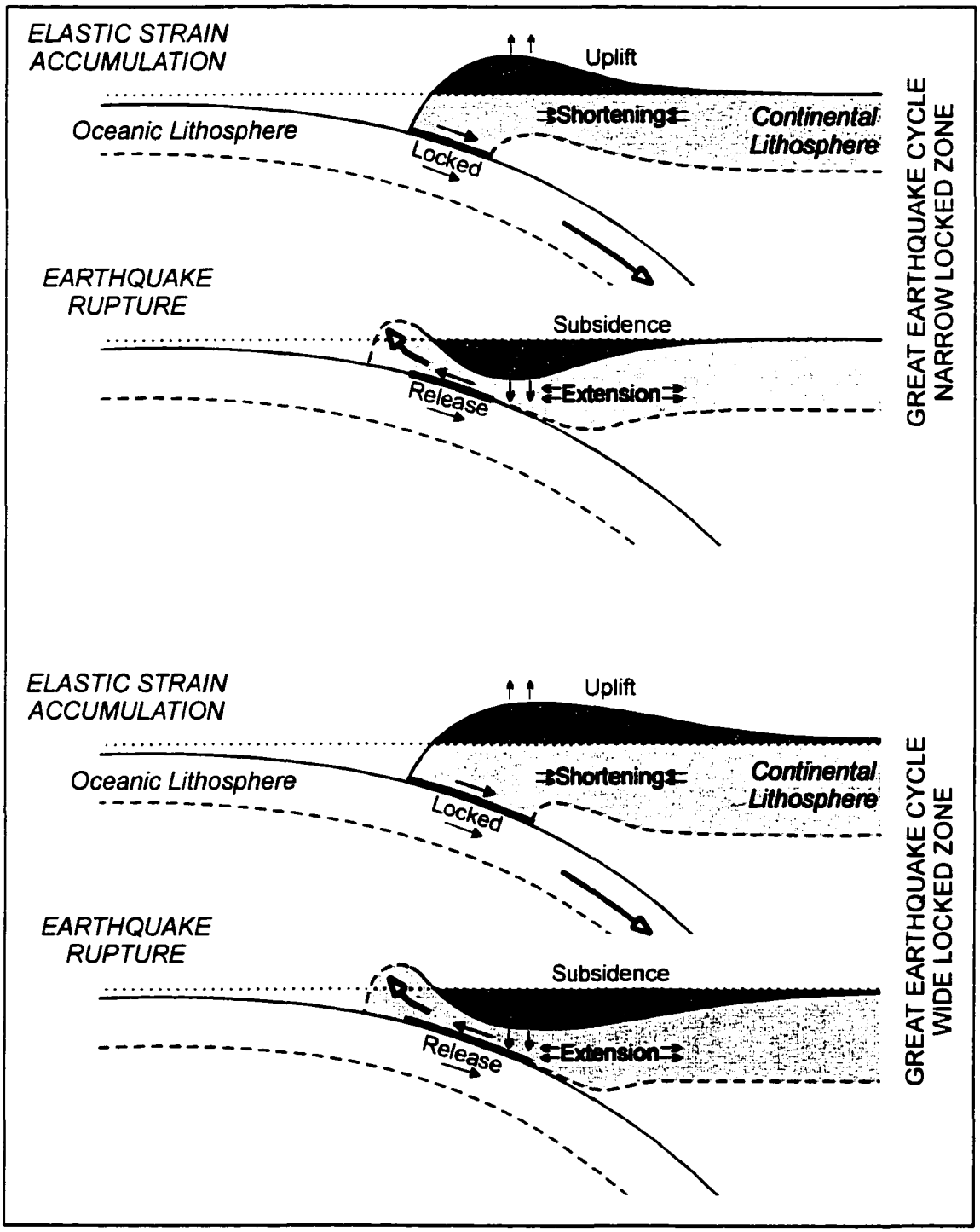

Figure 2.4. Simplified earthquake cycle model for two locked zone widths [after *Dragert et al.*, 1994].

CHAPTER 3 - GPS APPLICATIONS FOR STUDYING REGIONAL DEFORMATION

3.1 - Introduction

The Global Positioning System (GPS) was originally developed by the U.S. Department of Defense (DoD) to be an all-weather, real-time aid to navigation for the military. The system is based upon an orbiting constellation of satellites (Figure 3.1 & Figure 3.2). The advancement of miniaturized computer technology and reduction in cost of GPS receivers has led to the system being applied to a broad range of applications, primarily in the fields of navigation and precise surveying. Numerous texts [*e.g. Wells et al.*, 1986; *Hofmann-Wellenhof et al.*, 1993; *Leick*, 1995] discuss the details of GPS technology.

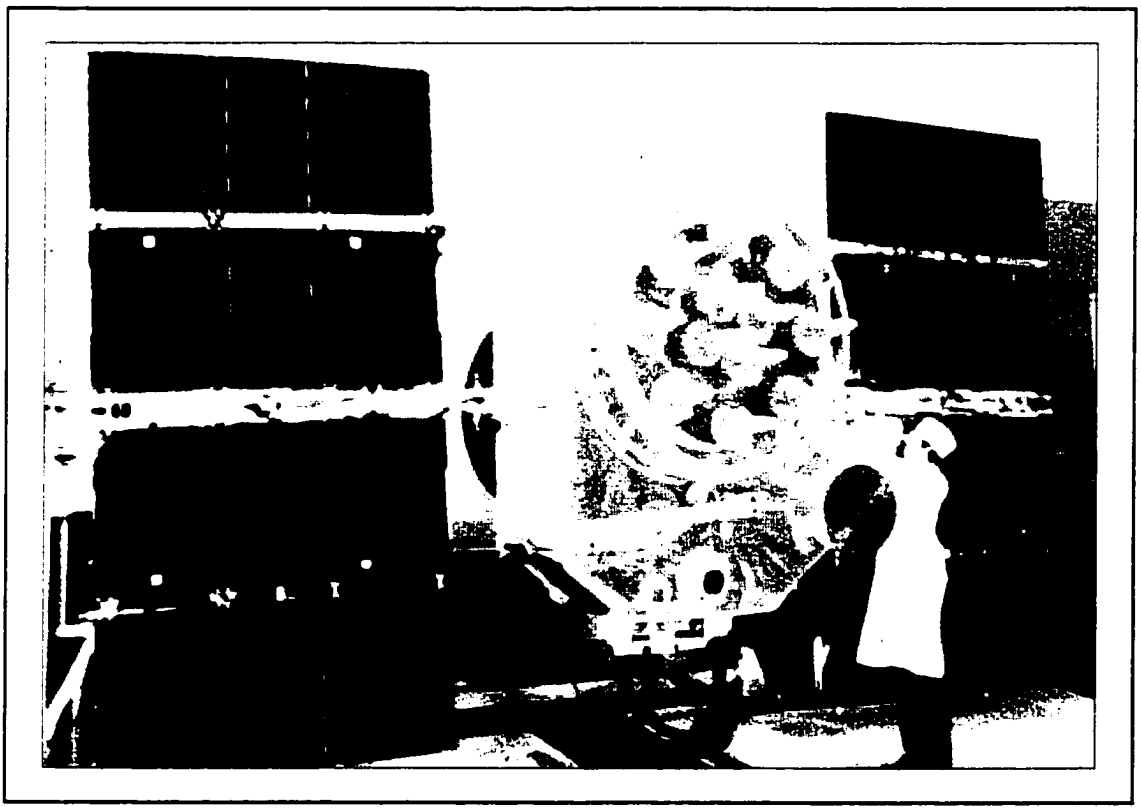

Figure 3.1. GPS NAVSTAR Block II satellite (*from* www.navcen.uscg.mil).

This chapter describes the applications of GPS for monitoring regional-scale crustal deformation in the northern Cascadia Subduction Zone (CSZ) and the infrastructure used in this study.

For the GPS studies of crustal deformation in the northern CSZ described in this work, differential techniques have been employed such that the positions of permanent

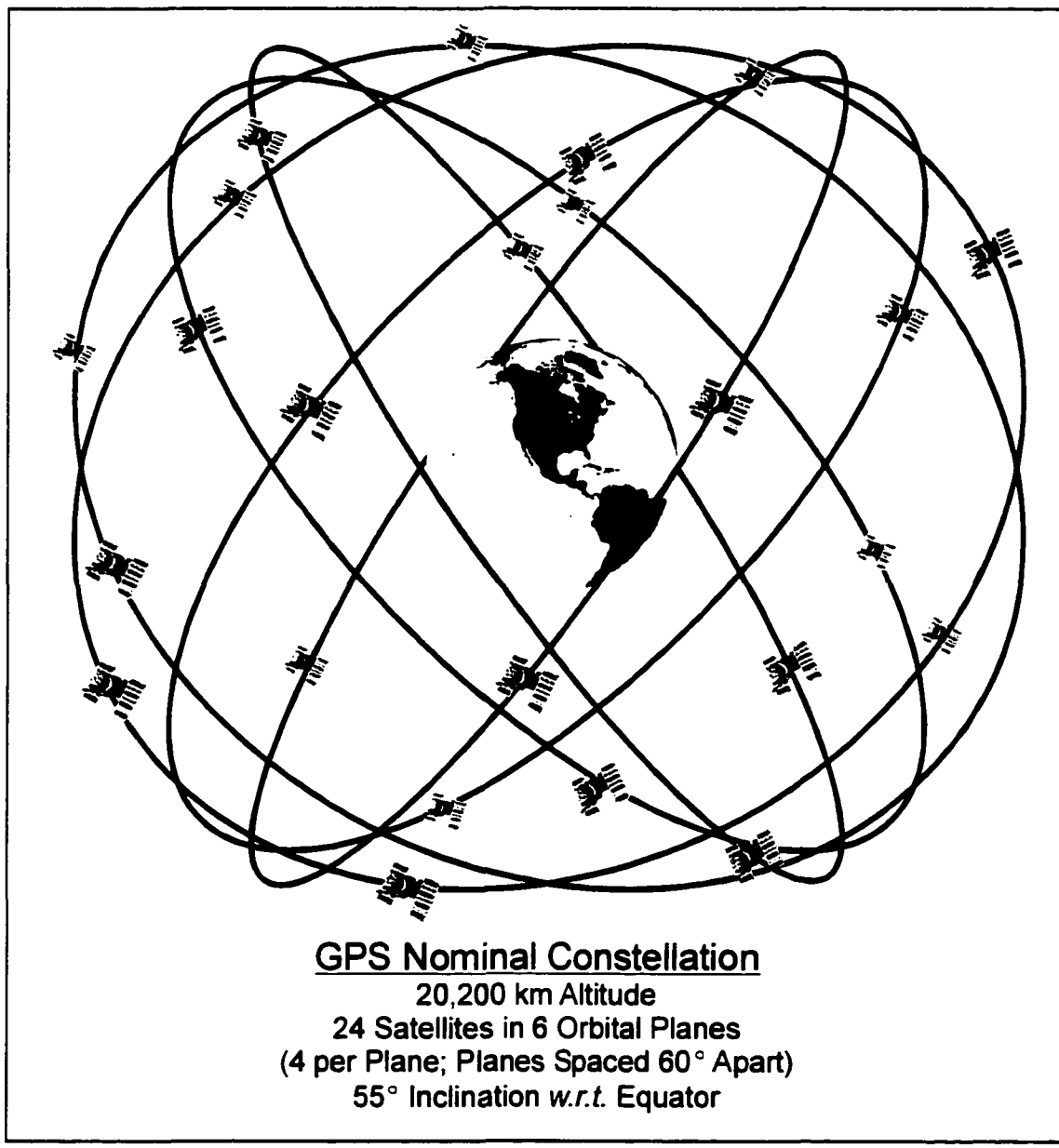

Figure 3.2. GPS satellite constellation [modified after *Dana*, 1998].

survey markers are measured with respect to some reference site over a period of time. The reference site is chosen to be sufficiently remote from the deforming areas of the Cascadia margin so that it can be considered to be part of stable North America, yet close enough to enable the elimination of common systematic errors in the analysis of GPS data (Figure 3.3). Two types of GPS measurements were used in this study: (1) continuous GPS data from a relatively sparse network of GPS tracking stations, and (2) GPS field campaign data collected through repeated surveys of more densely spaced strain networks.

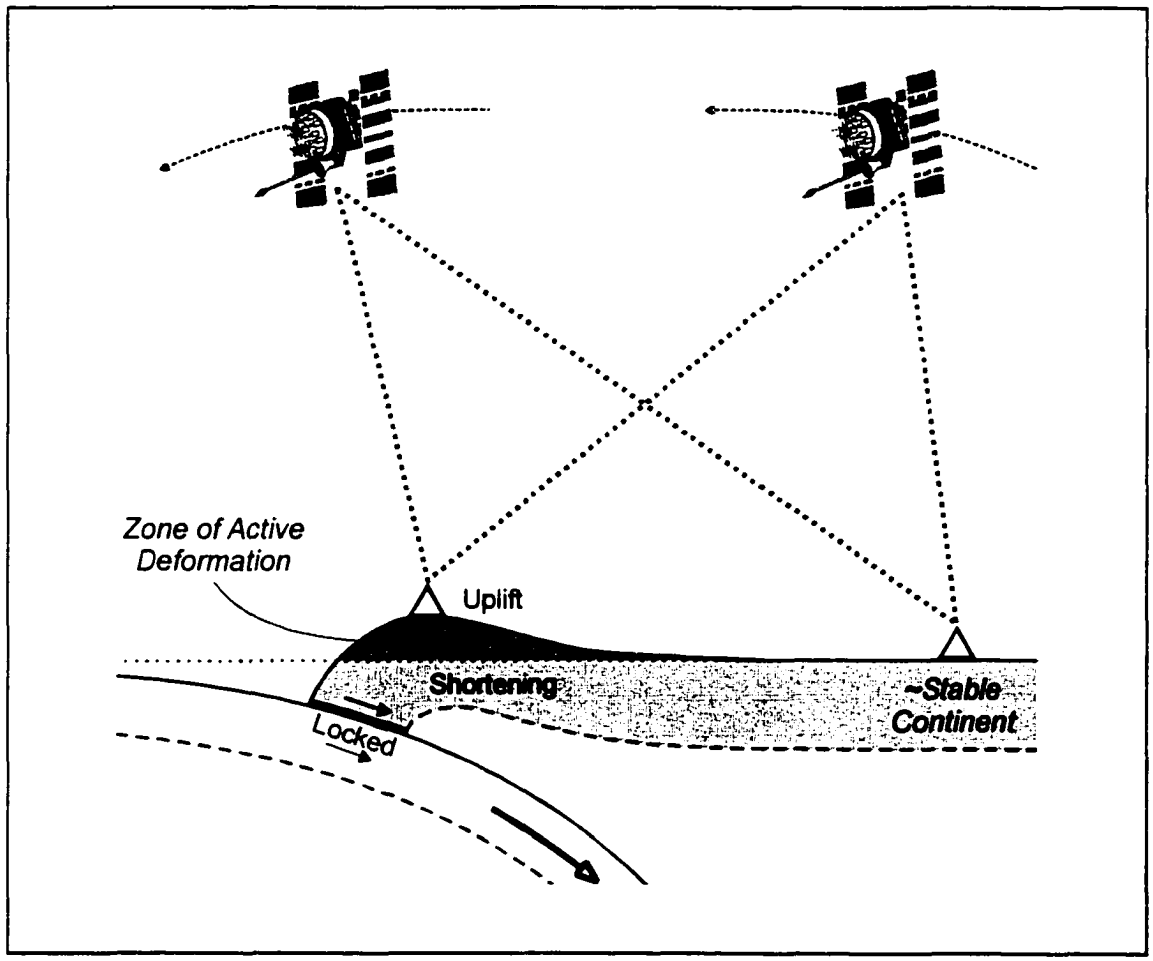

Figure 3.3. Regional-scale differential GPS.

3.2 - Continuous Network Deformation Monitoring

The Western Canada Deformation Array (WCDA) [*Dragert et al.*, 1995] is a network of automated continuous Global Positioning System (GPS) tracking stations located in southwestern B.C., operated from the Pacific Geoscience Centre (PGC) office of the Geological Survey of Canada (GSC), located near Victoria, B.C. The WCDA provides a precise regional reference frame for campaign surveys as well as continuously monitoring crustal deformation at a few points with a precision of several millimetres over baselines measuring hundreds of kilometres (Figure 3.4). The WCDA was one of the earliest

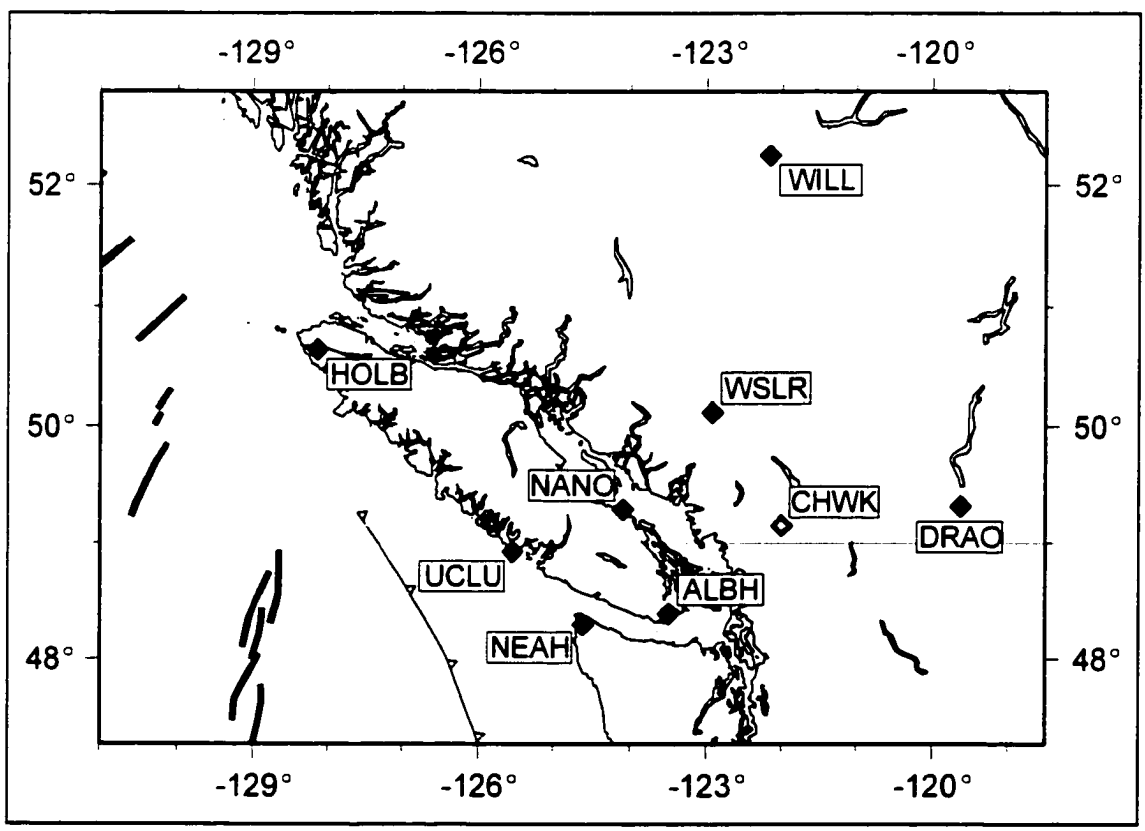

Figure 3.4. Continuous GPS tracker sites of the Western Canada Deformation Array (WCDA). (NEAH is a University of Washington site installed in cooperation with the GSC. CHWK is a site installed in the Fall, 1998 and is not analysed in this study.)

permanent GPS arrays in North America. Its establishment began in 1991 with the installation of the site DRAO at the Dominion Radio Astrophysical Observatory near Penticton, B.C. (*refer to* Table D.1, Appendix D).

The WCDA monuments consist of concrete piers usually anchored to glacially-scoured bedrock (Figure 3.5 & Figure 3.6). Geodetic-quality choke-ring (multipath reducing) antennae are mounted on force-centred bases, mounts that force the antenna to be centred on the geodetic reference point. The antenna cable runs to the local GPS receiver and tracker system package. The tracker systems include high-speed modems for communication and uninterruptable power supplies (and, at most sites, precise frequency standards). Data are downloaded (at least daily) from each site to the PGC data analysis centre through an automated computer routine.

For this study, DRAO serves as the reference site such that the motions of the other continuous trackers are calculated relative to this site. The assumption is that DRAO, located ~500km from the CSZ trench, is in a region of the North America (NA) plate undergoing no (or very little) active deformation. If DRAO is situated on the stable portion of the NA plate, the motions observed at the other tracker sites would represent deformation of the surface relative to the stable plate. Analysis of globally-distributed VLBI (Very Long Baseline Interferometry) sites [*Argus and Gordon*, 1996] indicate statistically insignificant motion of a VLBI site co-located at DRAO with respect to the stable NA plate reference frame. Analyses of global GPS tracker sites [*Argus and Heflin*, 1995; *Larson et al.*, 1997] also show insignificant DRAO-NA motion (less than 2mm/yr). Analysis of WCDA data is covered in subsequent chapters.

Figure 3.5. WCDA tracker site UCLU near Ucluelet, B.C. (Photo courtesy of Mike Schmidt, Geodynamics Group, PGC-GSC).

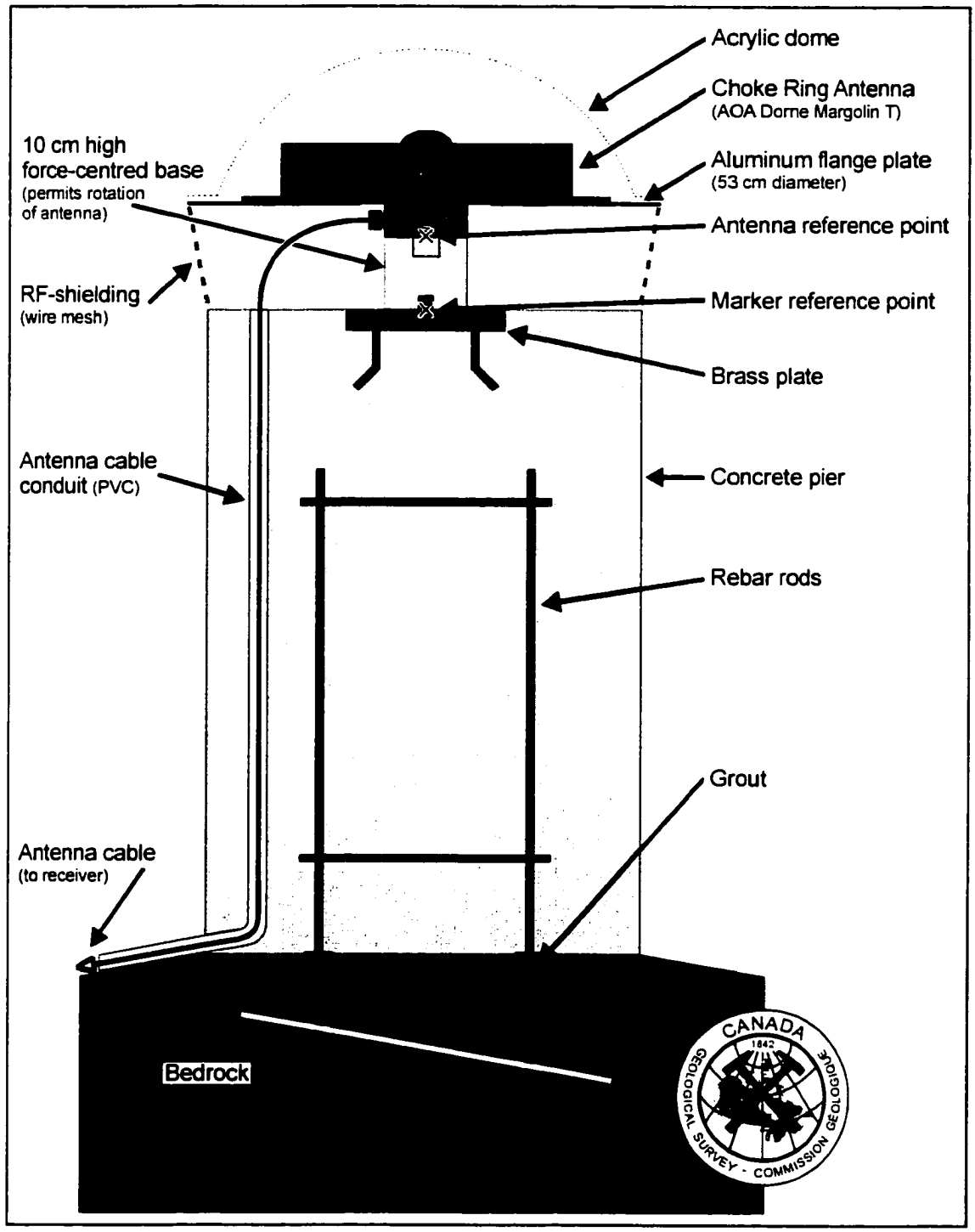

Figure 3.6. Schematic illustration of a typical WCDA monument.

3.3 - GPS Campaign Surveys

The monitoring of relative positions using WCDA data has excellent temporal (daily) sampling, but sparse spatial sampling (~100 to 200 km spacing). Repeated GPS field surveys, in turn, give better spatial density (~20km spacing, Figure 3.7) but have poor temporal sampling, with usually one, and for a few sites, two re-occupations over 4 to 5 years. With denser sampling, spatial variations of strain rate are better resolved.

GPS campaign surveys on southern and central Vancouver Island involved occupying

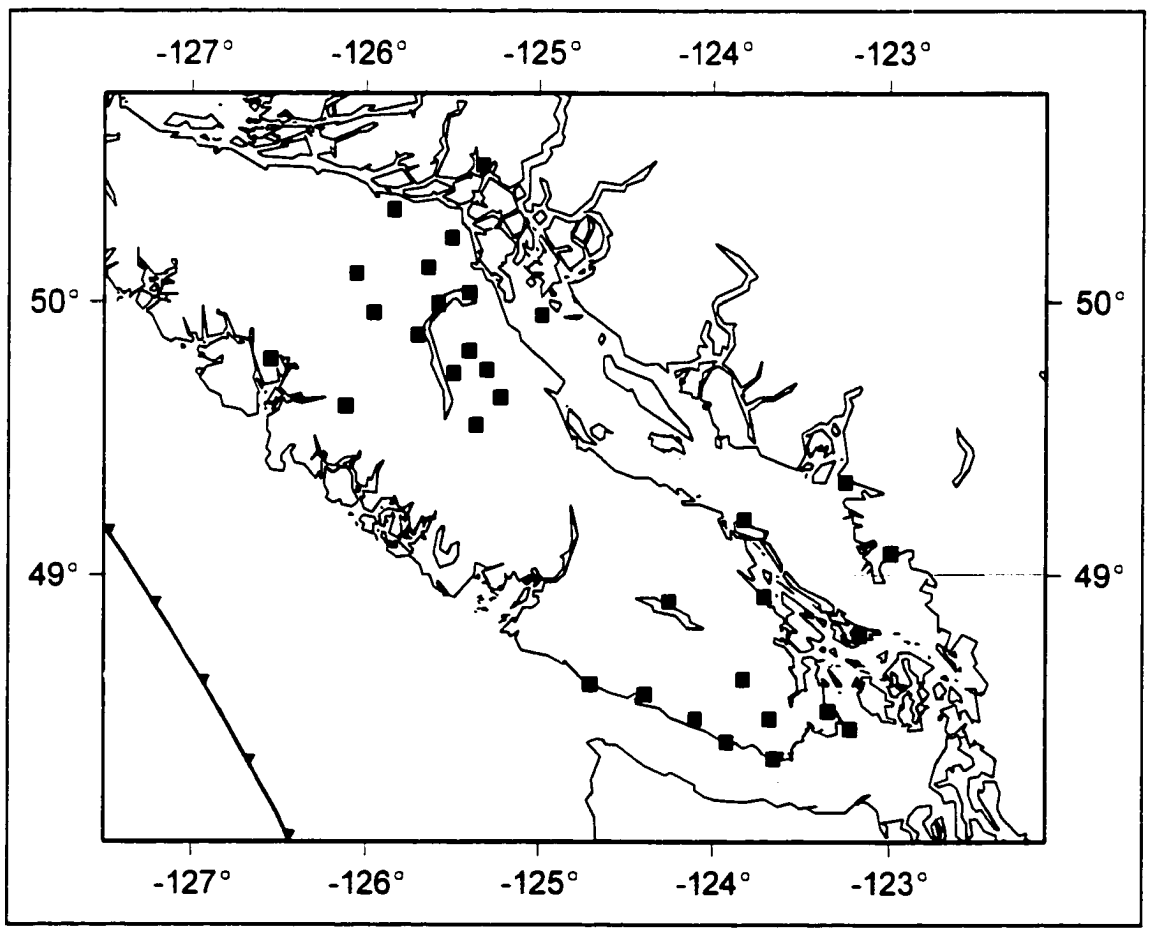

Figure 3.7. GPS campaign sites in southwestern British Columbia. The locations of repeated GPS campaign sites analysed in this study are shown with black squares.

(over a period of a few days) individual sites comprising a strain network with portable GPS geodetic-quality receivers and antennae which are mounted on tripods above permanent survey control markers (Figure 3.8 and Figure 3.9). Field surveys for the campaign data reported here were carried out by the Geodetic Survey of Canada (Natural Resources Canada), Ottawa. The site velocities are assumed to be constant (based upon data from the continuous sites) between the two observation times, and positions and motions are calculated relative to the WCDA reference station DRAO. As yet, vertical velocities cannot be obtained to useful accuracy for CSZ interseismic deformation rates. Processing and results of campaign data are covered in subsequent chapters.

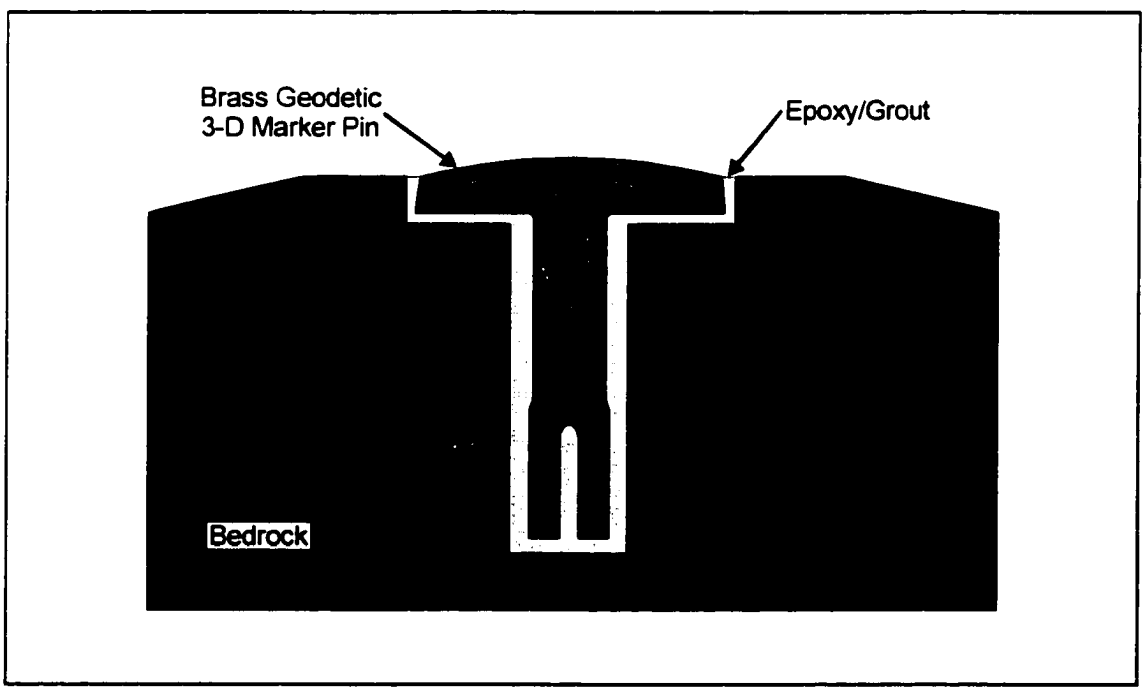

Figure 3.8. Typical geodetic marker pin installation shown in profile.

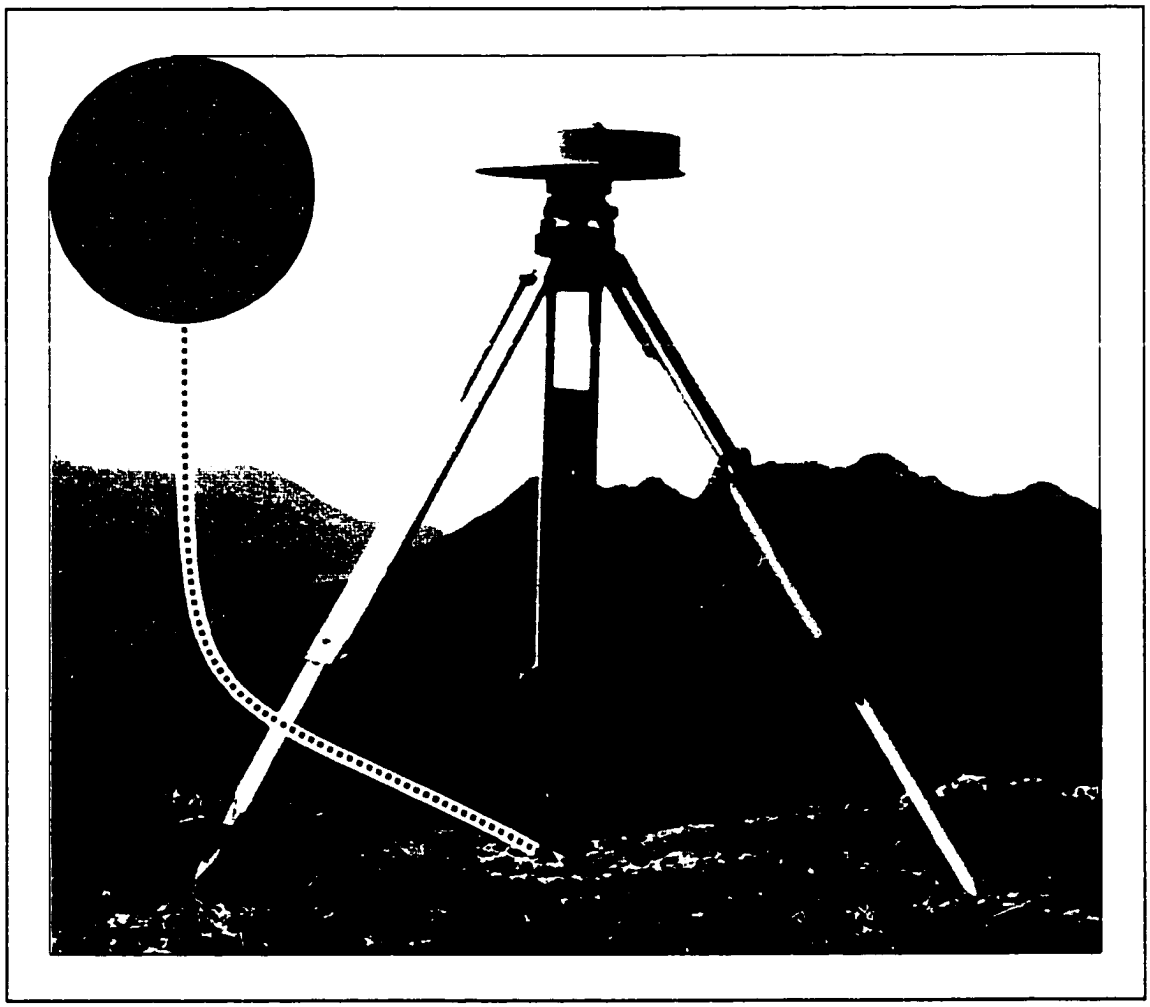

Figure 3.9. Photo of a typical campaign site occupation. The antenna is centred on a tripod above a geodetic marker pin mounted in bedrock. The top of the marker is illustrated in the top-left corner. (Photo courtesy of Alex Smith, University of Victoria, from a campaign-style GPS occupation on Mount Moresby, Queen Charlotte Inlands, British Columbia).

CHAPTER 4 - CONTINUOUS GPS DATA ANALYSIS & RESULTS

4.1 - Introduction

The continuous GPS station data processing carried out in this dissertation study was an integral part of the overall GPS data processing carried out at the Pacific Geoscience Centre (PGC) of the Geological Survey of Canada (GSC). This work was carried out in close collaboration with Herb Dragert of PGC-GSC. The processing consists of two primary sub-packages. The first part, individual site data handling, is carried out by the automated WCDA data acquisition routines that download dual-frequency GPS pseudorange and phase data from remote tracker sites, check the quality and completeness of the individual station data, and generate daily report files. The second package is used for combined station WCDA network data processing. Numerous texts [*e.g. Wells et al.*, 1986; *Hoffmann-Wellenhof et al.*, 1993; *Leick*, 1995] discuss the theory and terminology of GPS data processing.

4.2 - Continuous GPS Station Data Processing

In the WCDA processing scheme, the network is reduced to simultaneous data collected from pairs of stations, refered to as baselines, where common errors and bias (*e.g.* troposphere, satellite clocks, etc) may be minimized before the baseline soultions are combined into a network solution [*Wells et al.*, 1986]. The CGPS22 [*Kouba and Popelar*, 1991; *Kouba et al.*, 1991; *Kouba and Chen*, 1992; *Chen*, 1994; *Dragert et al.*, 1995] data

processing package of the GSC was used in this study for the WCDA continuous data. The double-differencing package was based upon the program GPS22 developed by Gerry Mader of the U.S. National Geodetic Survey (NGS). Originally installed on Sun Solaris (UNIX) Workstations at the Pacific Geoscience Centre in July, 1992, a number of in-house revisions

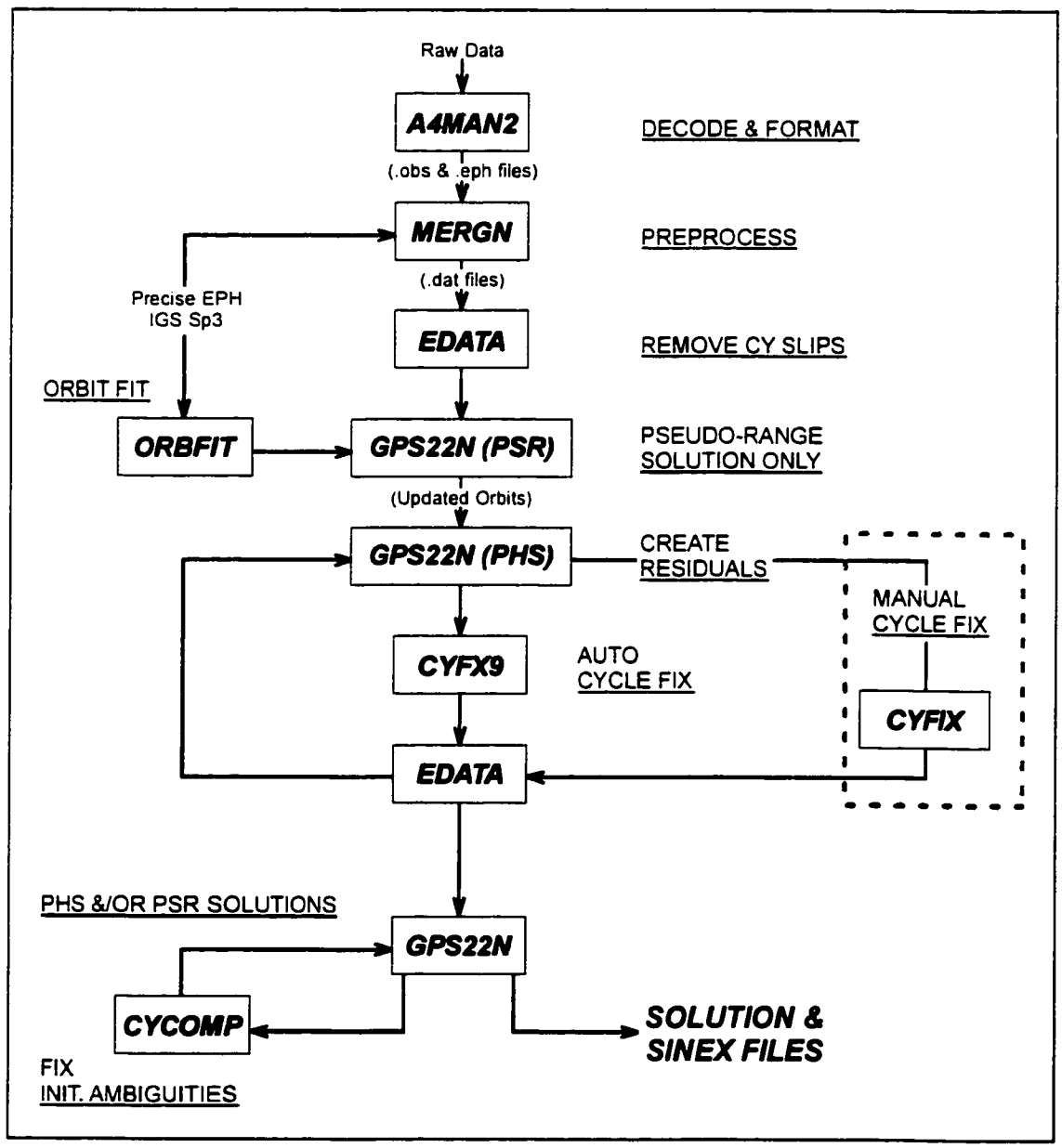

Figure 4.1. Flowchart of CGPS22 analysis stages (revised from *Dragert et al.*, 1995).

have since been made to speed data reduction and improve the precision of the processing results [*Dragert et al.*, 1995]. It is noted that network processing at PGC has recently been converted to the Bernese GPS Software Package [*Rothacher et al.*, 1996] whose basic processing strategy is similar to the CGPS22 package.

A flowchart depicting the analysis stages of the CGPS22 package is given in Figure 4.1 and the tasks of program modules are summarized in Table 4.1. The programs of the CGPS22 package are largely automated (by Yuan Lu, GSC-PGC) and run under a set of user-friendly, UNIX-shell environment script programs that facilitate data file management and enable data to be processed in a batch mode. Additionally, the analysis package has automated *ftp* scripts that download the required precise IGS orbit files (produced by the International GPS Service for Geodynamics (IGS) [*Mueller et al.*, 1994; *Mueller and Beutler*, 1992; *Beutler*, 1992]) that are essential for millimetre-level precision in baseline estimation.

The primary steps of WCDA network processing with CGPS22 are outlined in Figure 4.1. Network data for 24-hr (daily-UT) periods are processed separately and independently. The station DRAO, near Penticton, B.C., is held fixed (*i.e.* approximately with the North American plate; see discussion in Chapter 3), so that all solutions are differential with respect to DRAO (*refer to* Figure 3.3). Pseudorange and phase data are decimated from the typically recorded 30-sec to form 120-sec samples. Analysis was restricted to data from satellites with elevations 15° or greater above the horizon. The precise IGS satellite orbits are considered exact and are not adjusted in the processing. Initial station coordinates within the appropriate (*e.g.* orbit-specified) International Terrestrial Reference Frame are well-determined from at

least two weeks of continuous observations. A Hopfield mapping function [*e.g. Hopfield*, 1969; *Wells*, 1974] with a correlation time of 36000-sec (10-hr) is used to model the tropospheric delay. The *Pagiatakis* [1982] model is applied to correct local tidal (pole tide, solid earth tide, and ocean loading tide) displacements.

Module:	**Task:**
A4MAN2	Decode and reformat CONAN or RINEX raw data formats to stream different types of data; Screen (*e.g.* elevation mask, high RMS point outliers, etc)/smooth pseudorange data and create display files from various combination of pseudoranges/phases;
MERGN	Create the database for post-processing; Merge observations from all stations into a single undifferenced data file; Edit phases by using pseudoranges (triple difference if required); Fit orbits and station clocks with polynomials;
ORBFIT	Fit external precise (*e.g.* IGS, EMR, SIO, etc.) orbits with Chebyshev polynomials to enable interpolation;
CYFX9	Detect cycle slips by using triple differenced L_1/L_2 (GPS broadcast frequencies) phase residuals and double differenced L_3 (linear combination L_1 & L_2 that minimizes ionospheric effects) residuals;
CYFIX	Detect and fix cycle slips/outliers in phases using interactive graphics;
EDATA	Edit database by correcting for integer cycle slips identified by CYFX9 or CYFIX and by flagging outliers;
CYCOMP	Fix cycle ambiguities by a search technique;
GPS22N	Apply corrections to observations; Estimate parameters (station coordinates, station clock biases, initial cycle ambiguities, cycle biases, tropospheric delay, initial Kepler orbit elements) by a weighted least-square algorithm using double-differenced pseudorange and/or phase observations; Create residual files for display and quality check;

Table 4.1. Tasks of CGPS22 Analysis Software Modules [after *Dragert et al.*, 1995].

The network solutions employ double-differenced phase observations in which phase ambiguities were not fixed to integer values. Solutions are calculated using the linear combination L_3 phase defined as:

$$L_3 = \frac{1}{f_1^2 - f_2^2}\left(f_1^2 L_1 - f_2^2 L_2\right) \tag{4.1}$$

that largely eliminates any ionospheric path delay and thus is often referred as the ionosphere-free combination; where f_1 (1575.42 Mhz) and f_2 (1227.60 MHz) are the two sinusoidal carrier frequencies corresponding to the observed signals L_1 and L_2, respectively [*e.g. Wells et al.*, 1986; *Hoffmann-Wellenhof et al.*, 1993; *Leick*, 1995].

4.3 - Linear Regression of Continuous Baseline Data

Daily variations in WCDA station baseline components (latitude, longitude, & radial), from a nominal station position determined relative to the reference site DRAO are plotted in Appendix A as Figures A.1-A.7 [data from *Dragert et al.*, 1998; *Henton et al.*, 1998]. The data plots exhibit predominately linear trends over time which are inferred to be tectonic deformation rates. Often there is a sinusoid of annual-period large enough in amplitude to visually identify in the baseline time-series (see discussion below).

Dragert et al. [1998] have corrected the time series for datum-offsets (*i.e.* steps) typically associated with physical alterations affecting the antennae at tracker sites or reference frame changes. Although the time of occurrence of these steps can be documented, their magnitudes generally cannot be determined exactly. For WCDA sites, changes in the vertical position of the antenna phase centres as large as ~1.9 cm have been observed to

accompany changes in the physical mounting of the antennas [*Dragert et al.*,1998]. Recent changes in reference frames produce small ($\leq$ 1mm) apparent datum offsets. The datum biases were removed by *Dragert et al.* [1998] by permitting step functions to be fit during the linear-regression process. *Dragert et al.* [1998] also simultaneously fit an annual (365.25-day) period sinusoid to the data during regression. Regression results for horizontal baseline components are given in Table 4.2 (vertical rates are provided in Table D.2, Appendix D).

Station	North Velocity (mm/yr)	95% Error (mm/yr)	East Velocity (mm/yr)	95% Error (mm/yr)	Number Obs
UCLU	6.9	0.2	8.9	0.4	1609
NEAH	5.4	0.3	7.3	0.3	1016
ALBH	2.2	0.3	4.1	0.3	1985
NANO	2.5	0.4	4.1	0.2	1234
WSLR	0.6	0.5	1.6	0.8	726
HOLB	2.8	0.4	-1.1	0.3	1981
WILL	-0.4	0.1	-2.0	0.2	1627

Table 4.2. WCDA Horizontal Velocities from Regression by *Dragert et al.* [1998]

4.4 - Differential North American Plate Motion Corrections

The North American Plate undergoes a rigid body rotation around an Euler pole (Figure 4.2) located near equatorial, northwestern South America [*DeMets & Dixon*, 1999; *DeMets et al.*, 1990, 1994]. The individual stations of the WCDA are each subject to the

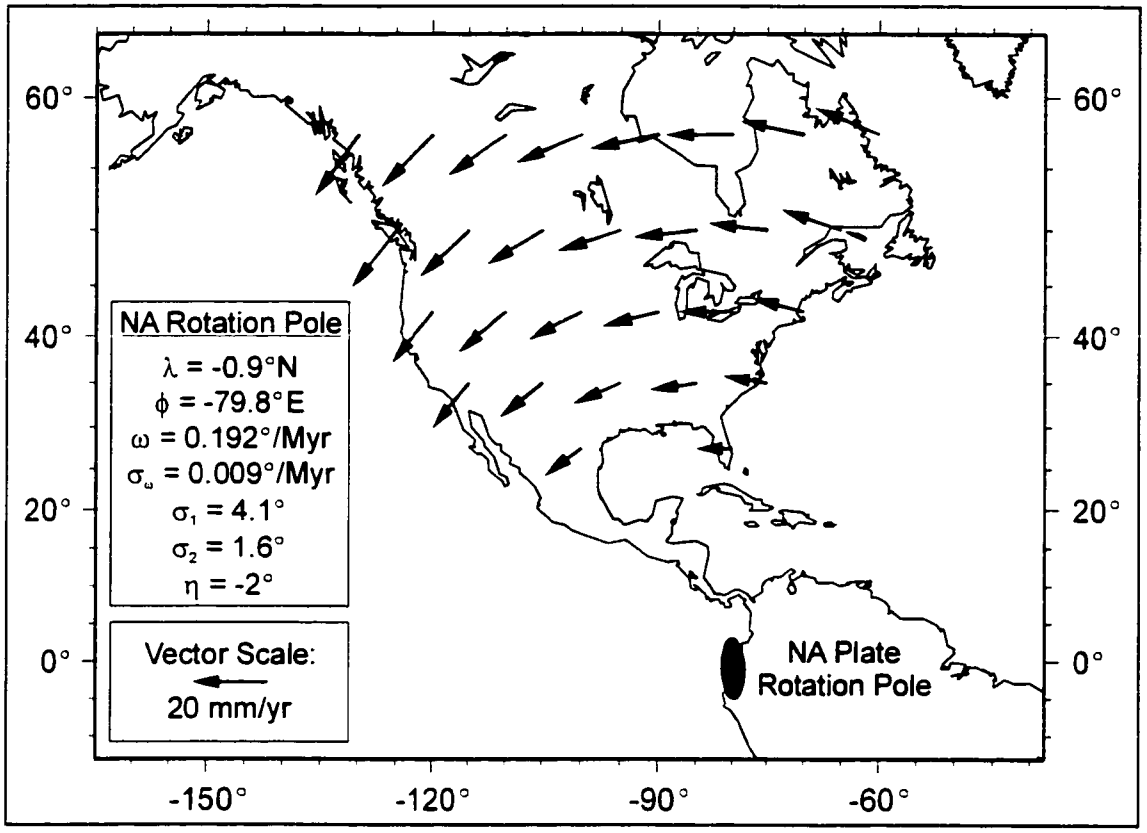

Figure 4.2. North American plate rotation pole and predicted velocities for the North American plate. The NA plate rotation pole is from *DeMets & Dixon* [1999] and the arrow lengths are proportional to the rates at their origin point. λ, φ, and ω are the latitude, longitude, and angular rotation rate of the NA rotation pole, respectively. σ_ω is the standard error on the angular rotation rate. σ_1 and σ_2 are the lengths (in degrees) of the 1-sigma semi-major and semi-minor axes of the pole error ellipse. η is the azimuthal direction of the semi-major error ellipse axis in degrees clockwise from north.

absolute NA plate motion. They additionally experience a small differential plate motion relative to the reference station DRAO which is held fixed during network processing. Because the intention is to display *deformation* vectors for motions relative to a common reference site, the component of differential NA plate motion between DRAO and the individual WCDA sites is removed. Although the magnitude is this correction is quite small (≤ 1mm/yr), it is applied to most accurately reflect the deformation velocities with respect to a common reference site on "stable" North America (*refer to* Section 3.2).

4.5 - WCDA Deformation Vectors

Horizontal velocity estimates [*Henton et al.*, 1999] based on linear trends in daily positions of the continuous network sites in southwestern British Columbia, are are shown in Figure 4.3 (with values given in Table 4.3). For southwestern B.C., the Cascadia locked subduction thrust-signal clearly dominates. Deformation velocities, directions and magnitudes, are consistent with the strain accumulation (direction and magnitude) expected from a locked subduction fault (*see* Chapter 6). The vector directions are all nearly parallel within the estimated uncertainties and largely agree with the direction of Juan de Fuca Plate

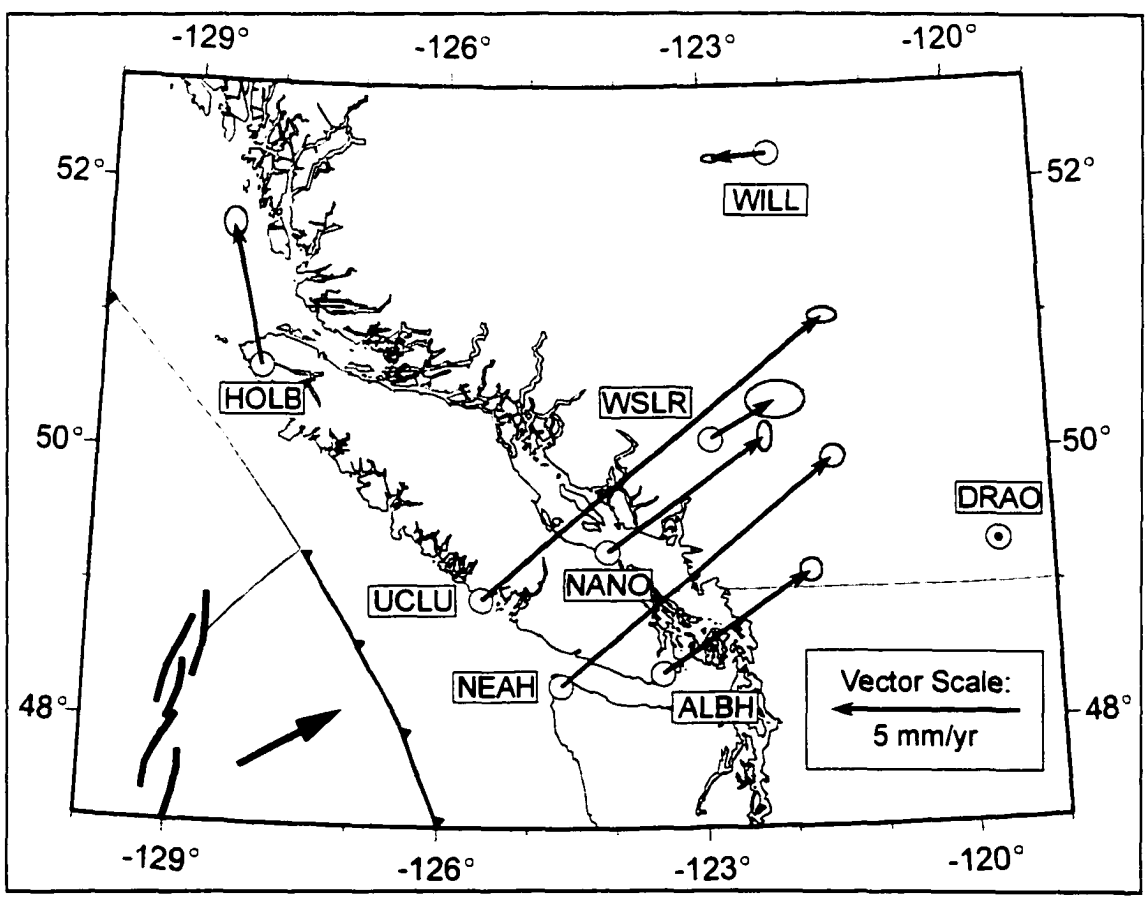

Figure 4.3. WCDA horizontal velocity field. Velocity vectors are shown with their 95% confidence ellipses based upon regressions of *Dragert et al.* [1998]. Velocities have been corrected for differential North American plate motion between each tracker sites and DRAO, the reference site.

convergence. The highest velocities occur towards the outer coastal margin and decrease landward away from the Cascadia Subduction Zone (CSZ) deformation front.

Station	North Velocity (mm/yr)	95% Error (mm/yr)	East Velocity (mm/yr)	95% Error (mm/yr)
UCLU	7.6	0.2	8.8	0.4
NEAH	6.0	0.3	7.1	0.3
ALBH	2.7	0.3	3.9	0.3
NANO	3.0	0.4	4.1	0.2
WSLR	1.0	0.5	1.7	0.8
HOLB	3.7	0.4	-0.9	0.3
WILL	-0.1	0.1	-1.5	0.2

Table 4.3. Horizontal Component Velocities with Respect to DRAO Corrected for Differential Motion due to North American Plate Rotation

North of the CSZ, deformation measurements also provide evidence for crustal strain that is not expected from a locked subduction thrust fault. The north-by-northwesterly motion of station HOLB, located on northern Vancouver Island adjacent to the Juan de Fuca-North America-Pacific triple junction, is more consistent with the shear strain expected from margin-parallel Pacific/North America interaction across northwest trending strike-slip faults. This character of crustal strain at the northern end of the Juan de Fuca plate may play a role in the origin of large crustal earthquakes on central Vancouver Island. Additionally, the small velocity at station WILL, near Williams Lake, B.C., is not obviously affected by CSZ seismotectonics. It remains possible that WILL may better represent "stable" North

America than DRAO which suggests a small residual motion at DRAO relative to the North American plate. However, the implications of choosing WILL as the reference site are minimal for the subsequent discussions on measured strains and modeling.

This network, currently comprised of 8 sites, now provides significant constraints to models (*see* Chapter 6) of contemporary crustal dynamics taking place within the northern CSZ. While horizontal velocities are fundamental to mapping crustal strain, accurate vertical deformation rates would provide an additional, more sensitive control that can be used to further constrain models of the CSZ megathrust surface. Unfortunately, solutions of vertical rates are still a factor of 2-3 poorer than corresponding horizontal solutions. Improving the vertical GPS velocities requires further future study.

4.6 - Significant Periodic Signals Observed in the GPS Baselines

The long-term trends in the relative motion of sites, especially in the vertical, can be biased by instrumental effects and/or signals of non-tectonic origin. From geometric arguments alone (analogous to the poorer depth control in an earthquake hypocentre-solution relative to its epicentral location), the vertical position of GPS solutions are always the least precise component. Furthermore, predicted uplift rates for sites of the WCDA of less than ~4 mm/yr are generally a factor of 2-3 smaller than the corresponding horizontal rate. The result is the vertical GPS solution for the WCDA effectively has a signal-to-noise ratio that is 4-5 times worse than the horizontal solution. As periodic signals with amplitudes up to a few millimetres have also been identified in the vertical baselines, a preliminary investigation of the time series spectra was performed in this study.

4.6.1 - Data Set

For this study, variations in the differential baseline components from a nominal station position relative to the reference site were analyzed (see Appendix A: Figures A.1-A.7). The time series range from approximately 2 to 4.75 years, depending upon the date when each station commenced. The time period of this study is from day 1 to day 1758 past January 1, 1994. Data processed prior to 1994, before the distribution of IGS precise orbit products, used EMR (Geodetic Survey of Canada) precise orbit files and is excluded from the time-series analysis.

4.6.2 - Least Squares Spectral Analysis

To investigate the periodic constituents of the WCDA time series, least squares spectral analysis (LSSA) was employed. *Wells et al.* [1985] give a formal discussion of the LSSA method, a type of harmonic analysis where residuals are minimized in a least-squares sense. The routine LSSA (Version 4.2), provided by Spiros Pagiatakis of Geomatics Canada, was used during this study. For this investigation, the LSSA program had advantages over other spectral analysis schemes (refer to *Pagiatakis* [1999] for complete discussion). Firstly, although the time series from the GPS baselines are nearly complete with uniform (*i.e.* daily) spacing, there are occasional data gaps due to instrumental or data transfer problems. LSSA is designed to incorporate unequally-spaced data. Additionally, LSSA removes linear trends (differential vertical velocities in this investigation) present in the time series in order to maintain a mean value of zero through the length of the time series.

4.6.3 - Annual Signals

The least squares amplitude spectra for periods of 20 to 500 days for the WCDA baselines are plotted in Appendix B as Figures B.1-B.7. There is, in general, significant annual-cycle energy present in the time series, especially in the vertical component. The amplitudes of semi-annual signals present in a number of the baseline time series are comparatively much smaller. As there are only a few complete annual cycles, the peaks are broad. Nevertheless, there is an annual-period signal of approximately 365 days with statistically significant amplitudes. Table 4.4 gives the LSSA determined amplitudes (A) and phases (φ) at a forced 365.25 day annual-period. The phases reported in this chapter are all relative to a common reference at January 1,1994.

The amplitude (A) of these signals indicates that accurate determination and removal of this annual-period energy from the GPS baseline time series is a critical step in attaining higher accuracy and more reliable long-term tectonic (linear) trend estimates. This correction is particularly crucial in the vertical component for which the amplitude of these periodic signals is usually the largest but whose expected tectonic uplift or subsidence rates are relatively small.

Although the source of the annual periodic signal is unknown, meteorologic forcing (*e.g.* GPS signal transmission delay or perhaps atmospheric loading) is a likely cause, particularly because the annual period signal is greatest in the vertical component. The vertical component of a GPS solution is most sensitive to observations at lower elevation angles where the GPS signal-path through the troposphere is proportionally longer compared to the zenith path. For this study, preliminary investigations of the spectra of differential

temperature and differential pressure measurements were investigated for annual-period energy.

Component	Station	A (mm)	σ_A (95%)	φ (days)	σ_φ (95%)
VERT (T = 365.25)	ALBH	3.2	0.25	183.6	14.4
	HOLB	5.2	0.26	130.1	14.8
	UCLU	3.7	0.26	171.8	15
	WILL	0.5	0.21	157	12
	NANO	1.5	0.27	187.3	15.6
	NEAH	1.2	0.33	204	18.1
	WSLR	4.2	0.33	268.4	21.6
LONG (T = 365.25)	ALBH	1.2	0.15	147.9	8.4
	HOLB	2	0.14	163.8	7.8
	UCLU	1	0.14	152.3	7.9
	WILL	1	0.12	194.6	7
	NANO	1.2	0.15	177.4	8.6
	NEAH	1.2	0.19	161.1	10.6
	WSLR	-0.3	-0.21	-338	-21.6
LATI (T = 365.25)	ALBH	0.8	0.09	108.9	5.2
	HOLB	0.9	0.1	359	5.6
	UCLU	1.1	0.09	43.2	5.1
	WILL	1.3	0.08	320.3	4.8
	NANO	1.3	0.1	88.7	5.6
	NEAH	0.8	0.11	101.7	6.9
	WSLR	-0.1	-0.13	-328.3	-7.3

Table 4.4. LSSA-Determined Amplitudes and Phases of Annual Period Signals in WCDA Baselines

Two continuous stations were chosen for comparison purposes, HOLB and WILL. HOLB, located on northern Vancouver Island, is subject to a coastal climate much different than the interior B.C. climate experienced by DRAO, the GPS analysis reference station located near Penticton. Furthermore, the HOLB-DRAO baseline displays the greatest annual-period sinusoidal amplitude (~5mm). However, WILL, located near Williams Lake, experiences an interior climate presumed similar to DRAO. Hence, if the annual cycle is meteorologically forced, the WILL-DRAO baseline may be expected to display significantly less atmospherically-forced annual energy. Indeed, the WILL-DRAO baseline exhibits the smallest annual period sinusoidal energy (~1.5mm). Figure 4.4 shows the locations of the meteorologic data ("met") stations nearest to WCDA sites HOLB, WILL, and DRAO. The met stations at Port Hardy, Williams Lake, and Penticton are designated (in this discussion) as PHAR, WLAK, and PENT, respectively. The meteorologic data are available through the

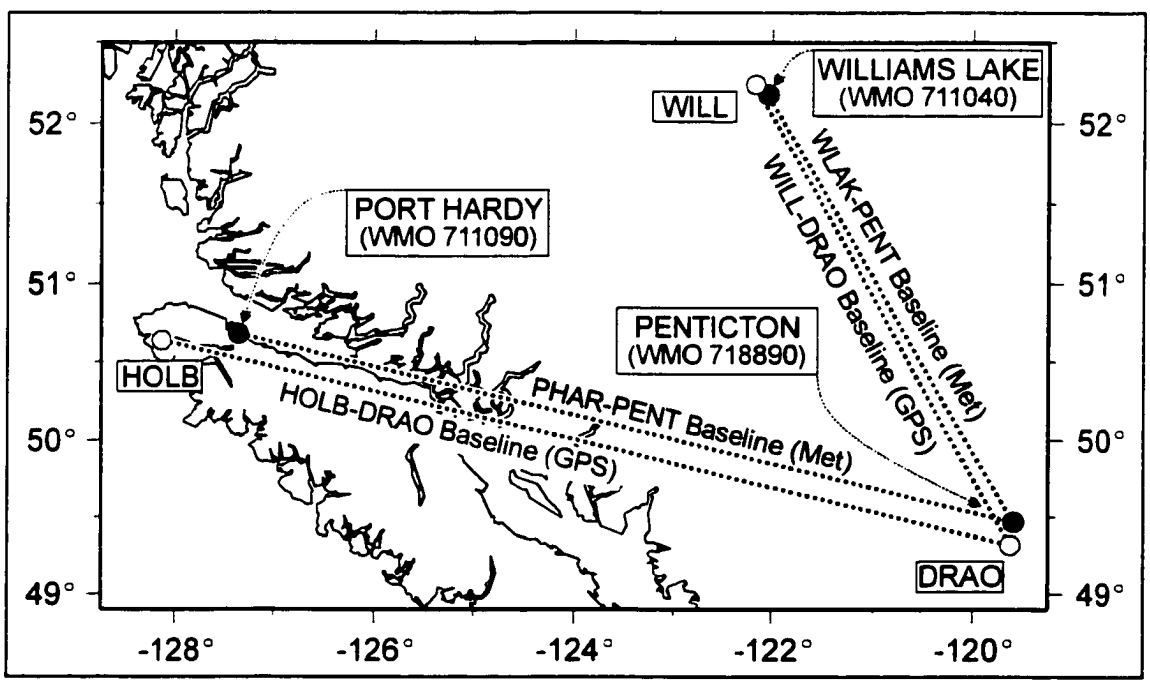

Figure 4.4. Map of GPS and meteorologic baselines compared in this study.

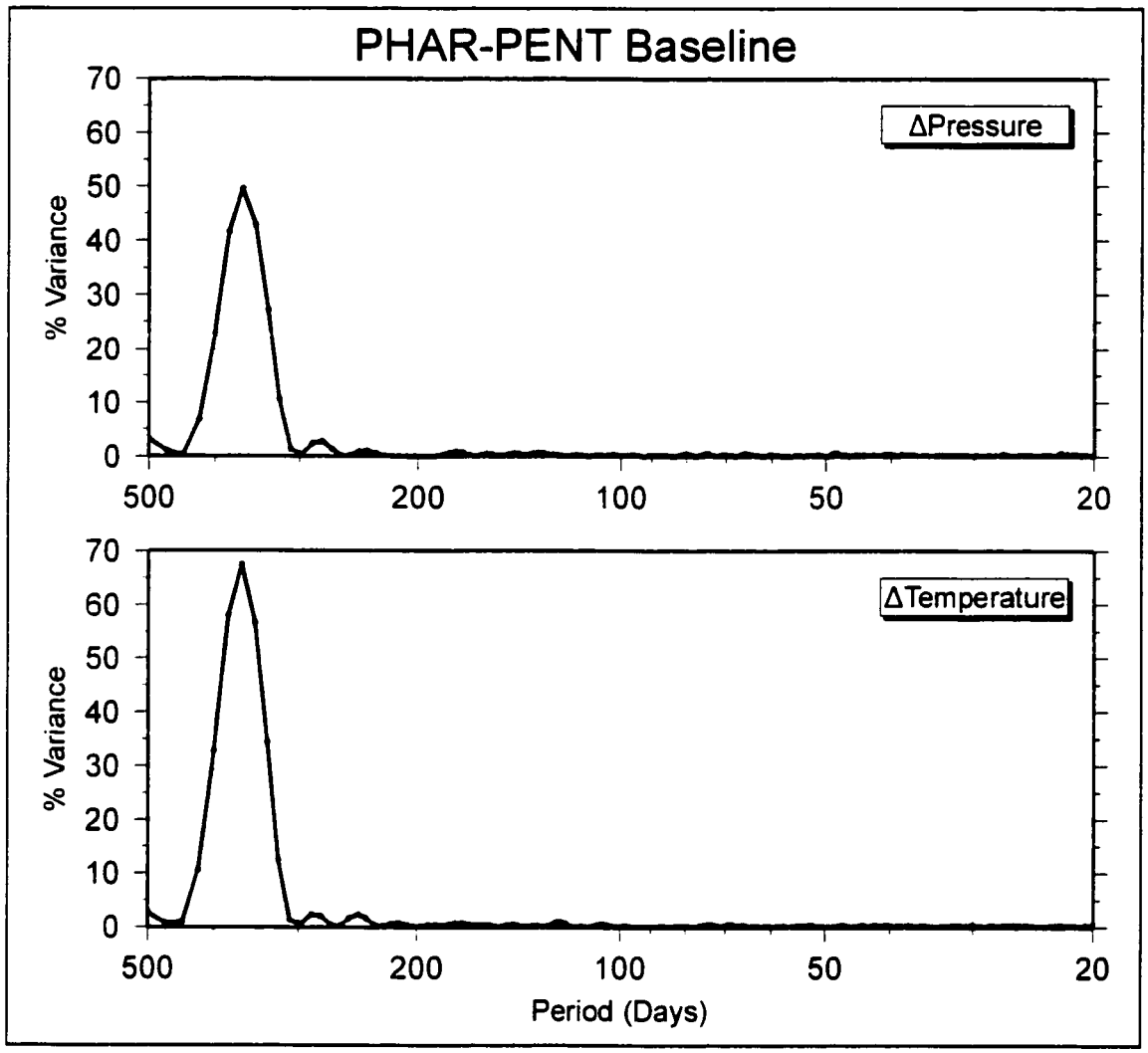

Figure 4.5. Spectra for PHAR-PENT differential pressure and temperature. The spectra were determined by the routine LSSA over a baseline between meteorologic stations near Port Hardy and Penticton, British Columbia.

National Weather Service of the National Oceanic and Atmospheric Administration (www.nws.noaa.gov).

A comparison of the vertical differential GPS HOLB-DRAO time series to the PHAR-PENT differential pressure and differential temperature time-series during the period of study is plotted in Appendix C as Figure C.1; Figure C.2 (Appendix C) shows the comparable time-series for the WILL-DRAO/WLAK-PENT baselines. Determined by the

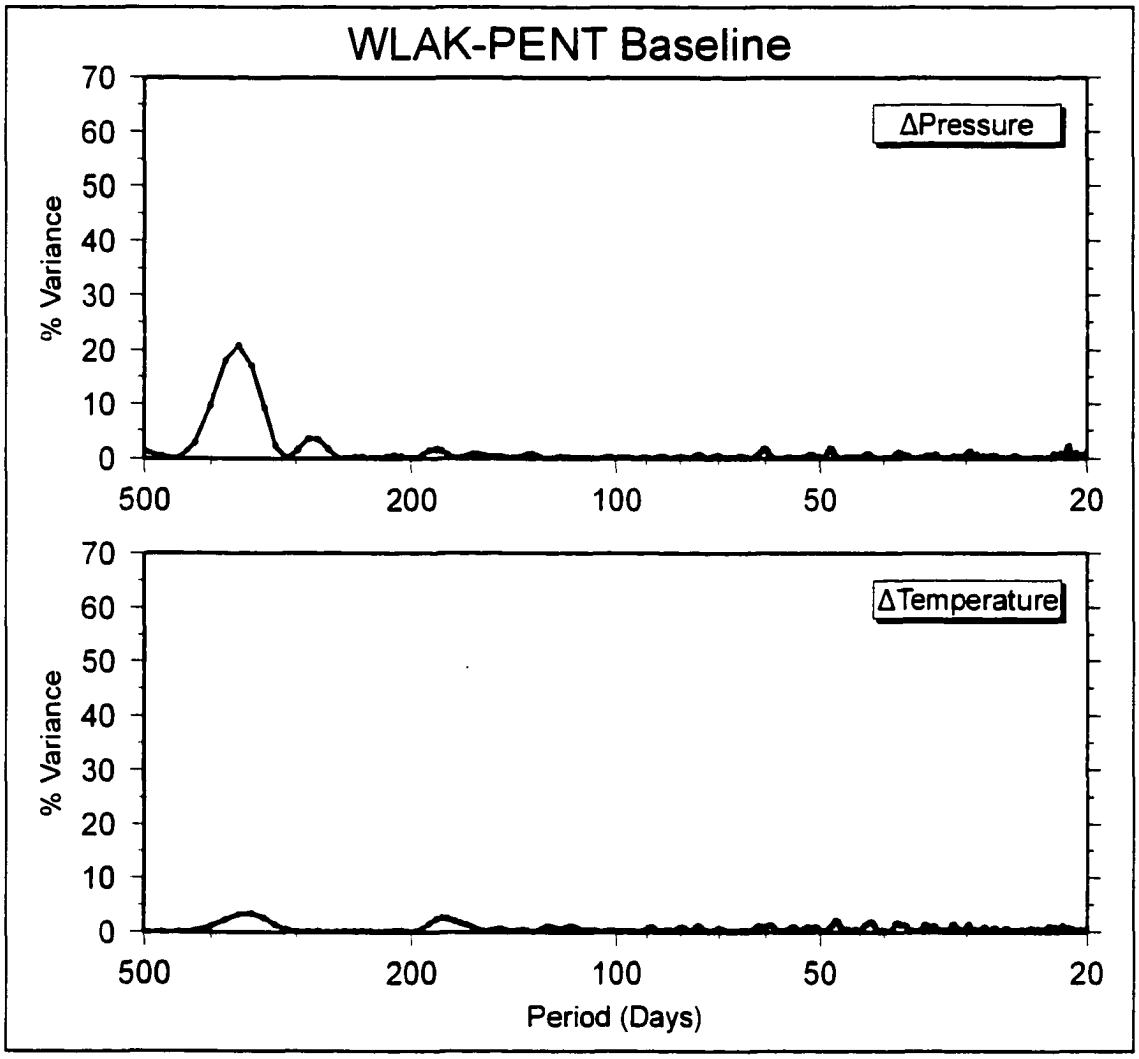

Figure 4.6. Spectra for WLAK-PENT differential pressure and temperature. The spectra were determined by the routine LSSA over a baseline between meteorologic stations near Williams Lake and Penticton, British Columbia.

LSSA routine. Figures 4.5. 4.6 show the amplitude spectrum of the differential pressure and differential temperature measurements for the Penticton (PENT) to Port Hardy (PHAR), and PENT to Williams Lake (WLAK) meteorological station baselines, respectively. The LSSA-determined amplitudes and phases of the met-station baseline time-series are given in Table 4.5.

Baseline	Parameter	Amplitude	Phase
PHAR-PENT	ΔTemperature	5.9 ± 0.1 °C	10.0 ± 5.6 days
	ΔPressure	6.4 ± 0.2 mbar	183.3 ± 8.7 days
WLAK-PENT	ΔTemperature	1.0 ± 0.1 °C	155.2 ± 7.0 days
	ΔPressure	2.6 ± 0.1 mbar	189.0 ± 6.7 days

Table 4.5. LSSA-Determined Amplitudes and Phases of Annual Period Signals in Meteorologic Station Baselines

For the PHAR-PENT observations, strong annual signals are present within both the differential pressures and differential temperatures. The respective amplitudes for the more climatically similar sites of the WLAK-PENT baseline are comparatively much smaller. The differential pressure observations exhibit nearly the same phase for both baselines. If we speculate that higher atmospheric pressures load and, as a result, depress the crustal surface, periods of higher atmospheric pressure should result in correspondingly lower differential elevations. Thus, for such a process, the phase of any possible atmospheric loading effect should be approximately 180° out of phase with the loading implied from the GPS baselines. However, the phases of the 365.25 period in the radial HOLB-DRAO and WILL-DRAO baselines are about 130 ± 15 days and 157 ± 12 days, respectively. This energy is therefore unlikely to result from atmospheric loading.

The differential temperature observations, whose phases are not consistent, do not offer any straightforward answer to the cause of the annual-period energy. It may be possible that many meteorologic phenomena act together, perhaps in a non-linear fashion, to produce the annual-period signal present in the GPS baselines. It also remains possible that the

tropospheric delay modeling routine within the CGPS22 processing software may be overcorrecting for some atmospheric-driven effect. Future work, including a comparison to the results produced by the Bernese GPS Software package, may help resolve these questions.

4.6.4 - Short-Period Signals

The WCDA baseline spectra for 9 to 20 day periods (plotted in Appendix B as Figures B.8-B.14) exhibit very little periodic energy except for an unexpected peak at a period of 13.6 days present in the vertical component of most of the baselines. This period is coincident with the fortnightly M_f ocean tide. Although this relatively short-period energy (for geodetic data) should not affect long-term estimates of the relative vertical velocities, its source is nonetheless intriguing.

In the continuous time series, it was observed that the amplitude of M_f-period energy changed with time. It is largely absent from the latter (*i.e.* more recent) portions of the HOLB-DRAO and UCLU-DRAO time series, the two baselines where its amplitude had been greatest in the early data. Figures B.8-B.14 (Appendix B) represent the spectral energy averaged over the entire length of a given time series. To assess the stability of the M_f-period energy, the spectra were calculated as a function of time for the six vertical baselines with the longest time-series. A least squares spectrum was calculated for a moving 82-day window, corresponding to approximately six complete M_f cycles, stepped at seven day intervals. The contoured results are plotted in Figures 4.7a–c. The spectral amplitudes of the fortnightly-period peak vary over time. For the period of 1994 through 1996, there are distinct occasions where the M_f-period energy is pronounced (estimated amplitudes in excess

of 1cm). Beginning in late 1996, this energy is almost completely absent from all baselines, with equivalent amplitudes well below 1 mm. Because the signal is not stationary, its phase cannot be well-determined.

The cause of the 13.6 day period energy remains elusive. The gravitationally-forced fortnightly M_f ocean tidal amplitude is too small to provide a significant ocean loading effect. Additionally, the spatial wavelength of this tidal constituent is too large to produce the observed *differential* GPS signals over the baseline lengths of the WCDA. Also, this effect should produce coherent amplitude modulations at similar coastal sites, such as UCLU at HOLB, if this energy resulted from some regional, non-linear effects. However, the modulation of spectral amplitudes for the UCLU-DRAO and HOLB-DRAO baselines do not correlate well, other than for the abrupt disappearance of M_f-energy during the latter part of the time series. While shallow-water M_f tides could be produced due to the interaction of the K_2 and M_2 tidal constituents, they are a contribution about 10% of the direct gravitationally forced M_f, and the interaction of the K_1 and O_1 constituents to produce fortnightly period tides would be smaller yet [*Crawford*, 1980].

Atmospheric forcing was also investigated as the source of the M_f-period energy. Least-squares spectra have been computed for differential pressure and differential temperature data recorded at meteorologic stations near specific WCDA sites. However, the 13.6 day peak could not be resolved from these atmospheric data. Additionally, it is expected that a climatic signal should be coherent over a large spatial areas, and, as noted above, the positions of the spectral peaks and gaps vary across the different WCDA baselines.

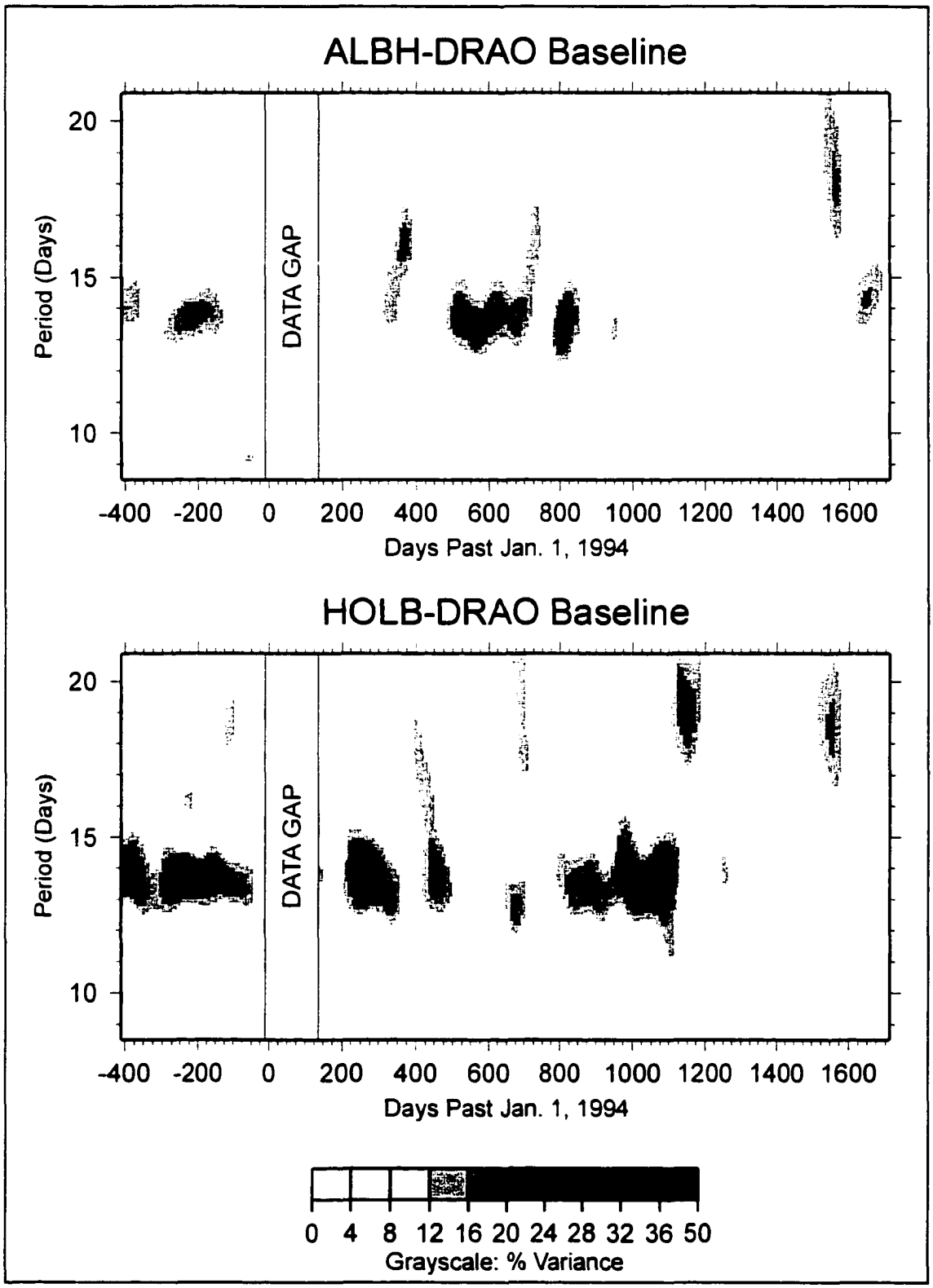

Figure 4.7a. Short-period spectra variation with time for ALBH-DRAO and HOLB-DRAO baselines. Spectra calculated with an 82-day window stepped at 7-day intervals.

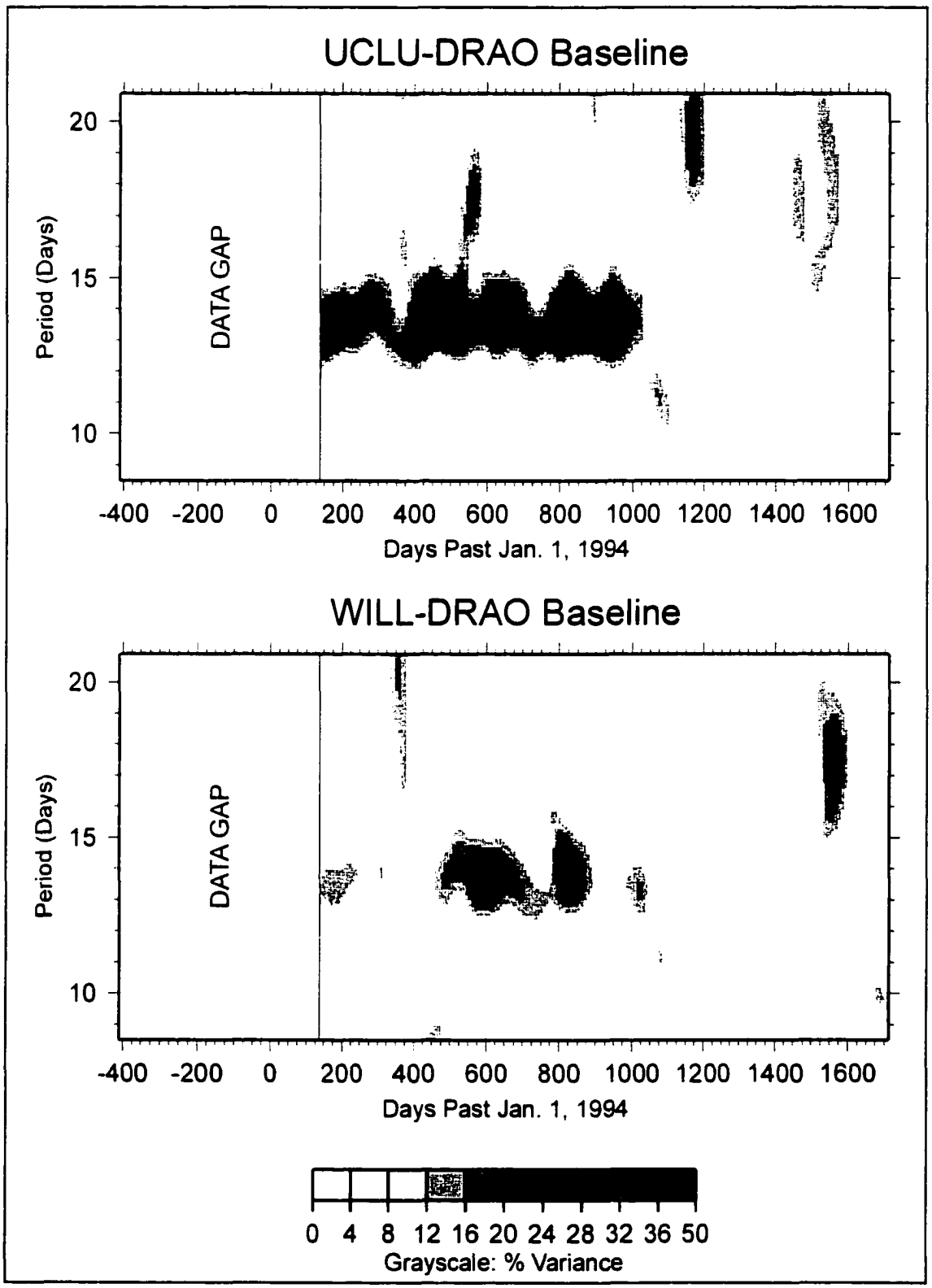

Figure 4.7b. Short-period spectra variation with time for UCLU-DRAO and WILL-DRAO baselines. Spectra calculated with an 82-day window stepped at 7-day intervals.

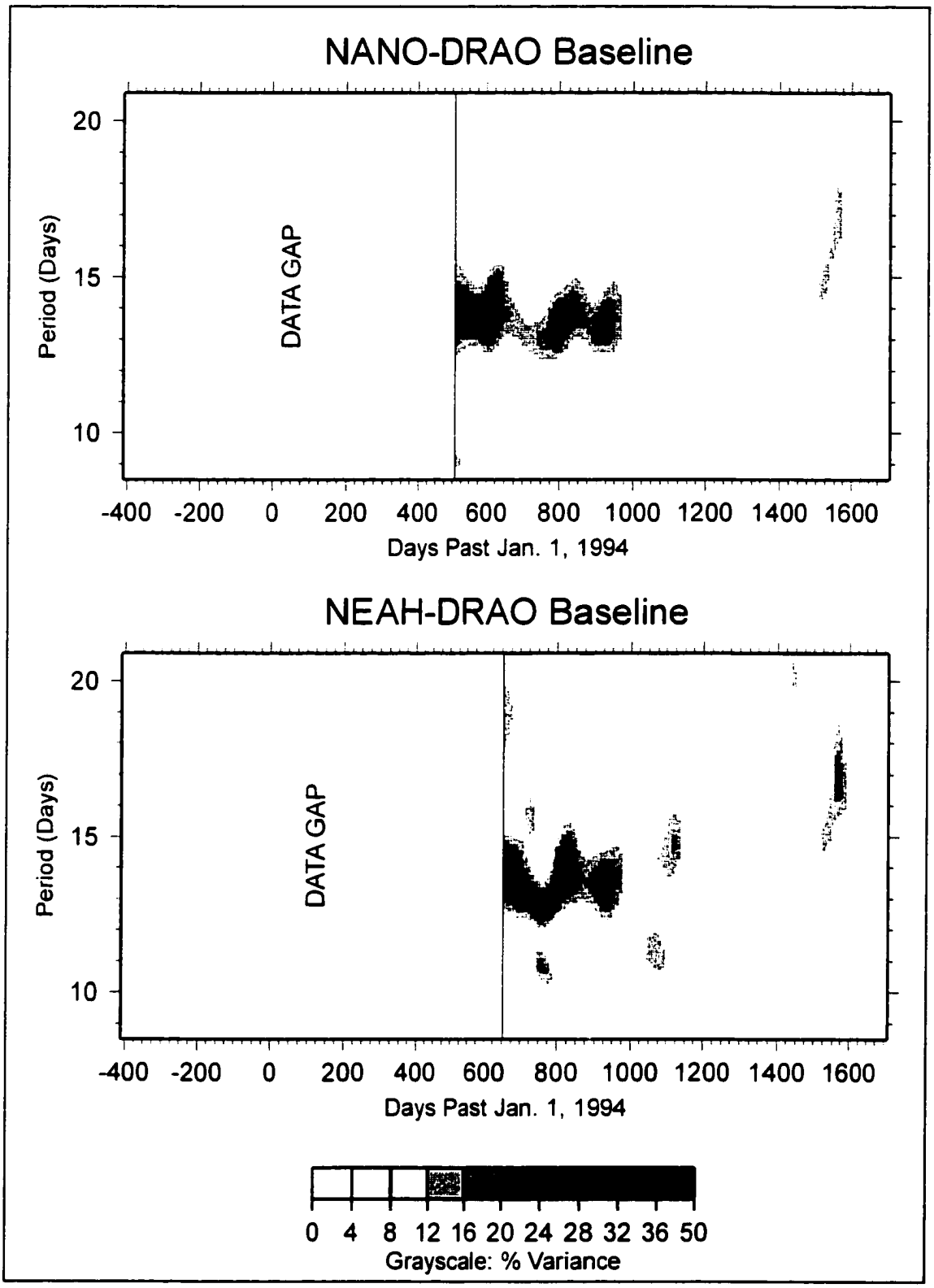

Figure 4.7c. Short-period spectra variation with time for NANO-DRAO and NEAH-DRAO baselines. Spectra calculated with an 82-day window stepped at 7-day intervals.

There may be a local forcing that is driving the modulation of the fortnightly-period energy. However, the disappearance of the signal at all sites at approximately the same time (as nearly as can be resolved) suggests that this energy does not stem from a physical process but rather from some process within the network analysis. However, any signal within the precise orbits should affect the regional-scale WCDA sites in much the same way which is not the case. While the cause of the 13.6 day signal remains puzzling, it should not affect or bias the linear tectonic signal in a long-interval geodetic time series.

CHAPTER 5 - CAMPAIGN GPS DATA ANALYSIS & RESULTS

5.1 - Introduction

The WCDA data discussed in the previous chapter have good temporal (daily) sampling but sparse spatial sampling. Repeated campaign-style surveys, in turn, give good spatial density but have poor temporal sampling and thus are complementary. This chapter outlines the processing and displays the results for two GPS campaign networks on southern Vancouver Island and adjacent areas: the Juan de Fuca and Central Vancouver Island GPS Strain Networks.

5.2 - Juan de Fuca GPS Strain Network Processing

The Juan de Fuca (JdF) GPS Strain Network is located in southwestern British Columbia (Figure 5.1 and Figure 5.2) with most sites on southern Vancouver Island. Fifteen sites (Table 5.1 and Table 5.2) were surveyed in October, 1991, and resurveyed in August,

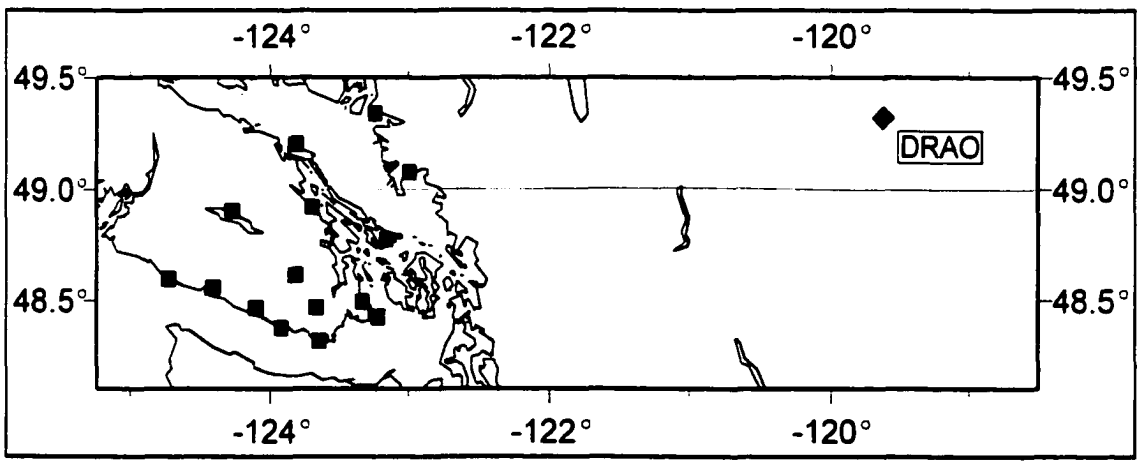

Figure 5.1. Juan de Fuca GPS Campaign Network and the WCDA reference site DRAO.

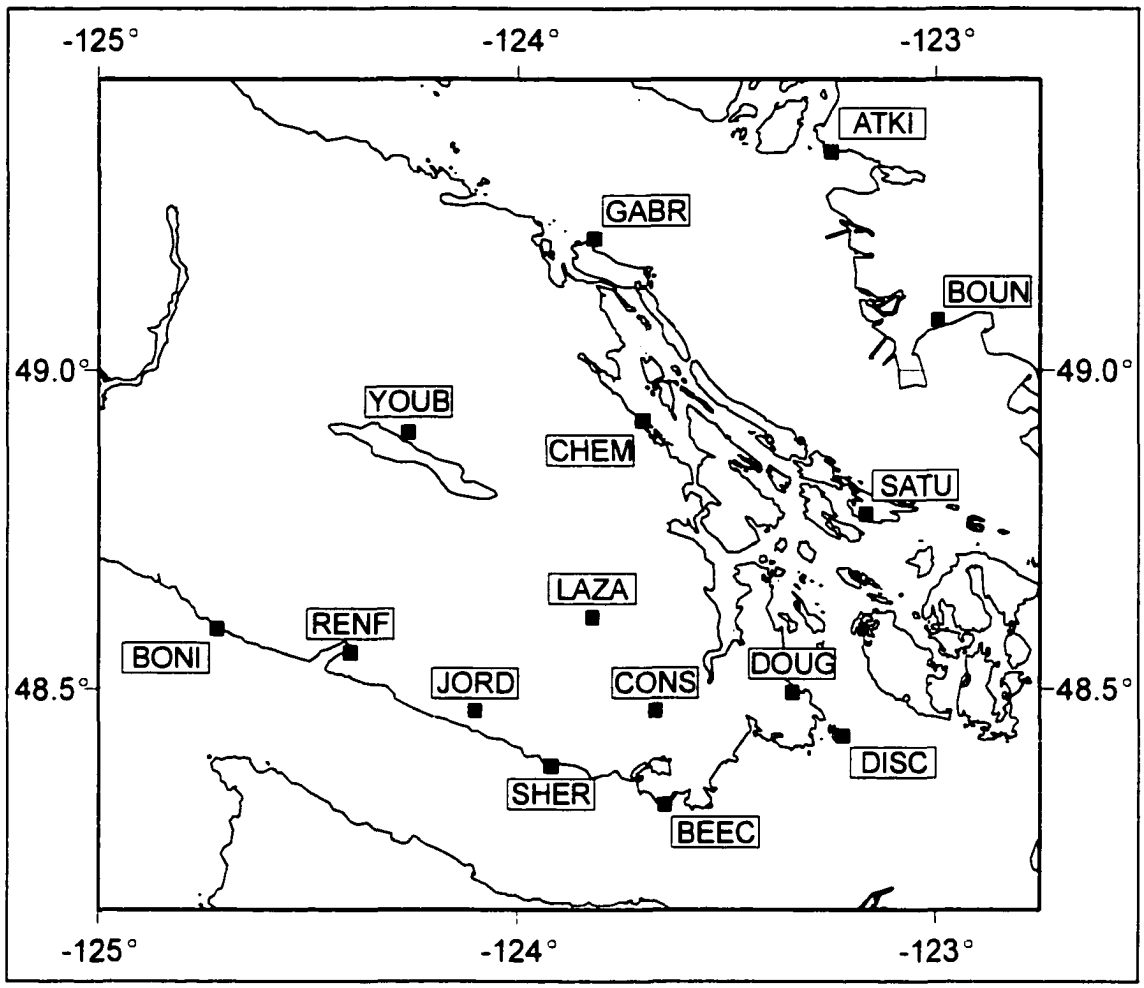

Figure 5.2. Juan de Fuca GPS campaign sites.

1996, with both surveys being carried out by the Geodetic Survey of Canada. The JdF network was processed with the CGPS22 processing package (*outlined in Chapter 4*) with DRAO as the fixed reference station.

Typical of high accuracy GPS network processing packages, CGPS22 requires rather precise (decimetre level) nominal starting coordinates for a particular reference frame. For the JdF network, initial site Cartesian coordinates were determined using the 1996 data set in an ITRF94 reference frame realization using the preprocessing steps shown in Figure 5.3 and discussed below. The 1996 survey data was chosen for the determination of starting

coordinates because of the availability of better quality precise emphemerides (SP3-format) and satellite clock products. Additionally, in 1996, the sites were surveyed with the improved package of Ashtech Z-12 receivers and Ashtech (Dorne-Margolin element) choke-ring antennae.

PROCESSING NAME	SITE NUMBER	STATION NUMBER	STATION NAME (*or* Geographic Name/Location)
ATKI	9501	50C9501	HS 128-1950 (Point Atkinson)
BEEC	1099	79H1099	BH LOOKOUT (Beechey Head)
BONI	1704	31704	BONILLA 3 (Bonilla Point)
BOUN	7004	767004	BDY B.AIRPORT (Boundary Bay Air.)
CHEM	7152	897152	CHEMAINUS
CONS	7019	097019	CONSPICUOUS
DISC	0700	10700	DISCOVERY (Discovery Island)
DOUG	1703	11703	DOUGLAS (Mount Douglas)
GABR	7153	897153	GABRIOLA (Gabriola Island)
JORD	7156	897156	JORDAN RIDGE
LAZA	7155	897155	LAZAR (Mount Lazar)
RENF	7025	877025	PORT RENFREW
SATU	9763	8779763	SATURNA (Saturna Island)
SHER	2900	7872900	0210B (Sheringham Point)
YOUB	7154	897154	YOUBOU

Table 5.1. Station Names of the Juan de Fuca GPS Network

The initial step of preprocessing corrects for the low accuracy Ashtech clock. The internal Ashtech clock is an inexpensive oscillator with significant drift. The internal clock is adjusted to stay within ±1 millisecond of GPS master time by being periodically reset by 1 millisecond at a time. Jeff Freymeuller (Univ. of Alaska, Fairbanks) developed the routine CLOCKPRP (*distributed as* ClockPrep) to correct this problem in RINEX files. CLOCKPRP is run on all of the daily RINEX observation files for the JdF network sites.

SITE	LATITUDE	LONGITUDE	ELEVATION (m)
ATKI	49° 20′ 14.39917″	-123° 15′ 11.92944″	-14.469
BEEC	48° 18′ 57.34460″	-123° 39′ 3.00424″	49.612
BONI	48° 35′ 38.18742″	-124° 42′ 58.34210″	-15.575
BOUN	49° 4′ 39.28872″	-122° 59′ 45.07297″	-18.743
CHEM	48° 55′ 11.90255″	-123° 42′ 11.23066″	-1.156
CONS	48° 27′ 55.53112″	-123° 40′ 24.77802″	657.913
DISC	48° 25′ 31.66256″	-123° 13′ 36.84956″	12.056
DOUG	48° 29′ 35.07228″	-123° 20′ 48.33900″	206.093
GABR	49° 12′ 9.27431″	-123° 49′ 10.81028″	-14.805
JORD	48° 27′ 53.14434″	-124° 6′ 12.54963″	552.169
LAZA	48° 36′ 43.73796″	-123° 49′ 27.04532″	827.678
RENF	48° 33′ 22.57898″	-124° 24′ 1.73386″	23.206
SATU	48° 46′ 26.89335″	-123° 10′ 17.12687″	381.816
SHER	48° 22′ 37.58771″	-123° 55′ 15.20272″	-5.530
YOUB	48° 54′ 3.82648″	-124° 15′ 43.92084″	766.776

Table 5.2. Station Locations of the Juan de Fuca GPS Network

The next step was to iteratively improve the starting coordinates for the JdF sites. The header of the daily RINEX site observation files contain only approximate station coordinates provided by the survey agency. The refinement of these starting coordinates was accomplished by employing the routine GPSPACE (GPS Processing using ACS precise Clock and Ephemerides), a single-point, precise GPS processing program from the Geodetic Survey Division, Natural Resources Canada [*Héroux and Kouba*, 1995]. The corresponding daily IGS precise orbit files and precise clock files from the EMR Analysis Centre of the IGS (operated by the Geodetic Survey of Canada [*Kouba et al.*, 1993]) were downloaded via *ftp* and used with GPSPACE. Starting with the RINEX-header supplied coordinates, which

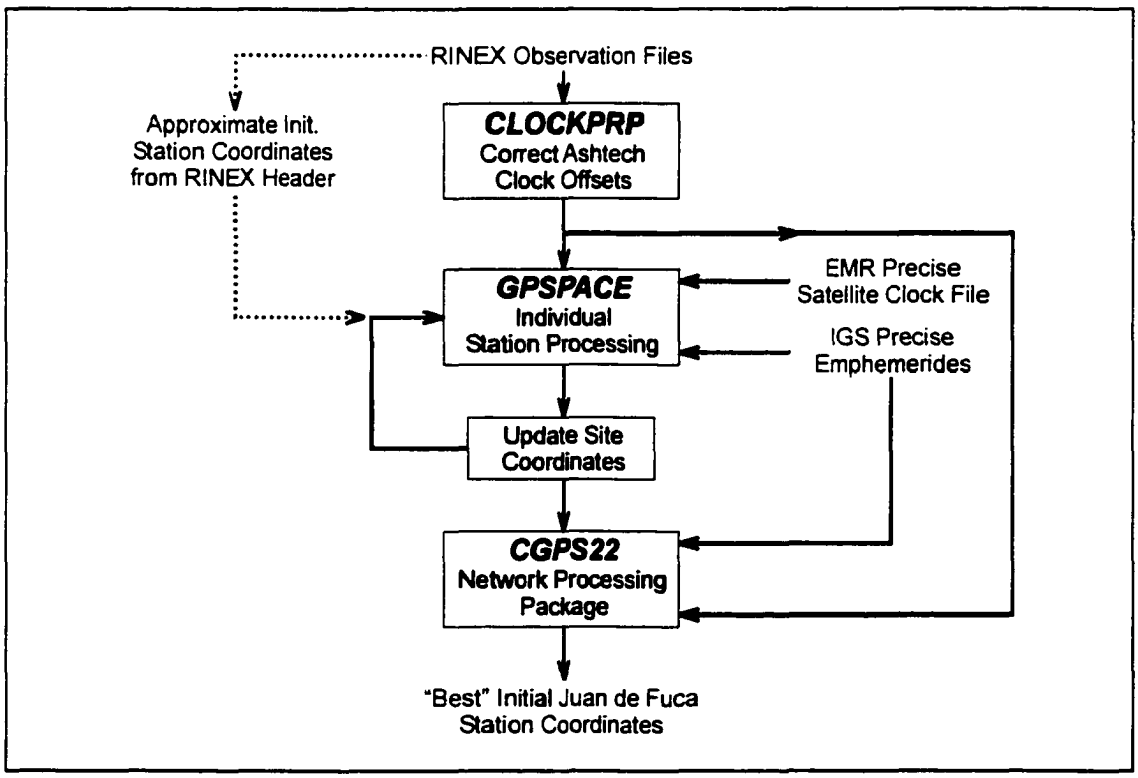

Figure 5.3. Preprocessing steps for 1996 Juan de Fuca campaign data.

were subsequently replaced by coordinates produced by the precise GPS positioning routine, this iterative process was repeated on a station-by-station basis until the updated site coordinates produced by successive runs of GPSPACE converged.

The resultant point-positioned station coordinates were then processed collectively, day-by-day relative to DRAO to produce precise network determined site coordinates. This was achieved with the CGPS22 network processing package (*outlined in Chapter 4*). The clock drift-effect corrected daily Ashtech RINEX files (amended by CLOCKPRP) were again used along with IGS precise emphemerides in the network processing. The WCDA site DRAO, located inland from the region of margin deformation, was employed as the reference site (for reasons previously outlined). Daily data from the continuous WCDA sites ALBH, NANO, and UCLU along with University of Washington sites NEAH and SEAT (Seattle, WA on the UW campus) were processed to provide a day-by-day regional framework with improved station coordinates in an ITRF94 realization that were then constrained in the reprocessing of the 1996 campaign data and the processing of 1991 campaign data.

Additional pre-processing of the 1991 data was required in order to make it consistent with the 1996 survey epoch. For the 1991 data prior to network processing, problems associated with Ashtech receiver clock-drift effects in the daily site RINEX observation files were again corrected with CLOCKPRP. IGS precise satellite orbits are not available for 1991. However, the Scripps Orbit and Permanent Array Center of the Scripps Institute of Oceanography (SIO) is major analysis centre participant in the IGS and does provide GPS satellite products including precise orbits (SP3 format) dating back to mid-1991. Available

via *ftp* or through web browsers (http://lox.ucsd.edu), the SIO emphemerides for this survey epoch are in the ITRF91 reference frame. Using the general form of transformation between two reference frames with 7 transformation parameters [e.g. *Boucher and Altamimi*, 1996], the daily 1991 SIO orbit files were transformed to ITRF94 using the routine TRNFSP3 obtained from the Geodetic Survey of Canada. The antennae used in the 1991 survey were the original Ashtech Geodetic L1/L2 (700228-Revision A) model. Appropriate average phase centre offsets estimated to be -0.002m north and 0.002m east in the horizontal [*Mader*, 1997] were used to correctly map this antenna type to the now standard choke-ring/Dorne-Margolin geodetic quality antennae.

The final network analyses of the 1996 and 1991 JdF campaign data were carried out with the CGPS22 software on a day-by-day basis in largely the same manner as the routine WCDA data processing outlined in Chapter 4 (ocean loading, however, was not applied to the JdF sites). To correct cycle slip offsets and delete single-point outliers, an important requirement for obtaining the highest quality solutions, manual visual editing of the data was again performed with the CGPS22 program CYFIX. Tables 5.3 and Table 5.4 give the Julian dates of the data processed for the 1996 and 1991 campaigns, respectively. All sites have a minimum of two occupations per campaign year.

To achieve the best final site position for a survey epoch, site coordinate estimates and the corresponding covariance information for an entire survey period were combined in a common least-squares sense to produce average network site solutions relative to the fixed site DRAO. This post-processing employed the day-by-day SINEX (Software INdependent EXchange format) files generated by the CGPS22 package. The SINEX format was

originally developed and used by IGS Global Network Associated Analysis Centres to combine regional GPS continuous network solutions with global solutions.

SITE	JULIAN DATES OF PROCESSED DATA (1996)					
	217	218	219	220	221	222
ATKI					X	X
BEEC	X		X	X		
BONI	X	X				
BOUN					X	X
CHEM				X	X	X
CONS			X	X		
DISC			X	X		
DOUG				X	X	
GABR					X	X
JORD		X	X			
LAZA		X		X		
RENF	X	X				
SATU					X	X
SHER	X		X			
YOUB		X				X

Table 5.3. Dates of Processed GPS Data for JDF Network - 1996 Campaign

SITE	JULIAN DATES OF PROCESSED DATA (1991)										
	275	276	277	278	279	280	281	282	283	284	285
ATKI			X	X							
BEEC	X	X			X	X				X	X
BONI						X			X		
BOUN			X	X							
CHEM			X	X			X	X			
CONS		X						X		X	
DISC					X					X	
DOUG	X	X						X		X	
GABR			†	X							
JORD	X	X			X	X					X
LAZA							X	X	X		X
RENF						X	X				
SATU				X				X			
SHER	X	X			X	X			X		
YOUB			X				X		X		

Table 5.4. Dates of Processed GPS Data for JDF Network - 1991 Campaign
(† denotes data excluded from final solution.)

For JdF network post-processing, the SINEX file generating routine of the CGPS22 package was slightly modified to tightly constrain ($\leq$1mm) the reference site DRAO position. Daily SINEX files include site names, coordinate estimates and the corresponding covariance information (along with details on site instrumentation and monumentation). All of the daily network site coordinate estimates for a survey period were thus averaged

(constrained in part by the covariance information) in a common least-squares estimation sense to produce site solutions relative to the fixed DRAO position. 1996 campaign data were processed together with data from the continuous sites ALBH, NANO, UCLU, NEAH, and SEAT to provide additional regional stability and day-to-day continuity. These continuous sites did not exist at the time of the 1991 survey.

5.3 - Juan de Fuca Network - Deformation Velocities

The difference between the average 1991 position for a given site and its average 1996 position determines the individual site displacements shown in Figure 5.4 (*see also*

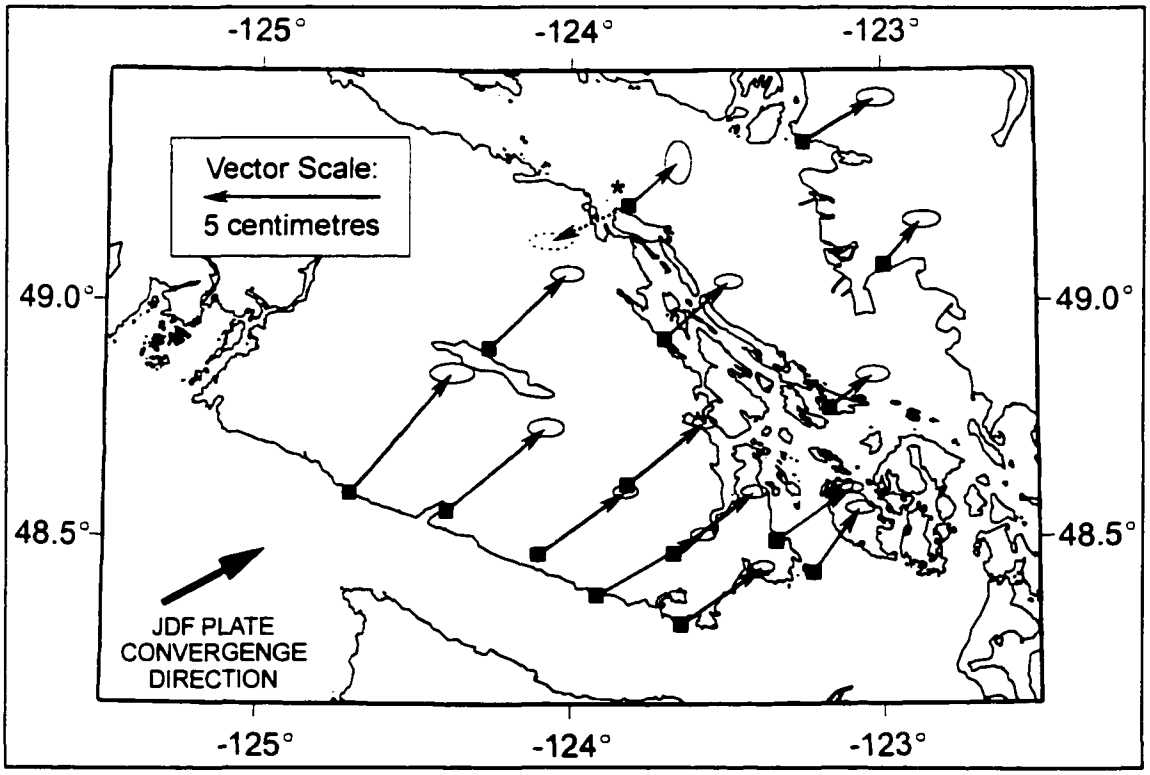

Figure 5.4. Juan de Fuca GPS campaign network site displacements between 1991 and 1996. The initial processing results are shown with their estimated 95% confidence ellipses. Additional data for site GABR (denoted with an asterisk) were collected in 1998 and used to produce the expected 1991-1996 value plotted above. The initial GABR displacement estimate was biased by a poor solution in 1991 and is indicated by the dashed arrow (see discussion in text).

Table D.3 in Appendix D). As the deformation rate is assumed to be constant between survey epochs, the site displacements divided by the time between surveys provides site velocities. Assigning true representative error estimates [*e.g. Zhang et al.*, 1997; *Johnson and Agnew*, 1995] to these displacements remains a problem particularly when site position estimate regressions cannot be carried out, as is the case for only two survey epochs. The formal errors for site positions in each survey were deemed optimistic, reflecting precisions over survey periods of one to two weeks rather than true accuracy. Consequently the confidence ellipses presented for the JdF survey were determined by scaling by the square root of squares of the estimated coordinate errors by a factor of 5. This produces confidence ellipses that are approximately twice as large those of the established regional continuous sites. Given the uniform displacement field for this survey with respect to the regional continuous GPS deformation field, it is felt that these confidence ellipse estimates are fairly realistic as well as giving good relative error estimates.

The vector directions are all nearly parallel within the estimated uncertainties and largely agree with the direction of Juan de Fuca Plate convergence. The displacements are consistent with the deformation signal expected from a locked CSZ subduction thrust surface. The largest displacements (~5cm) occur towards the coastal margin and decrease landward away from the CSZ deformation front. One site, GABR, located on Gabriola Island, did not follow this pattern. The daily solutions for the two site occupations in 1991 are not consistent at the $\leq$ 1 cm level. The solution for GABR on day 278 alone would provide a displacement that is congruous with the remainder of the network. However the solution for GABR on day 277 alone yields a displacement with respect to 1996 that is larger

in magnitude and in the opposite direction.

Additional data for GABR was collected with an Ashtech Z-12 receiver with a choke-ring antenna on days 195 and 197 of year 1998 by Alex Smith of the University of Victoria and GSC-PGC. The 1998 GABR data was processed in a network analysis with DRAO fixed using the CGPS22 package. Preprocessing work consisted of correcting for the Ashtech clock offsets in the daily RINEX files (using CLOCKPRP). IGS emphemerides were employed in processing after being transformed from ITRF96 to ITRF94 realizations. The 1998 GABR data was processed with the continuous GPS sites ALBH, NANO, UCLU, NEAH, SEAT, and WSLR to provide a more robust network solution. Additionally, ALBH, NANO, UCLU, NEAH, SEAT, and WSLR were processed for 1998 days 194, 196, and 198

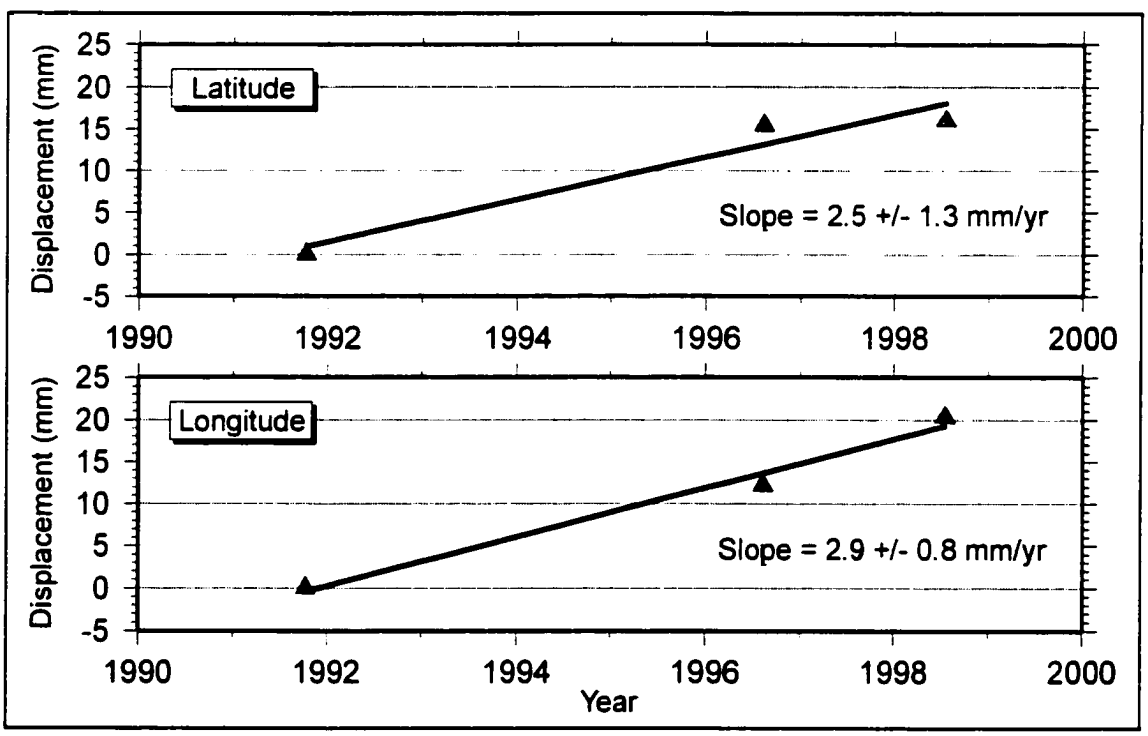

Figure 5.5. Site GABR velocity regression plots. The change in position in latitude (top panel) and longitude (bottom panel) with time are shown [data from Henton et al., 1998]. The reference location for 1991 is based on the Day 278 solution.

in the same scheme as with the site GABR included on days 195 and 197. This further solidifies the overall solution when combining the daily SINEX files to get a 1998 average network solution for GABR. The 1996 to 1998 site displacement is consistent with the day 278 of year 1991 to 1996 displacement (Figure 5.5). Taken together, through a linear regression estimate, they provide a deformation rate that agrees well with the remainder of the JdF velocity field. As the deformation rate is constant (as determined from the continuous WCDA sites in the region) between survey epochs, the site displacements divided by the time between surveys provides site velocities relative to DRAO. The rate of differential, rigid-body North American plate motion (*see Section 4.4*) between individual JdF sites and DRAO is removed to produce the velocity field shown in Figure 5.6.

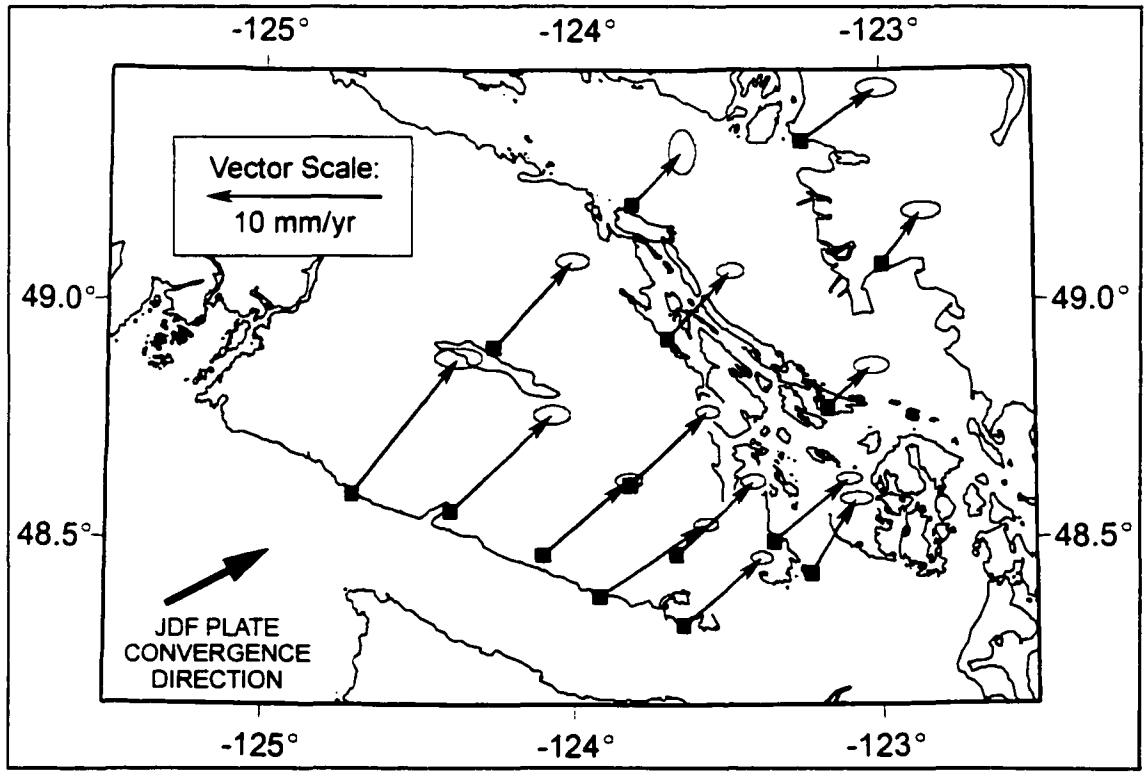

Figure 5.6. Juan de Fuca GPS campaign velocity field. Velocity vectors have been corrected for differential NA plate motion between the individual sites and the reference site, DRAO, near Penticton, B.C.

5.4 - Central Vancouver Island GPS Strain Network Processing

The sites of the Central Vancouver Island (CVI) GPS Strain Network (Figure 5.7 and Figure 5.8) lie predominantly on central Vancouver Island in southwestern B.C. The 17 CVI sites (Table 5.5 and Table 5.6) used in this study were surveyed in late-July/early-August, 1992 (Table 5.7) and reoccupied in September, 1997 (Table 5.8) by the Geodetic Survey of Canada. The CVI network data were processed with the Bernese GPS Software Version 4.0 [*Rothacher and Mervart*, 1996] package developed by the Astronomical Instititute, University of Berne (AIUB). Although a very brief overview of Bernese Version 4.0 follows, the interested reader is referred to the *Bernese GPS Software Version 4.0* user manual edited by *Rothacher and Mervart* [1996].

It is noted that during the period of the 1992 survey, the U.S. Department of Defense implemented intermittent testing of Anti-Spoofing (AS). The inability of CGPS22 to provide precise ($\leq$ 1cm) solutions under this condition, coupled with the relatively recent availability of Bernese V4.0 at PGC led to the switch in processing packages. By eliminating the process of routine manual data editing, Bernese V4.0 offers some time

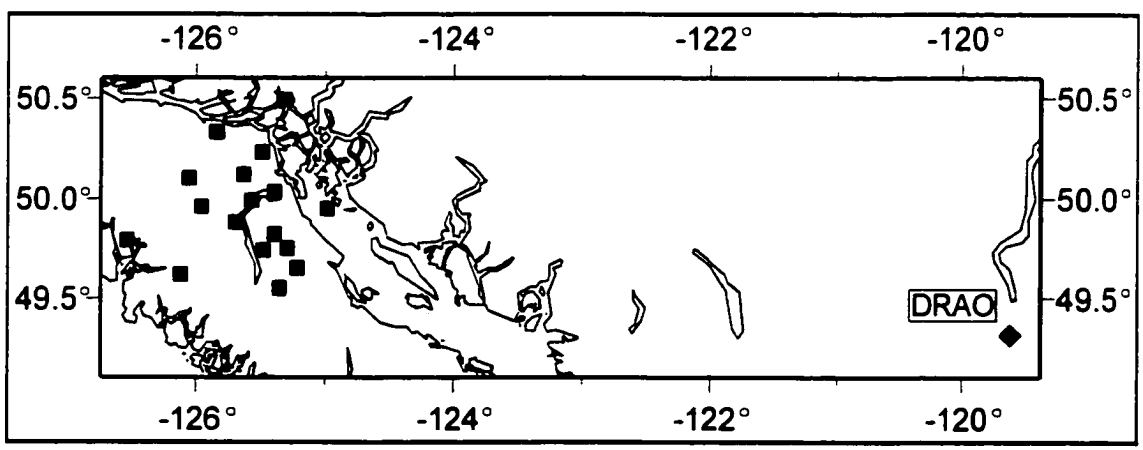

Figure 5.7. The Central Vancouver Island GPS campaign network and the WCDA reference site DRAO.

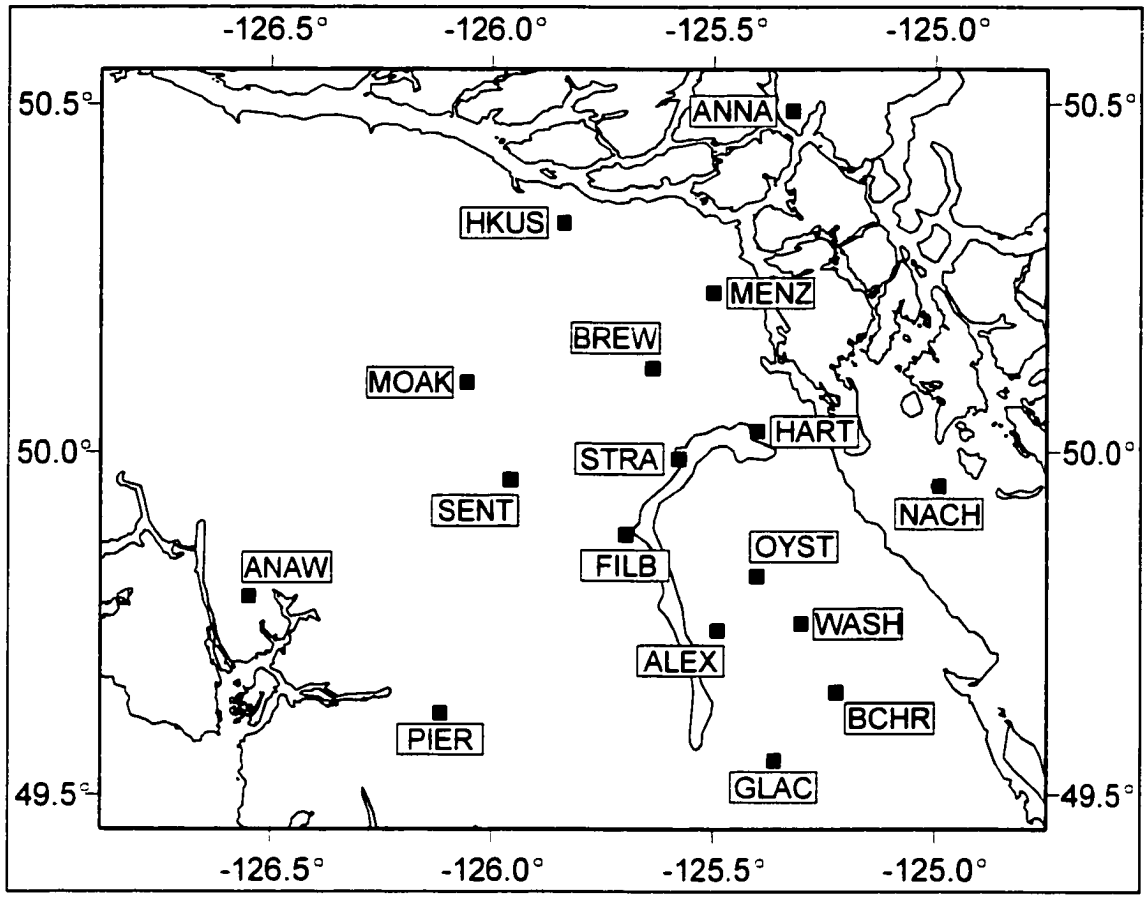

Figure 5.8. Central Vancouver Island GPS campaign sites.

efficiency over CGPS22.

The Bernese GPS Software provides high accuracy results and good processing speed for a number of GPS applications including campaign network processing. Version 4.0 is menu driven for user-friendliness and consists of five primary parts whose functional flow is shown in Figure 5.9. Running the programs of Bernese V4.0, the Bernese Processing Engine (BPE) was developed by AIUB jointly with the University NAVSTAR Consortium (UNAVCO) to efficiently automate routine network data processing and obviating the need for manual intervention. This software package has been recently implemented at the PGC for automated WCDA processing.

PROCESSING NAME	SITE NUMBER	STATION NUMBER	STATION NAME (*or* Geographic Name/Location)
ALEX	N030	34HN030	ALEXANDRA (Mount Alexandra)
ANAW	7008	827008	ANA
ANNA	7013	667013	ANNA
BCHR	N034	34HN034	BEECHER (Mount Beecher)
BREW	7167	897167	BREWSTER
FILB	3018	77C3018	9032-77 (Filberg)
GLAC	7002	847002	GLACIER GEOD (Comox Glacier)
HART	7169	897169	HART
HKUS	7010	667010	HKUSAM (Hkusam Mountain)
MENZ	7012	667012	MENZIES (Mount Menzies)
MOAK	7168	897168	MOAKWA
NACH	7170	897170	NACH (Mitlenatch Island)
OYST	7166	897166	OYSTER
PIER	0095	46H0095	PIERCE (Pierce Range)
SENT	7006	827006	SENTINAL GEOD (Horseshoe Mtn.)
STRA	3001	8873001	9812-88 (Strathcona Dam)
WASH	7011	927011	WASH (Mount Washington)

Table 5.5. Station Names of the Central Vancouver Island GPS Network

SITE	LATITUDE	LONGITUDE	ELEVATION (m)
ALEX	49° 44′ 16.93308″	-125° 29′ 34.02324″	1968.262
ANAW	49° 47′ 20.40000″	-126° 32′ 49.35796″	1104.480
ANNA	50° 29′ 26.32872″	-125° 18′ 55.07995″	1144.999
BCHR	49° 38′ 59.70464″	-125° 13′ 24.50054″	1370.132
BREW	50° 7′ 28.77467″	-125° 38′ 23.82052″	272.094
FILB	49° 52′ 58.10598″	-125° 41′ 52.73705″	221.194
GLAC	49° 33′ 7.85136″	-125° 21′ 51.91372″	1951.138
HART	50° 1′ 57.33001″	-125° 23′ 50.66617″	165.912
HKUS	50° 20′ 5.49100″	-125° 50′ 26.61065″	1656.052
MENZ	50° 13′ 50.11862″	-125° 29′ 48.71844″	1222.635
MOAK	50° 6′ 15.74383″	-126° 3′ 29.42411″	370.227
NACH	49° 56′ 56.68890″	-124° 59′ 55.26723″	-8.711
OYST	49° 49′ 23.83200″	-125° 3′ 58.24706″	742.596
PIER	49° 37′ 8.30198″	-126° 7′ 19.0040″	1387.234
SENT	49° 57′ 22.73420″	-125° 57′ 27.98000″	1724.158
STRA	49° 59′ 41.38101″	-125° 34′ 57.41364″	215.028
WASH	49° 45′ 8.52321″	-125° 17′ 49.01164″	1561.034

Table 5.6. Station Locations of the Central Vancouver Island GPS Network

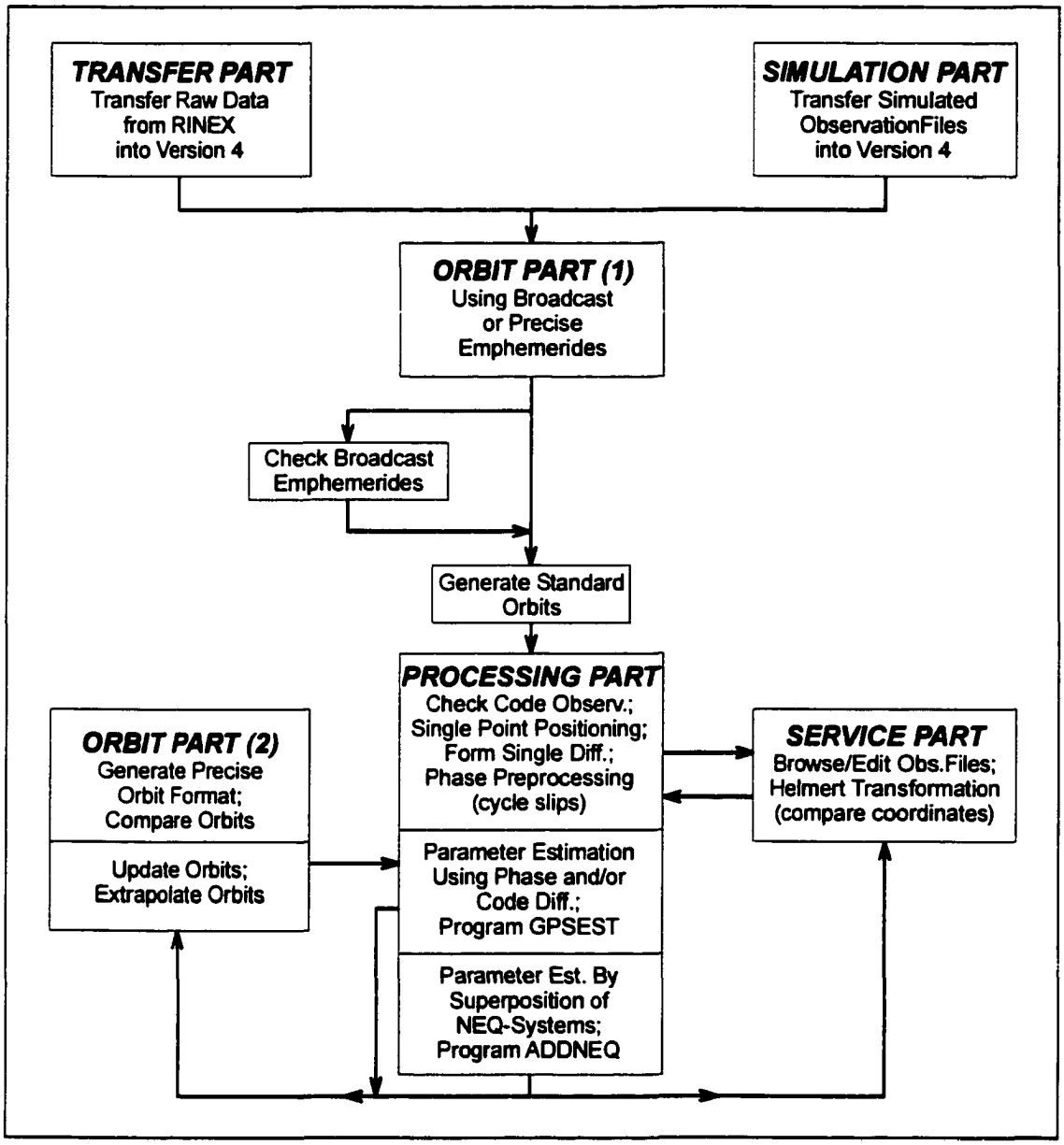

Figure 5.9. Functional flow diagram of the modules of Bernese GPS Software Version 4.0.

For the CVI network. site coordinates were determined from the 1997 data set in an ITRF94 realization through the preprocessing steps outlined in Figure 5.10 and discussed below. The 1997 survey data were chosen for preprocessing because of the availability of better quality precise satellite orbits from the IGS. Furthermore, the 1997 data were collected with the improved (relative to the 1992 campaign) package of Ashtech Z-12

receivers and Ashtech (Dorne-Margolin element) choke-ring antennae.

The first step of preprocessing was again to correct for the drift of the low accuracy internal Ashtech clock by using the routine CLOCKPRP on all of the campaign RINEX files. The network preprocessing was initiated using the BPE procedure control file GEN_BPE. GEN_BPE is a general purpose, procedure control script for network processing of data with baselines ranging between 10 and 2000 km. The GEN_BPE file and it associated scripts were developed at and distributed by the University NAVSTAR Consortium (UNAVCO) (*at:* http://www.unavco.ucar.edu/processing/bernese/bpe_dist/gen_bpe.html). By using precise single-station positioning, this network processing script is capable of improving the

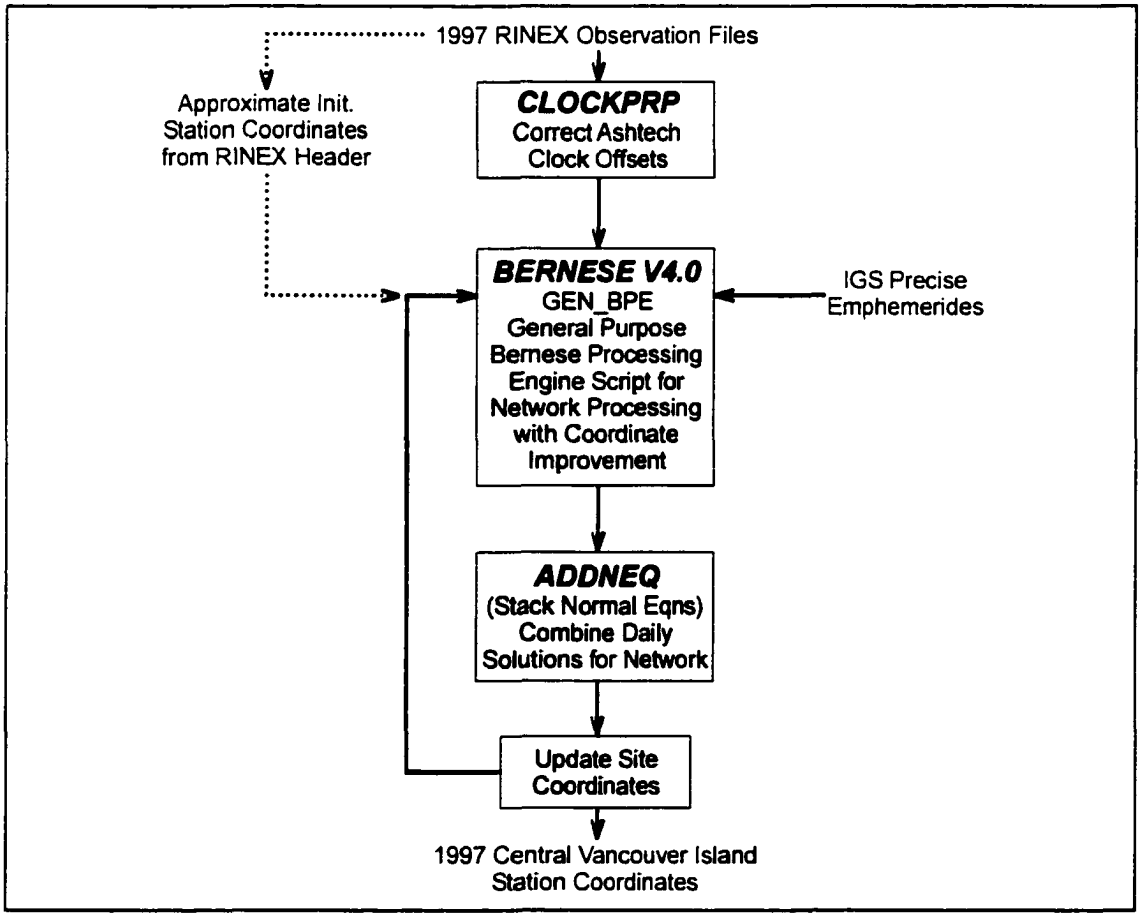

Figure 5.10. Preprocessing steps for 1997 Central Vancouver Island GPS network data.

approximate station coordinates provided in the header of daily RINEX site observation data files. The WCDA site DRAO, located inland from the region of margin deformation, was again adopted as the reference site and held fixed during all of the CVI network processing.

The daily solutions for the network were combined by stacking the normal equation systems using the Bernese V4.0 menu program ADDNEQ [*Rothacher and Mervart*, 1996]. Because the approximate coordinates provided in the header of the RINEX observation file may be of relatively poor or limited accuracy, network processing was repeated using the updated coordinates (produced by the stacked combination of daily solutions) as the initial, nominal starting coordinates for subsequent network processing. This procedure of revising the network site coordinates was repeated (commonly 3-4 iterations) until the updated site coordinates produced by successive network processing runs converged. Daily site coordinates were then examined and compared to check that all of the daily position solutions at each site were self-consistent at the sub-centimetre level. Only one solution, site FILB on day 262, did not meet this criteria and the corresponding data file was excluded from subsequent processing (Table 5.7). Network processing was then performed to achieve final 1997 CVI station coordinates. Again, to provide additional network solution stability, the daily data files for the WCDA sites ALBH, HOLB, NANO, UCLU, and WSLR were processed with the 1997 CVI campaign data.

SITE	JULIAN DATES OF PROCESSED DATA (1997)									
	253	254	255	256	257	258	259	260	262	263
ALEX	X	X							X	
ANAW									X	X
ANNA			X	X	X					
BCHR	X	X	X							
BREW						X	X	X		
FILB				X	X				‡	
GLAC	X	X								X
HART	X	X	X	X	X					
HKUS					X	X	X			
MENZ					X	X	X			
MOAK						X	X	X	X	
NACH	X	X	X							
OYST	X	X	X							
PIER									X	X
SENT					X	X	X		X	
STRA				X	X	X				
WASH	X	X	X							X

Table 5.7. Dates of Processed GPS Data for CVI Network - 1997 Campaign

(‡ - Data excluded from final solution; discussed in the text.)

SITE	JULIAN DATES OF PROCESSED DATA (1992)									
	211	212	213	216	217	218	219	220	223	224
ALEX	X		X							
ANAW		X	X							
ANNA				X	X					
BCHR	X								X	
BREW				X		‡	X			‡
FILB		X	X			X		X		
GLAC	X								X	
HART				X	X	‡		X		X
HKUS				X					X	
MENZ				X	‡				X	
MOAK			X	X			X			
NACH					X	X			X	
OYST	X				‡	X	X	X		
PIER		X	X							
SENT		X			X					
STRA		X				X	X		X	X
WASH								X		X

Table 5.8. Dates of Processed GPS Data for CVI Network - 1992 Campaign

(‡ - Data excluded from final solution; discussed in the text.)

Additional pre-processing of the 1992 CVI data was required in order to make it consistent with the 1997 survey epoch. Prior to network processing, problems associated with Ashtech receiver clock-drift in the daily site RINEX observation files were first corrected (with CLOCKPRP). As for the case of the 1991 JdF survey, IGS precise orbit products were not available for 1992. Again, precise orbit files referenced to ITRF93 were obtained from SIO and transformed to ITRF94 using TRNFSP3.

The antennae used in the 1992 survey were the physically similar Ashtech Geodetic L1/L2 700228-Revision A and 700228-Revision B models. The rigorous correction of phase-centre variations for these antennae was directly impacted by the intermittent testing of GPS Anti-Spoofing (AS) during the period of this survey. This involved encryption of the normally available P-code (precise code) used by GPS systems. The net effect on almost all civil GPS receivers at the time was poorer tracking of satellite signals. The resulting noisier GPS data degraded the precision of both the global orbit determinations and the calcluated positions of survey sites. In the face of this increased noise and in order to streamline processing, only the appropriate average vertical L_1 and L_2 phase centre offsets determined by *Mader* [1997] were adopted to map this antenna series to the standard choke-ring/Dorne- Margolin element geodetic quality antennae used in the 1997 survey.

The procedure control file GEN_BPE obtains satellite clock information from the precise ephemerides file found in IGS orbit products since 1994. However precise satellite clock corrections were not available in 1992 precise orbit files, especially in periods when AS was turned on and off. For the last stage of 1992 CVI network pre-processing, "Bernese-friendly" daily satellite clock files were produced. Broadcast navigation files for each day

of the 1992 survey were first downloaded (in RINEX format) from the Scripps Orbit and Permanent Array Center of SIO via *ftp*. The navigation files were translated from RINEX into the Bernese broadcast format using the Bernese GPS Software Version 4.0 menu program RNXBV3. Daily satellite clock files were then generated with the Bernese menu program SATCLK. These new clock files were used in the network processing of the 1992 data.

The final processing of 1992 CVI GPS campaign network data was likewise carried out with the Bernese GPS Software Version 4.0 (using the automated processing script GEN_BPE). DRAO was again held fixed. The final coordinates from the processed 1997 data were applied as the initial, starting coordinates for the 1992 survey processing. The daily data files from the WCDA sites ALBH and HOLB were processed with the campaign observations in order to provide additional network solution stability. Site displacements of ALBH and HOLB between the 1992 and 1997 surveys were estimated from their respective velocities relative to DRAO (*discussed in Chapter 4*). Predicted 1992 positions were then calculated for these two sites by adjusting the 1997 survey epoch coordinates (determined by 1997 CVI network processing) with their appropriate site displacements. The estimated 1992 survey-period coordinates for sites ALBH and HOLB were tightly constrained during network processing.

Upon completion of initial 1992 CVI network processing, daily coordinates were then compared on a site-by-site basis for solutions that were not consistent at the ~centimetre level. Five 1992 daily site-solutions (Table 5.8) did not meet this modest criteria and were excluded from subsequent processing: site OYST on day 217, site MENZ on day 217, site

HART on day 218, and site BREW on days 218 and 224 (refer to site locations in Figure 5.8). Station OYST solutions for days 211, 218, 219, and 223 are all highly consistent with one another, with the solution for day 217 incongruous from the other four site determinations. Likewise the coordinates estimated for station HART on day 218 diverge at the ~cm level from the self-consistent set of four solutions for the days 216, 217, 220, and 224. Site MENZ solutions for the two days 216 and 223 are highly consistent but day 217 is dissimilar. Unlike the identification of outliers for the three previously discussed sites, the exclusion of data for station BREW was not as easily justified. Site BREW had four occupations in 1992 with the self-consistent pair of days 216 and 219 differing from the self-similar pair of days 218 and 224. BREW site occupations on days 218 and 224 were eliminated from network processing because a 1992-1997 displacement calculated from this pair would yield a motion direction opposite to the remainder of the CVI displacement field while the pair of days 216 and 218 provide a vector whose motion is parallel to the main CVI deformation. As for site GABR in the Juan de Fuca GPS campaign network described previously in this chapter, new data collection at BREW is needed to resolve with certainty the motion of this site.

5.5 - Central Vancouver Island Network - Deformation Velocities

Excluding the data from the inconsistent solutions, 1992 CVI network processing was again executed to achieve the final daily station coordinates relative to DRAO. The daily solutions for the network were then combined by stacking the normal equation systems using the Bernese V4.0 menu program ADDNEQ with DRAO again held fixed and the WCDA

sites ALBH and HOLB constrained to their estimated 1992 survey-epoch positions. The difference between the average 1992 position for a given site and its average 1997 position gives the individual site displacements shown in Figure 5.11.

As the deformation rate is assumed to be constant between survey epochs, the site displacements divided by the time between surveys determines site velocities relative to the reference site DRAO. The rate of differential, rigid-body North American plate motion (*see Section 4.4*) between individual CVI sites and DRAO is again removed to produce the velocity field with respect to a stable North America (Figure 5.12; *see also* Table D.4 in Appendix D). The 95% confidence ellipses are determined by multiplying by a factor of ten

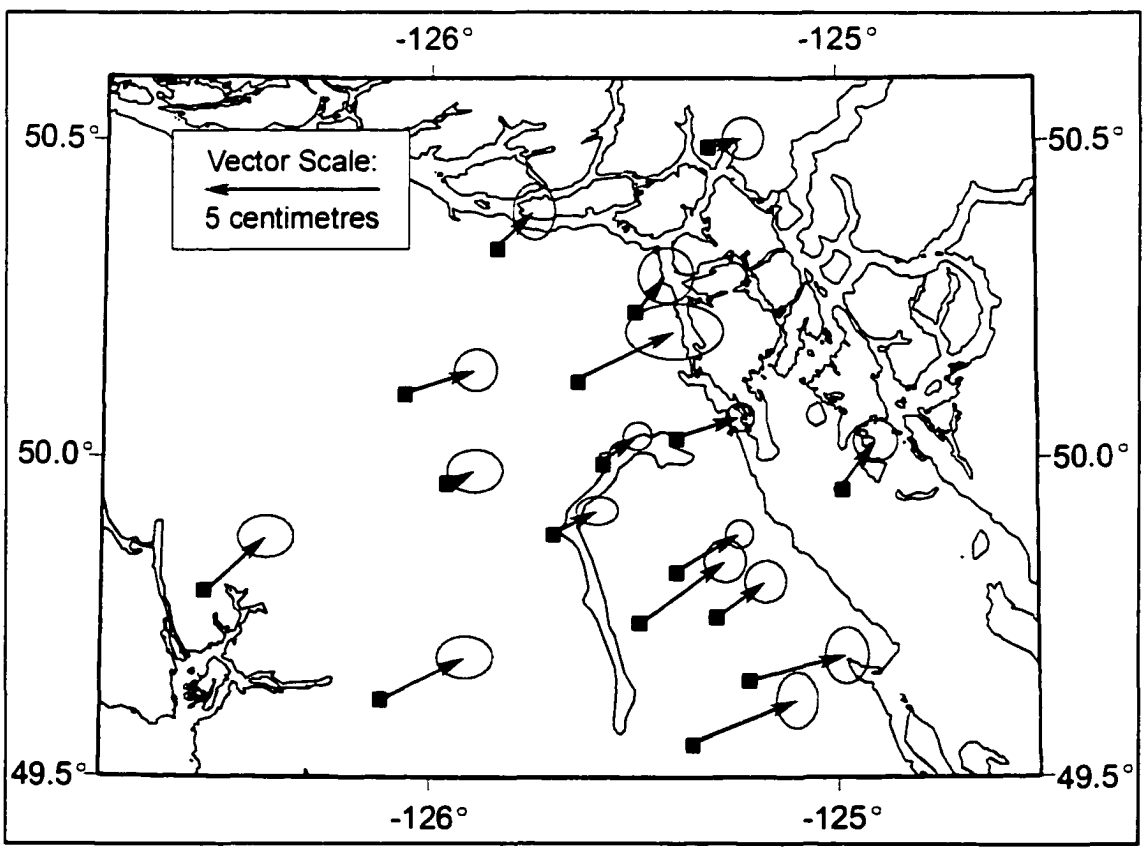

Figure 5.11. Central Vancouver Island GPS campaign network site displacements (with estimated 95% confidence ellipses) between 1992 and 1997.

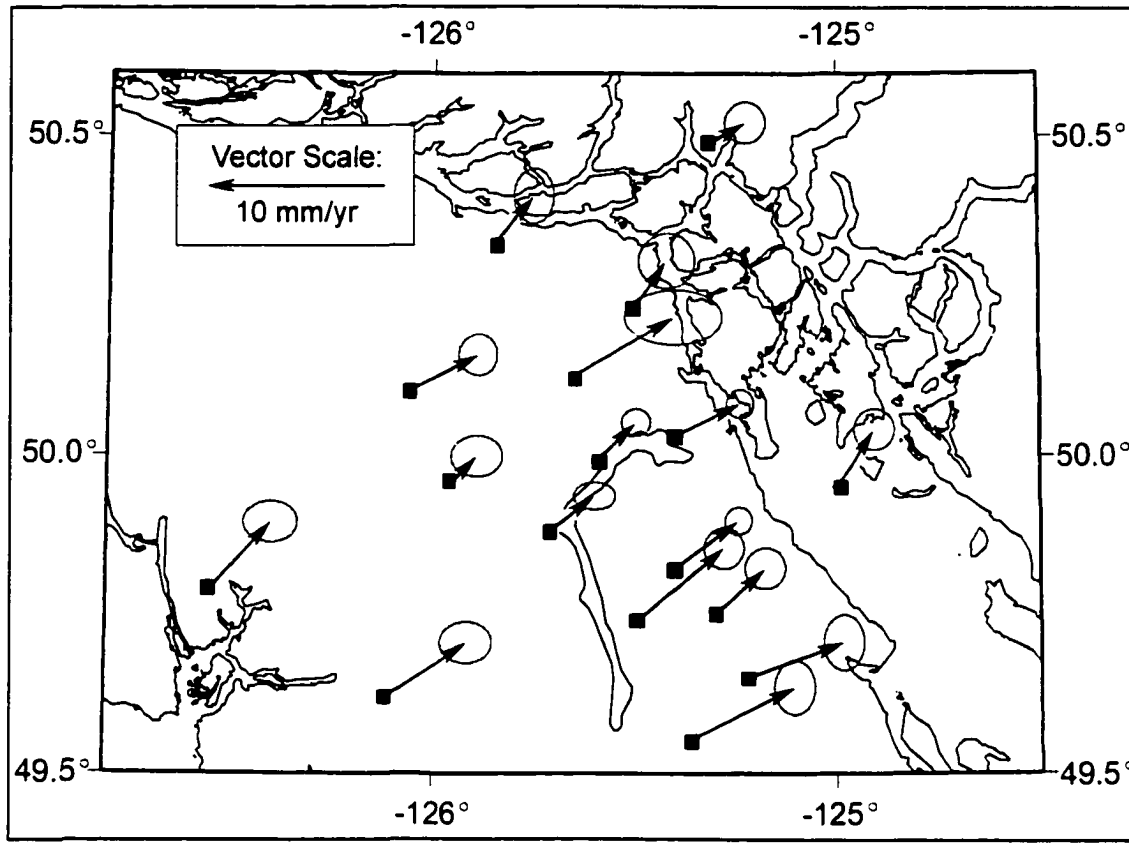

Figure 5.12. Central Vancouver Island GPS campaign velocity field. Velocity vectors have been corrected for differential NA plate motion between the individual sites and the reference site, DRAO, near Penticton, B.C.

the RMS error calculated by the ADDNEQ routine on the 1992 data. The 1997 RMS error values estimated by ADDNEQ are, to the one supplied significant digit, uniform. Additionally the 1997 data contributes less to the overall solution noise budget than the 1992 data whose ADDNEQ-determined RMS error value is 3 to 4 times greater than that of 1997 solution. Although not rigorously determined, this scaling provides error ellipses that appear reasonable for the survey region.

The error ellipses for the Central Vancouver Island network are seen to be generally larger (and with more distribution in size) than the Juan de Fuca (JDF) network solution. At first thought, one might expect the JdF survey, whose first occupation was 1991 compared

to 1992 for CVI, would be subject to greater error. The poorer CVI solutions (by a factor up to ~2) are likely a consequence of GPS broadcast modifications and testing (*i.e.* anti-spoofing) during the period of the 1992 survey.

CHAPTER 6 - GPS NETWORK STRAIN RATE RESULTS

6.1 - Introduction

This chapter consists of two primary components. The first section discusses the determination of network principle strain rates. The second section compares these results to previously determined geodetic strain rates.

6.2 - Basic Strain Theory

As this work focuses upon the horizontal deformation field, the following discussion will be limited to two-dimensions, ignoring the component of vertical deformation. Most of the equations below are adapted from *Chou & Pagano* [1967] and *Turcotte & Schubert* [1982].

A point may be displaced through a combination of rigid-body motion, for which its relative position to neighboring points remains constant, and strain, for which there is relative motion between adjacent points (assuming infinitesimal strain):

$$u_i = \left(u_0\right)_i + \frac{\partial u_i}{\partial \xi_j} d\xi_j \tag{6.1}$$

where the displacement vector, u_i, is a function of position, $u_i(\xi_1, \xi_2)$. The magnitude and direction, Θ_{u0}, of the net rigid body translation, u_0, may be represented, respectively, as:

$$u_0 = \sqrt{(u_0)_x^2 + (u_0)_y^2} \quad \text{and} \quad \Theta_{u_0} = \tan^{-1}\left\{\frac{(u_0)_y}{(u_0)_x}\right\} \qquad (6.2)\ \&\ (6.3)$$

The gradient, $\partial u/\partial \xi_j$, of the displacement vector u, is a tensor that may be expressed as the following sum:

$$u_i = (u_0)_i + \frac{1}{2}\left(\frac{\partial u_i}{\partial \xi_j} + \frac{\partial u_j}{\partial \xi_i}\right) d\xi_j + \frac{1}{2}\left(\frac{\partial u_i}{\partial \xi_j} - \frac{\partial u_j}{\partial \xi_i}\right) d\xi_j \qquad (6.4)$$

and rewritten as:

$$u_i = (u_0)_i + e_{ij} d\xi_j + \omega_{ij} d\xi_j \qquad (6.5)$$

where e_{ij} is the symmetric strain tensor and ω_{ij} is the anti-symmetric rotation tensor. The components e_{ij} and of ω_{ij} are, respectively:

$$e_{ij} = \frac{1}{2}\left(\frac{\partial u_i}{\partial \xi_j} + \frac{\partial u_j}{\partial \xi_i}\right) \quad \text{and} \quad \omega_{ij} = \frac{1}{2}\left(\frac{\partial u_i}{\partial \xi_j} - \frac{\partial u_j}{\partial \xi_i}\right) \qquad (6.6)\ \&\ (6.7)$$

The normal (e_{xx}, e_{yy}) and shear (e_{xy}) strains are then:

$$e_{xx} = \frac{1}{2}\left(\frac{\partial u_x}{\partial x} + \frac{\partial u_x}{\partial x}\right) = \frac{\partial u_x}{\partial x} \qquad (6.8)$$

$$e_{yy} = \frac{\partial u_y}{\partial y} \qquad (6.9)$$

$$e_{xy} = e_{yx} = \frac{1}{2}\left(\frac{\partial u_x}{\partial y} + \frac{\partial u_y}{\partial x}\right) \qquad (6.10)$$

Finally, the solid-body rotation, ω, around a vertical-axis is given by:

$$\omega \equiv \frac{1}{2}\left(\frac{\partial u_y}{\partial x} - \frac{\partial u_x}{\partial y}\right) = -\omega_{xy} \tag{6.11}$$

It is often convenient to express strains in a principal strain axis coordinate system. The principal axes of strain occur in an orientation where the shear strain (off-diagonal) components of the strain tensor, e_{xy}, are zero. Their magnitudes are defined as:

$$e_1 = \frac{1}{2}\left(e_{xx} + e_{yy}\right) + \left[e_{xy}^2 + \frac{1}{4}\left(e_{xx} - e_{yy}\right)^2\right]^{1/2} \tag{6.12}$$

$$e_2 = \frac{1}{2}\left(e_{xx} + e_{yy}\right) - \left[e_{xy}^2 + \frac{1}{4}\left(e_{xx} - e_{yy}\right)^2\right]^{1/2} \tag{6.13}$$

where e_1 is the principal extension axis and e_2 is the principal shortening axis. The direction, of e_2 is defined by:

$$\theta = \frac{1}{2}\tan^{-1}\left(\frac{2e_{xy}}{e_{xx} - e_{yy}}\right) \tag{6.14}$$

Finally, the above formulations may be applied to strain rate, $\dot{e}$, calculations where the displacement field is replaced by an analogous velocity field. As the deformation rate during the period of this study is assumed to be constant, site displacements divided by the time interval between surveys represent site velocities for the above equations [*Turcotte & Schubert*, 1982].

6.3 - Network Strain Rate Calculations

The program *strain_m* [by *Wang & Dragert*, 1999] is used to compute principal horizontal strain rates averaged over an entire region or network. There is not adequate

station density to map the strain field in more detail. The routine first projects the station positions into a geocentric (x,y,z) coordinate system assuming a spherical earth. A local 2-D coordinate system for the network (with x = east; y = north) is then established in the plane perpendicular to the center vector of the network. The center of the network is taken as the origin. The principal horizontal strains (or strain rates) are computed based upon the equations presented in the previous section. It is important to note that, because the results from this scheme describe the average strain over an entire network, this strategy is most appropriately applied to regions that are assumed to deform uniformly (or nearly so - *i.e.*, the gradients in velocity are nearly linear).

6.4 - Network Strain Rate Observations

Network strain rates were computed for two regions: Southern Vancouver Island and Central Vancouver Island (Tables 6.1a, 6.1b). Southern Vancouver Island is located on the northern portion of the Cascadia Subduction Zone (CSZ). The sites of the Juan de Fuca GPS network along with the continuous GPS trackers at ALBH, NANO, NEAH, and UCLU exhibit a rather smooth velocity field and are used to compute the network regional strain rate (Figure 6.1). The principal shortening-axis rate (negative values indicate shortening), $\dot{e}_2$, is $-46.6 \pm 4.6 \times 10^{-9}$ strain/yr in an azimuth (clockwise from north) of $62.8° \pm 1.0°$ (error values are 1-sigma values). The principal extension-axis rate, $\dot{e}_1$, is comparatively much smaller at $5.4 \pm 4.5 \times 10^{-9}$ strain/yr.

The principal axis of shortening corresponds to the direction of relative Juan-de-Fuca/North-America plate convergence (≈N62°E) for northern Cascadia (*refer to Chapter*

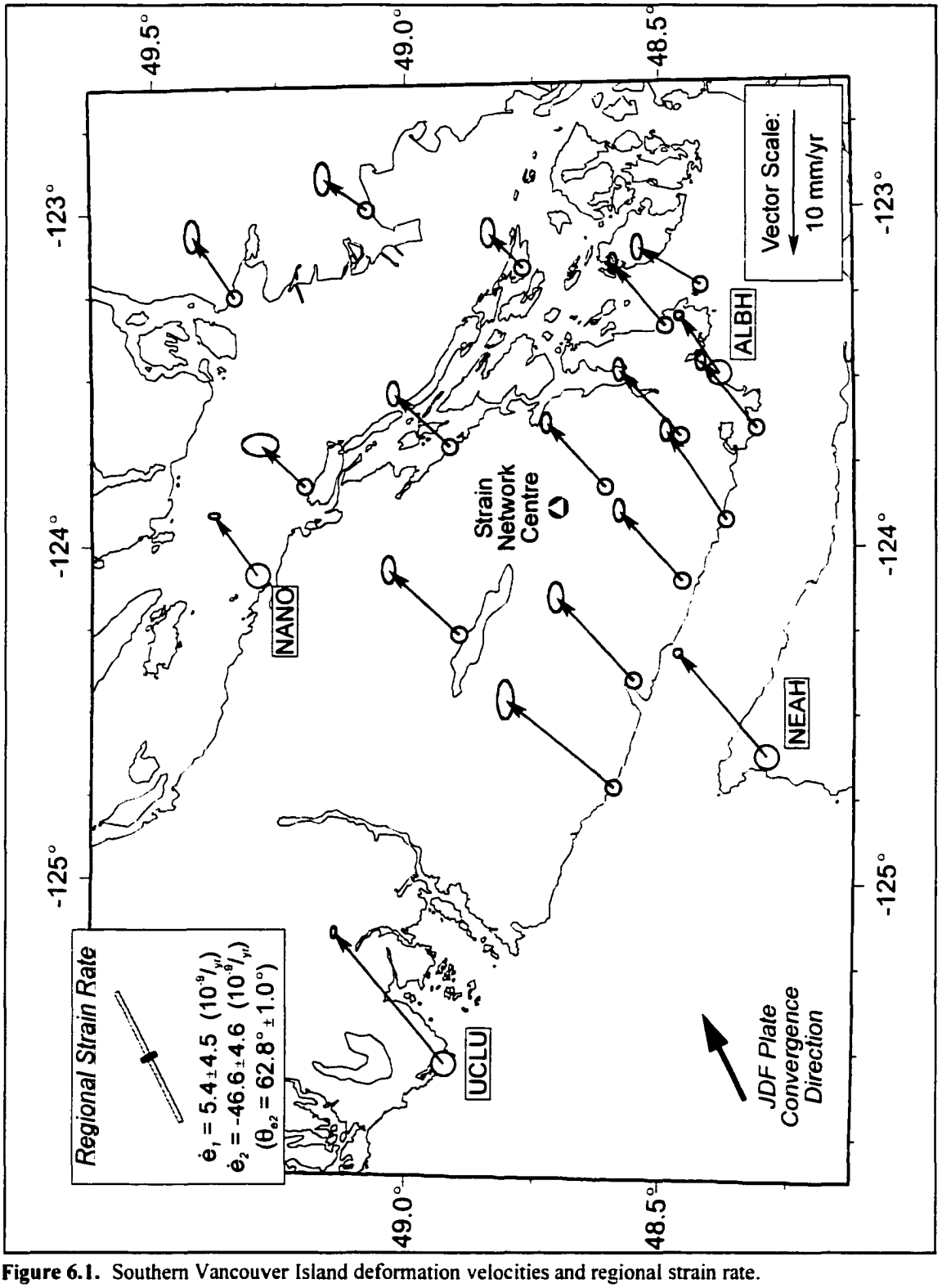

Figure 6.1. Southern Vancouver Island deformation velocities and regional strain rate.

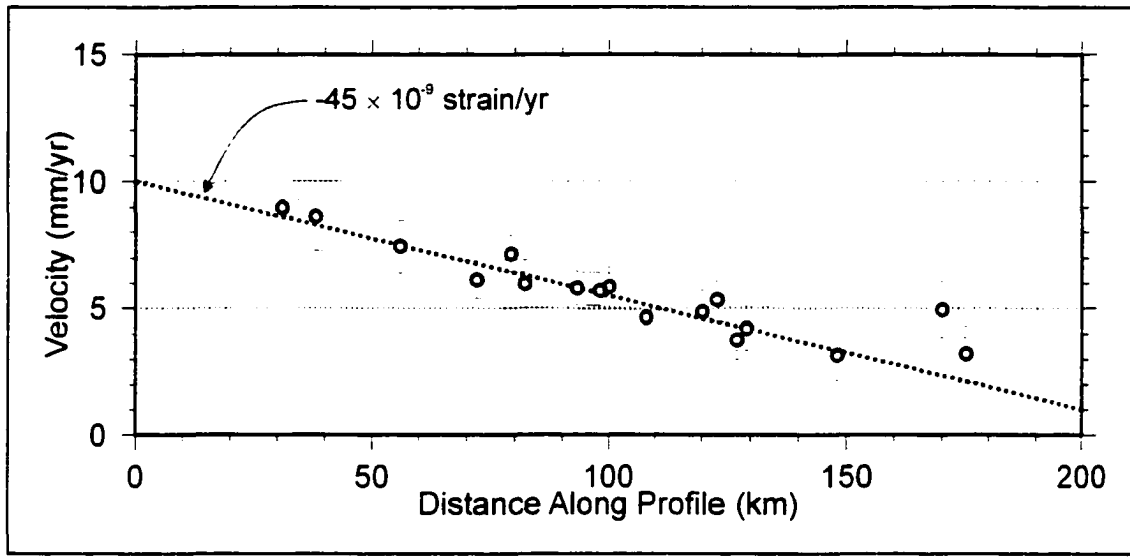

Figure 6.2. Velocities for the region of southern Vancouver Island projected onto a N62°E profile. Values shown are the component of velocity in a 062° direction projected onto a line. Data includes sites of the Juan de Fuca campaign network and WCDA sites ALBH and NEAH. The dotted line with slope -45 × 10^{-9} strain/yr is given for illustrative purposes only to approximate the nearly linear strain rate across southern Vancouver Island.

discussion). Furthermore, this region exhibits nearly uni-axial shortening ({magnitude of $\dot{e}_2$}>>{magnitude of $\dot{e}_1$}). Figure 6.2 shows Southern Vancouver Island deformation velocities projected onto a profile through the centre of the network oriented at N62°E. The deformation rate across this network appears uniform and nearly linear (the line with slope -45 ×10^{-9} strain/yr is given only for illustrative purposes). The deformation across Southern Vancouver Island appears to dominated by the CSZ signal.

The region of Central Vancouver Island is located near the northern edge of the of the subducting Juan de Fuca plate. This region is more tectonically complex and may be subject to interactions between the Juan de Fuca, North America, and Explorer plates. Additionally, two large crustal earthquakes (M ≥ 7) have occurred in this area over the past century. The sites of the Central Vancouver Island GPS network are used to compute the network regional strain rate (Figure 6.3). The value of $\dot{e}_2$, the principal shortening-axis rate,

is -28.1 ± 15.4 $\times 10^{-9}$ strain/yr with an azimuth (CW from north) of 32.4° ± 6.0° (error values are 1-sigma values), and $\dot{e}_1$ is 11.7 ± 15.4 $\times 10^{-9}$ strain/yr.

For this network, the principal axis of shortening deviates significantly from the N62°E direction of JDF/NA plate convergence averaged for northern Cascadia. Additionally, this region suggests increased margin-parallel extension, as expected, to accommodate the north-northwest motion of the WCDA site HOLB on northern Vancouver Island. The CSZ again appears to produce the primary deformation signal for central Vancouver Island.

Network	LAT	LONG	$\dot{e}_1$ (10^{-9}/yr)	$\dot{e}_2$ (10^{-9}/yr)	$\theta_{\dot{e}2}$
SVI	48.707°	-123.885°	5.4	-46.6	62.8°
	(1-sigma errors:)		(± 4.5)	(± 4.6)	(± 1.0°)
CVI	49.943°	-125.614°	11.7	-28.1	32.4°
	(1-sigma errors:)		(± 15.9)	(± 15.4)	(± 6.0°)

Table 6.1a. Network Centre and Strain Rates

Network	Translation Rate	Direction$_{(Translation)}$	Rotation Rate
SVI	6.2 ± 0.1 mm/yr	N47.5°E ± 0.7°	-0.41 ± 0.04 °/Ma
CVI	4.1 ± 0.2 mm/yr	N54.1°E ± 2.7°	0.84 ± 0.22 °/Ma

Table 6.1b. Network Translation & Rotation (+*CCW*) Rates (± 1σ)

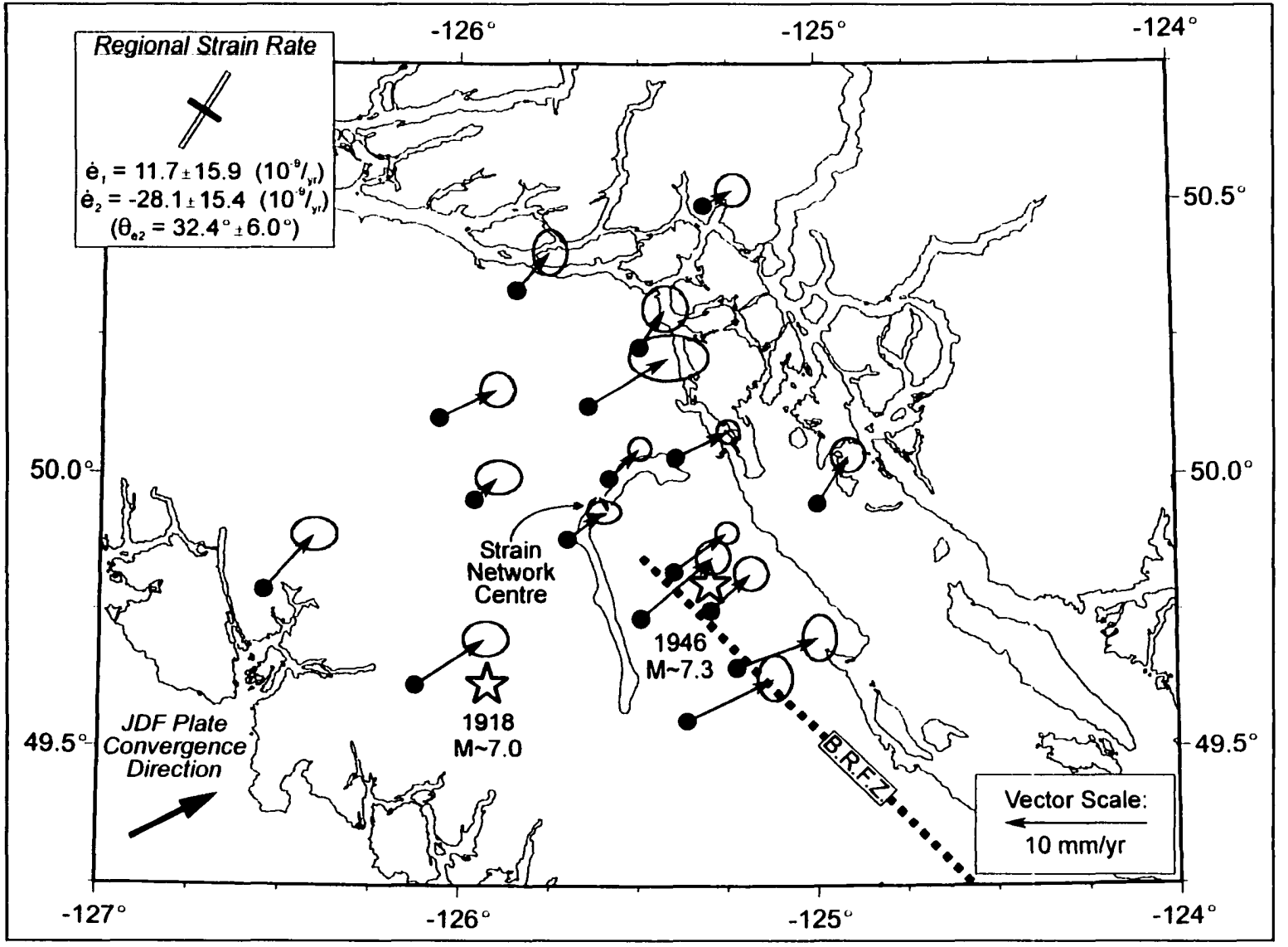

Figure 6.3. Central Vancouver Island deformation velocities and regional strain rate.

6.5 - Comparisons to Previous Geodetic Surveys

In the region of interest in this study of central and southern Vancouver Island there are four strain networks that were established previously for monitoring crustal deformation along the northern portion of the Cascadia margin. Most sites are mountain-top benchmarks allowing long lines of sight. The first surveys were triangulation only. Laser-ranging trilateration techniques have been used on Vancouver Island since 1982 for three horizontal strain networks: the Gold River Network (surveyed in 1982, 1985, and 1988); the Johnstone Strait Network (1984 and 1988); and the Port Alberni Network (1986 and 1990) [*Dragert & Lisowski*, 1990, *Dragert et al.*, 1994]. The Gold River and Johnstone Strait Networks include numerous original triangulation points established mid-century to which the recent trilateration measurements can be compared, thus allowing horizontal strain to be computed over the past few decades [*Dragert & Lisowski*, 1990; *Wang et al.*, 1994; *Dragert et al.*, 1994]. The previous Juan de Fuca Strait Network data employed a 1987 GPS survey compared with earlier triangulation surveys [*Lisowski et al.*, 1989; *Dragert & Lisowski*, 1990]. Because these earlier geodetic data do not resolve all components of the horizontal strain tensor, the strain is assumed to be uniaxial shortening [*Dragert & Lisowski*, 1990, *Dragert et al.*, 1994; *Wang et al.*, 1994]. The results from these earlier studies are included in Table 6.2 and shown in Figure 6.4. (The tabulated results of the Olympic Mountains Network [*Savage et al.*, 1991] are included for comparison.) This discussion will focus on the strain rates determined from networks in the region of Central Vancouver Island (*e.g.*

Johnstone Strait and Gold River) and from the Juan de Fuca Strait Network, and the comparison of this earlier data to the results of this study for those regions.

Network	Interval	μStrain Rate (yr^{-1})	Direction	Reference
Johnstone Str.	1966-1988	-0.15 ± 0.06	N7°E ± 11°	1^{H}
Gold River	1947-1982	-0.23 ± 0.12	N56°E ± 12°	1
Port Alberni	1986-1990	-0.12 ± 0.05	N18°E ± 11°	2,3
Juan de Fuca Str.	1892-1987	-0.18 ± 0.04	N64°E ± 5°	4^{I}
	1942-1987	-0.09 ± 0.03	N82°E ± 8°	
Olympic Mtns.	1982-1990	-0.09 ± 0.03	N59°E ± 7°	5

Table 6.2. Results of previous strain measurements for northern Cascadia margin

Original references are: 1, *Dragert & Lisowski* [1990]; 2, *Dragert* [1991]; 3, *Dragert et al.* [1994]; 4, *Lisowski et al.* [1989]; and 5, *Savage et al.* [1991]. (^{H}denotes a revised value published by *Wang et al.* [1994] is given; ^{I} denotes a revised value from *Dragert et al.* [1994] is given). Quoted uncertainties are one-sigma.

For the older Juan de Fuca Strait Network results, the orientation of the principal axis of shortening agrees well with the direction of plate convergence. The more recent data of the Southern Vancouver Island (SVI), described in a previous section, also shows that the principal axis of shortening corresponds very well to the direction of relative Juan-de-Fuca/North-America plate convergence (≈N62°E) for northern Cascadia. Furthermore, from the SVI data, the assumption of largely uni-axial shortening (comparatively small magnitude of $\dot{e}_1$) for this region is valid. The magnitude of shortening rates determined by these two techniques, is, however significantly different. For the older data [*e.g. Lisowski et al.*, 1989] the average strain rate is -0.18 ± 0.04 μstrain/yr for the time interval 1892-1987, but is -0.09

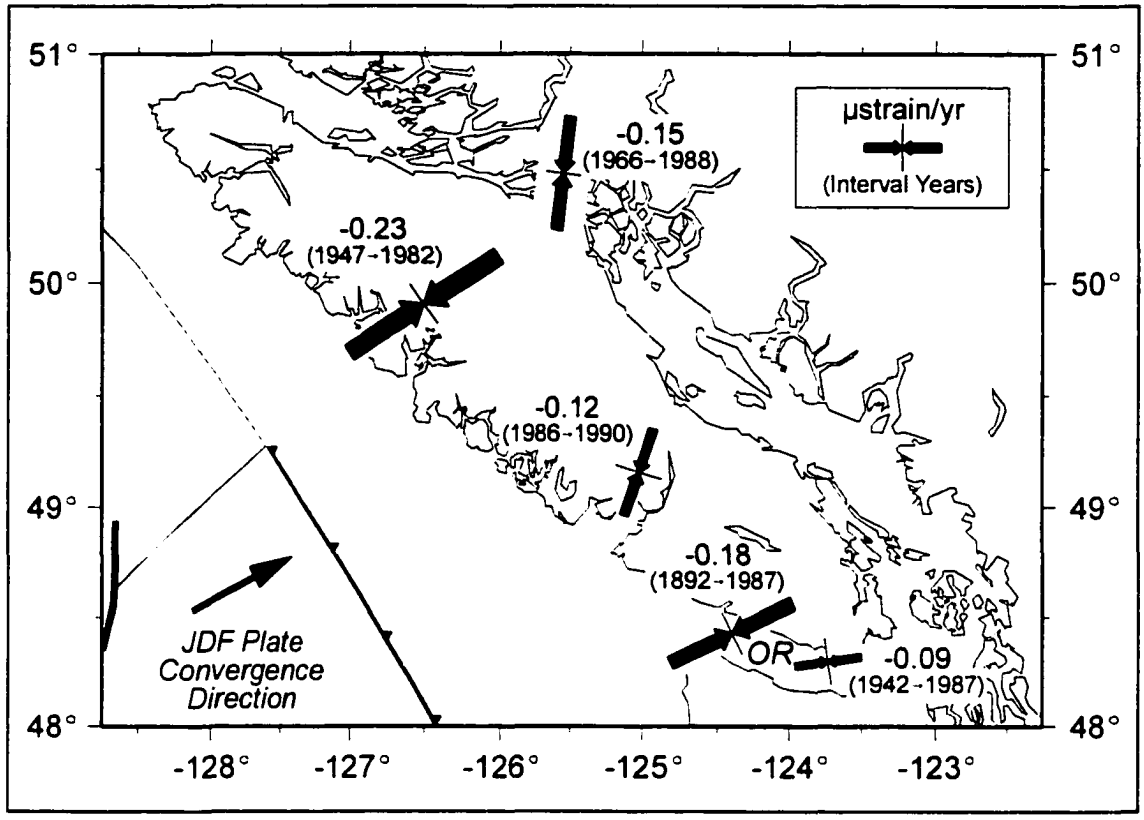

Figure 6.4. Strain rates estimated from previous horizontal control surveys. Strain rate values correspond to values given in Table 6.2 and are given in μstrain/yr (*i.e.* parts per million per year) for the bracketed survey interval. Plot is revised after *Dragert & Lisowski* [1990].

± 0.03 μstrain/yr for the interval 1942-1987. The value of $\dot{e}_2$ for SVI [*e.g.* this study] is -0.047 ± 0.005 μstrain/yr which is approximately ½ to ¼ the strain rate calculated in the previous work. It is possible that there is a temporal change in strain rate, with the strain rate rapidly decreasing over the last century, though this seems unlikely. More likely are unrecognized measurement biases in the older data sets as well as biases between the different measurement techniques.

The centre of the Central Vancouver Island (CVI) GPS Network lies between the Gold River (GOL) and Johnstone Strait (JST) Networks and the CVI GPS Network includes sites from each of the two older geodetic networks. As the region is assumed to be largely

elastic, it is expected that the CVI strain field reflects some average of the deformation recorded by the GOL and JST networks. The principal axis of shortening for the more seaward GOL network is oriented at N56°E ± 12°, exhibiting a shortening-direction largely parallel to the direction of plate convergence. The JST region exhibits a principal shortening direction, N7°E ± 11°, that is oblique to plate convergence. The $\dot{e}_2$-azimuth of the new (*e.g.* GPS-determined) CVI data is N32E°± 6.0° which reflects an average of the GOL and JST networks. Again, the magnitude of maximum shortening rates determined from the older data versus the new data is significantly different. For the older data [e.g. *Dragert & Lisowski*, 1990] the maximum shortening rate for GOL is -0.23 ± 0.12 μstrain/yr and for JST is -0.15 ± 0.06 μstrain/yr. For the newer, GPS-determined CVI data, $\dot{e}_2$ is -0.028 ± 0.015 μstrain/yr. The value of $\dot{e}_1$ for the CVI data is 0.012 ± 0.016 μstrain/yr.

However, the earlier geodetic data does not resolve the complete horizontal strain tensor and the strain was assumed to be uniaxial shortening. By invoking the assumption of uniaxial shortening, the total shear strain, γ, (defined, by convention, as twice the maximum shear strain of the strain tensor:

$$\gamma \equiv 2\left(e_{xy}\right)_{MAX} = \left(e_2 - e_1\right) \tag{6.15}$$

where e_1 and e_2 are magnitudes of the principal axes of strain) is implicitly interpreted as uniaxial shortening oriented in the direction of convergence [*Wang et al.*, 1994; *Chou & Pagano*, 1967; *Turcotte & Schubert*, 1982]. Furthermore, assuming pure strain (equal partitioning in orthogonal directions) reduces values to half those determined by invoking uniaxial shortening [*Dragert et al.*, 1994]. Calculating an equivalent total shear strain rate

($dy/dt = [\dot{e}_2 - \dot{e}_1]$) provides a value of -0.04 μstrain/yr which is still much smaller than the rates determined for GOL and JST. Similarly, assuming pure strain at GOL and JST implies values of -0.12 and -0.08 μstrain/yr, respectively, which again are much larger than the CVI data.

Again it is possible that there is a temporal change in strain rate, with the strain rate rapidly decreasing over the past few decades. Figure 6.5 suggests a possible decrease in strain rate in the vicinity of CVI. This region has experienced two large (M~7) relatively shallow crustal earthquakes in the last century [*e.g. Rogers and Hasegawa*, 1978; *Cassidy et el.*, 1988]. However, measurement biases in the older data sets seem more likely. Referring to Figure 6.5, the two most recent Gold River Network strain rates were determined for the intervals 1982-1985 and 1985-1988. Although these three surveys were

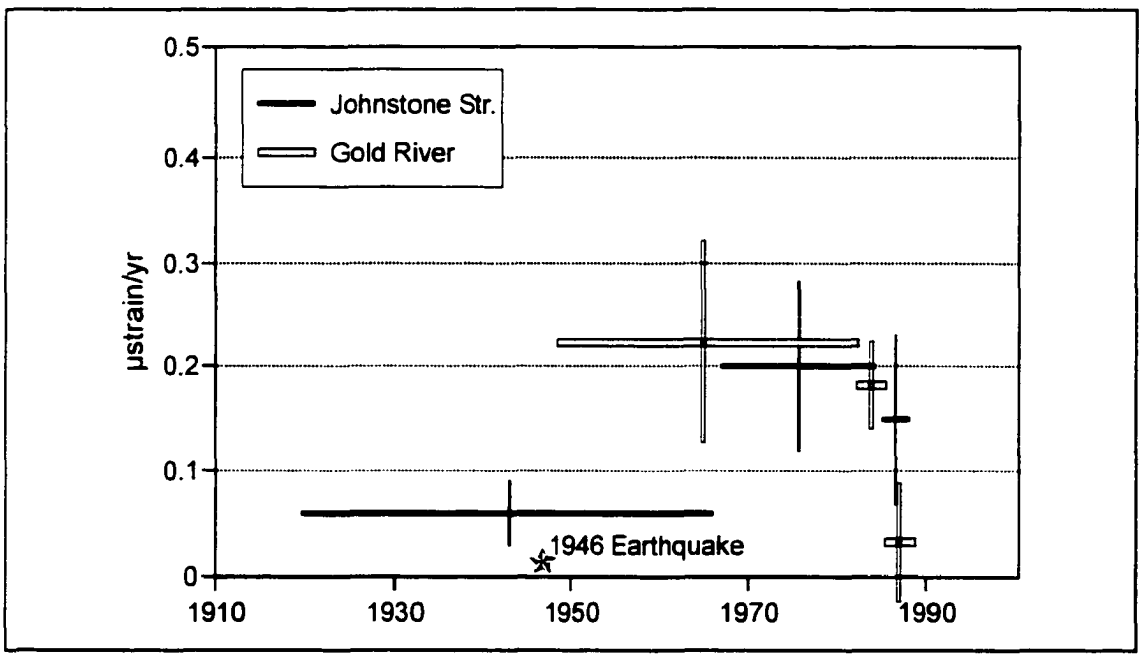

Figure 6.5. Net horizontal shear strain rates determined from horizontal control surveys for the Gold River and Johnstone Strait networks (after *Dragert & Lisowski* [1990]). The vertical bars are 2-sigma error estimates. Horizontal bars mark the interval of the survey. The star marks the time of the 1946 crustal earthquake.

each carried out by the Geodetic Survey of Canada using the same laser ranging trilateration technique [refer to: *Dragert & Lisowski*, 1990], the strain rates calculated for these two intervals are significantly different and distinct at the two-sigma error estimate limits. The strain rate from the interval 1982-1985 is reported as approximately -0.18 μstrain/yr, while the strain rate of approximately -0.04 μstrain/yr determined from the last GOL survey interval (1985-1988) is very similar to the CVI GPS determined result. It seems unlikely, however, that the actual accumulation of strain decreased so dramatically over an approximately three year period without some significant release of seismic moment in the last 15 years. The cause of this difference is uncertain. Given the comparative precision of GPS measurements and their agreement with deformation velocities expected for a subduction zone, the CVI strain rate given above is taken to be more reliable.

CHAPTER 7 - MODEL COMPARISONS

7.1 - Introduction

This chapter consists of two primary components. The first section discusses elastic dislocation modeling, including deformation models for the northern Cascadia Subduction Zone. The second section compares the GPS-determined results to the velocities and strain rates predicted by these models.

7.2 - Basic Theory of Elastic Dislocation Models

The simplest model for the deformation between great subduction earthquakes is the purely elastic dislocation model. Although theoretical problems are recognized in the use of elastic models for defining interseismic locked zones [e.g. *Douglass and Buffett*, 1995, 1996; *Savage*, 1996; *Wang*, 1995], the previous geodetic data from the region landward of the Cascadia Subduction Zone have been in good agreement with the predictions of simple 2-D elastic dislocation models [e.g. *Savage et al.*, 1991; *Dragert et al.*, 1994; *Dragert and Hyndman*, 1995; *Hyndman and Wang*, 1993, 1995].

The first study of elastic dislocation theory applied to seismotectonics and crustal deformation predictions is credited to *Steketee* [1958]. The basic equation of a surface displacement field $u_i(x_1, x_2, x_3)$ resulting from a dislocation $\Delta u_j(\xi_1, \xi_2, \xi_3)$ across a surface Σ in an isotropic elastic half-space is given by:

$$u_i = \frac{1}{F}\iint_{\Sigma} \Delta u_j \left[\lambda \delta_{jk} \frac{\partial u_i^n}{\partial \xi_n} + \mu \left(\frac{\partial u_i^j}{\partial \xi_k} + \frac{\partial u_i^k}{\partial \xi_j} \right) \right] \upsilon_k d\Sigma \qquad (7.1)$$

where u_i^j is the i-th component of displacement at point (x_1, x_2, x_3) due to the j-th direction of point force dislocation of magnitude F at (ξ_1, ξ_2, ξ_3); λ and μ are Lamé constants; δ_{jk} is the Kronecker delta function; and v_k is the direction cosine of the normal vector to the surface element $d\Sigma$ [*Steketee*, 1958]. *Okada* [1985] reviews previous theoretical work and derives a set of analytic equations to calculate the surface deformation displacements, strains, and tilts resulting form both rectangular and point source dislocations for shear faults in an elastic half-space. Okada's point source representative geometry for a fault surface is given in Figure 7.1.

The suite of equations provided by *Okada* [1985] are readily applicable to modelling coseismic deformation resulting from slip across a fault-surface during an earthquake.

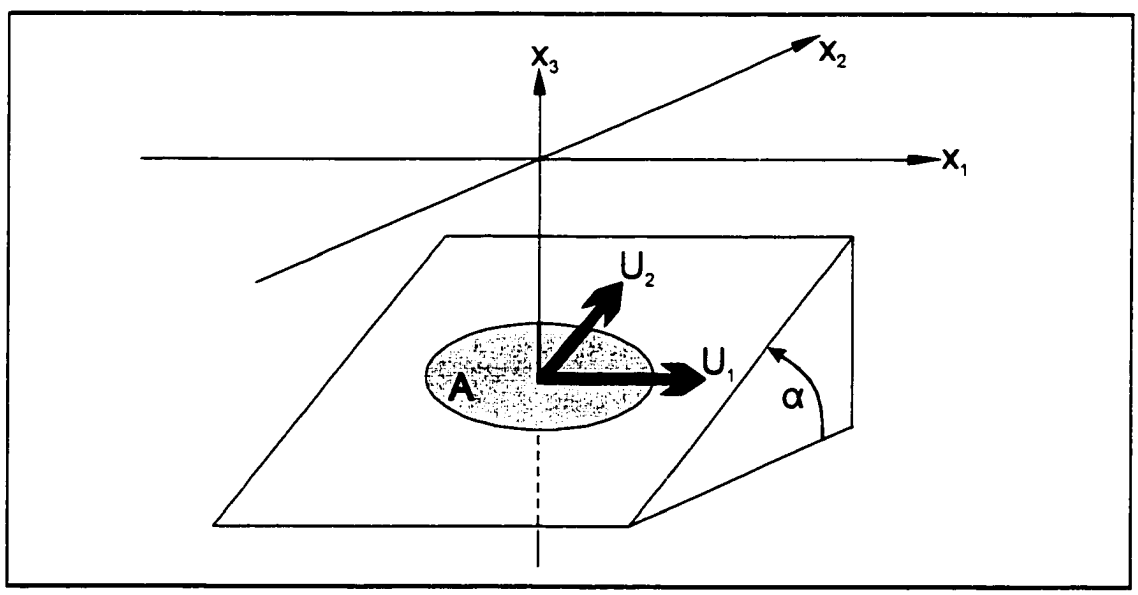

Figure 7.1. Source geometry for the point-source solution (after *Flück* [1996]). A point source with area A lies on a fault plane with dip angle α. U1 and U2 are the components of slip in the strike and dip directions, respectively.

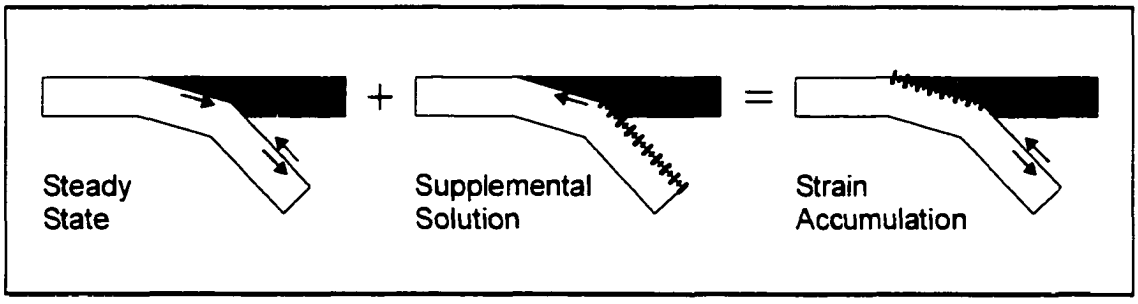

Figure 7.2. Elastic dislocation model of interseismic strain accumulation for a locked subduction zone (after *Savage* [1983]). Arrows give direction of relative plate motion; hachured lines indicate hypothetical locking of the fault surface.

Savage [1983] approached the issue of predicting deformation across a subduction zone during the interseismic period where the plates are locked across some portion of the fault surface. He advanced a model where the accumulation of elastic strain at a subduction zone is modelled as the superposition of a *steady-state* subduction process and a *supplemental solution* as shown in Figure 7.2. The steady state subduction occurs at the rate of relative plate convergence and the supplemental solution parallels normal-faulting slip (or backslip) on the shallow portion of the thrust surface. Kinematically, this approach results in a thrust interface that is locked with no slip over the shallow portion of the subduction zone.

The strategy described above also permits the inclusion of a transition zone where fault slip decreases from zero at its updip boundary (the downdip limit of the locked zone) to the full convergence rate at its downdip limit. The transition zone minimizes the existence of a physically unrealistic point or discontinuity at the downdip limit of the locked zone that would require infinite stresses to maintain. Hence, in dislocation modelling, the interplate surface may be characterized by four regimes (see Figure 7.3). Proceeding landward, or downdip, there is first an undip region of stable sliding, of variable width. For Cascadia this region is narrow, limited to the frontal thrusts. From the deformation front, extending

downdip, the plates remain fully locked between great earthquakes. Then a transition zone from fully locked to stable sliding occurs. Finally stable sliding resumes at greater depths. The model predictions from varying widths of these zones are then compared with surface patterns and rates of crustal motion and strain.

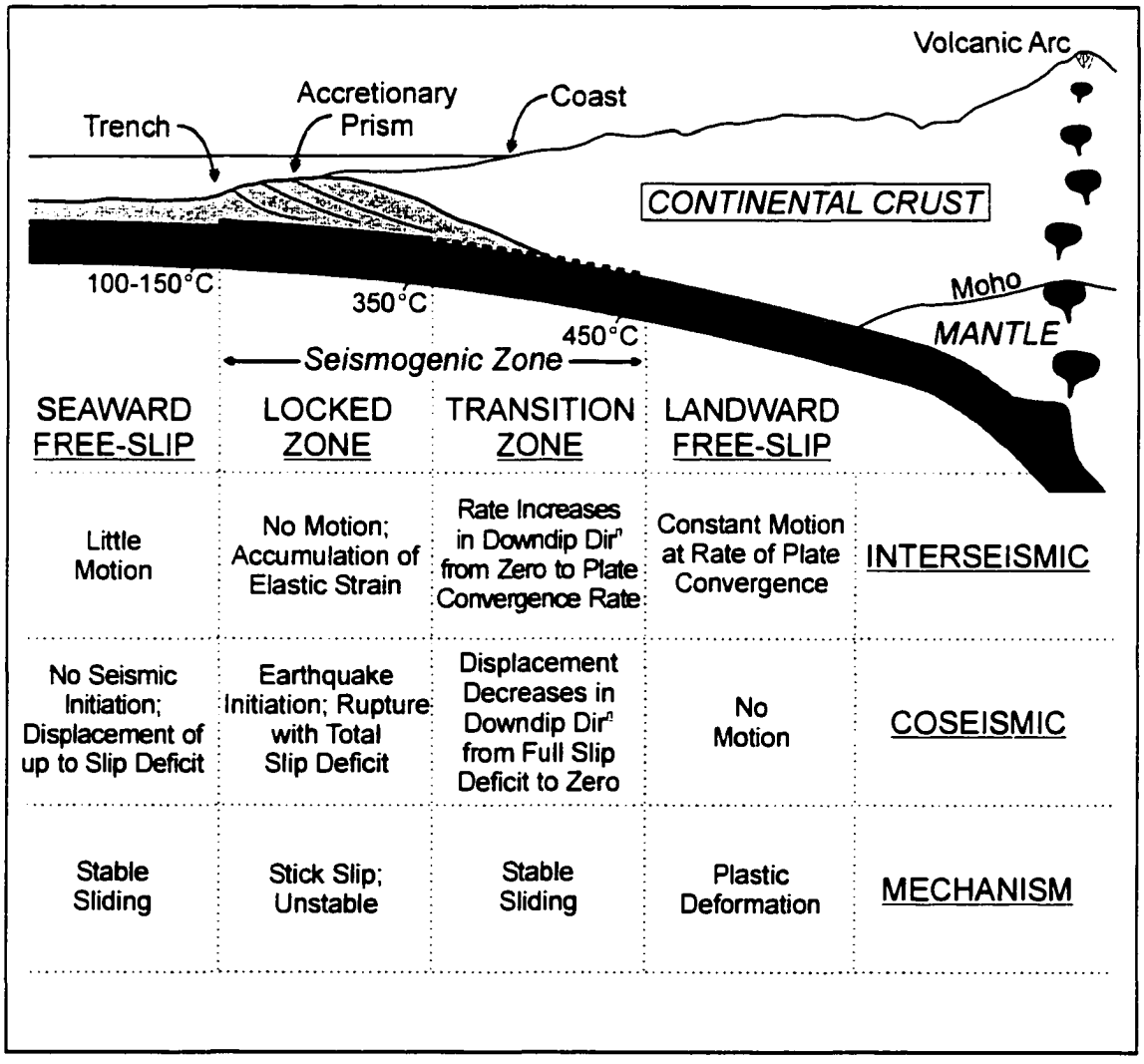

Figure 7.3. Schematic representation of a subduction zone in profile. The characteristics of four zones for coseismic and interseismic periods is summarized in the table (modified from *Flück* [1996]; originally based upon *Hyndman & Wang* [1993]).

7.3 - Flück/Wang 3-D Elastic Dislocation Model of the Cascadia Subduction Zone

Recognizing the geometric limits of previous 2-D models, namely the varied widths and dips of the transition and locked zones along the Cascadia margin, *Flück* [1996] applied the point source solutions of *Okada* [1985] to a 3-D surface made up of triangular elements. This model employs a locked subduction thrust strategy similar to Savage [1983] for investigating crustal deformation during the interseismic period and incorporates a linear transition zone. (The reader is referred to *Flück* [1996] and *Flück et al.* [1997] for a more thorough discussion on the specific characteristics and limits of this 3-D modelling technique).

To produce a smoother fault surface, Kelin Wang (GSC-PGC) has refined the original 3-D elastic dislocation model of *Flück* [1996] to approximate the shallow (seismogenic), cross-strike portion of the thrust surface with circular arcs that more accurately fit the geometry of the down-dip profiles specified by the user. The refined model was published in *Flück et al.* [1997]. Figure 7.4 illustrates the Cascadia subduction-thrust locked and transition zones as: (a) a three-dimensional view of fault-model elements from the southeast, (b) a sample cross-section of the subduction slab, and (c) a half-space geometric approximation, as required by the dislocation model, that corrects for surface topography. The depth contour geometry of the megathrust fault surface was determined from a suite of data including offshore multichannel seismic reflection surveys, seismic refraction studies, Benioff-Wadati seismicity, seismic tomography, and teleseismic receiver waveform analyses [*Flück*, 1996].

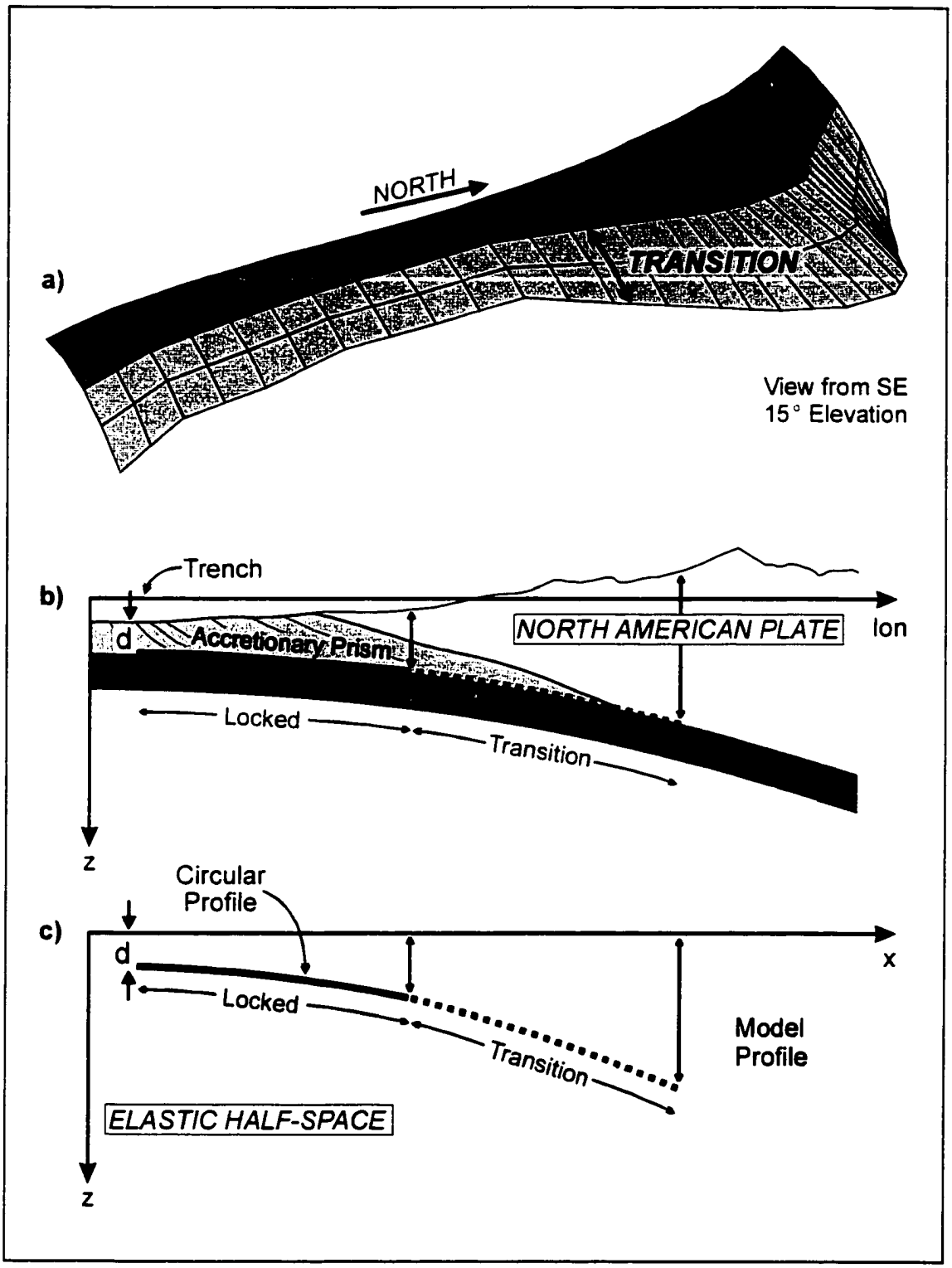

Figure 7.4. Schematic illustrations of the 3-D elastic dislocation model (after *Flück et al.* [1997]). Figure panels are: (a) a three-dimensional view of fault-model elements from the southeast; (b) a sample cross-section reflecting realistic geometry for the subducting slab; and (c) a half-space geometric approximation (*i.e.* a regional Lambert conformal conic projection) that corrects for surface topography.

This Cascadia model locked and transition zone limits (Figure 7.5) are based upon all previous horizontal and vertical geodetic as well as thermal data. The inferred potential rupture zone off southern Vancouver Island is comprised of a roughly 60 km wide locked zone extending landward from the trench plus a 60 km transition zone extending to near the coast. The downdip extent of the locked/transition zone widens to about 100 plus 100km off northern Washington and then narrows again to approximately 40 plus 40 km off Oregon and northern California. These extents are in good agreement with those predicted from thermal limits of 350°C for the locked and 450°C for the transition zone to free slip [e.g. *Hyndman and Wang*, 1993, 1995; *Hyndman et al.*, 1997; *Oleskevich*, 1996; *Oleskevich et al.*, 1999].

In previous dislocation modelling, *Flück* [1996] and *Flück et al.*, [1997] adopted a Juan de Fuca/North America convergence rate of 42mm/yr at an azimuth of N69°E from plate motion studies by *DeMets et al.* [1990]. This vector was also held constant along the full length of the convergent margin. However, this study found that observed crustal motions for southern and central Vancouver Island are more consistent with a convergence direction of N62°E being applied in the dislocation model. This more northerly direction is in agreement with the convergence proposed by *Riddihough* [1984] pole for northern Juan de Fuca averaged over the last 1 Ma.

The resulting horizontal velocity vectors (mm/yr) predicted by the (revised direction) three-dimensional Cascadia subduction-thrust dislocation model are shown in Figure 7.6. The arrow lengths are proportional to the rates at their origin point. Deformation velocities show the expected pattern with the highest velocities near the coast (and hence nearer the modelled underlying fault surface) and decreasing landward. The vectors near the coast

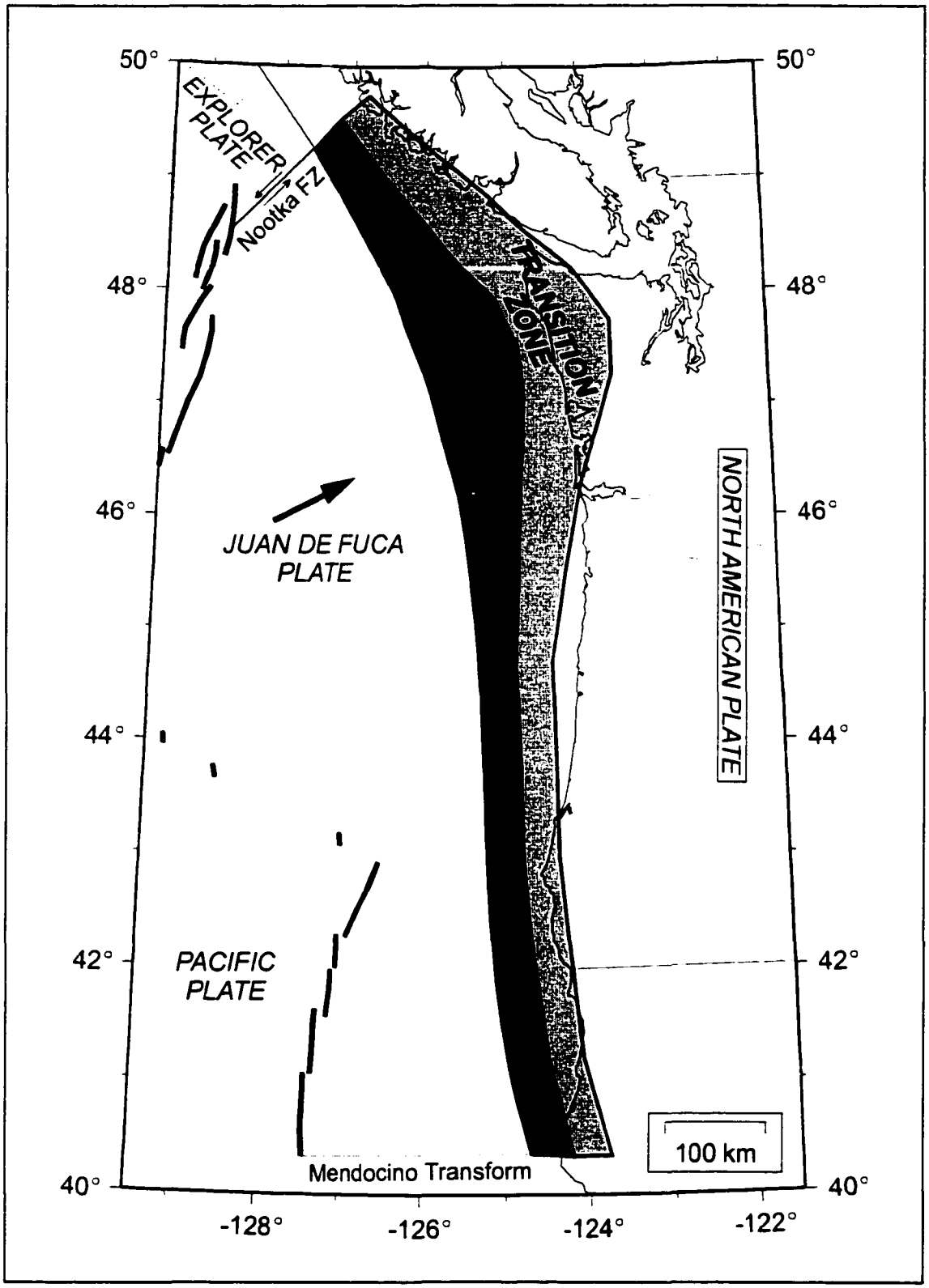

Figure 7.5. Map of locked and transition zones used in modeling the seismogenic portion of the Cascadia subduction thrust surface.

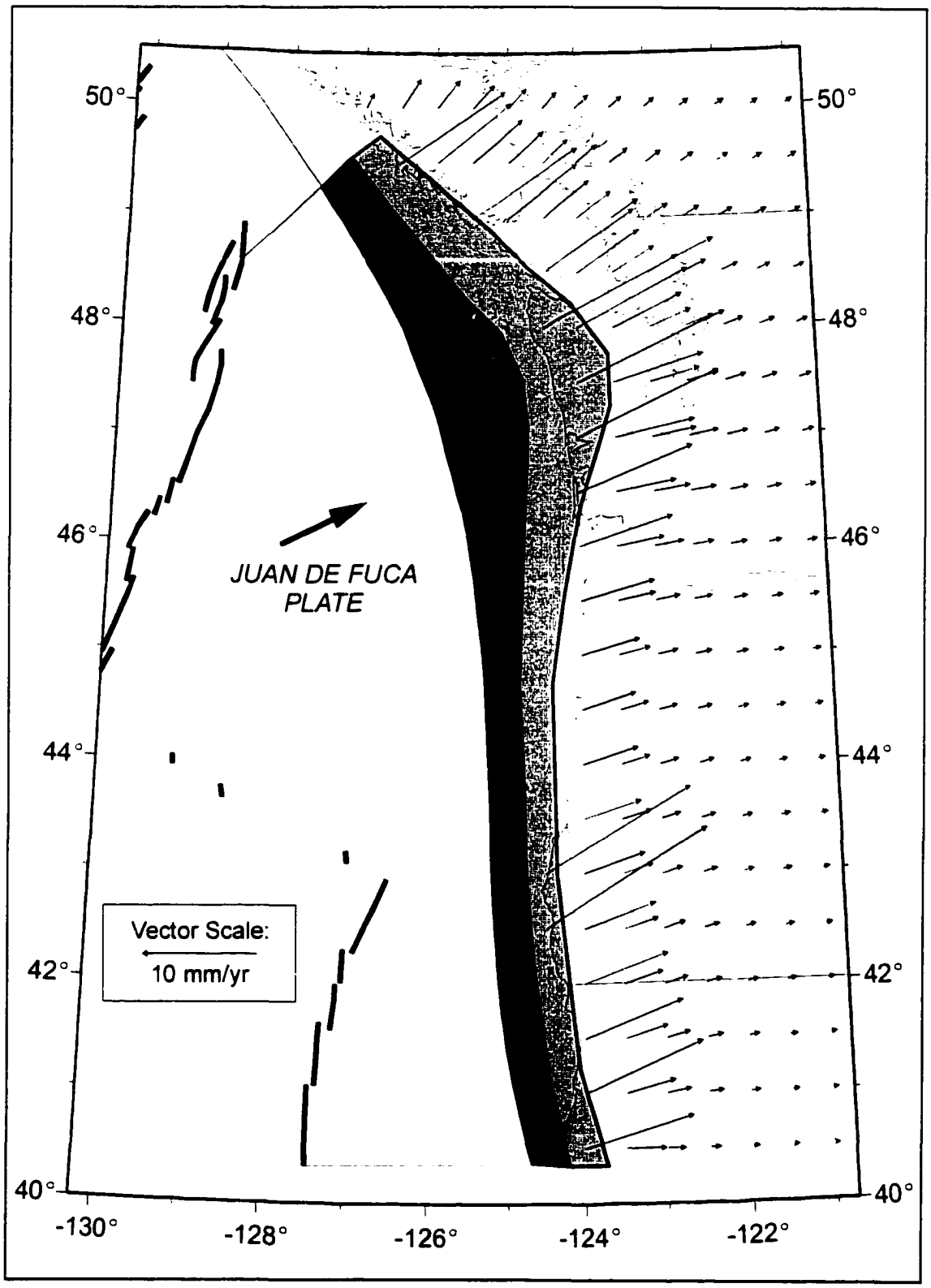

Figure 7.6. Horizontal velocity field predicted by the 3-D elastic model.

more closely reflect the convergence direction, with the deformation velocity direction rotating to more (with respect to the fault) strike-perpendicular going inland.

It should be noted that because of the close proximity of the pole of rotation for the relative motion between the Juan de Fuca and North American plate, convergence directions become significantly more northerly for the southern Oregon /northern California portion of the Cascadia margin. In this study no attempt was made to optimize the model parameters for this southern region and caution must be exercised in using the presented model for interpreting crustal motions observed within the southern region of Cascadia.

The horizontal velocities predicted by the three-dimensional Cascadia model (grey arrows) are shown in Figure 7.7 compared with the velocities determined from the continuous GPS sites of the WCDA (black arrows with 95% uncertainty ellipses). There is general agreement in the magnitude and direction of the observed versus predicted velocities for the southern Vancouver Island region and southwestern British Columbia. The margin-parallel motion at HOLB and the velocity at WILL are not predicted by the model since these sites lie beyond the northern boundary of the Juan de Fuca Plate in different tectonic regimes. The following sections focus on the comparison of the 3-D model with observations in coastal southwestern British Columbia, and refinements to the simple model.

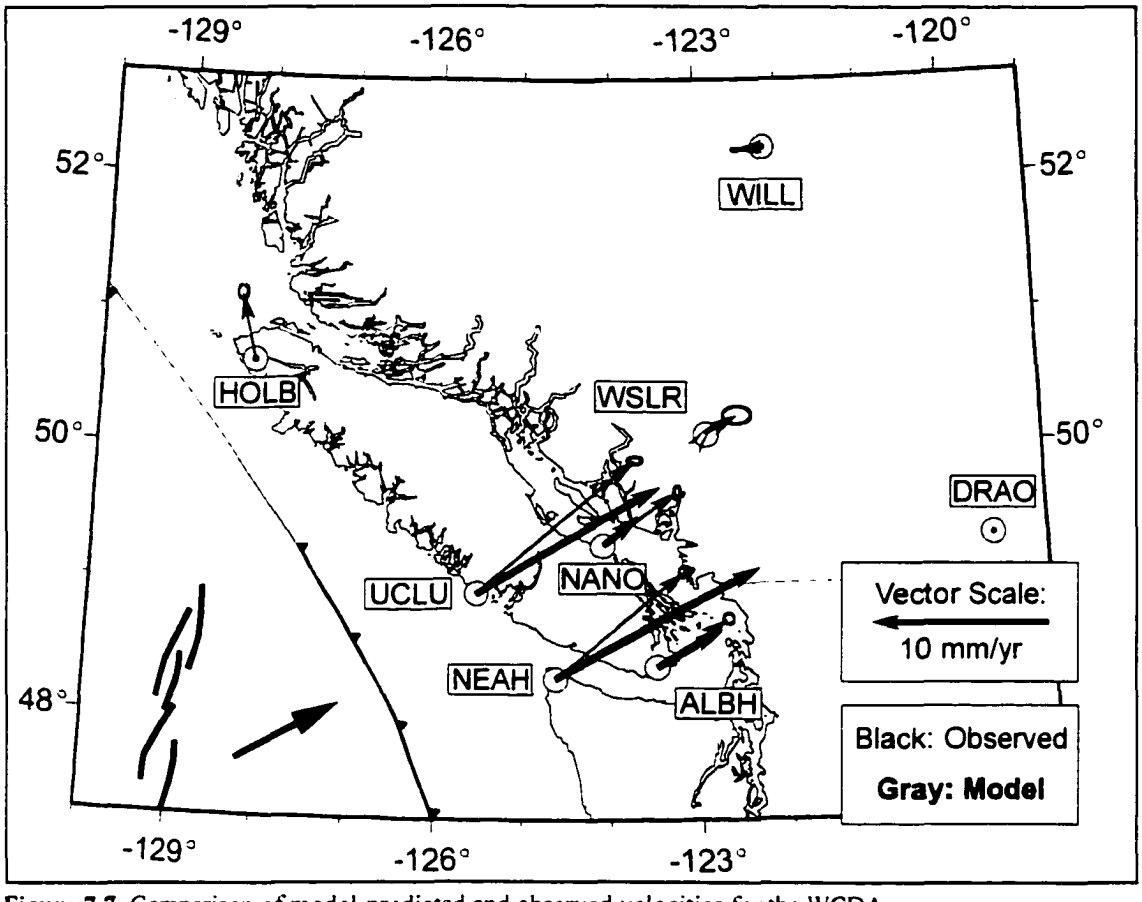

Figure 7.7. Comparison of model-predicted and observed velocities for the WCDA.

7.4 - Velocity Comparisons to the Cascadia Model

For southern Vancouver Island, the dislocation model predicts motions with uniaxial shortening in the direction of plate convergence. This agrees well with the observed velocity field for SVI (see Figure 7.8). Although the magnitude of the velocity vectors from the model were comparable to the measurements near the seaward coast of Vancouver Island, the rates of the more landward model-predicted vectors are significantly smaller than the observed rates. As a result, the model predicts slightly more shortening should be accommodated across the island than recorded by the observations. However, overall the

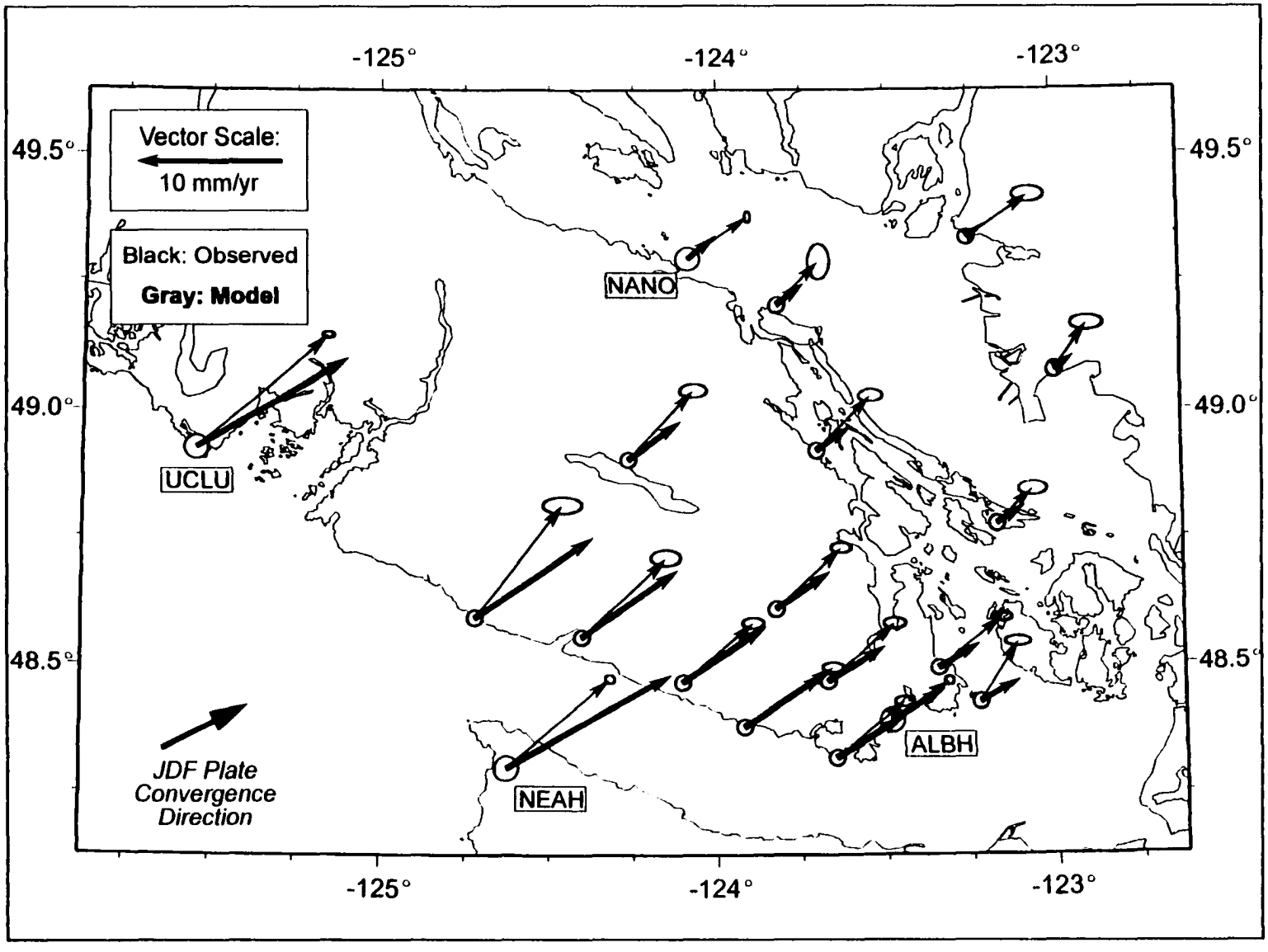

Figure 7.8. Comparison of model-predicted and observed velocities for southern Vancouver Island.

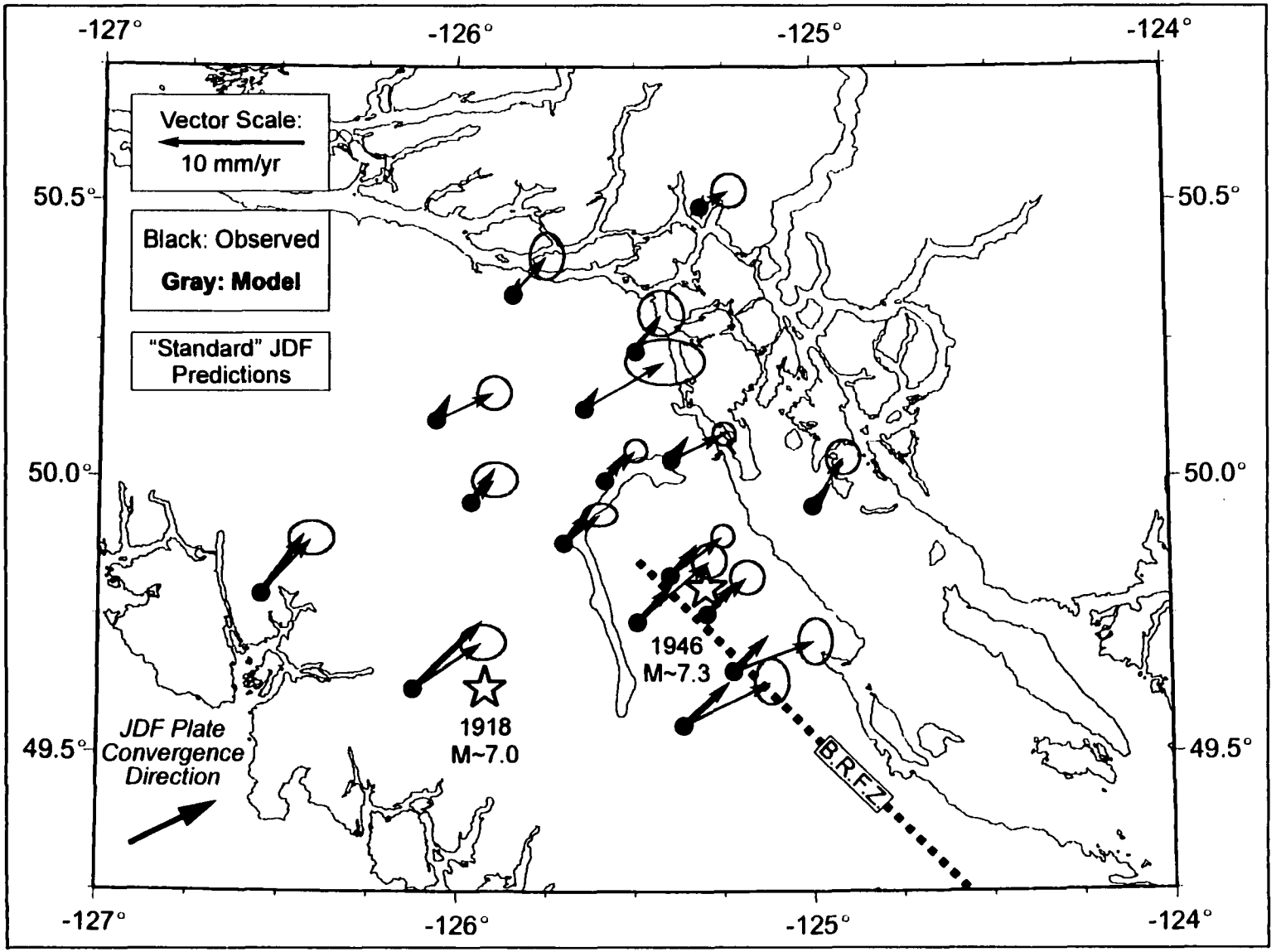

Figure 7.9. Comparison of model-predicted and observed velocities for central Vancouver Island.

three-dimensional elastic dislocation model for a fully locked subduction thrust fits the observations well to first-order.

The model predictions for central Vancouver Island also match the CVI GPS-determined velocity field rather well (Figure 7.9), although the GPS data for this region are quite noisy. The dominant signal observed appears to match the velocity field predicted at the northern terminus of the subducting Juan de Fuca plate. The effect of deformation associated with the crustal earthquakes is not evident in the data. (However, if the direction of this second-order deformation occurs roughly parallel to the NA-JDF plate convergence direction, its signal could be hidden within the deformation signal interpreted for the CSZ). Refinements and additions to the model predictions are possible for this region through modeling the possible effects of the Nootka Fault Zone and subduction of the Explorer slab adjacent to the northern terminus of the Juan de Fuca plate.

7.5 - Refinements to the Modeling

7.5.1 - Nootka Fault Zone Model

Because the previous dislocation models of the Juan de Fuca plate simply terminate the subduction thrust with a free-slip boundary at the northern end, modeling of this boundary was attempted. The Nootka Fault Zone (NFZ) marks the boundary between the Juan de Fuca Plate to the south and the Explorer sub-Plate to the north [*Hyndman et al.*, 1979]. The NFZ is a broad shear zone that runs from coastal Nootka Island seaward and southeasterly to near the northern end of the Juan de Fuca Ridge (see Figure 2.1) [*Hyndman et al.*, 1993]. The geometry of the model fault surface is shown in Figure 7.10. The NFZ

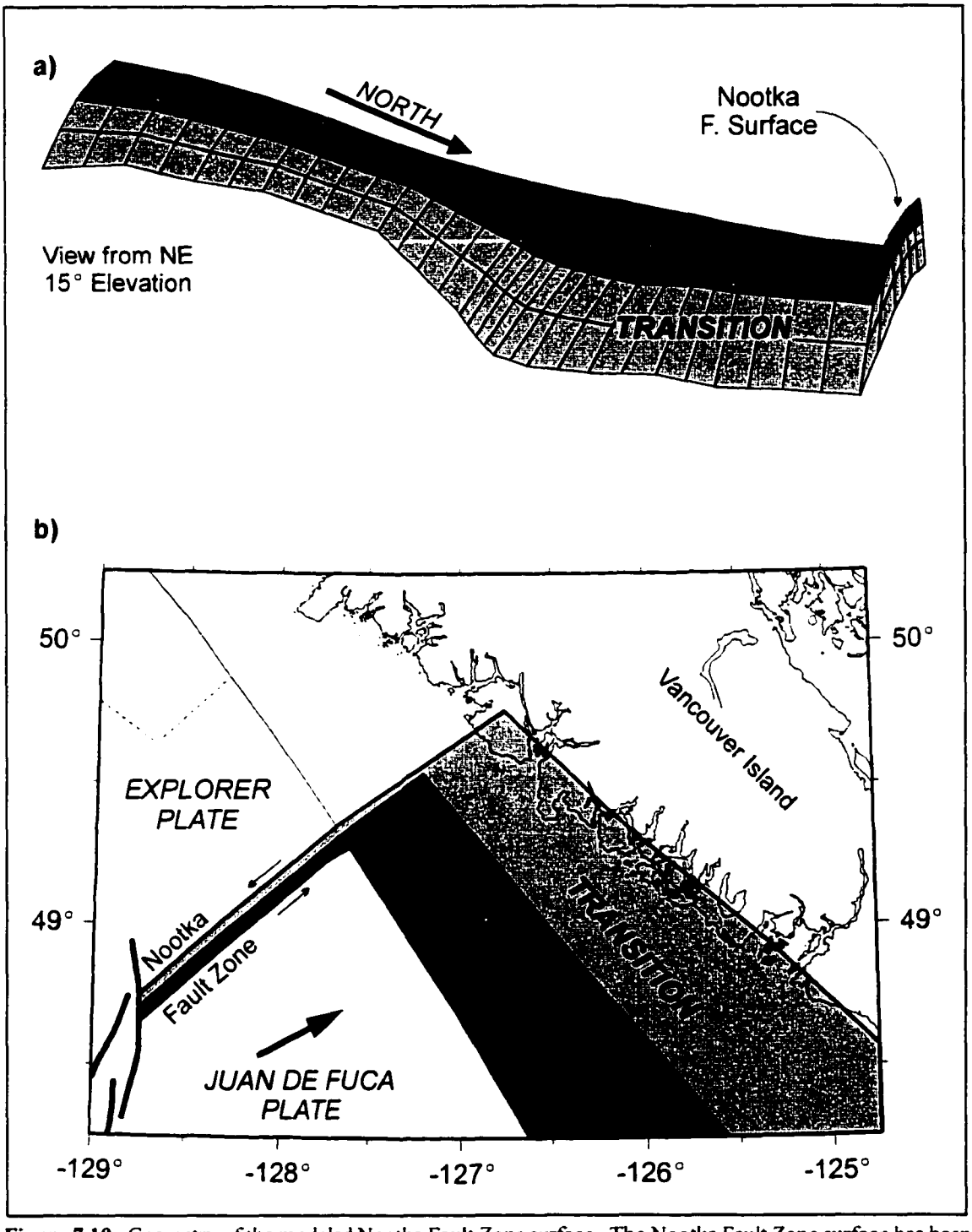

Figure 7.10. Geometry of the modeled Nootka Fault Zone surface. The Nootka Fault Zone surface has been added to the northern terminus of the "standard" Juan de Fuca plate model and is shown: a) obliquely from the NE, and b) in map view.

is modelled by a single near-vertical fault surface extending (~15 km deep) from the northern end of the 3-D Cascadia model. The Explorer Plate is assumed fixed with respect to North America in this test, resulting in the highest possible slip-deficit across the NFZ. The effect of including a locked surface for the Nootka Fault in the model is negligible, resulting in a very small counterclockwise rotation of the predicted deformation vectors. This is expected

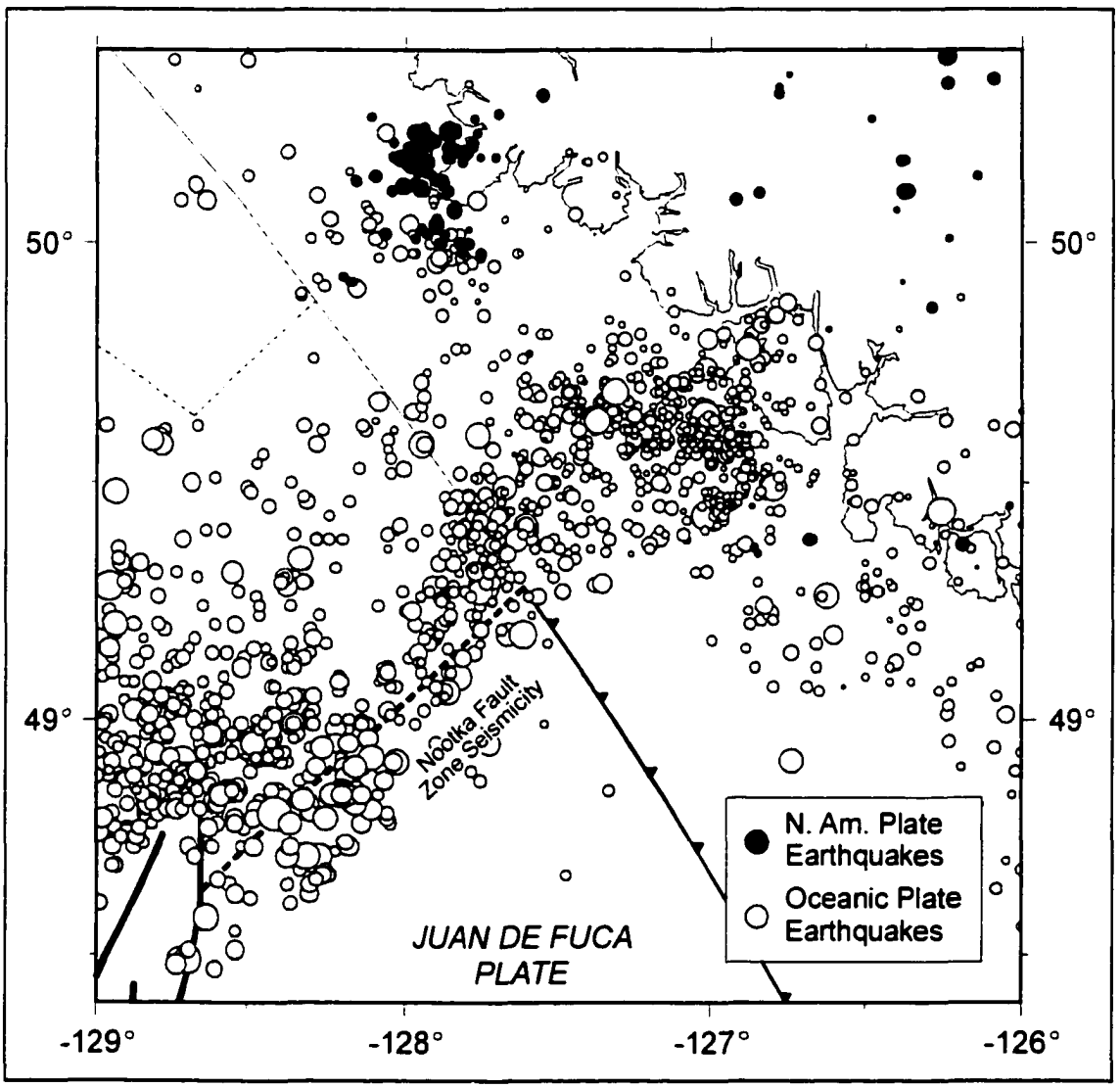

Figure 7.11. Earthquake pattern in the region of the Nootka Fault Zone. Circles represent instrumentally recorded seismicity for the period 1980-1996 (*data from* PGC Seismology Group) and are scaled by magnitude.

since the Nootka fault possesses little areal extent and because it is deeper and further offshore than the subduction thrust. Finally, the differential JDF/EXP slip as defined by seismicity takes place in a broad zone rather than along one fault [*Hyndman et al.*, 1993] (see Figure 7.11), implying this net slip occurs over many smaller structures.

7.5.2 - Explorer Plate Model

To determine the surface crustal-deformation velocities that would be generated by a separate locked Explorer/North America interface, a separate slip dislocation model was developed for coastal northern Vancouver Island. The location of the model is shown in

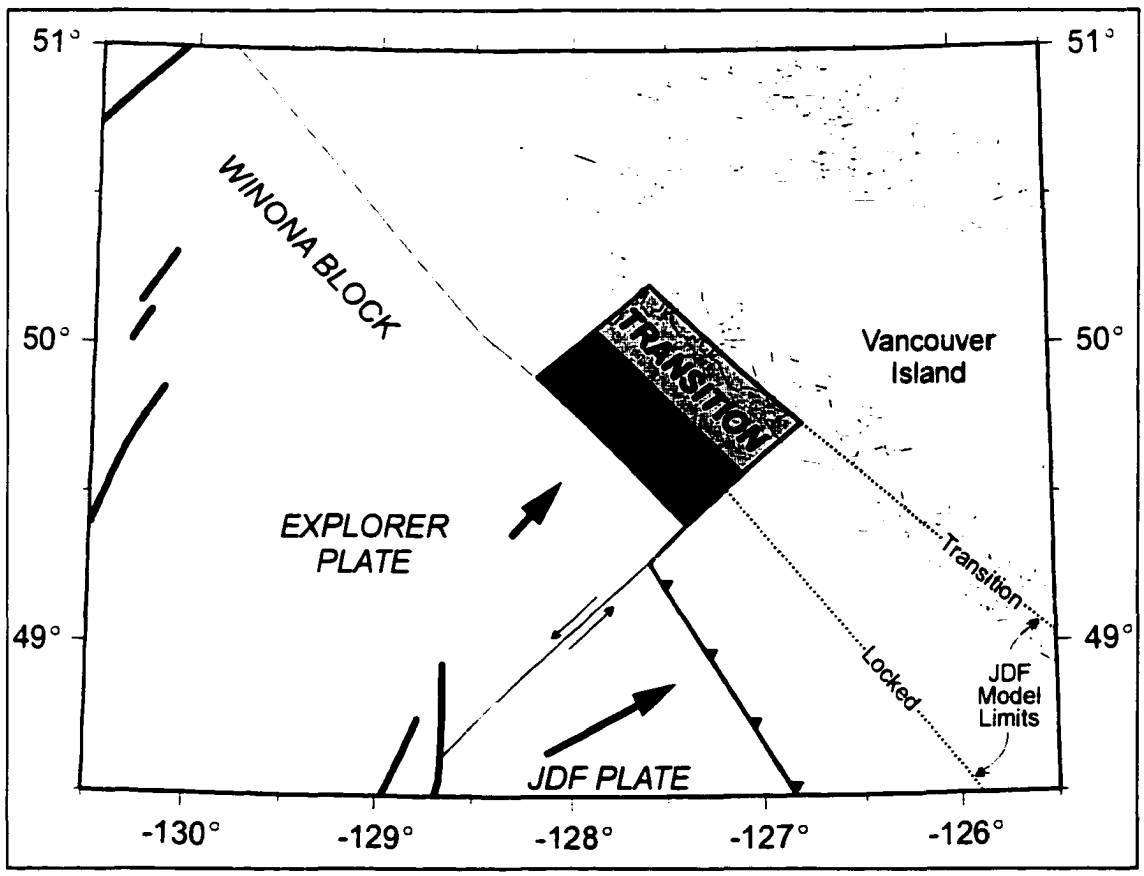

Figure 7.12. Map of locked and transition zones used in modeling a Explorer plate thrust surface.

Figure 7.12. The model runs along the strike of the trench from the Nootka Fault Zone north to the Brooks Peninsula (*i.e.* to the Winona Block) [*Carbotte et al.*, 1989]. South of the Nootka Fault Zone, the model limits of the locked and transition zones for northernmost Juan de Fuca are shown for comparison. Although the limits for Explorer plate have not been determined in a rigorous manner, thermal arguments suggest that the locked and transition zone widths are narrower than those for the Juan de Fuca plate because the Explorer Plate at the trench is especially young, slowly underthrusting, and therefore hot. The Explorer deformation front is also closer to the coast. The extent of Nootka Fault Zone seismicity (*refer to* Figure 7.11) to mid-Nootka Island, a proxy for brittle rock rheology, is used as the landward downdip limit of the model transition zone. The approximate depths to the top of the thrust surface were determined from a suite of data including offshore and onshore seismic surveys [*Clowes et al.*, 1997; *Dehler and Clowes*, 1992; *Davis and Currie*, 1993; *Davis and Hyndman*, 1989] and teleseismic receiver function analyses on northern Vancouver Island [*Cassidy et al.*, 1998].

Although not well-constrained, *Riddihough's* [1984] Explorer-North America Euler pole lies on the Olympic Pennisula (Figure 7.13). As the rotation pole is quite close, the relative convergence directions and magnitudes vary considerably across the microplate. An Explorer-North America plate convergence rate of 21 mm/yr with a direction of N42°E from *Riddihough* [1984] was used to represent the average velocity near the center of the model seismogenic thrust surface. However, *Rohr and Furlong* [1995] (and subsequently *Kreemer et al.* [1998]) conclude that the Explorer Plate is being broken by a margin-parallel shear zone rather than converging towards Vancouver Island. Thus, the model presented here is

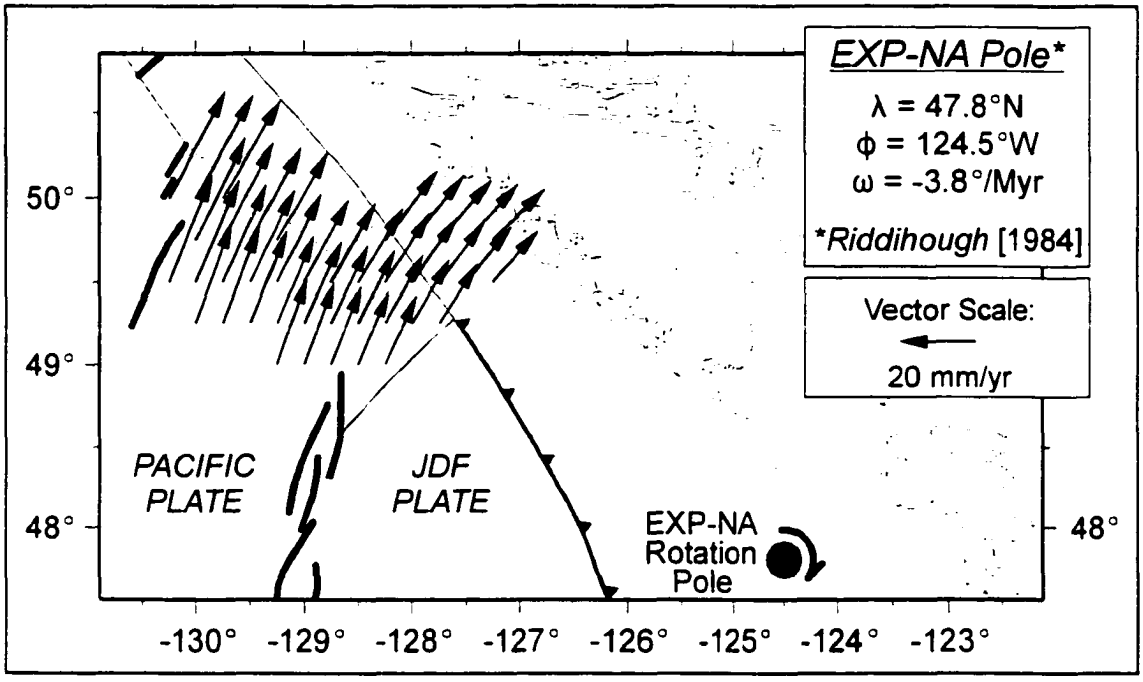

Figure 7.13. Explorer-North America rotation pole. Rotation pole is from *Riddihough* [1984].

to be regarded as an end-member using a simple geometry with the highest published convergence rate.

The deformation velocities predicted by the Explorer Plate Model are shown in Figure 7.14. The horizontal velocities (mm/yr) predicted by the three-dimensional Explorer subduction thrust dislocation model are shown by the arrows whose lengths are proportional to the motion at their origin point. The maximum rates predicted by the model, located on the outer coast, are small (about 5 mm/yr) and decrease rapidly landward. The predicted seafloor subsidence rate is up to ~10 mm/yr for this model. If accumulated over several hundred years, this rate implies possible coseismic uplift of several metres which has potential for large tsunamis.

To a first order, the small locked Explorer subduction zone is predicted to contribute very little to the surface strain rate at the present Central Vancouver Island sites. Because

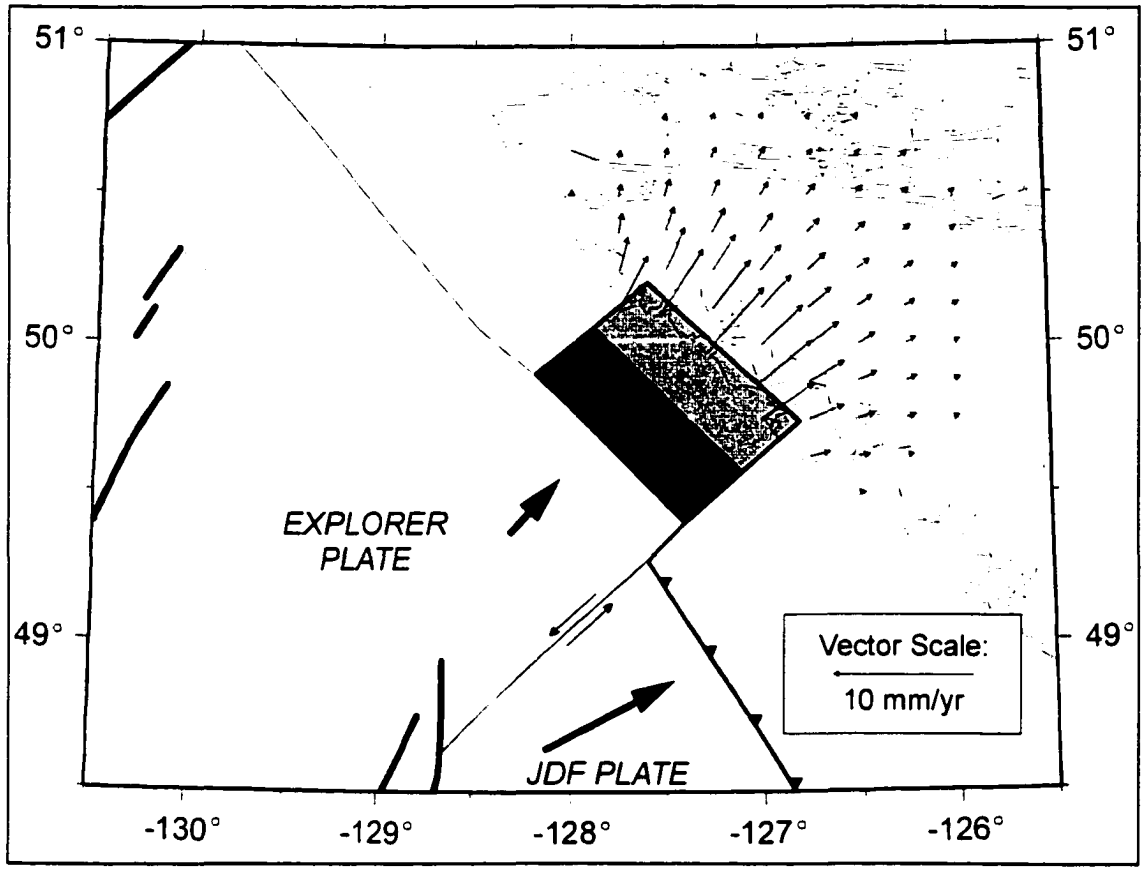

Figure 7.14. Velocity field predicted by the Explorer plate model.

the dislocation model is elastic, the predictions from the Cascadia model and the Explorer Plate model can be summed. The results are shown in Figure 7.15. There appears to be a very modest improvement in the model fit to the observation from the Central Vancouver Island GPS network results. The hypothesis of a locked Explorer sub-plate is ultimately testable by one or two new sites along the coast of northern Vancouver Island. Two GPS stations are currently planned to be installed during the summer of 2000 and their data will provide valuable constraints for resolving the kinematics of the Explorer Plate.

It is noted that this model does not address the transition between the margin-perpendicular Cascadia signal and the margin-parallel result at the south end of the Queen Charlotte transform fault system.

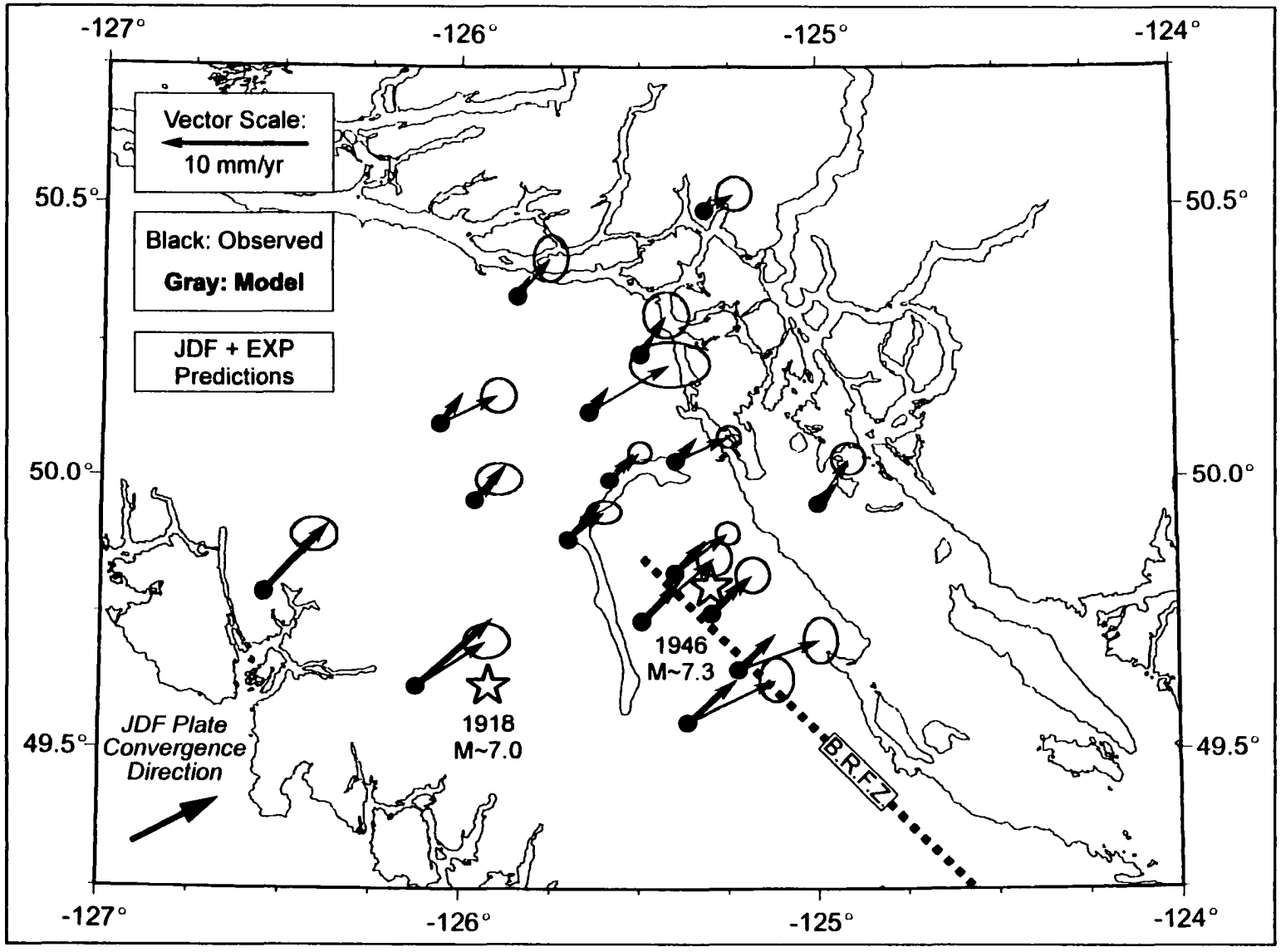

Figure 7.15. Comparison of JDF+EXP model-predicted and observed velocities for central Vancouver Island.

7.5.3 - Extended Juan de Fuca Plate Model

The elastic model may produce corner effects near the edges of the dislocation surface. Note that at the north end of the Cascadia model (*refer to* Figure 7.6) the vectors rapidly rotate counterclockwise away from the convergence direction as if they were flowing around a corner. To try and address this possible phenomenon, the Cascadia model was extended to the northwest such that the northern end of the model was well away from the Central Vancouver Island network stations. While this is not tectonically realistic, it is presented as an attempt to model these sites with a 2½-D approximation. The depths and

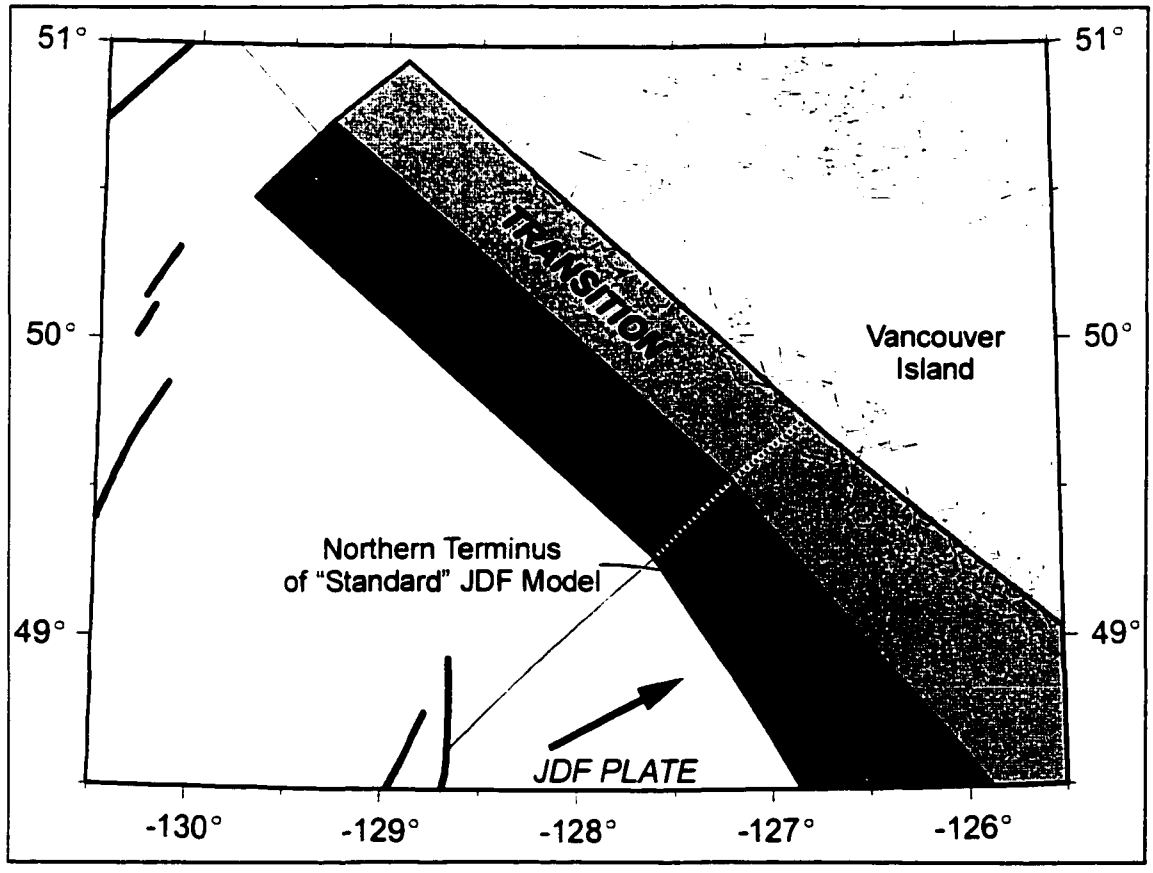

Figure 7.16. Geometry of the locked and transition zones for the northward "extension" of the JDF plate. This model is a 2½-D approximation for the northern terminus of the JDF model.

geometry of the northern terminus of the Cascadia model are preserved and extended along strike to offshore of northern Vancouver Island (Figure 7.16). The results of this model are shown in comparison to the observations for CVI in Figure 7.17. The directions of the model vectors appear to agree better with the observations while the fit of the magnitudes appears comparable.

7.6 - Addenda to Modelling the GPS Velocities on Vancouver Island

The model-predicted horizontal velocity vectors are plotted relative to DRAO. The components of dislocation model-predicted motion (typically $\leq$ ½ mm/yr) at DRAO are subtracted from the site model motions for comparisons with the data motions shown in this dissertation.

One significant question not yet addressed is why the model-predicted velocity vectors decrease more rapidly inland compared to the data. There are several possible explanations including: ① different elastic model parameters, ② limitations to the elastic dislocation model, ③ forearc deformation (*e.g.* 1946 & 1918 earthquakes), and ④ forearc block motions. As discussed below, it proved difficult to find elastic model parameters (locked and transition zone widths, etc.) that reproduce the observations (*i.e.* point ①). *Mazzotti et al.* [1999] and *Le Pichon et al.* [1998] found a similar discrepancy for SW Japan. They interpreted the discrepancy to forearc crustal deformation, but it may be that this disparity is a general feature of subduction zone deformation.

Attempts to replicate the observed crustal motions by varying the widths of the locked and transition zones of the elastic dislocation model over a wide range were not

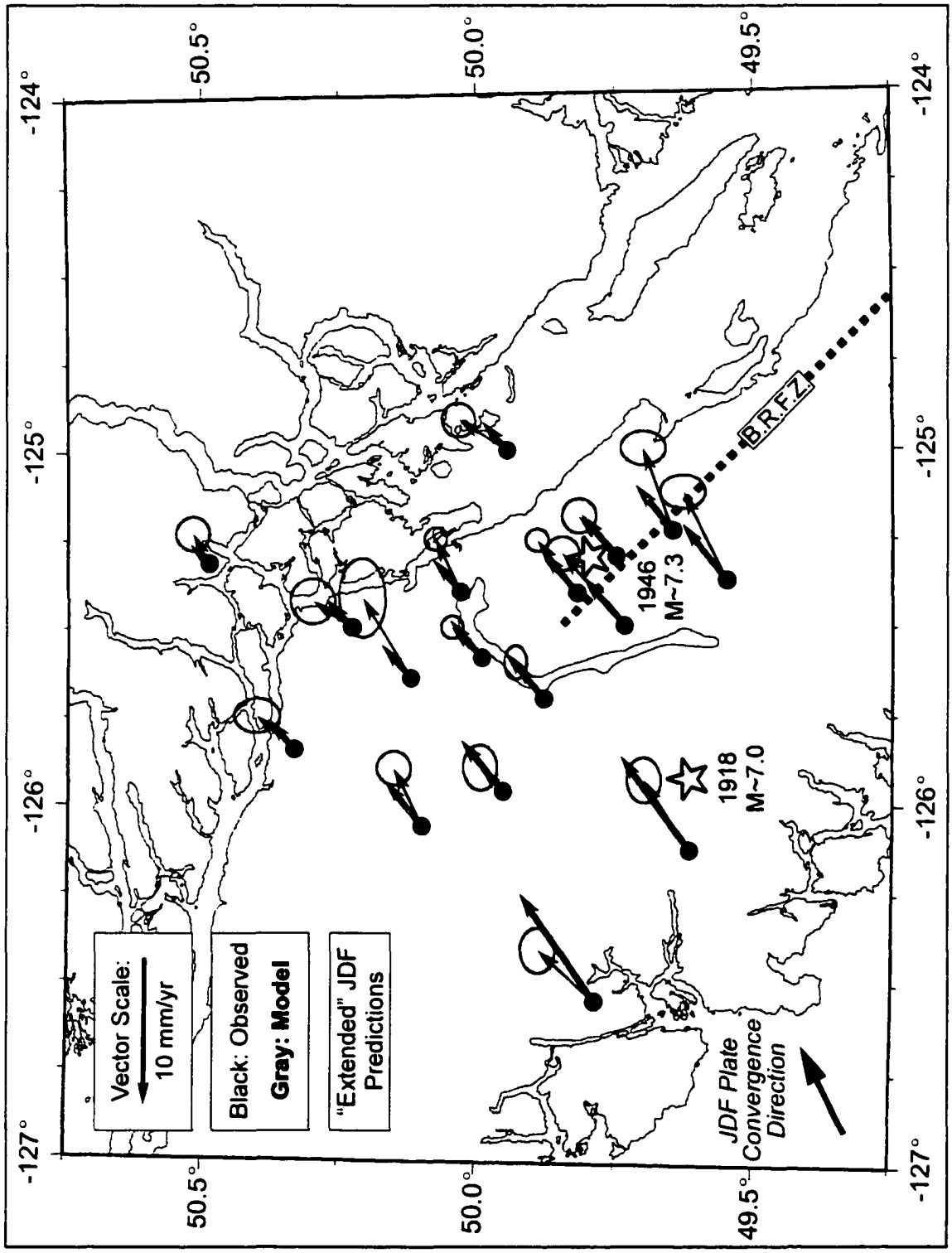

Figure 7.17. Comparison of the "extended" JDF model-predicted and observed horizontal velocities. Error ellipses give 95% confidence values.

successful. For example, doubling the width of the transition zone produces model-predicted velocity vectors that fit well the observations for sites on the inner (eastern) coast, but at the expense of greatly overestimating the predicted velocities for sites on the outer (western) coast.

Widening the transition zone while simultaneously narrowing the locked zone will again allow fitting the horizontal velocities on the outer coast, but the predicted velocities still underestimate the observations at the inner coastal sites. Consider the deformation

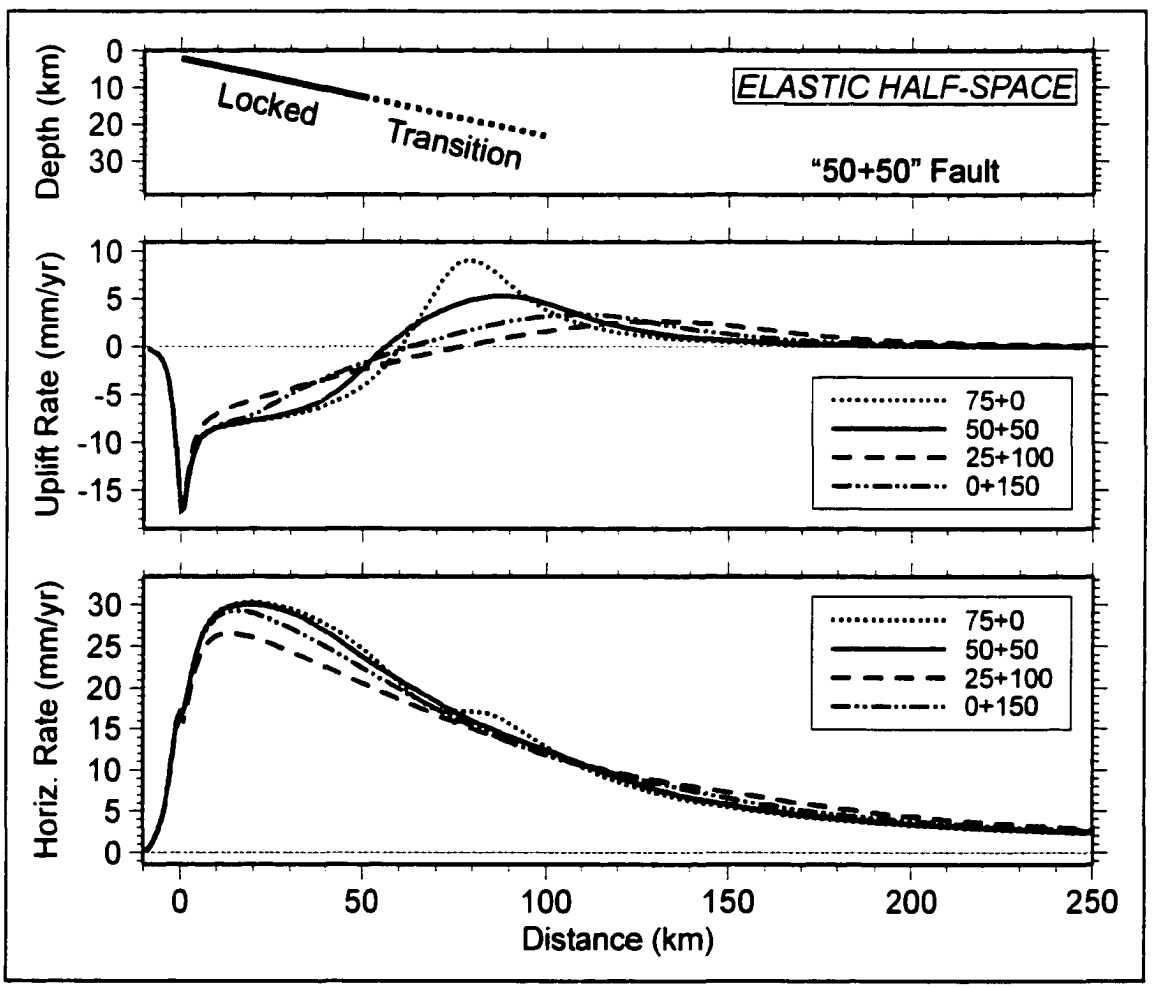

Figure 7.18. Influence of downdip transition zone widths. The curves represent interseismic deformation rates and are discussed in the text. The fault dips at 12° and is 1000 km long. The convergence rate is 42 mm/yr.

curves plotted in Figure 7.18 for a 2½-dimensional model. The 75+0, 50+50, 25+100, and 0+150 (locked zone width *plus* transition zone width) curves are remarkably similar, particularly on their landward tails. Because a linear decrease in slip-deficit is used to represent the transition zone, the addition of a 50 km transition zone acts much the same as adding a 25 km *net* fully locked zone for the horizontal velocity predictions. Likewise, 100 km and 150 km transition zones act similar to the additions of 50 km and 75 km *net* fully locked zones, respectively. Hence, the horizontal velocity predictions in Figure 7.18 exhibit the effect of a 75 km zone at the full slip-deficit rate.

Changing the geometry of the modeled fault surface could give a better fit of the predicted horizontal velocity vectors to the observations. The location and geometry of plate interface surface, however, cannot undergo significant changes and remain true to the relatively large volume of local studies mapping the position of the subducted Juan de Fuca plate. Additionally, predicted velocities for landward, onshore regions are not highly sensitive to either changes in interface dip angle (at the level of ±5°) or variations in depth. *Flück* [1996] provides comprehensive sensitivity tests of this type for the elastic dislocation model.

It is felt that the Flück/Wang model fits the observed horizontal data quite well to first order. Vertical uplift curves are more sensitive (than horizontal predictions) to the positions of the locked and transition zones. Repeated leveling data on southern Vancouver Island are consistent with the 3-D Flück/Wang elastic dislocation model for Cascadia [*Flück*, 1996, *Flück et al*, 1997]. Additionally, this model is in agreement with the positions of the locked and transition zones determined by thermal modeling work of *Hyndman and Wang*

[1993, 1995] and *Oleskevich et al.* [1999]. A more complex rheology model (*e.g.* viscoelastic) may be necessary for a more accurate representation of the observed horizontal velocities (*i.e.* point ②). However, such models are beyond the scope of this dissertation.

Forearc deformation (*i.e.* point ③) on central Vancouver Island is indicated by the M~7.3, 1946 and M~7, 1918 earthquakes. The location of the Beaufort Fault Zone on which the 1946 earthquake may have occurred is shown in Figures 7.9, 7.15, & 7.17. This fault has not been modelled, but no evidence of strain buildup on this fault is apparent in the data, nor of regional deformation associated with the 1918 event.

Regarding possible coastal crustal block motion (*i.e.* point ④), *Wells et al.* [1998] propose that the Oregon block extends approximately to the Columbia River. Additionally, there is no margin-parallel shortening determined by the strain calculations for SVI, and thus there does not appear to be significant along-coast "squeezing" from regions to the immediate or near south. The axis of principal shortening rate occurs in the direction of plate convergence. The network strain calculation for SVI observations gives an average network translation rate of about 6 mm/yr at ~N48°E ± 1° degrees (1σ), and the translation rate of the strain network centre for CVI occurs at ~N55°E ± 3° degrees (1σ). This suggests motion that is predominately margin-perpendicular and approximately in the direction of plate convergence.

A recent investigation of Juan de Fuca plate motion has been undertaken by the using underwater acoustic transponders on the sea-floor off the coast of southern Vancouver Island [*Spiess et al.*, 1998]. Preliminary results from *Chadwell et al.* [2000] indicate a convergence rate of 27 mm/yr in a direction of roughly N18°E. This rate is approximately two-thirds that

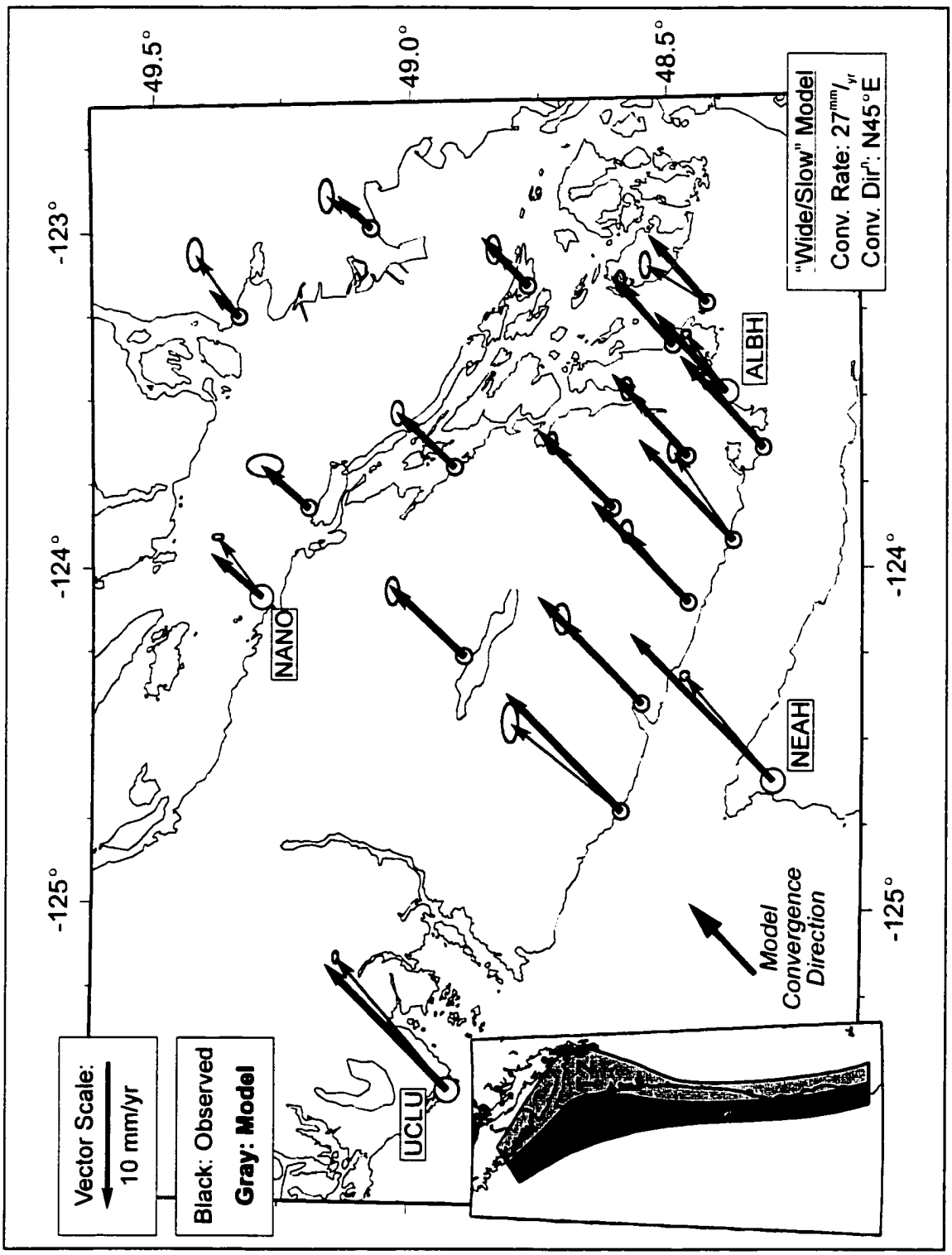

Figure 7.19. Comparison of "Wide/Slow" JDF model-predicted and observed velocities for southern Vancouver Island. Elastic dislocation modeling with a slower convergence rate in addition to wider locked and transition zones (L.Z. & T.Z., respectively, in the inset map) was attempted in order to fit the observed horizontal velocity vectors. Model is discussed in the text.

of *Riddihough* [1984] with a direction that is considerably more northward. Elastic dislocation modeling using the rate of 27 mm/yr and a convergence direction of N45°E was attempted in order to fit the observed horizontal velocity vectors. This lower convergence rate requires substantially (by a factor of ~1.5) wider locked and transition zones to match the observations. The horizontal velocity vectors predicted by this model fit the observations quite well (*refer to* Figure 7.19). However, this "end-member" model is inconsistent with thermal arguments. The slower convergence rate would lead to a marginally narrower seismogenic zone rather than the wider model limits that are needed to fit the observations. Again, a viscoelastic model is likely required to more accurately replicate the observed horizontal velocities.

7.7 - Model Strain Rate Predictions

The predicted strain rates may be calculated from the velocity field produced by the North Cascadia dislocation models. To compare these model results to the measured network strain rates, the program *strain_m* is again used to compute model-predicted principal horizontal strain rates averaged over the sites of each GPS network. The effective strain network centres remain the same because the same sets of stations were used in the calculations. The results for the Southern Vancouver Island (SVI) and Central Vancouver Island (CVI) regions are given in Table 7.1. Figure 7.20 shows the model predicted strain rates for the SVI and CVI regions using the standard Juan de Fuca plate model.

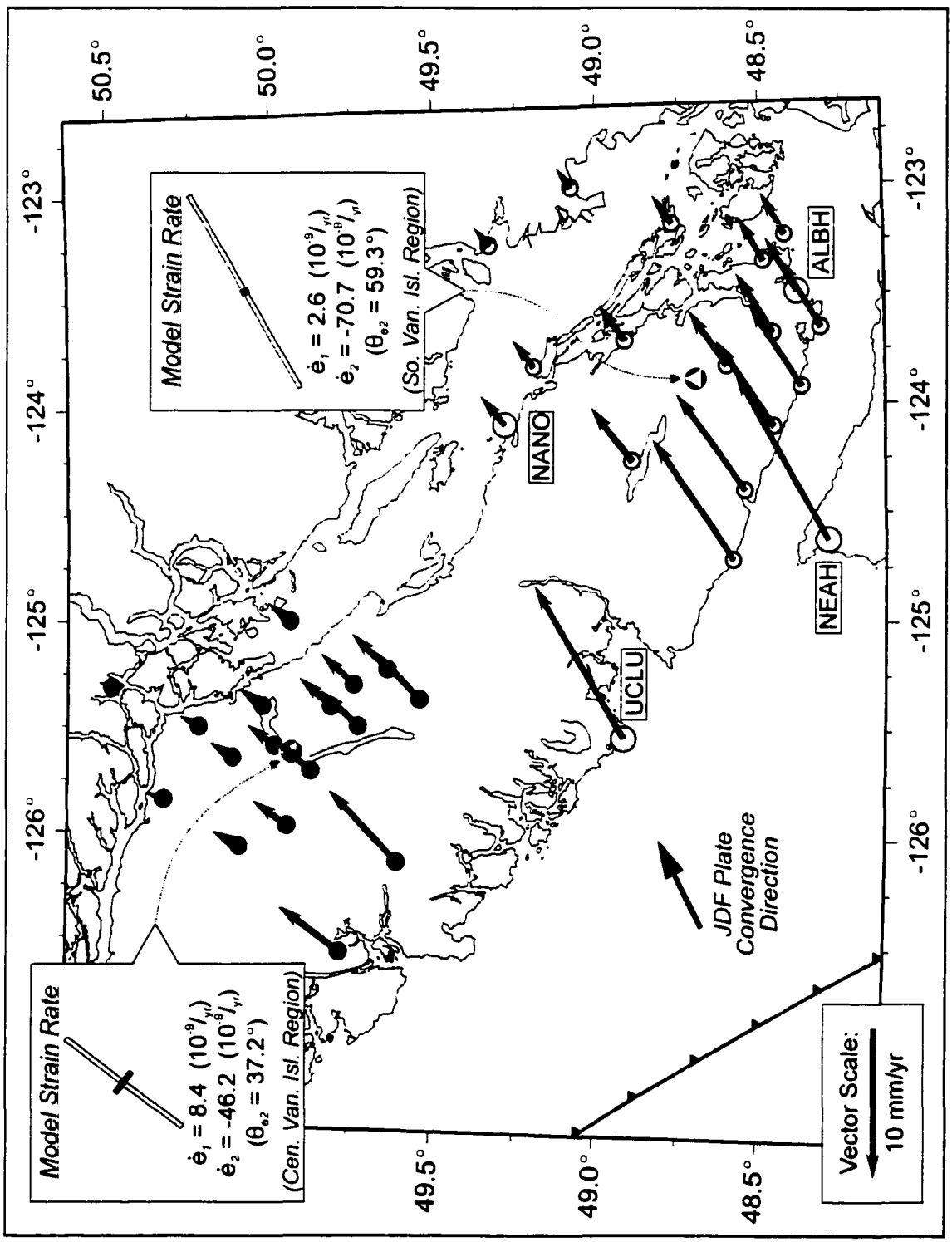

Figure 7.20. Regional model-predicted strain rates. The strain rates are determined from the "standard" Juan de Fuca plate model-predicted velocity field for the regions of central and southern Vancouver Island.

Region	Observations/Model	$\dot{e}_1$ (10^{-9} strain/yr)	$\dot{e}_2$ (10^{-9} strain/yr)	$\theta_{\dot{e}_2}$
SVI	SVI Observations (± 1σ)	5.4 ± 4.5	-46.6 ± 4.6	62.8°± 1.0°
	"Standard" JDF Plate	2.6	-70.7	59.3°
CVI	CVI Observations (± 1σ)	11.7 ± 15.4	-28.1 ± 15.4	32.4°± 6.0°
	"Standard" JDF Plate	8.4	-46.2	37.2°
	"Standard" JDF + EXP	5.2	-51.2	43.2°
	"Extended" JDF Plate	-0.3	-60.6	53.8°

Table 7.1. Comparison of observed and model-predicted strain rates for N. Cascadia

For southern Vancouver Island, the model predicts largely uniaxial shortening near the direction of plate convergence. This agrees well with the principal strain rates calculated from the observed velocity field for SVI. The model predicts a shortening rate that is approximately 1.5 times larger than measured. This was already evident from the comparison of the model velocity field to the observed velocity field (*refer to* Section 7.4). It was observed previously that, although the magnitude of the velocity vectors were comparable to the measurements near the outer coast of Vancouver Island, the rates of the more landward model-predicted vectors were significantly smaller than the observed rates. As a result, the model predicts a higher shortening rate across the island than the observations.

The top panel of Figure 7.21 shows the predicted model velocities projected onto a profile across southern Vancouver Island oriented in the direction of plate convergence (N62°E). Assuming uniaxial shortening, appropriate for southern Vancouver Island, the

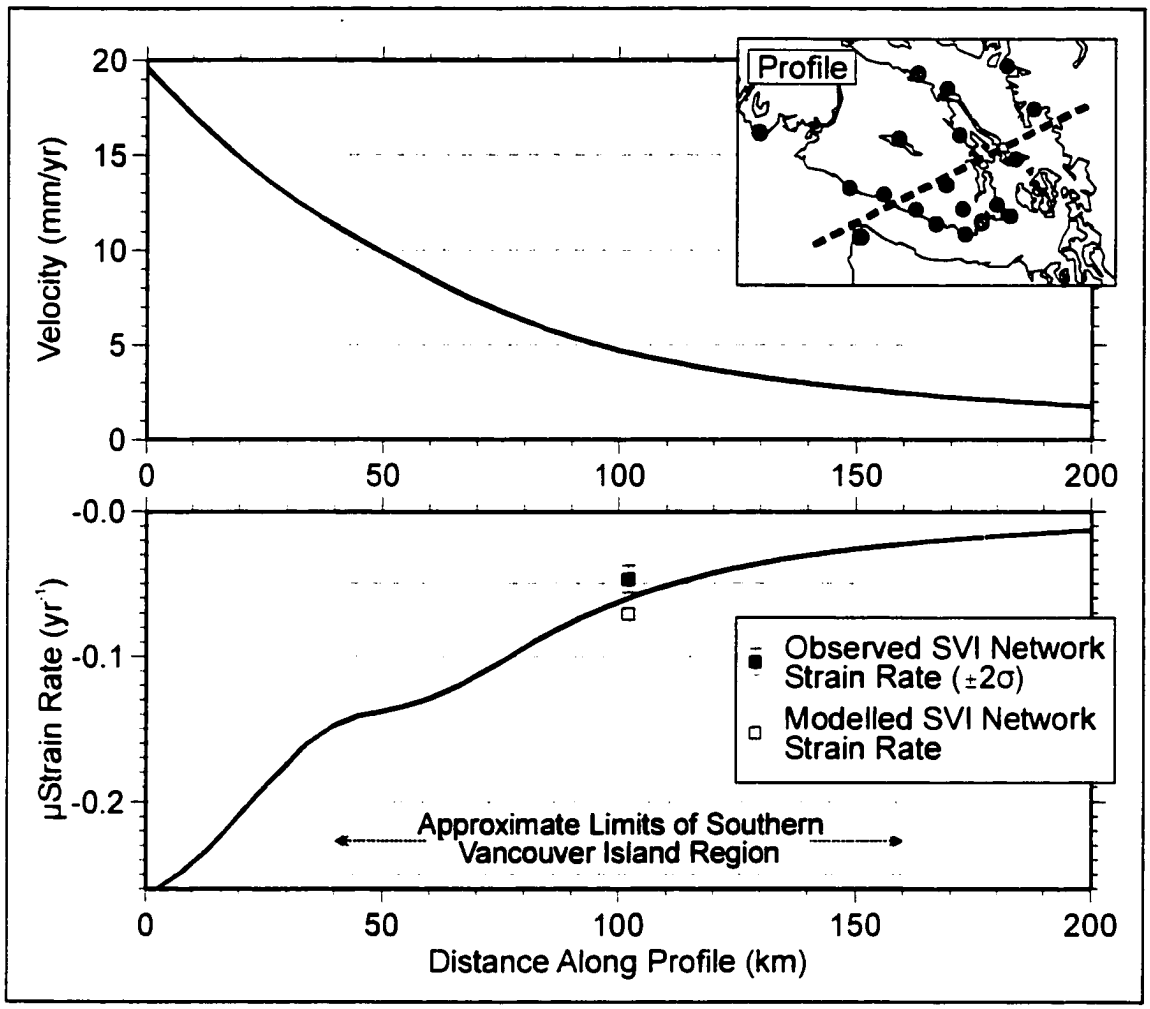

Figure 7.21. Model-predicted local velocities and strain rates along a southern Vancouver Island profile. The profile runs along a direction of N62°E. The position of the profile is given in the inset map along with the relative locations of the GPS sites for SVI (solid black circles indicate JdF campaign sites; grey-filled circles indicate continuous sites of the WCDA). The *average* network strain rates determined from the observed velocity field (solid black square with 2σ error-bar) and the model-predicted velocity field (white-filled square) are given for reference.

slope ($^{\partial V}/_{\partial x}$) of this model velocity curve was used to calculate a model-predicted strain rate curve along the same profile (bottom panel, Figure 7.21). The predicted change in strain rate across the island is quite rapid. The model predicts strain rates for points across SVI ranging from approximately -0.15 μstrain/yr near the outer coast to -0.02 μstrain/yr near the inner coast of Vancouver Island.

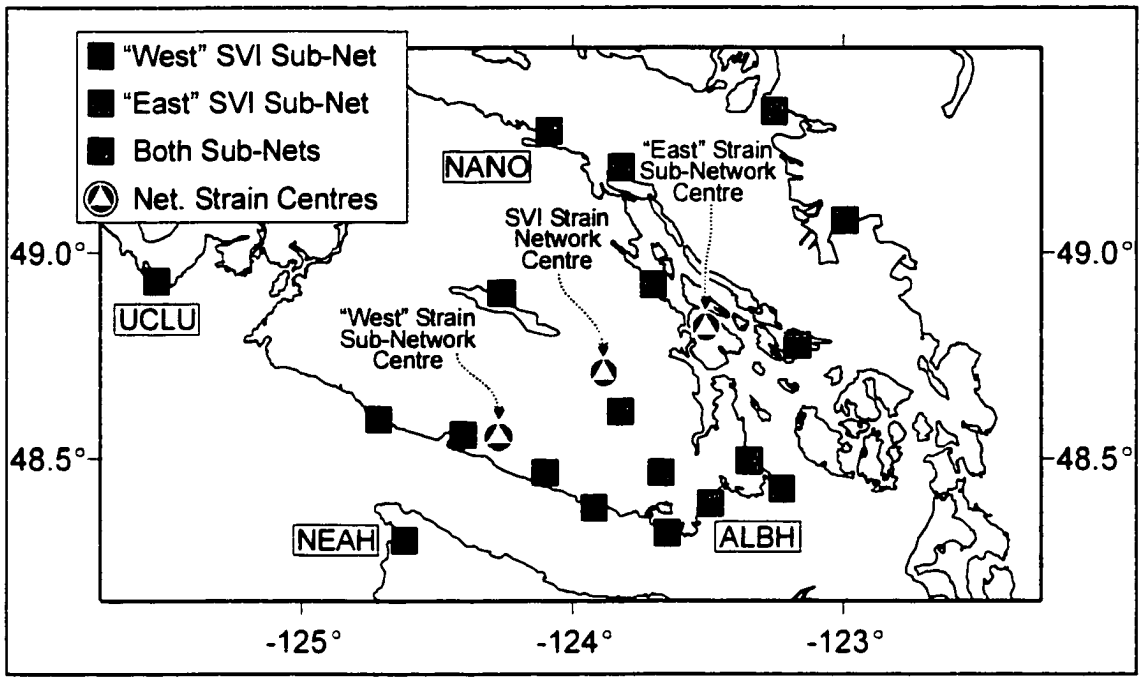

Figure 7.22. Strain sub-networks for southern Vancouver Island. The SVI network is broken down into two sub-networks. The 10 sites closest to the deformation front comprise the "West" sub-network, and the 11 most landward sites form the "East" sub-network. JdF sites CONS and LAZA are included in both sub-nets. The axes of principal strain rate calculated from the observed velocity field for these sub-networks are given in Table 7.2.

The observed SVI velocities, however, suggest a largely uniform deformation rate ($\dot{e}_2 \approx$-0.045 μstrain/yr) across this region (*refer to* Section 6.4 & Figure 6.2). This is further evident if the network is separated into two sub-networks (Figure 7.22): the first, "West SVI", encompassing the GPS sites nearer the outer coast of Vancouver Island, and the second, "East SVI", containing the sites nearer the inner coast. The program *strain_m* was again used to compute principal horizontal strain rates averaged over the sites of these two GPS sub-networks, and the results are given in Table 7.2. Because these sub-networks consist of a fewer number (~ ½) of sites, the standard errors are significantly increased over the strain rate results determined for the entire SVI region. The principal strain rates calculated for the two sub-networks are similar with each other, and with the complete, full

SVI network, at the one-sigma level (Table 6.2). Hence, the observations do not show a significant change in deformation rates across southern Vancouver Island.

The discrepancy between the *average* model-predicted *network* strain rate and the *average* observed strain rate across southern Vancouver Island is significant. This suggests that changes to the modeling are needed. For the elastic-dislocation model, model parameters may need to be modified. These include refinements to the geometry (*i.e.* location and widths) of the locked and transition zones, the convergence rate, and/or the coupling (in terms of percent slip-deficit) across the model fault surface. As discussed previously (Section 7.6), attempts to replicate the observed crustal motions by varying the widths of the locked and transition zones of the elastic dislocation model were not successful, nor have the attempts to refine the model kinematic parameters. Again, a viscoelastic model may be necessary for a more accurate representation of local deformation.

Obs/Model	Lat	Long	$\dot{e}_1$ (10^{-9} strain/yr)	$\dot{e}_2$ (10^{-9} strain/yr)	$\theta_{\dot{e}2}$
JDF Model	48.71°	-123.88°	2.6	-70.7	59.3°
SVI Obs (±1σ)	48.71°	-123.88°	5.4 ± 4.5	-46.6 ± 4.6	62.8°± 1.0°
"West" Obs (±1σ)	48.55°	-124.27°	6.7 ± 10.3	-49.0 ± 10.6	63.0°± 1.9°
"East" Obs (±1σ)	48.82°	-123.51°	-2.3 ± 14.1	-26.0 ± 18.4	67.0°± 4.3°

Table 7.2. Comparison observed strain rates for SVI network and sub-networks

The positions of the sites for the "West" and "East" SVI sub-networks are given in Figure 7.20. The latitude and longitude give the position of the strain network (or sub-network) centre. The JDF Model result is calculated from the model-predicted velocity field for the GPS sites of southern Vancouver Island and is given for reference.

For central Vancouver Island, the "standard" three-dimensional Juan de Fuca plate elastic-dislocation model predicts average network strain rates that agree well with the strain rates calculated from the observed velocity field for the CVI network (Table 7.3 & Figures 7.9, 7.18). With the increased noise in the GPS data, the model-predicted and the observed principal strain rates agree at the 95% confidence level. Additionally, the orientation of the principal axes of shortening are consistent at the 1σ level. Similar to the southern Vancouver Island results (Tables 7.1, 7.2), however, there is a suggestion that the average model-predicted principal rate of shortening ($\dot{e}_2$) is approximately 50% greater than the observed network average, again indicating possible viscoelastic effects. Although very noisy, the observed principal rate of extension ($\dot{e}_1$) indicates some small component of margin-parallel extension for the region of central Vancouver Island. Additionally, the magnitude of this margin-parallel extension rate is again best matched by the "standard" JDF plate model. As opposed to the largely uniaxial character for the region of southern Vancouver Island, the three-dimensional nature of the strain field at the northern end of the Juan de Fuca plate system is evident in both the observations and the JDF plate model.

Region	Observations/Model	$\dot{e}_1$ (10^{-9} strain/yr)	$\dot{e}_2$ (10^{-9} strain/yr)	$\theta_{\dot{e}2}$
"CVI" Central Vancouver Island	CVI Observations (± 1σ)	11.7 ± 15.4	-28.1 ± 15.4	32.4°± 6.0°
	"Standard" JDF Plate	8.4	-46.2	37.2°
	"Standard" JDF + EXP	5.2	-51.2	43.2°
	"Extended" JDF Plate	-0.3	-60.6	53.8°

Table 7.3. Comparison of observed and model-predicted strain rates for CVI region.

CHAPTER 8 - DISCUSSION AND CONCLUSIONS

In this thesis, current crustal deformation associated with large earthquake strain buildup has been estimated from GPS data in southwestern British Columbia. This area is subject to great subduction earthquakes and large crustal earthquakes in the forearc. Among the specific objectives were: (1) to determine whether the northern part of the subduction thrust is completely locked, (2) to refine the location of the locked zone, and (3) to determine whether the Explorer Plate zone to the north of the Nootka Fault zone is locked and can produce great earthquakes. Global Positioning System (GPS) data dating back to 1991 have been processed for the regions of southern and central Vancouver Island. These data consist of both continuous GPS tracker observations and repeated campaign-style GPS measurements. The horizontal deformation velocity field calculated from this combined data set has been compared to older geodetic measurements and to the predictions of three-dimensional elastic dislocation models for the northern Cascadia Subduction Zone (CSZ).

The horizontal deformation velocities determined from the continuous GPS tracker data appear to be accurate and robust at the 1 mm/yr level after one and one-half to two years of observations. The formal regression errors decrease with increased duration of the baseline time-series. The horizontal GPS-determined velocities exhibit velocities with respect to stable North America of approximately 1 cm/yr near the outer coast of Vancouver Island decreasing landward. Vertical velocities based on continuous GPS data are subject

to errors roughly three times greater. These larger errors mask the smaller vertical signals predicted by the models. It is worth noting that the newer network processing scheme using the latest Bernese GPS software package shows a pronounced improvement in the day-to-day scatter in the estimates of station heights. This holds great promise for better resolution of uplift rates which is required for model discrimination.

Periodic and abrupt transient signals are observed in the continuous baseline data. These signals primarily affect the vertical component of the GPS-determined positions and, with larger statistical scatter, give vertical uncertainties too large to permit significant model constraints. The dominant non-tectonic signals present in the GPS baselines possess annual periods with amplitudes up to 5 mm. While the exact cause of the annual signal is undetermined, it probably results from atmospheric effects. It is relatively easy to identify and remove. It is primarily in vertical component, with only small amplitudes in horizontal data baselines. A periodic energy with a fortnightly-period was also identified in the early portion of the vertical GPS time-series at all sites. This energy disappears for all time-series over the latter two years of data. The origin of this signal and an understanding of its behaviour remain elusive.

The horizontal velocity field determined from repeated campaign-style GPS measurements is consistent with continuous WCDA data for southern Vancouver Island, although at an accuracy typically one-half to one-third that provided by the continuous data. This agreement between temporal-regression based and survey-displacement based velocities confirms that observed motions are uniform and tectonic.

The higher accuracy, increased spatial coverage and common reference frame of the

GPS data set relative to prior geodetic data sets for the region leads to several conclusions. The pattern of deformation is generally consistent with a fully locked subduction megathrust fault surface. No free-slip zones along the strike of the northern Cascadia Subduction Zone margin are observed. As a result, the northern CSZ margin accumulates the full slip-deficit (*i.e.* at the rate of Juan de Fuca/North America relative plate convergence) along its length with no apparent abrupt changes in the width of the seismogenic zone. The observed horizontal velocity data, direction and magnitude, fit the elastic dislocation model well to first order. The widths of the locked zones off central Vancouver Island and southern Vancouver Island are approximately 55 km and 85 km, respectively, assuming equivalent widths for their respective transition zones. This is similar to the conclusions reached by *Hyndman & Wang* [1993] and *Dragert et al.* [1994].

However, observed velocities for the inland GPS sites are somewhat larger than predicted by the model. This may result from limitations in the elastic dislocation model. First, the region is not likely to be perfectly elastic. This region is seismically active and some crustal deformation may be accommodated through the release of seismic moment. Second, there may be effects from the time-dependent viscous deformation within mantle.

For central Vancouver Island, the velocity (and strain) field determined for the regional GPS campaign shows no clear deformation patterns that could be associated with the 1946 or 1918 shallow crustal earthquakes. The interseismic crustal earthquake deformation rate for this region must be less than about 1-2mm/yr, unless it occurs parallel to the direction of plate convergence and is thus masked by the larger subduction zone signal. Additional deformation effects of a subducting Explorer subplate are not seen in the

observations but modeling indicates it would have only a modest effect (*i.e.* at the noise-level) at the measured sites. Modeling indicates that in order to determine the nature of Explorer plate kinematics (*i.e.* the hypothesis of locked EXP subduction), stations are required towards the coast near the centerline of the slab. A program through the University of Victoria and the Geological Survey of Canada plans to install such stations this summer (2000).

The principal strain rates calculated from the observed velocity field for southern Vancouver Island (SVI) exhibit nearly uniaxial shortening near the direction of NA/JDF plate convergence. The principal shortening-axis rate, $\dot{e}_2$, is $-46.6 \pm 4.6 \times 10^{-9}$ strain/yr at an azimuth of $62.8° \pm 1.0°$ (error values are 1-sigma values). The observed SVI velocities display a largely uniform deformation rate across this region. Due to relatively high noise in the campaign data, it is difficult to partition strain into sub-networks because, as the sub-networks consist of a fewer number of sites, their standard errors are significantly increased. The value of $\dot{e}_2$ for SVI is approximately ½ to ¼ the strain rate calculated from previous geodetic strain measurements. Although it remains possible that this difference indicates some transient phenomena, it seems more likely that this particular discrepancy results from unrecognized measurement biases in the older data sets as well as biases between the different earlier measurement techniques.

For southern Vancouver Island, the three-dimensional elastic dislocation model of the locked NA/JDF thrust also predicts largely uniaxial shortening near the direction of plate convergence. The model, however, estimates an average shortening rate for the SVI region that is approximately 1.5 times larger than measured. As discussed preciously for this

discrepancy in the observed and modelled velocity fields, this difference likely results from limitations in the elastic dislocation model.

The principal extension-axis rate, $\dot{e}_1$, calculated for SVI is $5.4 \pm 4.5 \times 10^{-9}$ strain/yr and is comparatively much smaller than the regional principal shortening rate. This may suggest a small component of margin-parallel extension. *Khazaradze et al.* [1999], however, report north-south, margin-parallel shortening for western Washington state. This N-S shortening is consistent with the dominant orientation of P-axes in fault plane solutions for western Washington [*Qamar and Ludwin*, 1992; *Wang et al.*, 1995]. The microearthquake P-axes for southwestern British Columbia are again margin-parallel compressive, oriented NW-SE [*Wang et al.*, 1995], which appears to contradict the observed principal rate of extension for SVI. It may be possible that this region is currently subject to margin-parallel compression and that the *apparent* extension rates reflects a recent, temporal decrease in local compressive stress field. Hence, the area may be experiencing a relaxation from some unknown perturbation in the regional margin-parallel stress regime.

For the region of central Vancouver Island (CVI), the value of $\dot{e}_2$, the principal shortening-axis rate, is $-28.1 \pm 15.4 \times 10^{-9}$ strain/yr with an azimuth of $32.4° \pm 6.0°$ (error values are 1-sigma values). The principal axis of shortening thus deviates significantly from the direction of JDF/NA plate convergence for northern Cascadia. Additionally, this region suggests increased margin-parallel extension ($\dot{e}_1 = 11.7 \pm 15.4 \times 10^{-9}$ strain/yr). Again, the principal rate of shortening for the CVI region is approximately ½ to ¼ the strain rate calculated from previous geodetic strain measurements. Given the comparative precision of GPS measurements and their agreement with deformation velocities expected for a

subduction zone, the CVI strain rates given in this dissertation are taken to be more reliable than previous strain measurements.

As opposed to the largely uniaxial character for the region of southern Vancouver Island, the three-dimensional nature of the strain field at the northern end of the Juan de Fuca plate system is evident in both the observations and the JDF plate model. The subduction of the Juan de Fuca plate again appears to produce the primary deformation signal for CVI. Indeed, for central Vancouver Island, the "standard" three-dimensional Juan de Fuca plate elastic-dislocation model predicts average network strain rates that agree well with the strain rates calculated from the observed velocity field for the CVI network. With the increased noise in the GPS data, the model-predicted and the observed principal strain rates agree at the 95% confidence level. Additionally, the orientation of the principal axes of shortening are consistent at the 1σ level.

Similar to the southern Vancouver Island results, there is a suggestion that the average model-predicted principal rate of shortening is approximately 1.5 times greater than the observed network average, again indicating possible viscoelastic effects. Although the data are noisy, the observed principal rate of extension may suggest some small component of margin-parallel extension for the region of central Vancouver Island. The magnitude of this margin-parallel extension rate is best matched by the "standard" JDF plate model. Hence, the observations for central Vancouver Island are consistent with the absence of a *major* locked subduction thrust surface to the north of the Nootka Fault Zone.

BIBLIOGRAPHY

Adams, J., Paleoseismicity of the Cascadia subduction zone: Evidence from turbiditites off the Oregon-Washington margin, *Tectonics*, *9*, 569-583, 1990.

Argus, D.E., and R.G. Gordon, Test of the rigid-plate hypothesis and bounds on intraplate deformation using geodetic data from very long baseline interferometry, *J. Geophys. Res.*, *101*, 13,555-13,572, 1996.

Argus, D.E., and M.B. Heflin, Plate motion and crustal deformation estimated with geodetic data from the Global Positioning System, *Geophys. Res. Lett.*, *22*, 1973-1976, 1995.

Atwater, B.F., Evidence for great Holocene earthquakes along the outer coast of Washington State, *Science*, *236*, 942-944, 1987.

Atwater, B.F., A.R. Nelson, J.J. Clague, G.A. Carver, D.K. Yamaguchi, P.T. Brobrowski, J. Bourgeois, M.E. Darienzo, W.C. Grant, E. Hemphill-Haley, H.M. Kelsey, G.C. Jacoby, S.P. Nishenko, S.P. Palmer, C.D. Peterson, and M.A. Reinhart, Summary of coastal geologic evidence for past great earthquakes at the Cascadia subduction zone, *Earthquake Spectra*, *11*, 1-18, 1995.

Beutler, G., The impact of the International GPS Service for Geodynamics on the surveying and mapping community, *International Union of Surveying and Mapping (IUSM) Presented Papers of the Working Group Sessions*, 84-94, 1992.

Beulter, G., I.I. Meuller, and R.E. Neilan, The International GPS Service for Geodynamics (IGS): development and start of official service on January 1, 1994, *Bulletin Geodésique*, *68*, 1, 1994.

Boucher, C., and Z. Altamimi, International Terrestrial Reference Frame, *GPS World*, *7*, 71-74, 1996.

Carbotte, S.M., J.M. Dixon, E. Farrar, E.E. Davis, and R.P. Riddihough, Geological and geophysical characteristics of the Tuzo Wilson Seamounts: implications for plate geometry in the vicinity of the North America-Explorer triple junction, *Can. J. Earth Sci.*, *26*, 2365-2384, 1989.

Cassidy, J.F., R.M. Ellis, C. Karavas, and G.C. Rogers, The northern limit of the subducted Juan de Fuca plate system, *J. Geophys. Res*, *103*, 26,949-26,961, 1998.

Chadwell, C.D., J.A. Hildebrand, and F.N. Spiess, Seafloor monitoring within the Plate Boundary Observatory (abstract), *Seis. Res. Lett.*, *71*, 262, 2000.

Chen, X., Analyses of continuous GPS data from the Western Canada Deformation Array, *Proceedings of ION GPS-94* (Salt Lake City, Utah, USA: September 20-23, 1990), 1339-1344, 1994.

Chou, P.C., and N.J. Pagano, *Elasticity - Tensor, Dyadic, and Engineering Approaches*, 290pp., Dover Publications, New York, 1967.

Clague, J.J., and P.T. Bobrowski, Tsunami deposits beneath tidal marshes on Vancouver Island, British Columbia, *Geol. Soc. Amer. Bull., 106*, 1293-1303, 1994.

Clague, J.J., Evidence for large earthquakes at the Cascadia Subduction zone, *Rev. Geophys., 35*, 439-460, 1997.

Clowes, R.M., D.J. Baird, and S.A. Dehler, Crustal structure of the Cascadia subduction zone, southwestern British Columbia, from potential field and seismic studies, *Can. J. Earth Sci., 34*, 317-335, 1997.

Crawford, W.R., Sea level changes in British Columbia at periods of two days to a year, *Pacific Marine Science Report 80-8*, 46pp., Institute of Ocean Sciences, Sidney, B.C., Canada, 1980.

Dana, P.H., The Global Positioning System Overview (Web Page Module): The Geographer's Craft Project, Department of Geography, The University of Texas at Austin (http://www.utexas.edu/depts/grg/gcraft/notes/gps/gps_f.html), 1998.

Davis, E.E., and R.P., Riddihough, The Winona basin: structure and tectonics, *Can. J. Earth Sci., 19*, 767-788, 1982.

Davis, E.E., and R.G. Currie, Geophysical observations of the northern Juan de Fuca Ridge system: lessons in sea-floor spreading, *Can. J. Earth Sci., 30*, 278-300, 1993.

Davis, E.E., and R.D. Hyndman, Accretion and recent deformation of sediments along the northern Cascadia subduction zone, *Geol. Soc. Am. Bull., 101*, 1465-1480, 1989.

Dehler, S.A., and R.M. Clowes, Integrated geophysical modelling of terranes and other structural features along the western Canadian margin, *Can. J. Earth Sci., 29*, 1492-1508, 1992.

DeMets, C., and T.H. Dixon, New kinematic models for Pacific-North America motion from 3 Ma to present I: Evidence for stready motion and biases in the NUVEL-1A model, *Geophys. Res. Lett., 26*, 1921-1924, 1999.

DeMets, C., R.G. Gordon, D.F. Argus, and Seth Stein, Effect of recent revisions to the geomagnetic reversal timescale on estimates of current plate motions, *Geophys. Res. Lett., 21*, 2191-2194, 1994.

DeMets, C., R.G. Gordon, D.F. Argus, and Seth Stein, Current plate motions, *Geophys. J. Int.*, *101*, 425-478, 1990.

Douglass, J.J., and B.A. Buffett, The stress implied by dislocation models of subduction deformation, *Geophys. Res. Lett.*, *22*, 3115-3118, 1995.

Douglass, J.J., and B.A. Buffett, Reply to comment by J.C. Savage on "The stress implied by dislocation models of subduction deformation," *Geophys. Res. Lett.*, *23*, 2711-2712, 1996.

Dragert, H., and M. Lisowski, Crustal deformation measurements on Vancouver Island, British Columbia: 1976 to 1988, in *Global and Regional Geodynamics*, (International Association of Geodesy Symposia) edited by: P. Vyskocil, C. Reigber, and P.A. Cross, pp. 241-250, Springer-Verlag, New York, 1990.

Dragert, H., Recent horizontal strain accumulation on Vancouver Island, British Columbia (abstract), *Eos Trans., AGU*, *72*, 314, 1991.

Dragert, H., X. Chen, and J. Kouba, GPS monitoring of crustal strain in Southwest British Columbia with the WCDA, *Geomatica*, *49*, 301-313, 1995.

Dragert, H., and R.D. Hyndman, Continuous GPS monitoring of elastic strain in the northern Cascadia subduction zone, *Geophys. Res. Lett.*, *22*, 755-758, 1995.

Dragert, H., R.D. Hyndman, G.C. Rogers, and K. Wang, Current deformation and the width of the seismogenic zone of the northern Cascadia subduction thrust, *J. Geophys. Res.*, *99*, 653-668, 1994.

Dragert, H., J.A. Henton, and G. Khazararadze, Present-day strain variations along the north Cascadia margin (abstract), *Eos, Trans. AGU*, *79*, F982, 1998.

Dragert, H., M. Schmidt, and Y. Lu, The Western Canada Deformation Array: Measuring crustal motions in coastal British Columbia with continuous GPS (abstract), *Eos, Trans. AGU*, *79*, F191, 1998.

Flück, P., 3-D dislocation model for great earthquakes of the Cascadia subduction zone, Diploma Thesis, 106pp., Swiss Federal Institute of Technology (ETH), Zurich, Switzerland, 1996.

Flück, P., R.D. Hyndman, and K. Wang, Three-dimensional dislocation model for great earthquakes of the Cascadia subduction zone, *J. Geophys. Res.*, *102*, 20539-20550, 1997.

Henton, J.A., H. Dragert, R.D. Hyndman, and K. Wang, Geodetic monitoring of crustal deformation on Vancouver Island (abstract), *Eos, Trans. AGU*, *79*, F192, 1998.

Henton, J.A., H. Dragert, R.D. Hyndman, and K. Wang, Geodetic monitoring of crustal deformation and strain on Vancouver Island (abstract), *Eos, Trans. AGU, 80*, F276, 1999.

Héroux, P and J. Kouba, GPS precise positioning with a difference, *1995 Canadian Geomatics Proceedings (Ottawa, Ontario: June 13-15, 1995)*, (CD-ROM), 1995.

Hofmann-Wellenhof, B., H Lichtenegger, and J. Collins, *Global Positioning System, Theory and Practice*, 326pp., Springer-Verlag Wien, New York, 1993.

Hopfield, H.S., Two-quadratic tropospheric refractivity profile for correcting satellite data, *J. Geophys. Res., 74*, 4487-4499, 1969.

Hyndman, R.D., M. Yamano, and D.A. Oleskevich, The seismogenic zone of subduction thrust faults, *Island Arc, 6*, 244-260, 1997.

Hyndman, R.D., and K. Wang, The rupture zone of Cascadia great earthquakes from current deformation and the thermal regime, *J. Geophys. Res., 100*, 22133-22154, 1995.

Hyndman, R.D., and K. Wang, Thermal constraints on the zone of major thrust earthquake failure: The Cascadia subduction zone, *J. Geophys. Res., 98*, 2039-2060, 1993.

Hyndman, R.D., R.P. Riddihough, and R. Herzer, The Nootka fault zone - a new plate boundary off western Canada, *Geophys. J. R. Astro. Soc., 58*, 667-683, 1979.

Jarrard, R.D., Relations among subduction parameters, *Rev. Geophys., 24*, 217-284, 1986.

Johnson, H.O., and D.C. Agnew, Monument motion and measurements of crustal velocities, *Geophys. Res. Lett., 22*, 2905-2908, 1995.

Khazaradze, G., A. Qamar, and H. Dragert, Tectonic deformation in western Washington from continuous GPS measurements, *Geophys. Res. Lett., 26*, 3153-3157, 1999.

Kouba, J., and X. Chen, Near real time GPS data and quality control, *Proceedings of the Sixth International Geodetic Symposium on Satellite Positioning (The Ohio State University, Columbus, Ohio, USA: March 17-20, 1992), Vol. 2*, 823-835, 1992.

Kouba, J., and J. Popelar, GPS satellite monitoring and data analysis, *Proceedings of the Second International Symposium on Precise Positioning with GPS (Ottawa, Ontario: September 3-7, 1990)*, 656-662, 1991.

Kouba, J., J. Popelar, and D. Delikaraoglou, GPS orbit monitoring and data analysis, *Canada Advanced Space Research, 11*, 193-196, 1991.

Kreemer, C., R. Govers, K.P. Furlong, and W.E. Holt, Plate boundary deformation between

the Pacific and North America in the Explorer region, *Tectonophysics, 293*, 225-238, 1998.

Larson, K.M. J.T Freymueller, and S. Philipsen, Global plate velocities from the Global Positioning System, *J. Geophys. Res., 102*, 9961-9981, 1997.

Le Pichon, X., S. Mazzotti, P. Henry, and M. Hashimoto, Deformation of the Japanese Islands and seismic coupling based on GSI permanent GPS observations, *Geophys. J. Int., 134*, 501-514, 1998.

Leick, A., *GPS satellite surveying*, 560pp., John Wiley & Sons, New York, 1995.

Lisowski, M., W.H. Prescott, H. Dragert, and S.R. Holdahl, Results from the 1986 and 1987 GPS survey across the across the Strait of Juan de Fuca, Washington and British Columbia (abstract), *Seismol. Res. Lett., 60*, 1, 1989.

Mader, G.L., GPS Antenna Calibration at the National Geodetic Survey, http://www.grdl.noaa.gov/GRD/GPS/Projects/ANTCAL/ (*website*), Geosciences Research Division, National Geodetic Survey, National Oceanic and Atmospheric Administration, Silver Spring, MD, USA, 1999.

Mazzotti, S, P. Henry, X. Le Pichon, T. Sagiya, Strainpartitioning in the zone of transition from Nankai subduction to Izu-Bonin collision (Central Japan): implications for an extensional tear within the subducting slab, *Earth Plan. Sci. Lett., 172*, 1-10, 1999.

Milne, W.G., G.C. Rogers, R.P. Riddihough, G.A. McMechan, and R.D. Hyndman, Seismicity of western Canada, *Can. J. Earth Sci., 15*, 1170-1193, 1978.

Mitchell, C.E., P. Vincent, R.J. Weldon II, and M.A. Richards, Presnt-day vertical deformation of the Cascadia margin, Pacific Northwest, United States, *J. Geophys. Res., 99*, 12,257-12,277, 1994.

Molnar, P., and T. Atwater, Interarc spreading and cordilleran tectonics as alternates related to the age of the subducted oceanic lithosphere, *Earth Planet. Sci. Lett., 41*, 330-340, 1978.

Mueller, I.I., and G. Beutler, The International GPS Service for Geodynamics - Development and Current Structure, *Proceedings of the Sixth International Geodetic Symposium on Satellite Positioning* (The Ohio State University, Columbus, Ohio, USA: March 17-20, 1992), 628-637, 1992.

Okada, Y., Surface deformation due to shear and tensile faults in a half space, *Bull. Seismol. Soc. Am., 75*, 1135-1154, 1985.

Oleskevich, D.A., Thermal constraints on great earthquake rupture zones, M.Sc. Thesis,

170pp., University of Victoria, Victoria, B.C., Canada, 1996.

Oleskevich, D.A., R.D. Hyndman, and K. Wang, The updip and downdip limits to great subduction earthquakes: Thermal and structural models of Cascadia, south Alaska, SW Japan, and Chile, , *J. Geophys. Res., 104*, 14,965-14,991, 1999.

Pagiatakis, S.D., Stochastic significance of peaks in the least-squares spectrum, *J. Geodesy, 73*, 67-78, 1999.

Pagiatakis, S.D., Ocean tide loading, body tides, and polar motion effects on very long baseline interferometry, *Surveying Engineering Technical Report No. 2*, Department of Surveying Engineering, University of New Brunswick, Fredericton, N.B., Canada, 1982.

Qamar, A., and R.S. Ludwin, Stress directions in Washington and northern Oregon inferred form earthquake focal mechanisms, *Seis. Res. Lett., 63*, 23, 1992.

Riddihough, R., Recent movements of the Juan de Fuca plate system, *J. Geophys. Res., 89*, 6980-6994, 1984.

Rohr, K.M.M., and K.P. Furlong, Ephemeral plate tectonics at the Queen Charlotte triple junction, *Geology, 23*, 1035-1038, 1995.

Rothacher, M, L. Mervart (contributors and editors), G. Beutler, E. Brockmann, S. Fankhauser, W. Gurtner, J. Johnson, S. Schaer, T. Springer, and R. Weber (contributors), *Documentation of the Bernese GPS Software Version 4.0*, 418pp, Astronomical Institute, University of Berne, Berne, Switzerland, 1996.

Rogers, G.C., An assessment of the megathrust earthquake potential of the Cascadia subduction zone, *Can. J. Earth Sci., 25*, 844-852, 1988.

Rogers, G.C., Seismotectonics of British Columbia. Ph.D. thesis, University of British Columbia, Vancouver, B.C., 1983

Ruff, L., and H. Kanamori, Seismicity and the subduction process, *Phys. Earth Planet. Inter., 23*, 240-252, 1980.

Savage, J.C., Comment on "The stress implied by dislocation models of subduction deformation" by J.J. Douglass and B.A. Buffett, *Geophys. Res. Lett., 23*, 2709-2710, 1996.

Savage, J.C., M. Lisowski, and W.H. Prescott, Strain accumulation in western Washington, *J. Geophys. Res., 96*, 14,493-14,507, 1991.

Savage, J.C., A dislocation model of strain accumulation and release at a subduction zone,

J. Geophys. Res., 88, 4984-4996, 1983.

Scholz, C.H., *The Mechanics of Earthquakes and Faulting*, 439pp, Cambridge University Press, New York, 1990.

Spiess, F.N., C.D. Chadwell, J.A. Hildebrand, L.E. Young, G.H. Purcell Jr., and H. Dragert, Precise GPS / Acoustic positioning of seafloor reference points for tectonic studies, *Phys. Earth & Planetary Interiors, 108*, 101-112, 1998.

Steketee, J.A., On Volterra's dislocation in a semi-infinite elastic medium. *Can. J. Phys., 36*, 192-205, 1958.

Turcotte, D.L., and G. Schubert, *Geodynamics - Applications of Continuum Physics to Geological Problems*, 450pp, John Wiley & Sons, New York, 1982.

Wang, K., Stress-strain "paradox", plate coupling and forearc seismicity at the Cascadia and Naikai subduction zones, *Tectonophysics, in press*, 2000.

Wang, K., T. Mulder, G.C. Rogers, and R.D. Hyndman, Case for very low coupling stress on the Cascadia subduction fault, *J. Geophys. Res., 100*, 12,907-12,918, 1995.

Wang, K., and H. Dragert, FORTRAN code strain_m.f: computer routine to calculate the components of a strain tensor averaged over a network of sites, Pacific Geoscience Centre, Geological Survey of Canada,1999.

Wang, K., H. Dragert, and H.J. Melosh, Finite element study of uplift and strain across Vancouver Island, *Can. J. Earth Sci., 31*, 1510-1522, 1994.

Wang, K., Coupling of tectonic loading and earthquake fault slips at subduction zones, *Pure Appl. Geophys., 145*, 537-559, 1995.

Wells, D.E., N. Beck, D.Delikaraoglou, A. Kluesberg, E.J. Krakiwsky, G. Lachapelle, R.B. Langley, M. Nakiboglu, K.P. Schharz, J.M. Tranquilla, and P. Vaníček, *Guide to GPS Positioning*, Canadian GPS Associates, University of New Brunswick Graphic Services, Fredericton, New Brunswick, Canada, 1986.

Wells, D.E., P. Vaníček, and S. Pagiatakis, Least Squares Spectral Analysis Revisited, *Surveying Engineering Technical Report No. 84*, 68pp., University of New Brunswick, Fredericton, N.B., Canada, 1985.

Wells, D.E., *Doppler Satellite Control*, Department of Surveying Engineering, University of New Brunswick, Fredericton, N.B., Canada, 1974.

Wells, R.E., C.S. Weaver, and R.J. Blakely, Forearc migration in Cascadia and its neotectonic significance, *Geology, 26*, 759-762, 1998.

Zhang, J., Y. Bock, H. Johnson, P. Fang, S. Williams, J. Genrich, S. Wdowinski, and J. Behr, Southern California Permanent GPS Geodetic Array: Error analysis of daily position estimates and site velocities, *J. Geophys. Res., 102*, 18035-18055, 1997.

APPENDIX A

Variations in WCDA station baseline components (latitude, longitude, & height) from a nominal station position determined relative to the reference site DRAO are plotted in Appendix A as Figures A.1 -A.7. Time series are from Dragert et al. [1998] and have been corrected for datum-offsets. The data plots exhibit predominately linear trends over time which are inferred to be tectonic deformation rates. Often there is a sinusoid of annual period large enough in amplitude to visually identify in the baseline time-series.

These data are discussed in Sections 4.3. & 4.6.1.

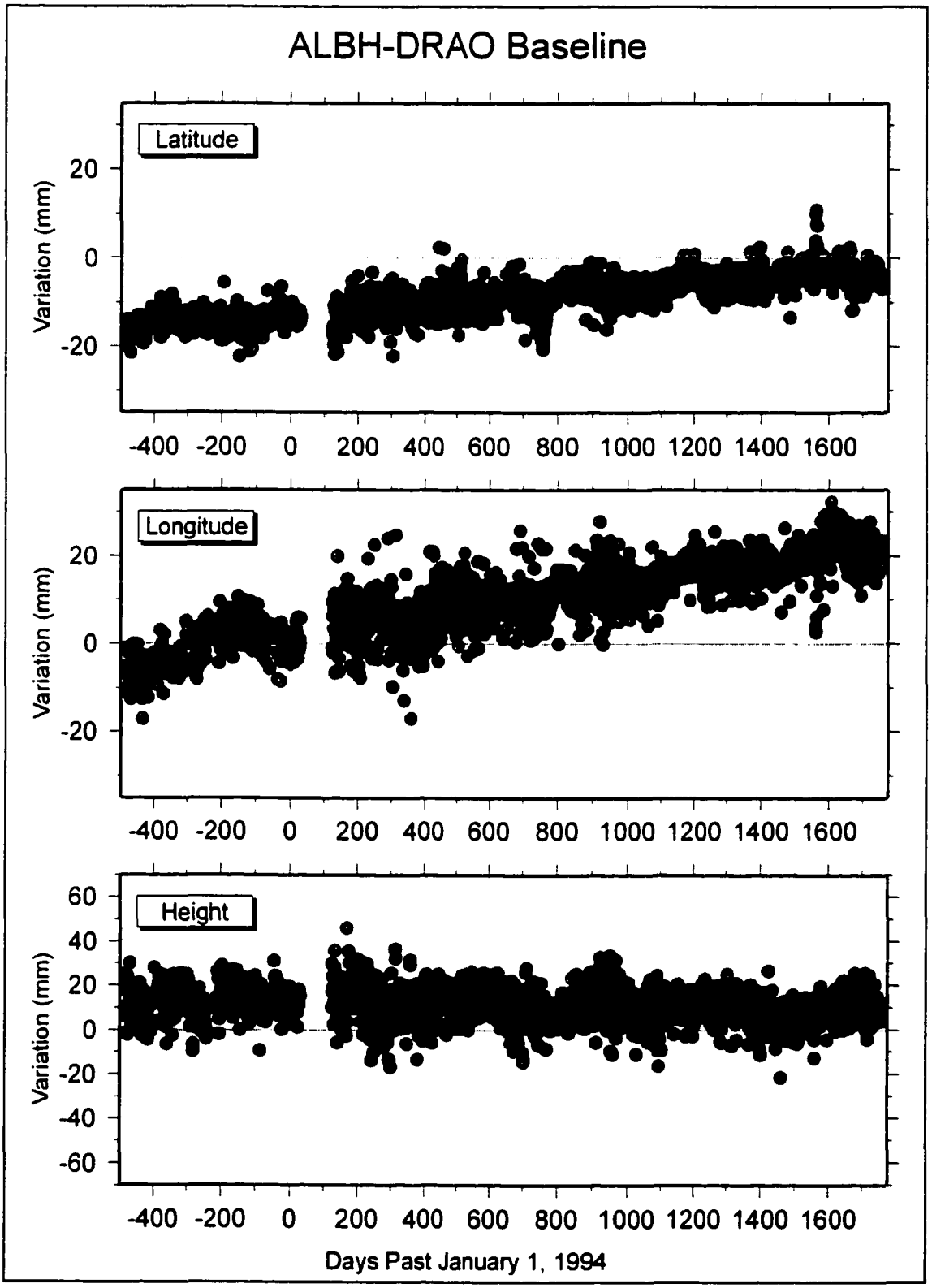

Figure A.1. Variations in ALBH baseline components from a nominal position determined relative to DRAO.

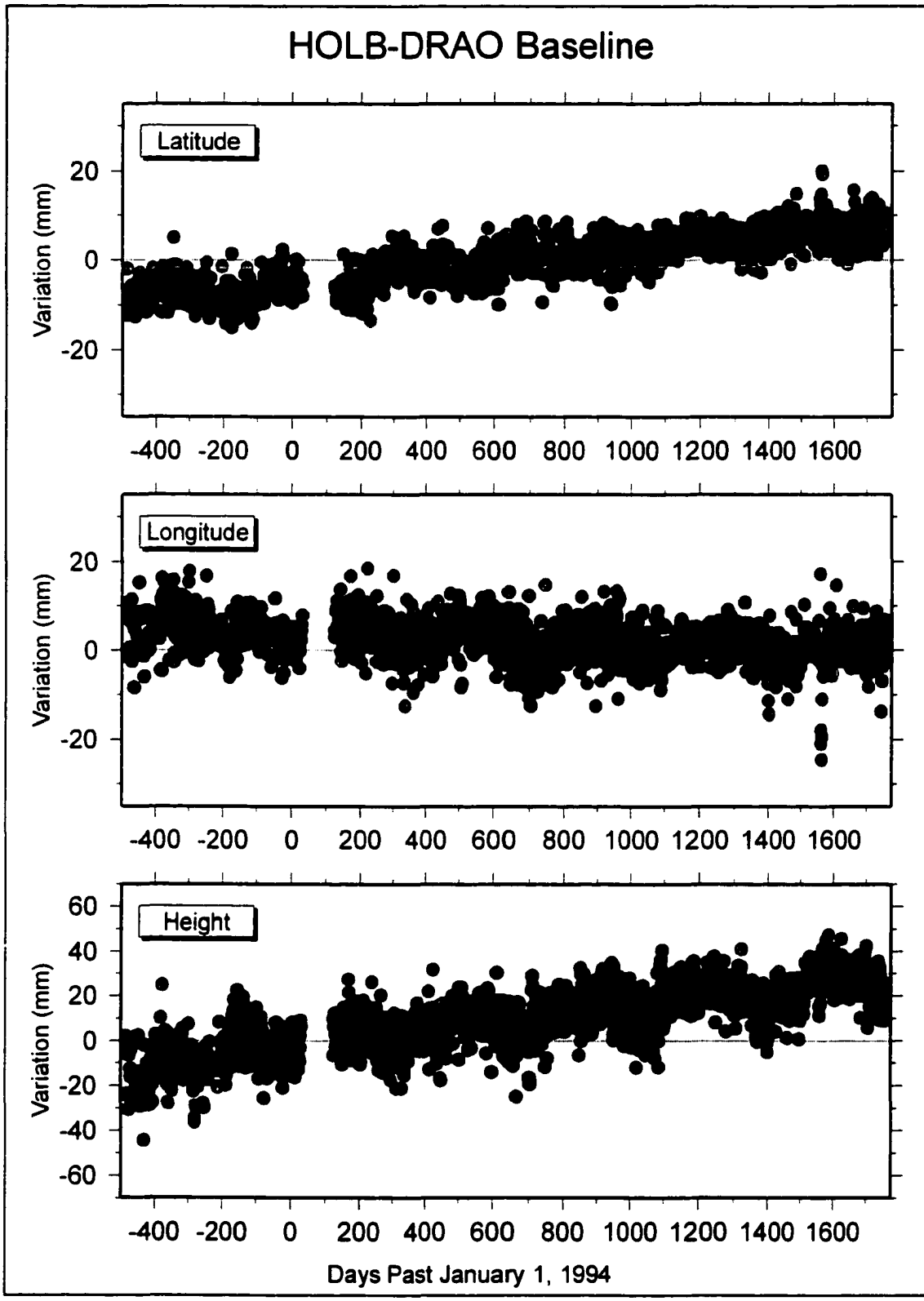

Figure A.2. Variations in HOLB baseline components from a nominal position determined relative to DRAO.

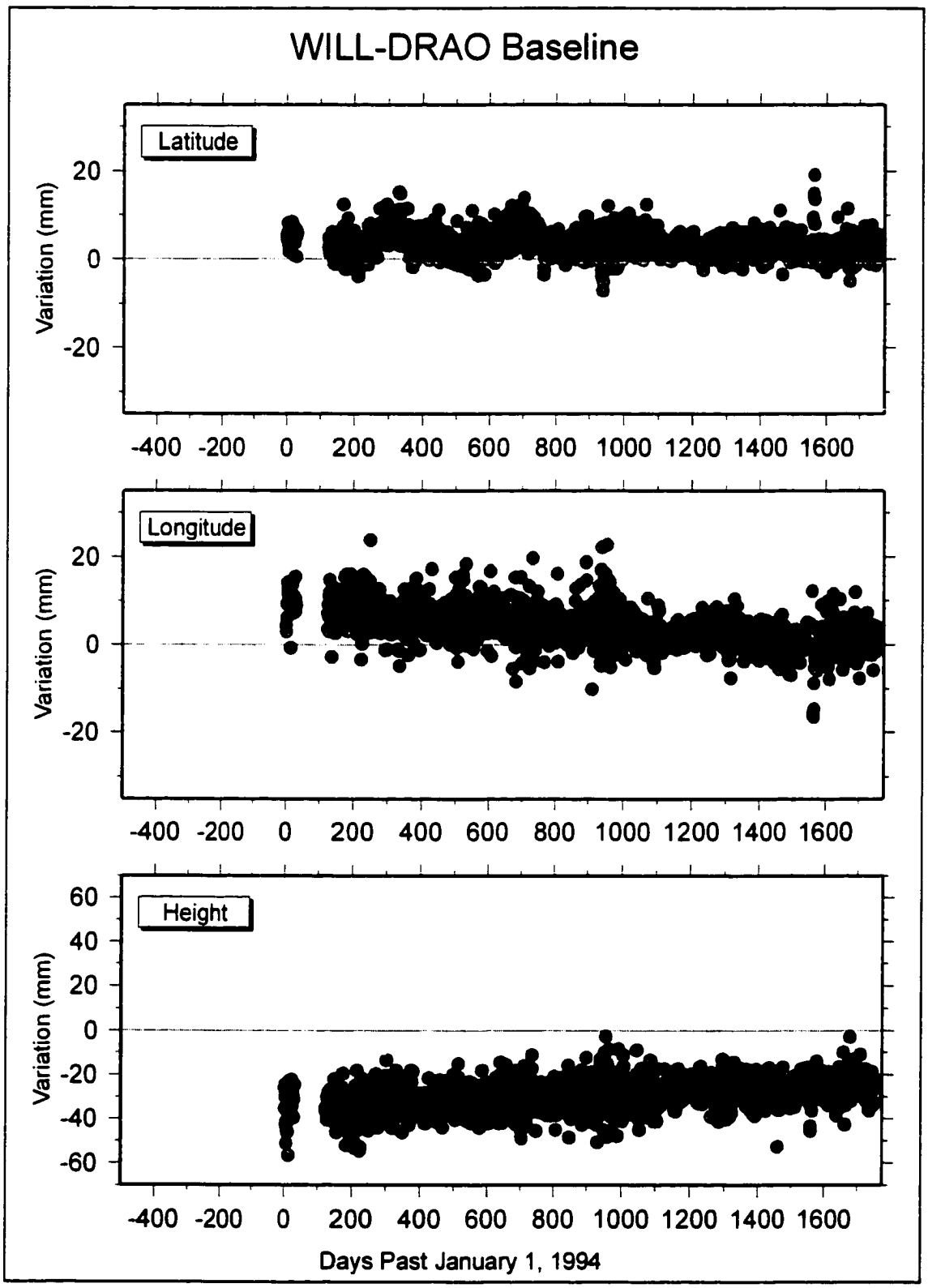

Figure A.3. Variations in WILL baseline components from a nominal position determined relative to DRAO.

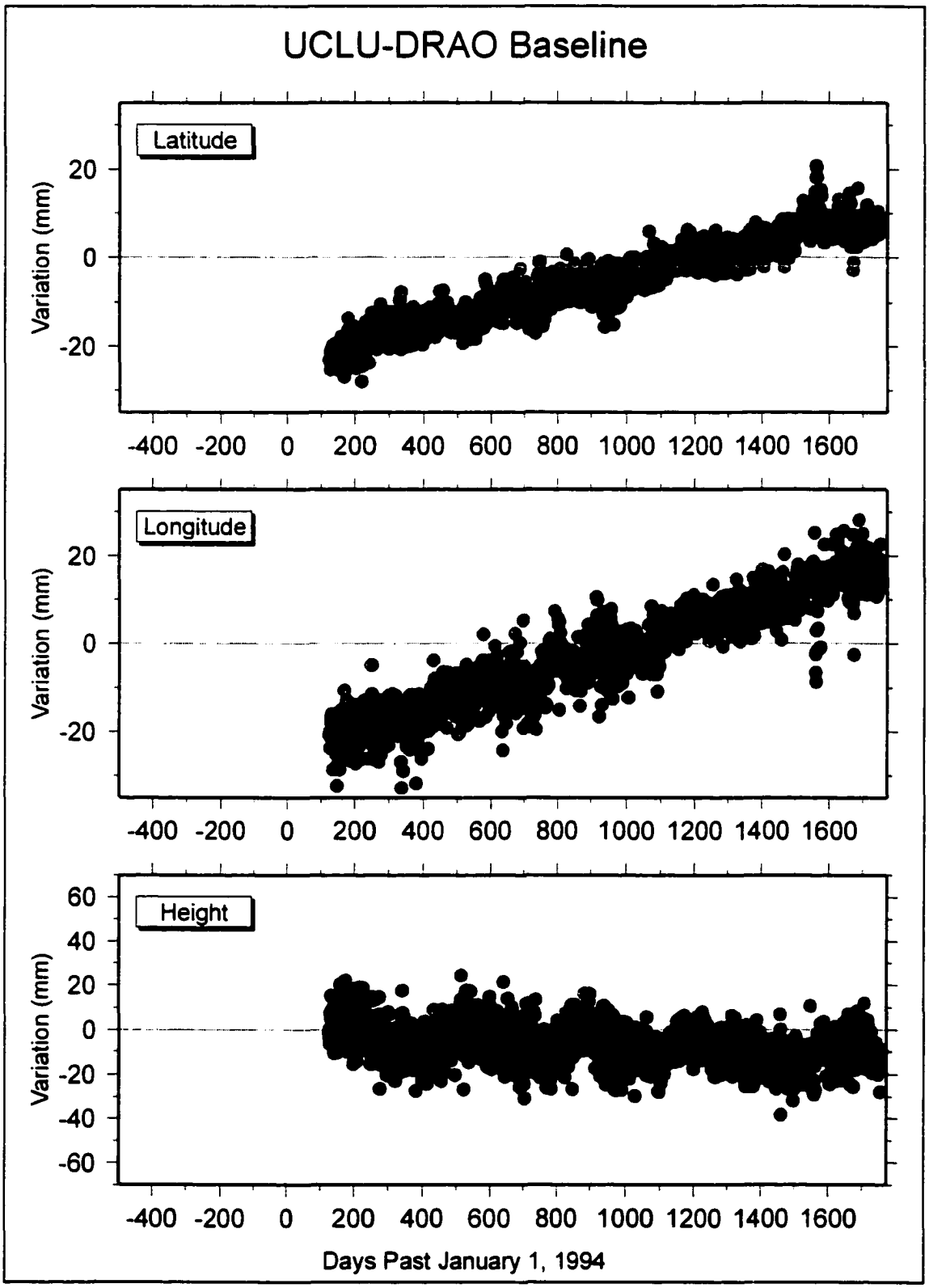

Figure A.4. Variations in UCLU baseline components from a nominal position determined relative to DRAO.

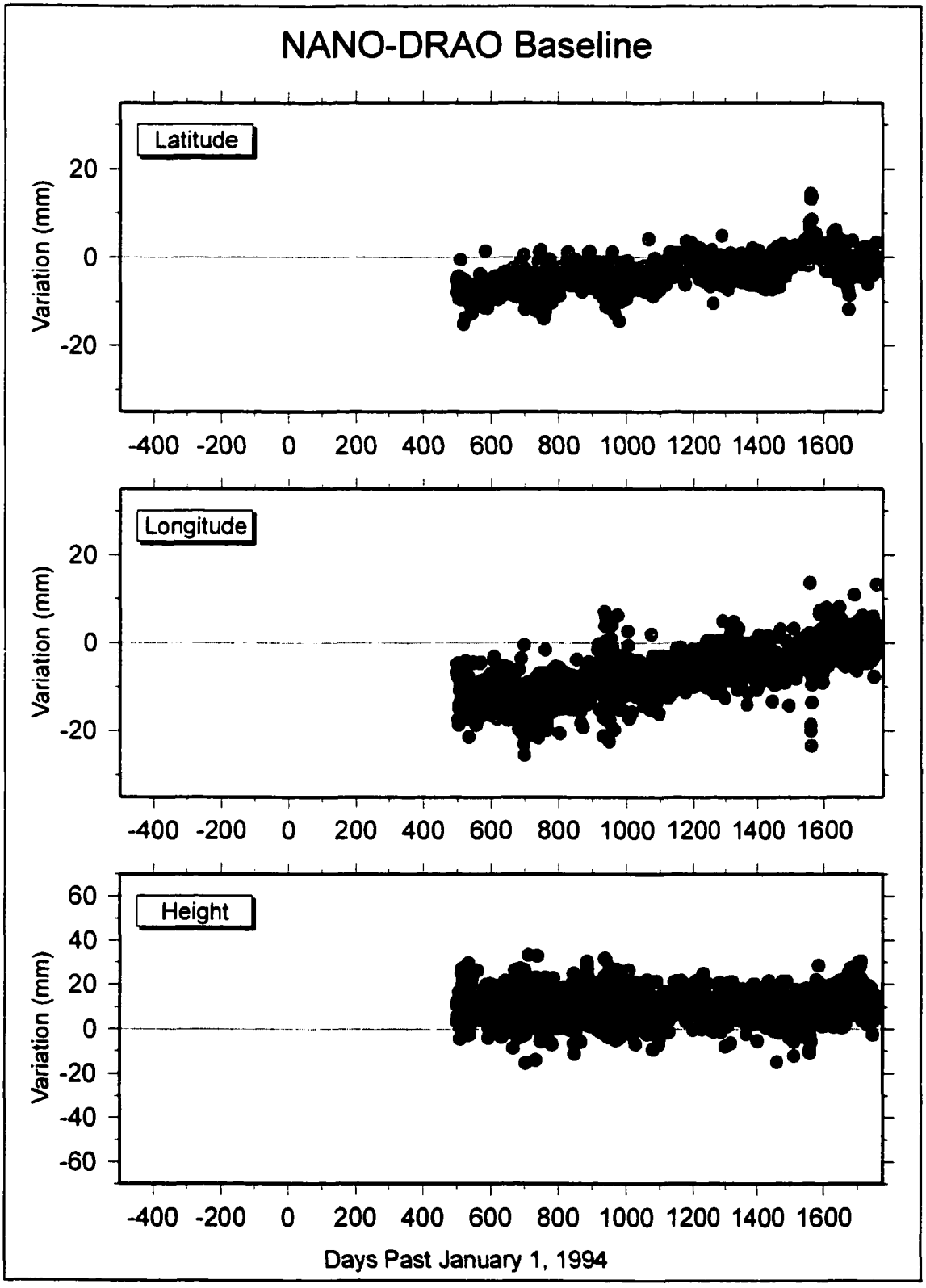

Figure A.5. Variations in NANO baseline components from a nominal position determined relative to DRAO.

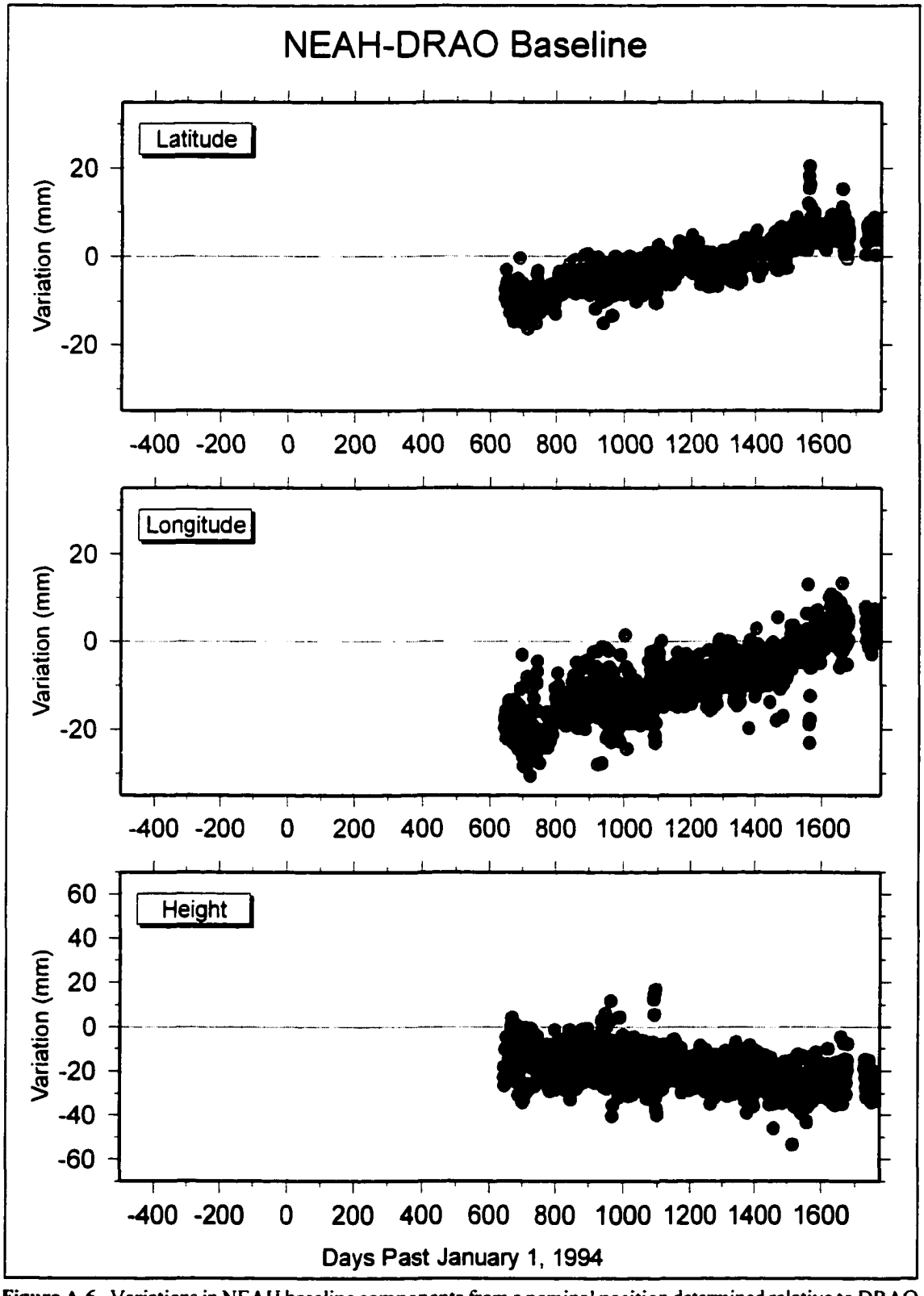

Figure A.6. Variations in NEAH baseline components from a nominal position determined relative to DRAO.

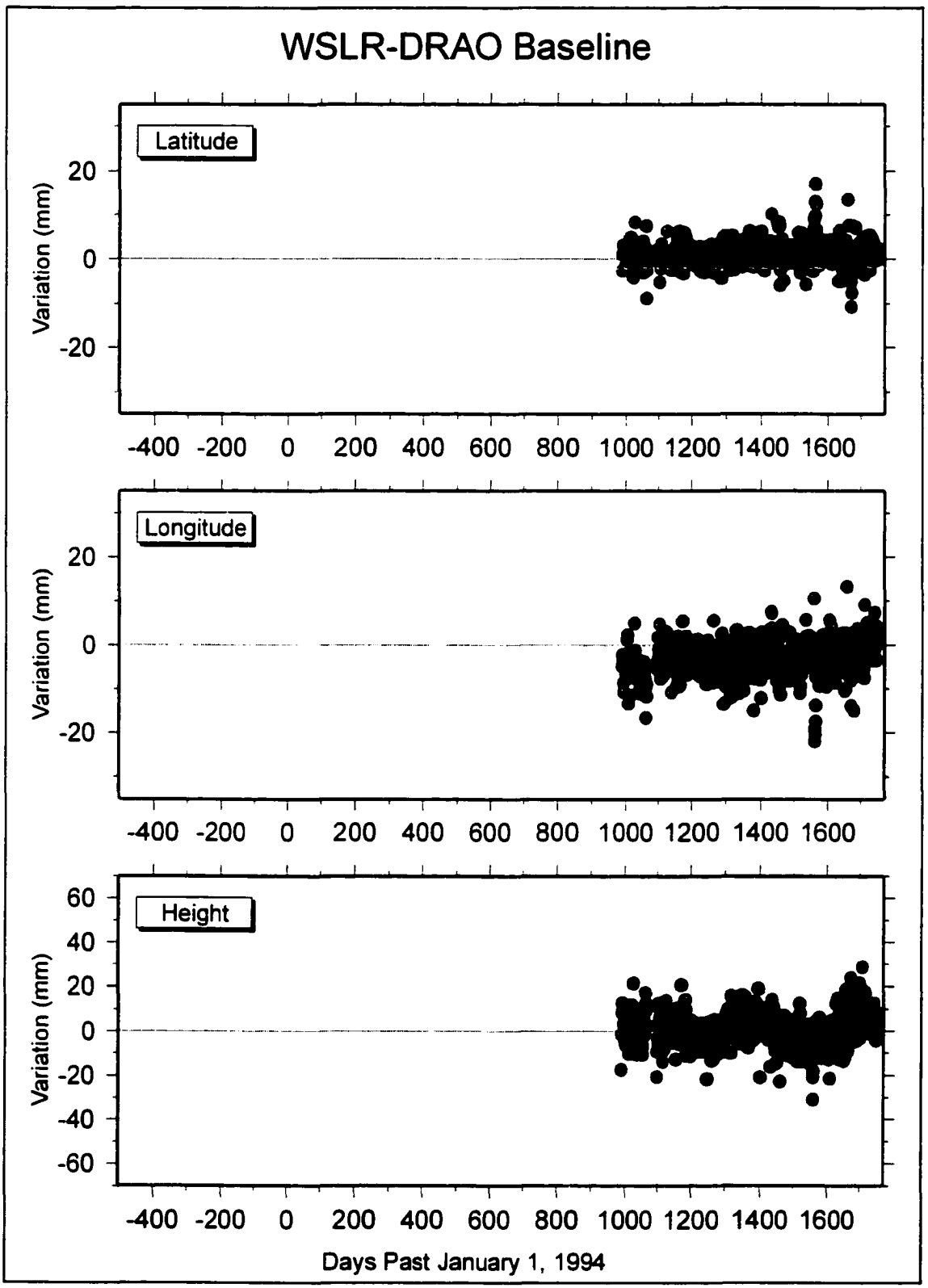

Figure A.7. Variations in WSLR baseline components from a nominal position determined relative to DRAO.

APPENDIX B

The least squares amplitude spectra for periods of 20 to 500 days for the WCDA baseline components (latitude, longitude, & height) are plotted in Appendix B as Figures B.1 -B.7. The predominate energy is annual period. The least squares amplitude spectra for periods of 9 to 20 days for the WCDA baseline components are plotted in Appendix B as Figures B.8 -B.14.

These data are discussed in Sections 4.6.3. & 4.6.4.

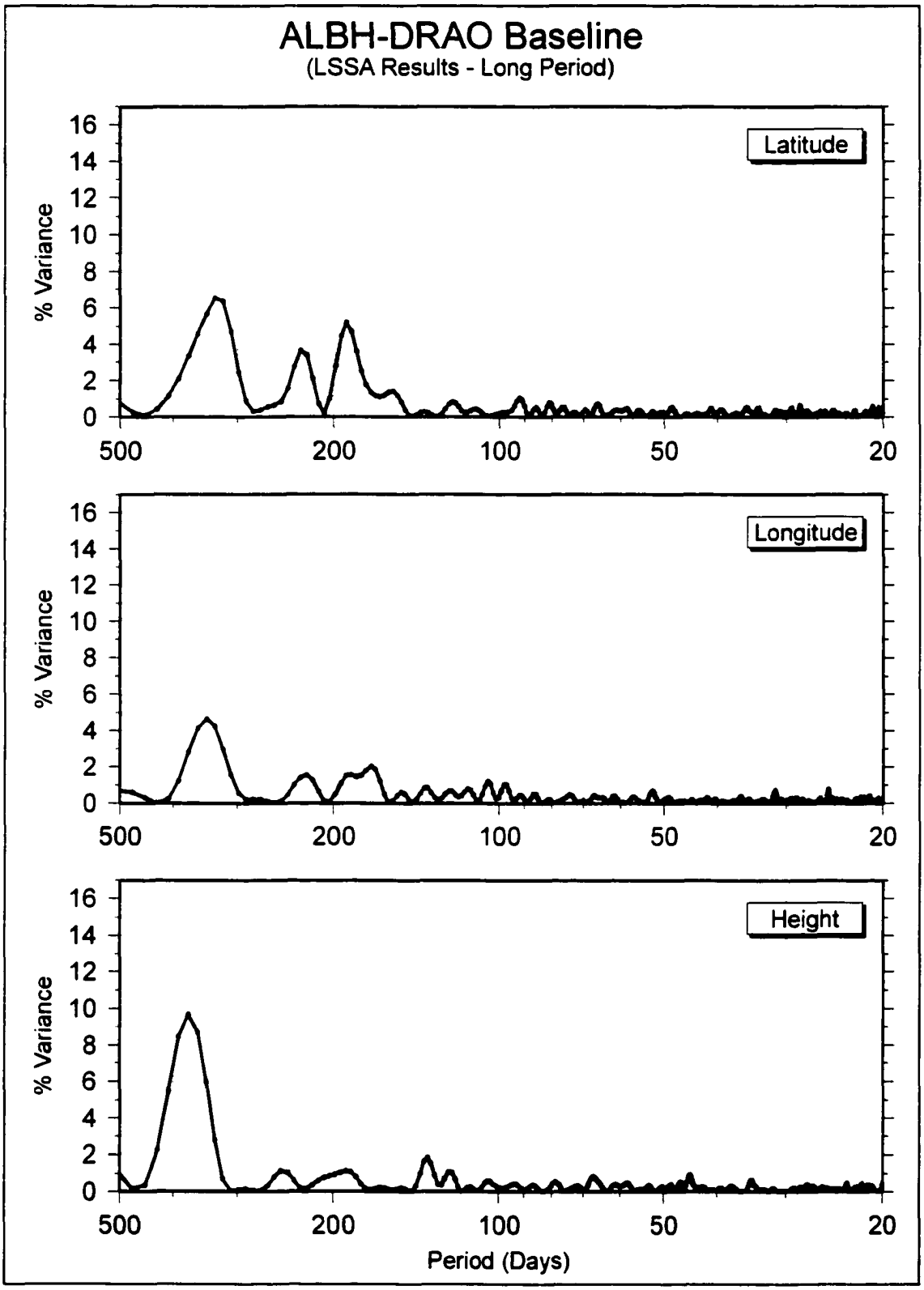

Figure B.1. Baseline spectra of 500 to 20 day periods for ALBH.

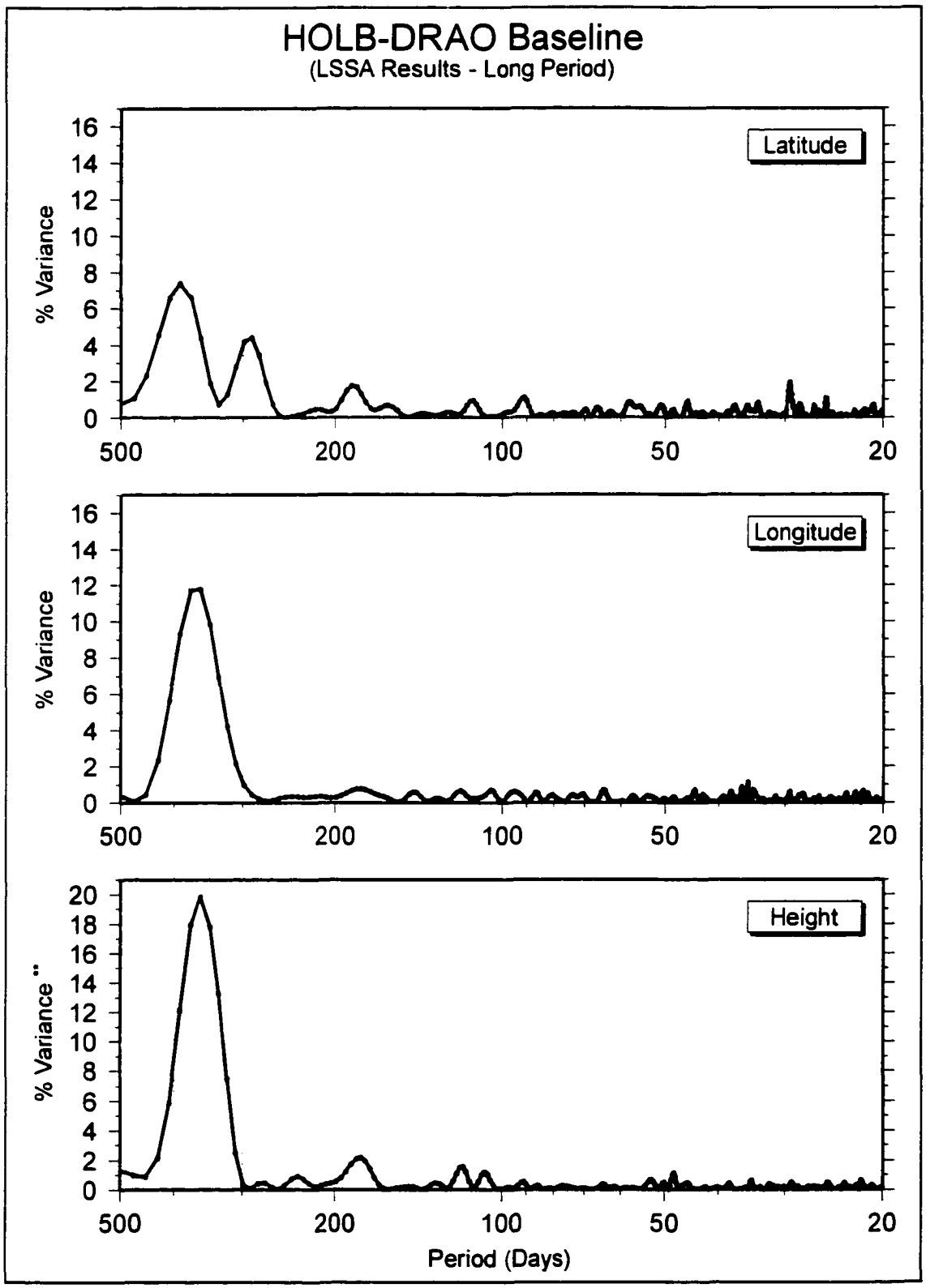

Figure B.2. Baseline spectra of 500 to 20 day periods for HOLB.

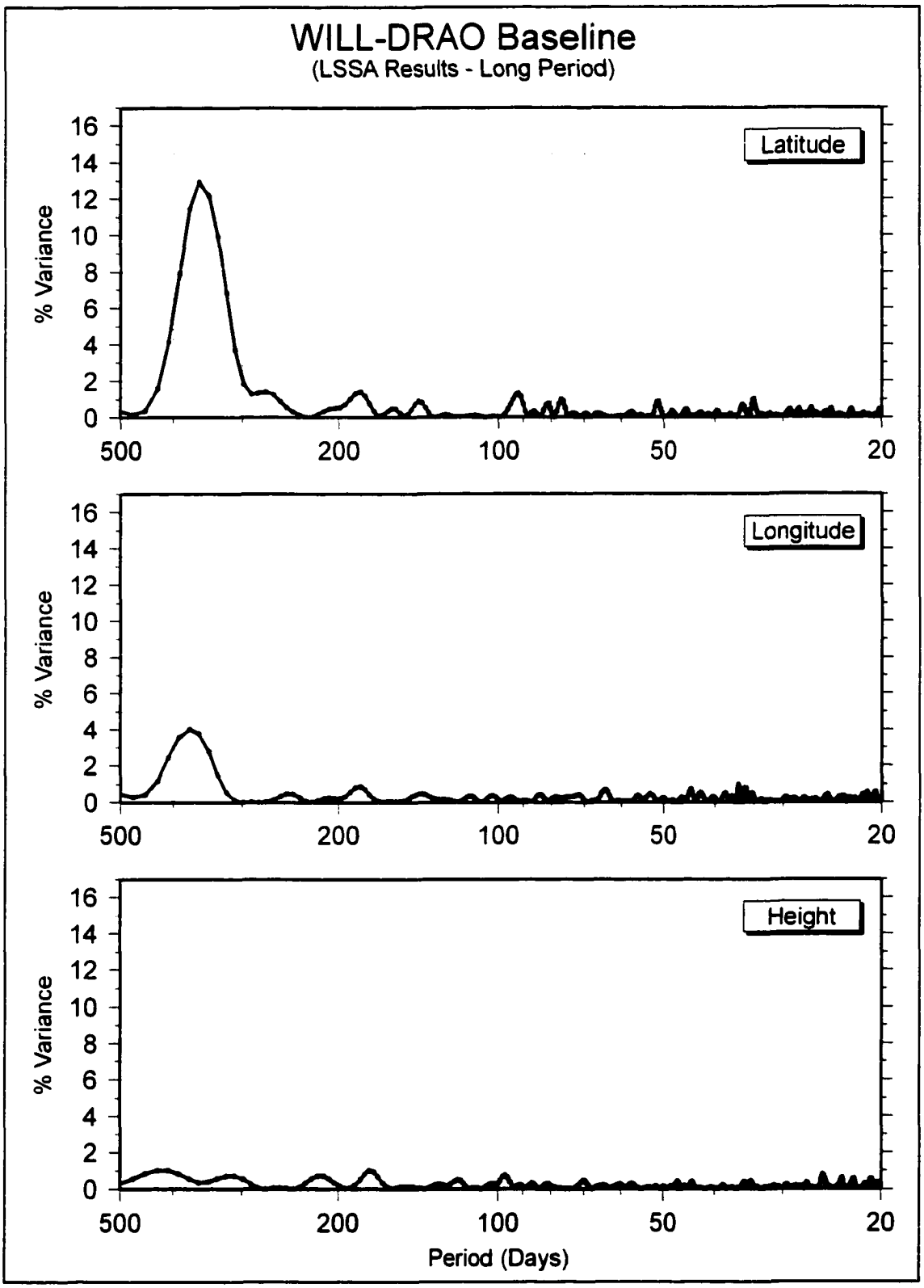

Figure B.3. Baseline spectra of 500 to 20 day periods for WILL.

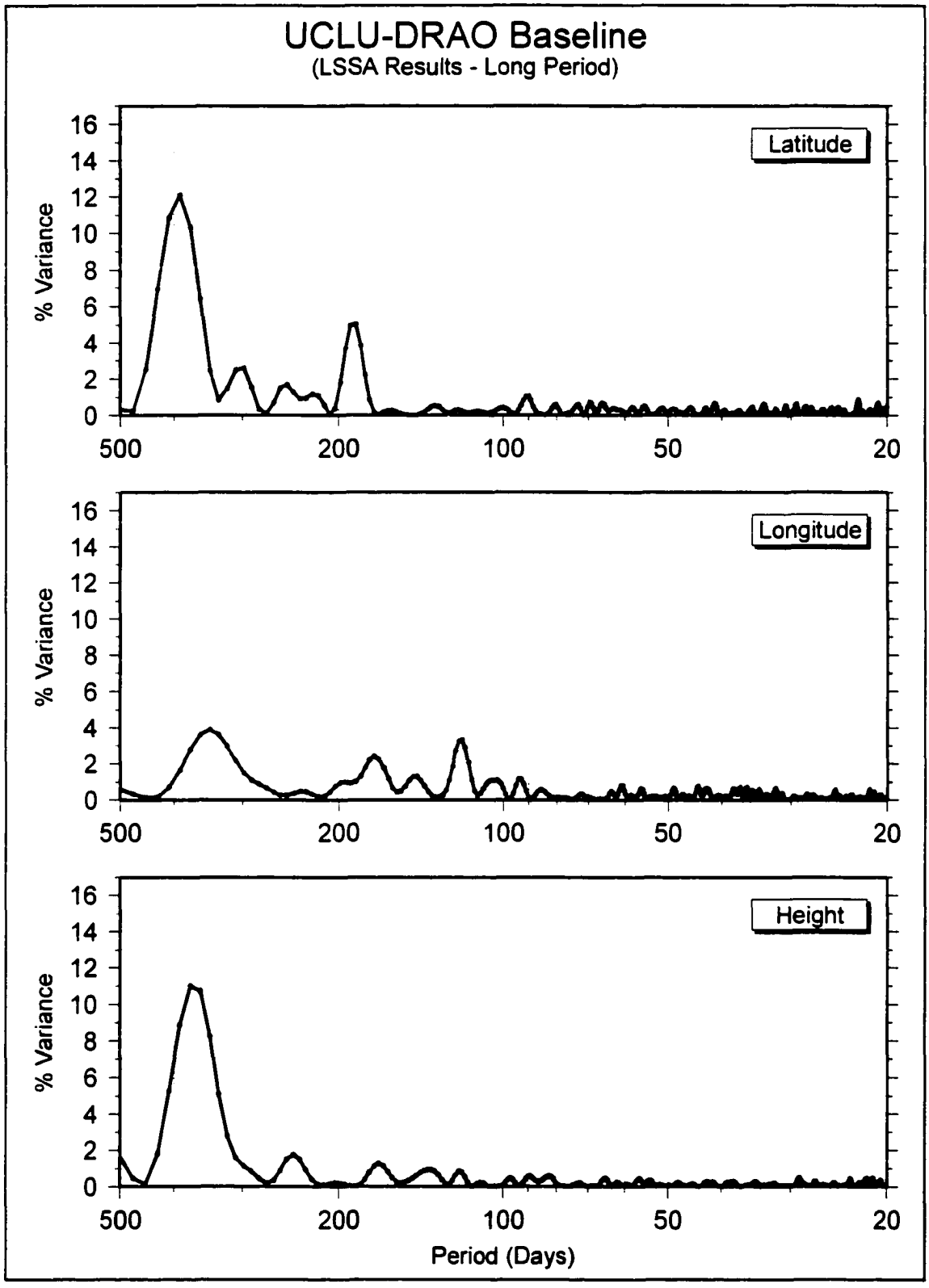

Figure B.4. Baseline spectra of 500 to 20 day periods for UCLU.

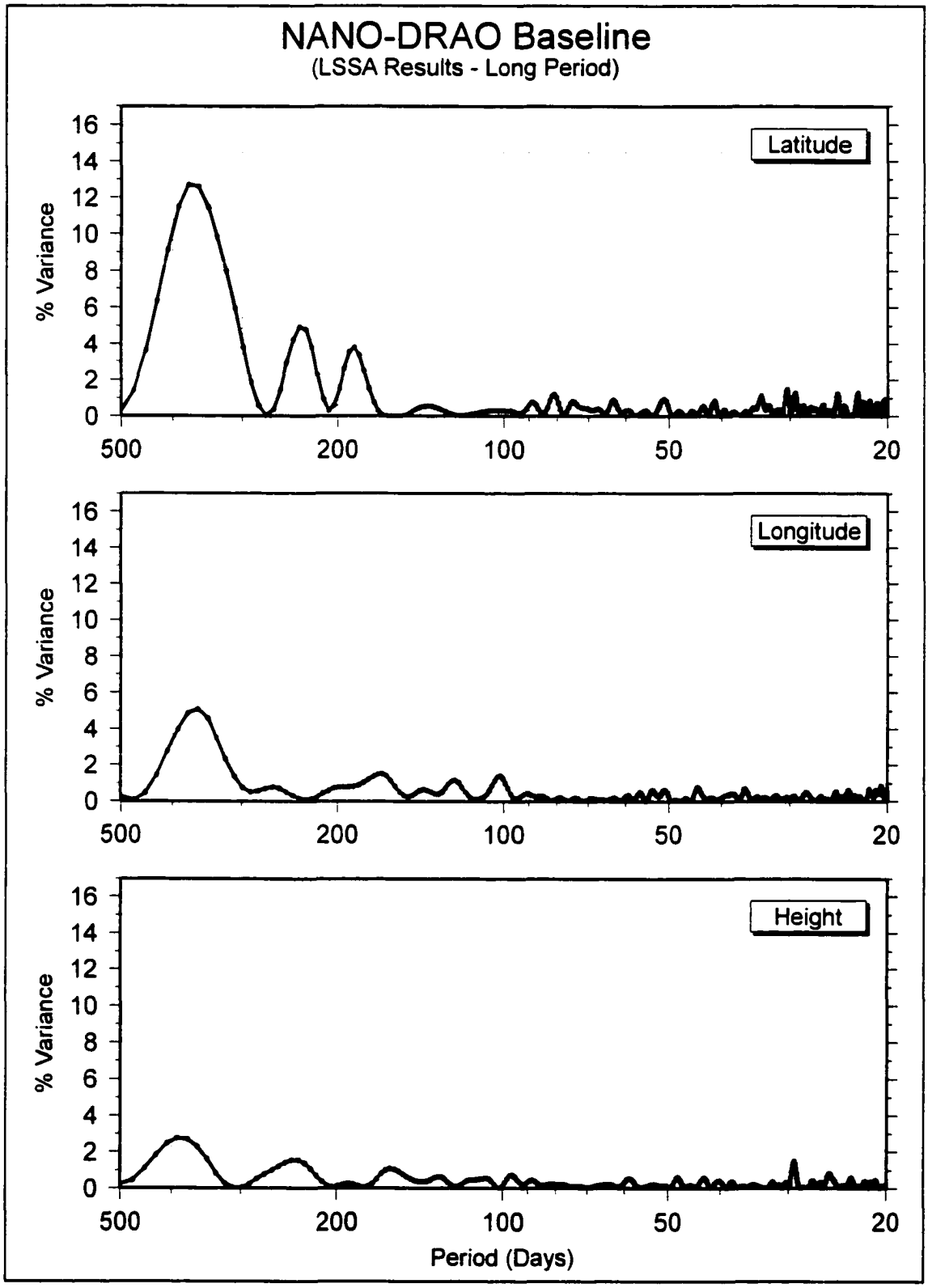

Figure B.5. Baseline spectra of 500 to 20 day periods for NANO.

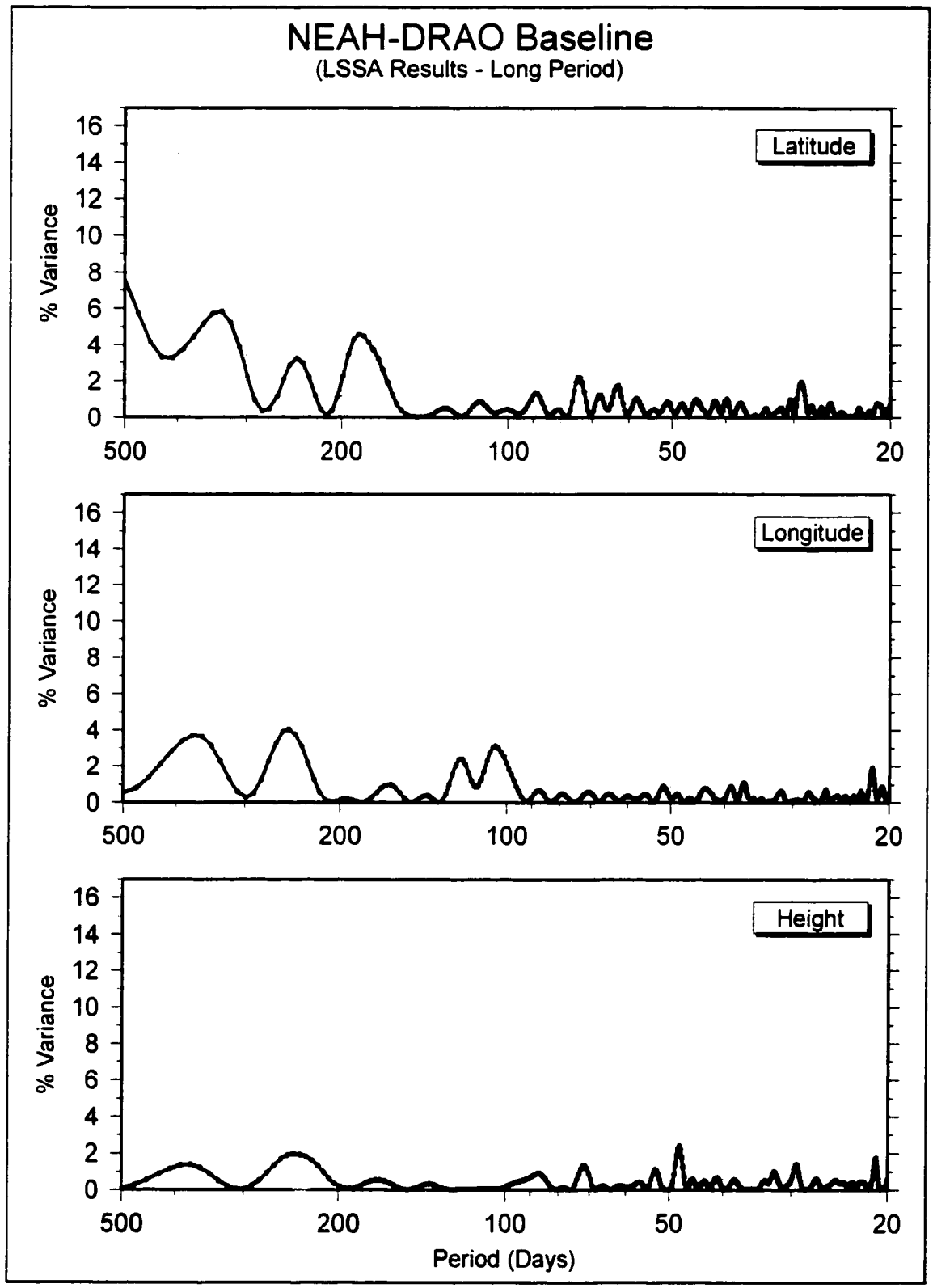

Figure B.6. Baseline spectra of 500 to 20 day periods for NEAH.

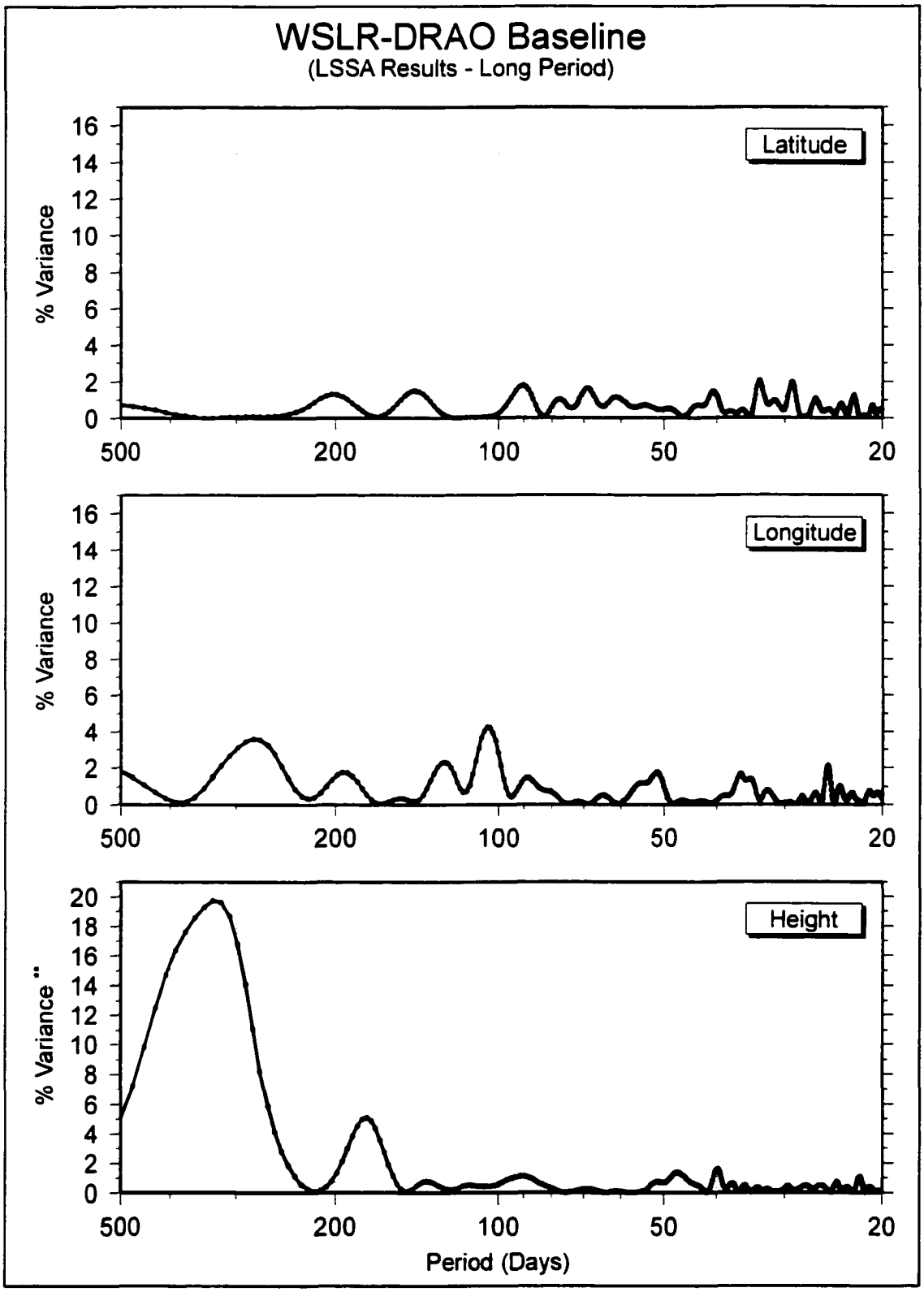

Figure B.7. Baseline spectra of 500 to 20 day periods for WSLR.

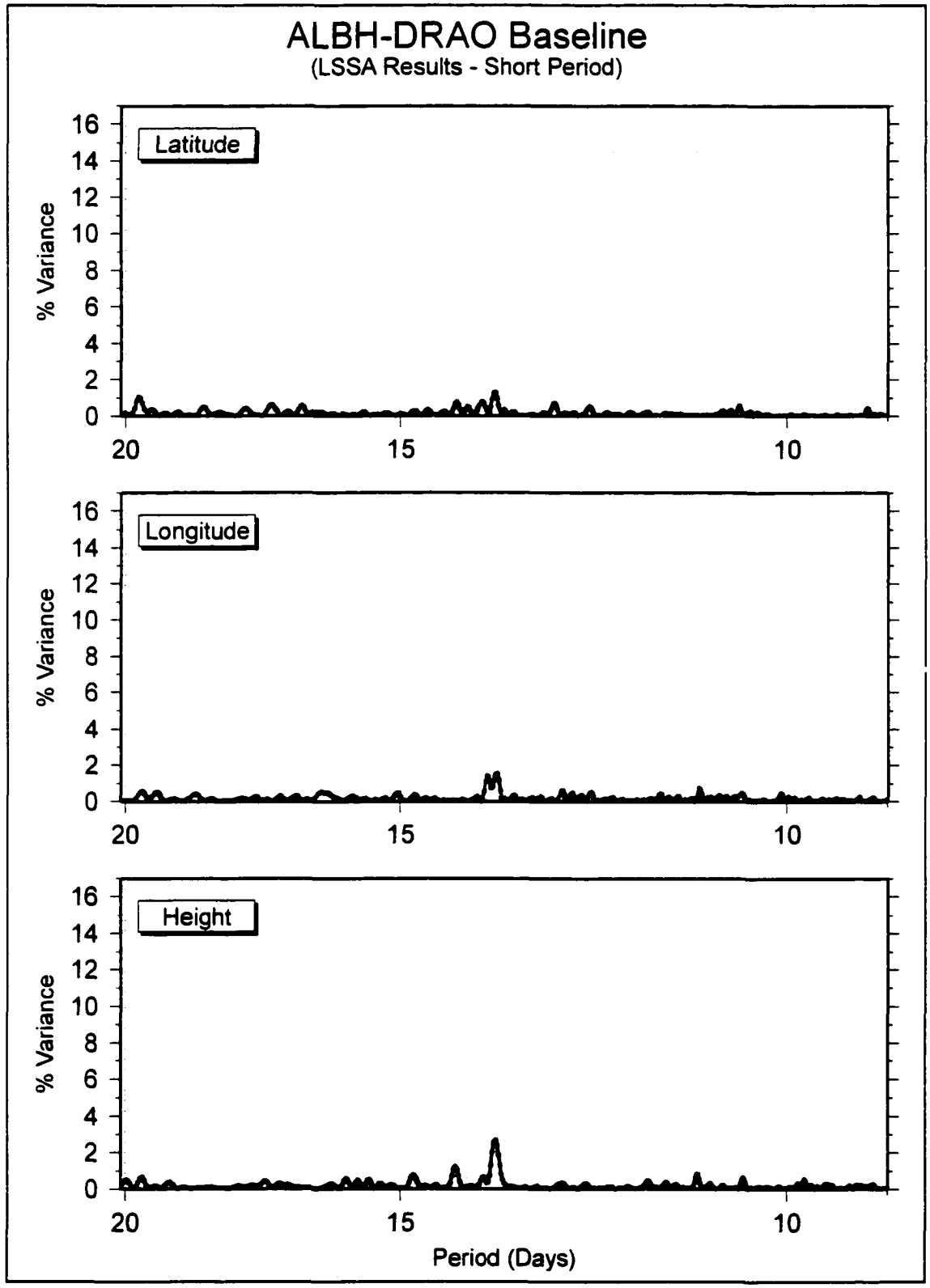

Figure B.8. Baseline spectra of 20 to 9 day periods for ALBH.

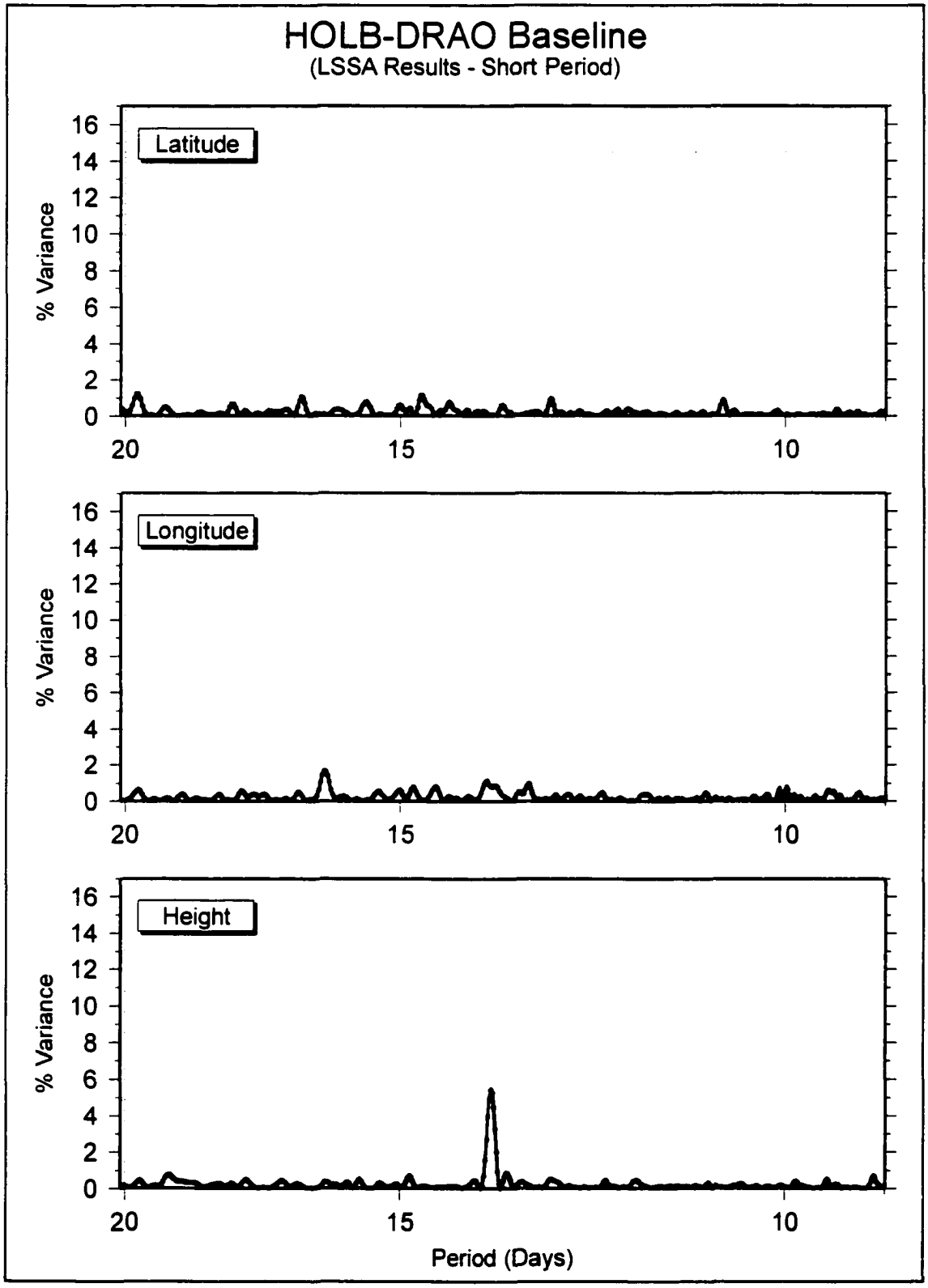

Figure B.9. Baseline spectra of 20 to 9 day periods for HOLB.

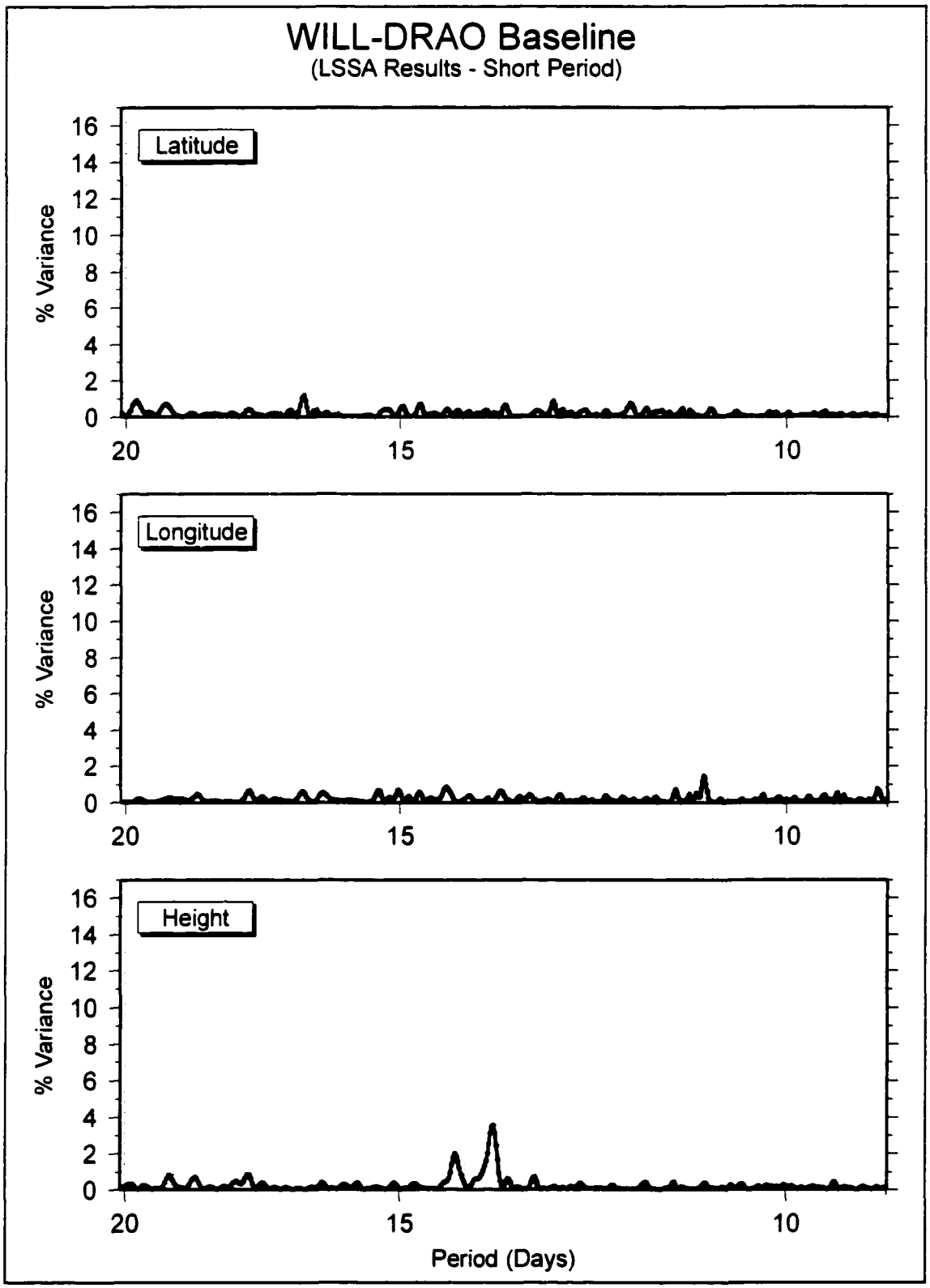

Figure B.10. Baseline spectra of 20 to 9 day periods for WILL.

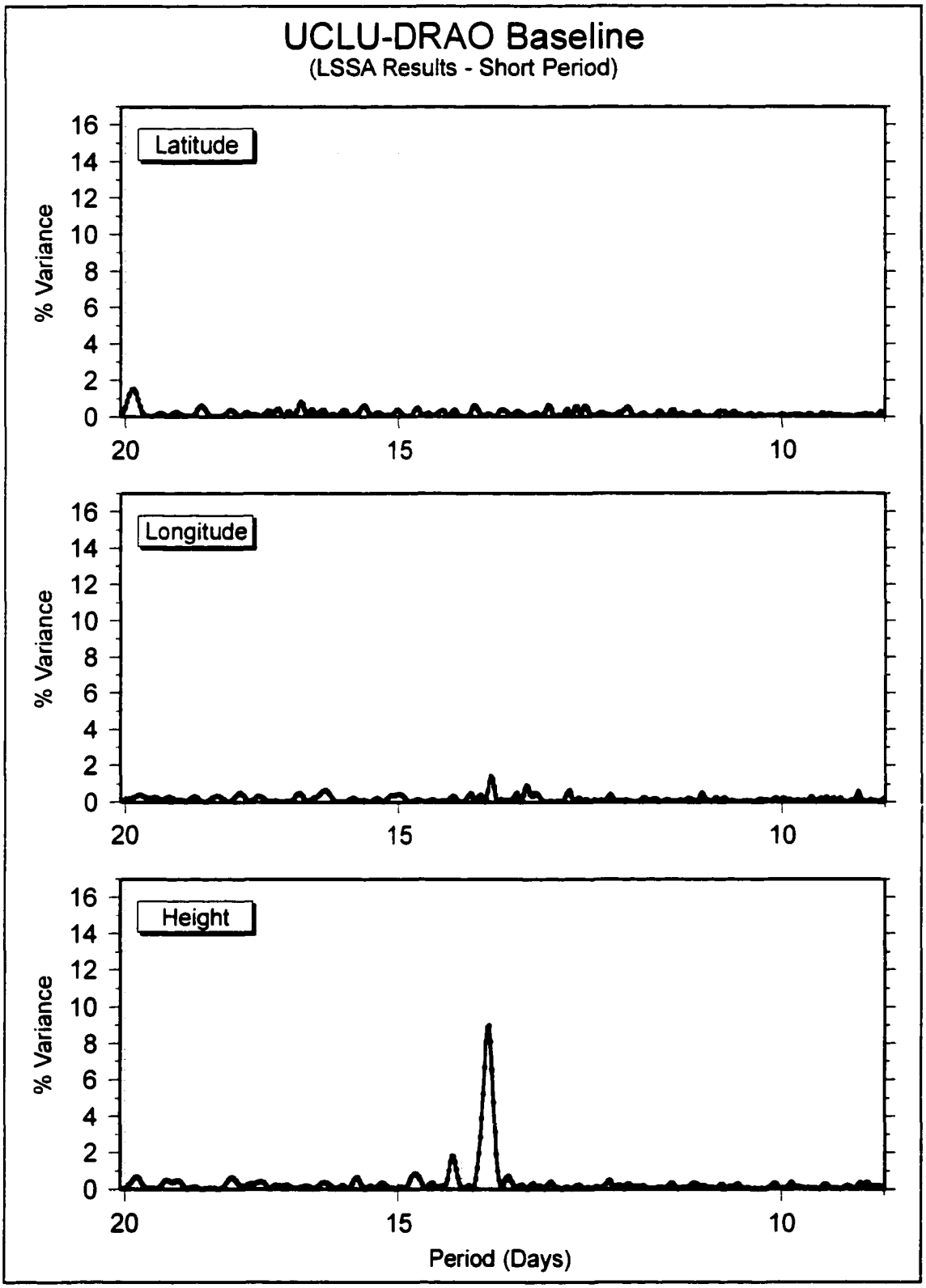

Figure B.11. Baseline spectra of 20 to 9 day periods for UCLU.

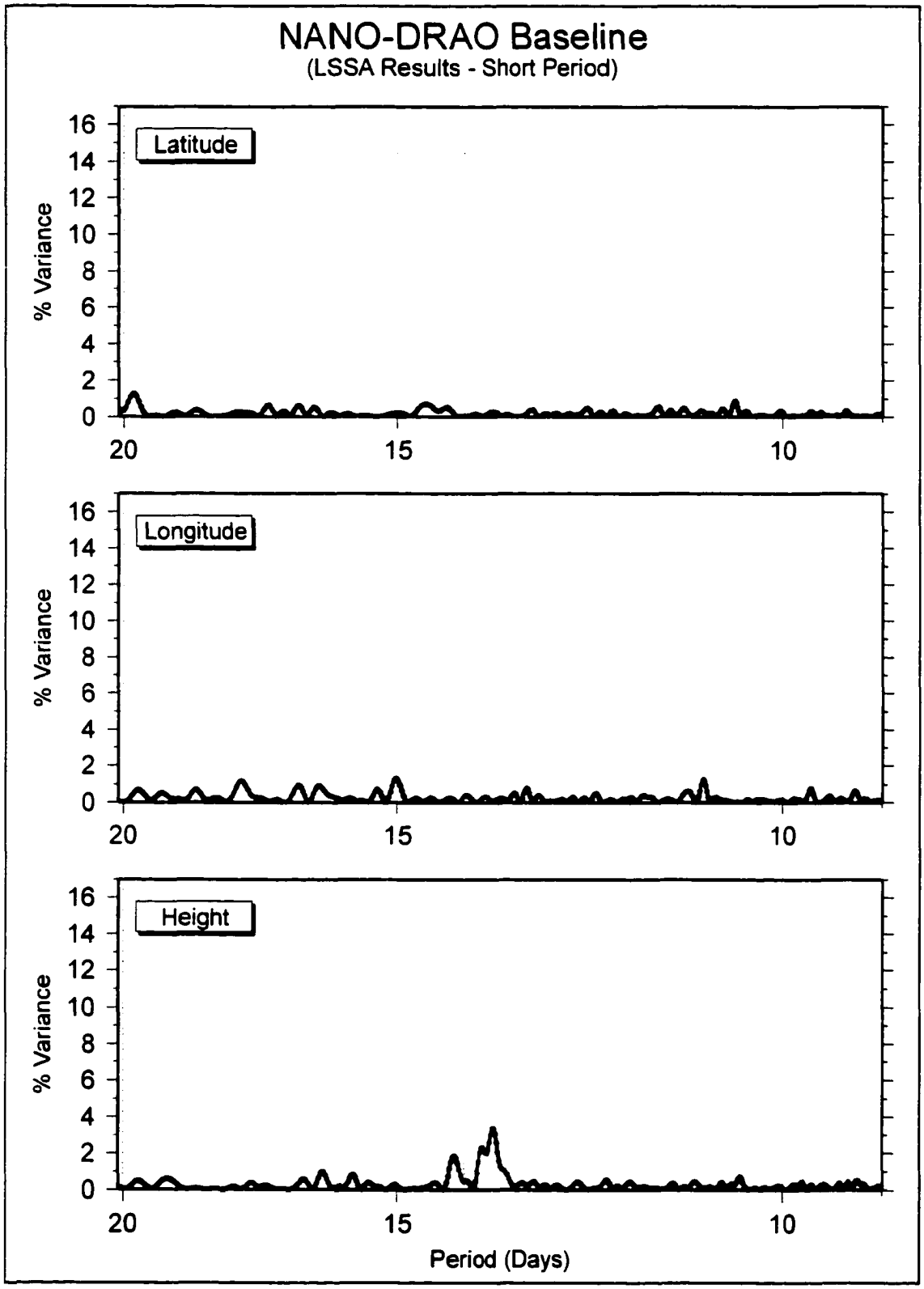

Figure B.12. Baseline spectra of 20 to 9 day periods for NANO.

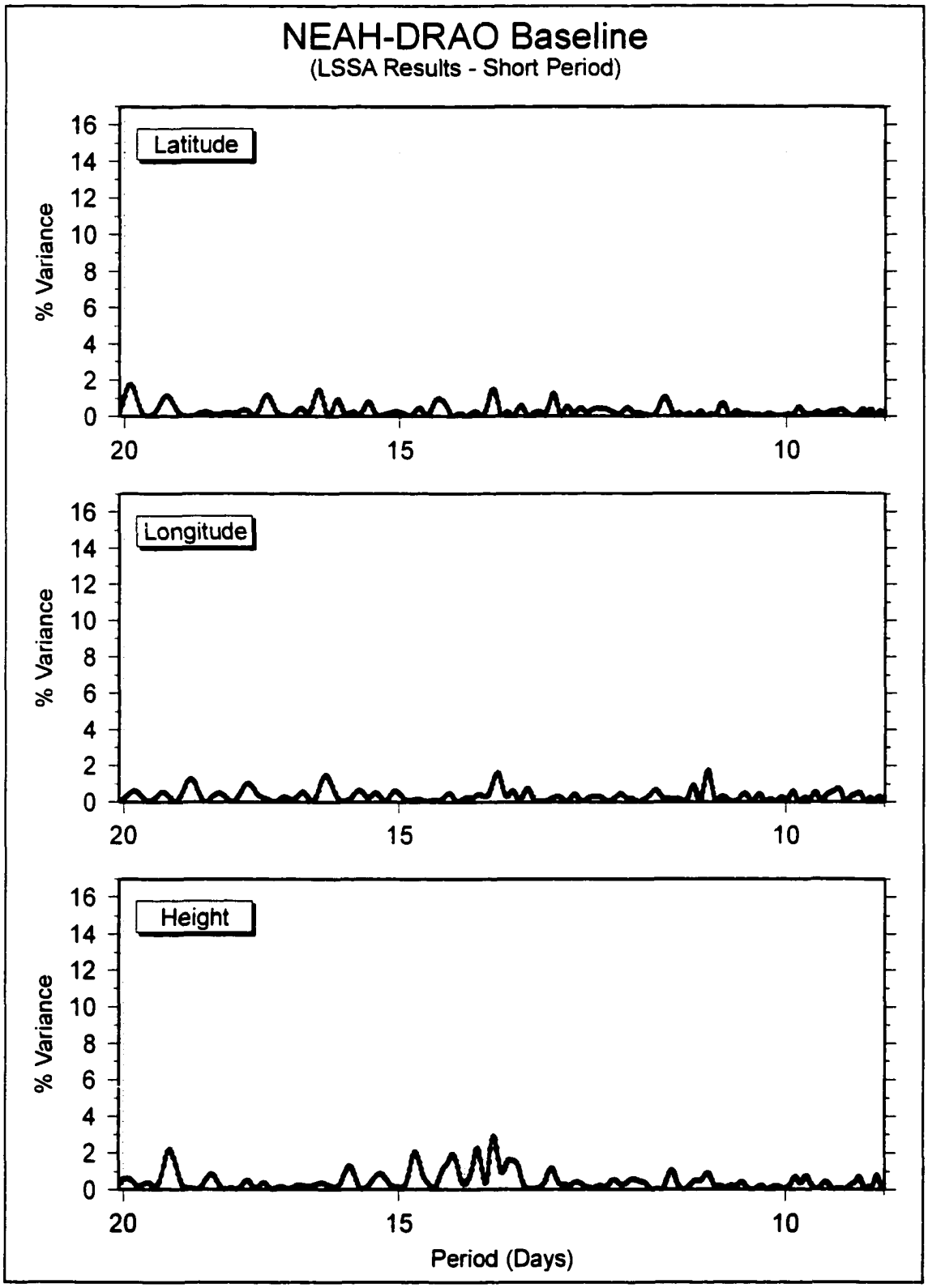

Figure B.13. Baseline spectra of 20 to 9 day periods for NEAH.

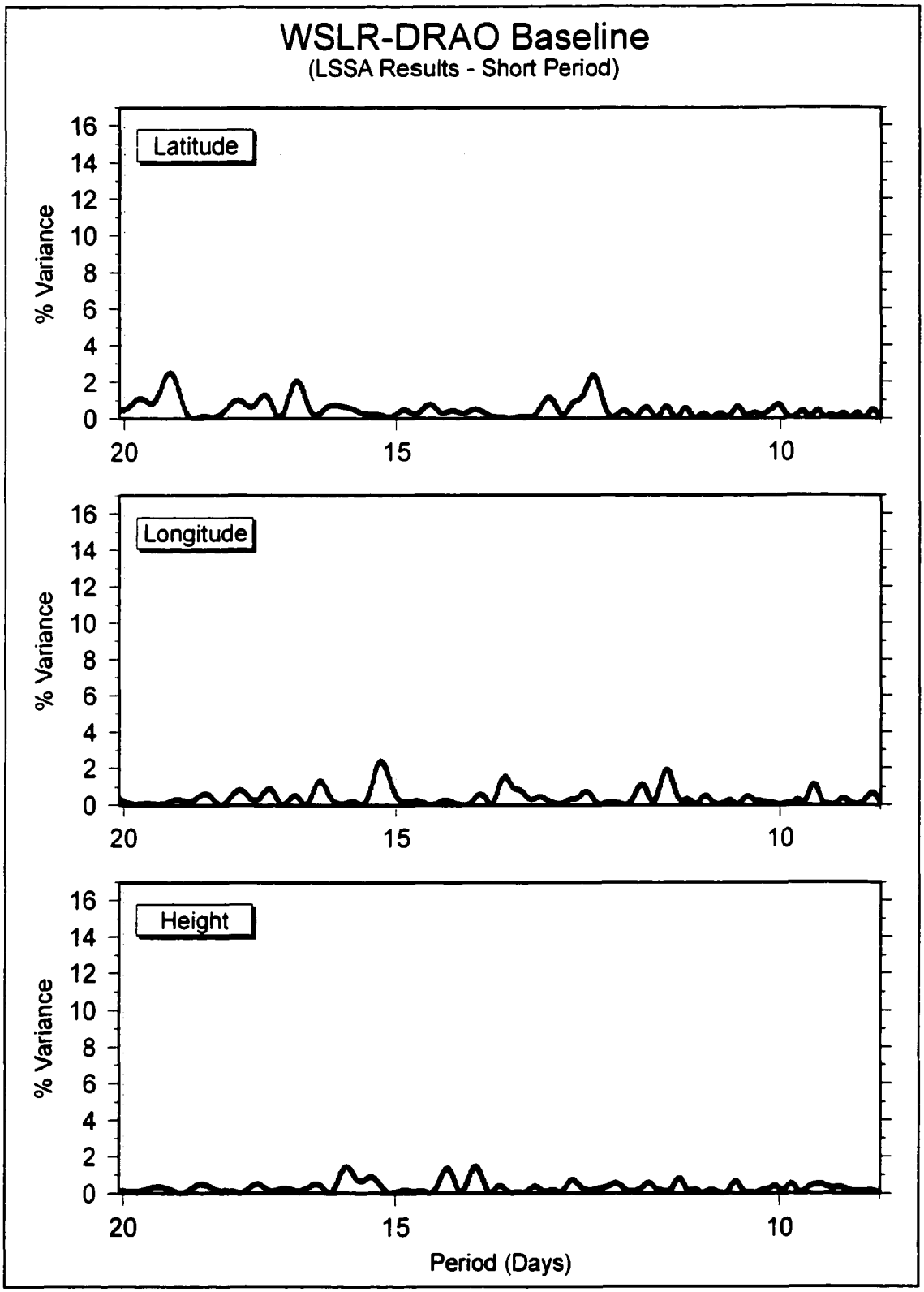

Figure B.14. Baseline spectra of 20 to 9 day periods for WSLR.

APPENDIX C

Comparisons of differential vertical GPS time series to meteorological time series of differential pressure and differential temperature are plotted for Holberg/Port Hardy-Penticton and Williams Lake-Penticton. The data plots exhibit sinusoids of annual period large enough in amplitude to visually identify in the baseline time-series.

These data are discussed in Section 4.6.3.

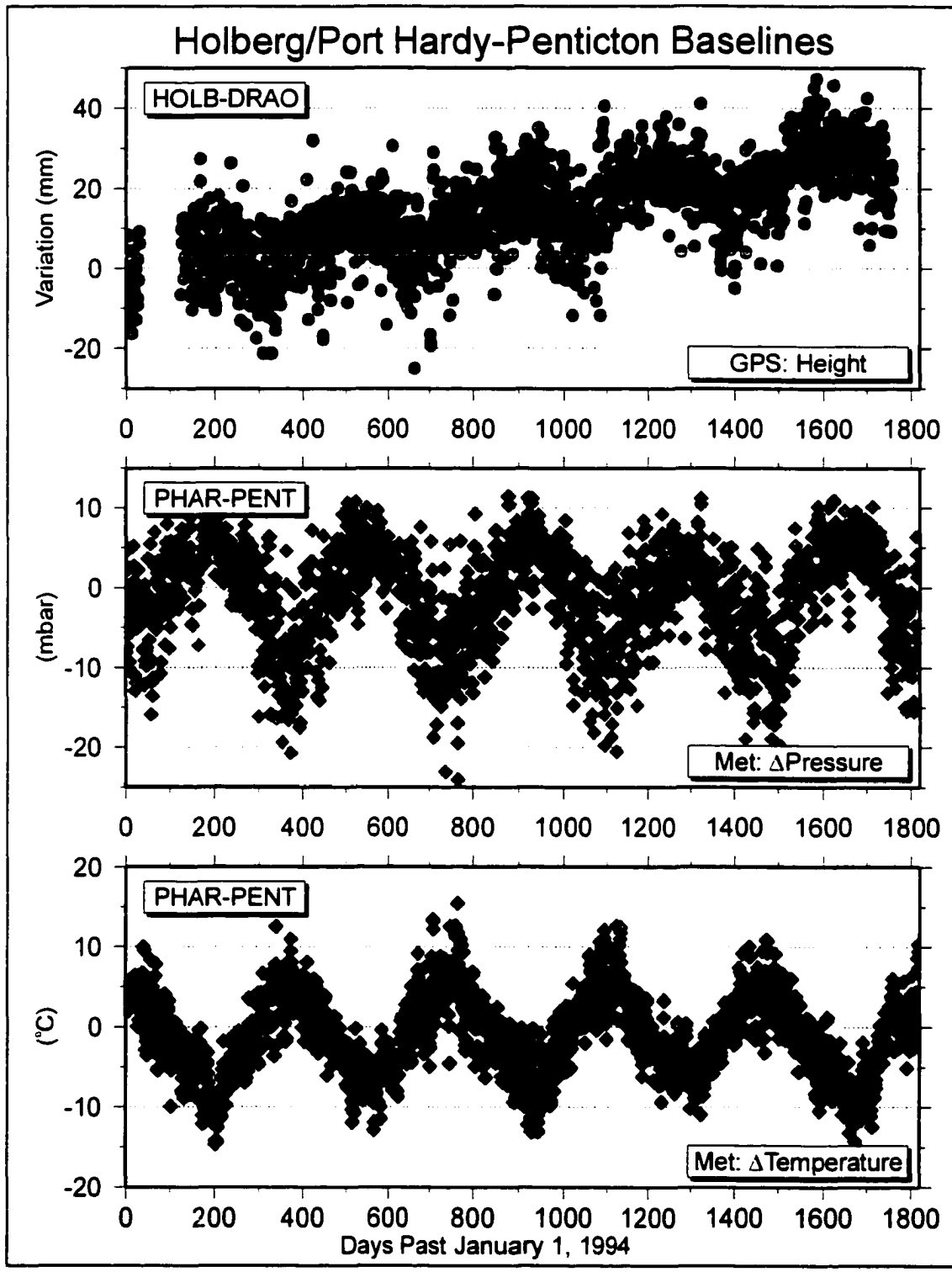

Figure C.1. Comparison of HOLB-DRAO vertical GPS time series to PHAR-PENT meteorological time series of differential pressure and differential temperature. (These data are discussed in Section 4.6.3.)

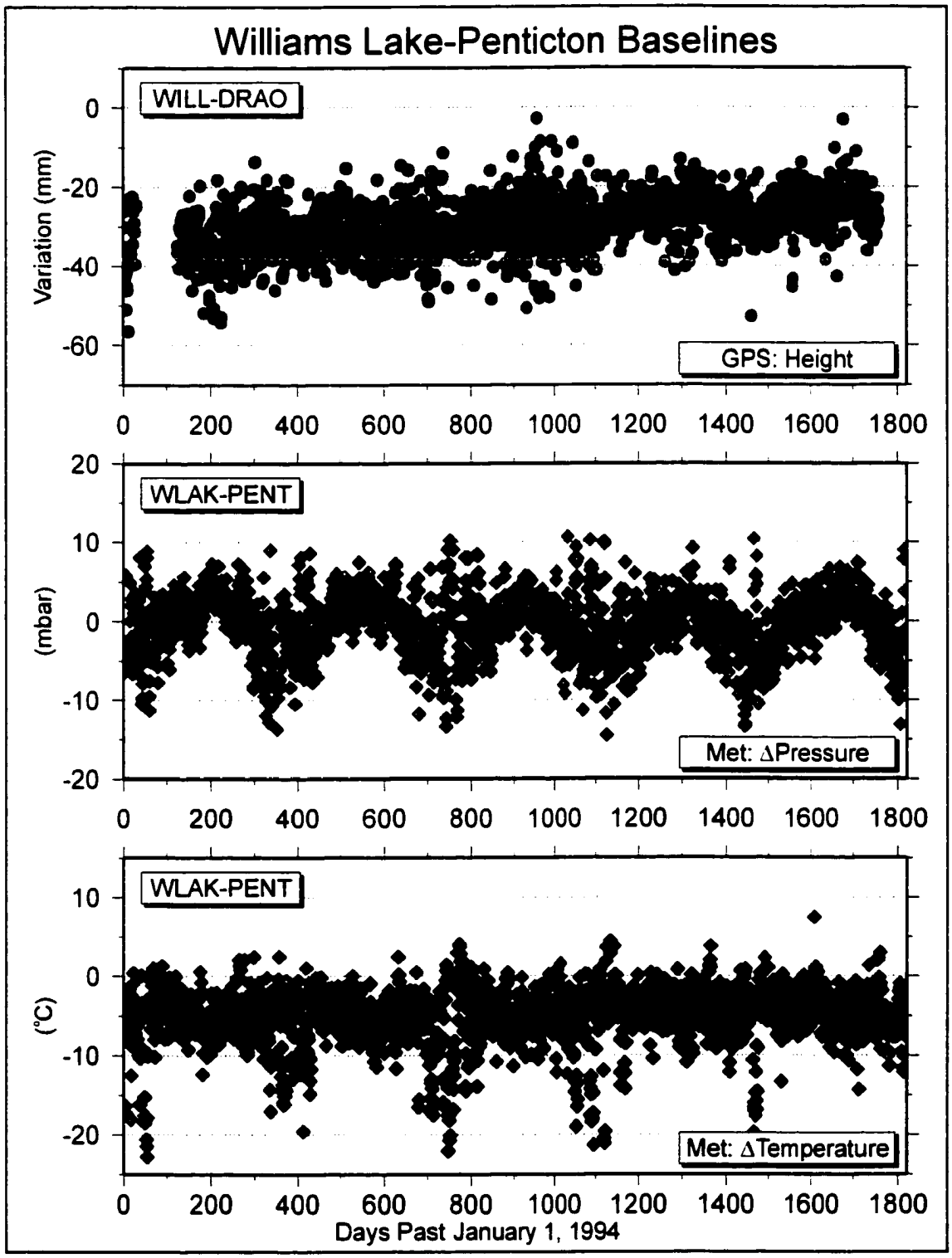

Figure C.2. Comparison of WILL-DRAO vertical GPS time series to WLAK-PENT meteorological time series of differential pressure and differential temperature. (These data are discussed in Section 4.6.3.)

APPENDIX D

(Miscellaneous Tables)

Station	Site Number	Latitude	Longitude	Height	Start Date
DRAO	40105M002	49° 19′ 21.48″	-119° 37′ 29.82″	537.29	FEB 1991
ALBH	40129M003	48° 23′ 23.27″	-123° 29′ 14.80″	27.01	MAY 1992
HOLB	40130M001	50° 38′ 25.34″	-128° 8′ 5.91″	554.81	JUL 1992
WILL	40134M001	52° 14′ 12.79″	-122° 10′ 4.01″	1091.11	OCT 1993
UCLU	40140M001	48° 55′ 32.35″	-125° 32′ 29.82″	5.28	MAY 1994
NANO	40138M001	49° 17′ 41.37″	-124° 5′ 11.23″	1.85	MAY 1995
NEAH	Cheeka Peak	48° 17′ 52.33″	-124° 37′ 29.58″	455.07	OCT 1995
WSLR	40141M001	50° 7′ 35.60″	-122° 55′ 16.18″	904.60	SEP 1996

Table D.1. Positions and Starting Dates of WCDA Sites Used in this Dissertation

WCDA Station	Vertical Velocity (mm/yr)	95% Confidence (mm/yr)	Number Obs.
ALBH	-0.9	0.6	1985
NANO	0.1	1.1	1234
UCLU	-2.6	1.1	1609
NEAH	-4.3	1.8	1016
HOLB	6.3	0.8	1981
WSLR	0.6	1.4	726
WILL	2.2	0.7	1627

Table D.2. WCDA Vertical Velocities from Regression by *Dragert et al.* [1998].

(Positive velocities denote uplift).

Site Name	Displacement North (cm)	North 1σ Error (cm)	Displacement East (cm)	East 1σ Error (cm)
ATKI	1.23	0.13	2.05	0.27
BEEC	1.59	0.08	2.32	0.16
BONI	3.36	0.14	2.93	0.33
BOUN	1.25	0.12	1.08	0.27
CHEM	1.62	0.10	1.80	0.20
CONS	1.74	0.09	2.28	0.19
DISC	1.81	0.09	1.34	0.22
DOUG	1.47	0.08	2.15	0.17
GABR‡	1.22	0.31	1.40	0.18
JORD	1.76	0.09	2.41	0.18
LAZA	1.73	0.08	2.19	0.17
RENF	2.33	0.13	2.83	0.25
SATU	0.93	0.11	1.22	0.24
SHER	1.70	0.08	3.01	0.18
YOUB	2.08	0.11	2.16	0.23

Table D.3. Site Displacements (1991–1996) for the Juan de Fuca GPS Network

‡ Station GABR displacement is from regression and includes data collected in the summer of 1998 (*refer to* discussion in Section 5.3). These values plotted in Figure 5.4 and are not corrected for differential North American plate motion between the site and DRAO.

Site Name	Displacement North (cm)	North 1σ Error (cm)	Displacement East (cm)	East 1σ Error (cm)
ALEX	1.78	0.3	2.48	0.3
ANAW	1.54	0.3	1.71	0.4
ANNA	0.24	0.3	0.93	0.3
BCHR	0.69	0.4	2.82	0.3
BREW	1.32	0.4	2.72	0.7
FILB	0.62	0.2	1.21	0.3
GLAC	1.18	0.4	3.04	0.3
HART	0.55	0.2	1.78	0.2
HKUS	0.96	0.4	1.05	0.3
MENZ	1.02	0.4	0.83	0.4
MOAK	0.61	0.3	1.94	0.3
NACH	1.37	0.3	1.02	0.3
OYST	1.03	0.2	1.80	0.2
PIER	1.20	0.3	2.41	0.4
SENT	0.42	0.3	0.76	0.4
STRA	0.70	0.2	1.01	0.2
WASH	0.96	0.3	1.37	0.3

Table D.4. Site Displacements (1992–1997) for the Central Vancouver Island GPS Network

These values plotted in Figure 5.11 and are not corrected for differential North American plate motion between the site and DRAO